

Dissertation
submitted to the
Combined Faculties for the Natural Sciences and for Mathematics
of the Ruperto-Carola University of Heidelberg, Germany
for the degree of
Doctor of Natural Sciences

Put forward by

Diplom-Physikerin (Medizinphysik) Bernadette Hartmann

Born in: Tübingen, Germany

Oral examination: November 6th, 2013

A Novel Approach to Ion Spectroscopy
of Therapeutic Ion Beams
Using a Pixelated Semiconductor Detector

Referees: Prof. Dr. Wolfgang Schlegel
Prof. Dr. Oliver Jäkel

Erklärung

Ich erkläre hiermit, dass ich die vorgelegte Dissertation selbst verfasst und mich dabei keiner anderen, als der von mir ausdrücklich bezeichneten Quellen und Hilfen bedient habe.

Heidelberg, den 19.09.2013

Bernadette Hartmann

Zusammenfassung

In der hochpräzisen Strahlentherapie mit Kohlenstoffionen entstehen durch die Fragmentierung von Primärkernen im Patienten leichtere Ionen. Da sich die radio-biologische Wirksamkeit verschiedener Primär- und Sekundärionen unterscheidet, müssen letztere in der Bestrahlungsplanung separat berücksichtigt werden. Bisher wurden zur Bestimmung der entsprechenden Spektren überwiegend sehr große Versuchsaufbauten benutzt, die auf Szintillationsdetektoren basieren. Dadurch sind jedoch die Flexibilität der Methoden und die Menge an verfügbaren Daten eingeschränkt. In dieser Arbeit wird eine neue Methode zur Ionenspektroskopie mittels eines kleinen Pixel-Halbleiterdetektors präsentiert. Der verwendete Timepix-Detektor wurde ursprünglich für die Bildgebung mit Photonen konzipiert. Er bietet eine hohe räumliche Auflösung, welche die Detektion einzelner Ionen ermöglicht.

Zuerst wurde das Ansprechverhalten des Detektors auf therapeutische Ionenstrahlung umfangreich charakterisiert. Es wurde festgestellt, dass sich der Detektor für Energieverlust-Messungen einzelner Protonen mit Energien zwischen 0.55 und 221 MeV eignet. Der mittlere Energieverlust weicht weniger als 10% von entsprechenden Berechnungen ab. Für die untersuchten schwereren Ionen wurden Abweichungen von bis zu 30% beobachtet.

Die präsentierte neuartige Methode zur Unterscheidung von Fragmenten beruht auf einer Mustererkennungs-Analyse des durch einzelne Ionen im Timepix-Detektor induzierten Signals. In gemischten Teilchenfeldern, die aus der Fragmentierung von ^{12}C -Ionen entstehen, können für ausgewiesene Anordnungen alle Ionensorten identifiziert werden. Um die Methode zu untersuchen wurden Referenzdaten einer etablierten Technik verwendet. Die gemessenen relativen Anteile von H-, He-, Be-, and B-Ionen stimmen innerhalb von $1.1 \Delta_{\text{ref}}$ (Unsicherheit der Referenz) überein. Für Lithium wurde eine Übereinstimmung innerhalb von $2.3 \Delta_{\text{ref}}$ festgestellt. Weiterhin werden Anwendungen der Methode vorgestellt, die für die Bewertung von physikalischen Modellen relevant sind, wie sie in Monte Carlo Simulationen und in der Bestrahlungsplanung verwendet werden. Durch den kleinen und flexiblen Aufbau ist die präsentierte Methode, unter Berücksichtigung der vorgeschlagenen Verbesserungen, vielversprechend die verfügbaren Datensätze zur Fragmentierung auszuweiten und somit das Potential von großen Versuchsaufbauten zu ergänzen.

Abstract

In highly precise carbon ion radiotherapy, fragmentation of the primary nuclei in the patient results in a spectrum of lighter ions. Due to their radio-biological effectiveness being different from the primary ions, they need to be considered separately in therapy planning. To determine secondary ion spectra, mainly large apparatus based on scintillation detectors have been used until now, limiting the flexibility of the methods and the amount of available data. In this thesis, a novel method for ion spectroscopy based on a small pixelated semiconductor detector is presented. The used Timepix detector, originally designed for photon beam imaging, offers a high spatial resolution enabling the detection of single particles.

At first, an extensive characterization of the detector response to therapeutic ion beams was performed. The detector was found suitable for energy-loss measurements on a single ion basis in proton beams between 0.55 and 221 MeV, providing mean energy-loss values, which deviate less than only 10% from calculations. For the investigated heavier ions, deviations of up to about 30% were observed.

The presented novel experimental approach to fragment distinction with the Timepix detector is based on pattern recognition analysis of the signal created by individual ions. For designated configurations, it enables identification of all ion species in mixed particle fields resulting from ^{12}C -fragmentation. The performance of the method was evaluated using reference data of an established technique. The relative fractions of H-, He-, Be- and B-ions agree within $1.1 \Delta_{\text{ref}}$ (uncertainty of the reference). For lithium, the agreement is within $2.3 \Delta_{\text{ref}}$. In addition, applications of the method relevant for benchmarking physical models used in Monte Carlo simulations and treatment planning are presented. Providing the advantages of a small and flexible set-up, together with the further improvements suggested, the method is promising to widely expand the available fragmentation data and to complement large experimental set-ups.

Contents

Contents	I
1 Introduction	1
2 Physical Background: Interactions of Ions with Matter	5
2.1 Electronic Interactions	6
2.1.1 Energy-Loss	6
2.1.2 Energy-Loss Straggling	7
2.1.3 Particle Range and Range Straggling	10
2.1.4 Dose	10
2.1.5 Linear Energy Transfer	11
2.2 Nuclear Interactions	11
2.2.1 Multiple Coulomb Scattering	11
2.2.2 Fragmentation	12
3 Previous Studies on Nuclear Fragmentation in Therapeutic Ion Beams	15
4 Physical and Biological Aspects of Nuclear Fragmentation with Clinical Impact	19
4.1 Physical Aspects of Nuclear Fragmentation in Heavy Ion Radiotherapy	19
4.2 Physical Aspects of Nuclear Fragmentation in Proton Radiotherapy . .	22
4.3 Relative Biological Effectiveness	22
5 Materials and Methods	27
5.1 Radiation Facilities	27
5.1.1 The Heidelberg Ion-Beam Therapy Center (HIT)	27
5.1.2 Van-de-Graaff Accelerators at IEAP in Prague and at MLL in Garching	29
5.2 The Timepix Detector	30
5.2.1 Detector Design and Principles of Operation	31
5.2.2 Charge Sharing Effect	34
5.2.3 Influences on the Charge Collection Efficiency	38
5.2.4 Detector Calibration for Energy Measurements	38

CONTENTS

5.2.5	Single Particle Detection in Ion Beams with the Timepix Detector	40
5.3	Phantoms Used for the Measurements	43
5.4	Software Used for Data Acquisition, Processing, and Evaluation	44
5.4.1	Data Acquisition with Pixelman	44
5.4.2	Data Processing and Evaluation with Matlab	46
5.4.3	libamtrack	46
6	Experiments	47
6.1	Characterization of the Detector Response in Therapeutic Ion Beams	47
6.1.1	Influence of the Acquisition Time on the Measured Signal	49
6.1.2	Influences of the Bias Voltage on the Measured Signal	52
6.1.3	Investigations of Small Clusters	53
6.1.4	Angular Dependency of the Detector Signal	53
6.1.5	Uniformity of the Detector Response over the Sensitive Area	54
6.1.6	Investigations of Detector Response Changes with Time	55
6.2	Energy-Loss Measurements	55
6.2.1	Measurements of the Mean Energy-Loss Free-in-Air and in Vacuum	55
6.2.2	Energy-Loss Straggling - Comparison of Measurements and Calculations	59
6.2.3	Measurements in Different Material Depths	60
6.3	Ion Spectroscopy	61
6.3.1	Identification of Ion Species by Measurements in Different Material Depths	64
6.3.2	Verification of the Identification	65
6.3.3	Application I: Lateral Fragment Distributions	65
6.3.4	Application II: Fragmentation in Different Materials	67
7	Results	69
7.1	Characterization of the Detector Response in Therapeutic Ion Beams	69
7.1.1	Influence of the Acquisition Time on the Measured Signal	69
7.1.2	Influences of the Bias Voltage on the Measured Signal	79
7.1.3	Investigations of Small Clusters	89
7.1.4	Angular Dependency of the Detector Signal	93
7.1.5	Uniformity of the Detector Response over the Sensitive Area	99
7.1.6	Investigations of Detector Response Changes with Time	106
7.2	Energy-Loss Measurements	112
7.2.1	Measurements of the Mean Energy-Loss Free-in-Air and in Vacuum	112
7.2.2	Energy-Loss Straggling - Comparison of Measurements and Calculations	118
7.2.3	Measurements in Different Material Depths	123

7.2.4	Mean Energy-Loss: Quantitative Comparison of All Measurements	124
7.3	Ion Spectroscopy	127
7.3.1	Identification of Ion Species by Measurements in Different Material Depths	128
7.3.2	Verification of the Identification	133
7.3.3	Application I: Lateral Fragment Distributions	136
7.3.4	Application II: Fragmentation in Different Materials	138
8	Discussion and Outlook	143
8.1	Characterization of Detector Response in Therapeutic Ion Beams	143
8.2	Energy-Loss Measurements	146
8.3	Ion Spectroscopy	149
8.4	Future Impact of the Results	153
9	Summary and Conclusions	155
	Appendices	159
	Bibliography	181

CONTENTS

1 Introduction

Using proton and heavier ion beams for radiotherapeutic patient treatment offers several advantages over the conventionally employed photon beams. In particular, ion beams provide a favorable depth dose distribution, as shown in the example in Figure 1.1. It is characterized by a low dose deposition in the entrance region and a strongly increased dose deposition in a well-defined area at the end of the ion range in matter, the so called Bragg peak^a. Behind the peak, the dose deposition sharply falls off. Ion beams are therefore well suited to treat deep seated tumors. The position of the Bragg peak in depth can be altered by changing the initial ion beam energy. Moreover, several ion energies can be used to create a so called spread-out-Bragg-peak (SOBP). Its distal extension can be tailored to the extension of the tumor. In combination with a beam application system using active deflection of thin ion pencil beams (Goitein and Chen (1983); Haberer et al. (1993)), the dose deposition can be highly localized to the target volume in three dimensions. Consequently, healthy tissue surrounding the target volume can be widely spared from irradiation. This is of particular interest when radiosensitive structures are in the vicinity of the target volume, e.g. optical nerves in the case of treatments of skull base tumors.

Decreased angular scattering and energy straggling of carbon ion beams compared to proton beams further enhance the possibility to gain a highly conformal dose distribution. Furthermore, the biological properties of carbon ion beams offer advantages over proton beams for therapeutic use. Differences between the ionization densities around the particle trajectory in the entrance and in the Bragg peak area of the carbon ion depth dose distribution lead to differences in the biological effects for the same physical dose deposition. In the entrance channel, i.e. at high particle energies, carbon ions produce damage, which is easier to repair compared to the damage induced towards the end of the particle range. In this region, the cell DNA suffers from highly concentrated or clustered lesions, which the cell internal repair system fails to correct (Amaldi and Kraft (2005)). As a consequence, the biological effectiveness of the radiation increases significantly. Accordingly, also the biological effective dose of carbon ion beams depicted in Figure 1.1 is enhanced in the peak compared to the plateau region.

The advantages of carbon ion beams for radiotherapy are partly degraded by nuclear fragmentation processes the ions undergo along their trajectories in tissue. In these

^aNamed after William Henry Bragg (Bragg and Kleeman (1904)).

1 Introduction

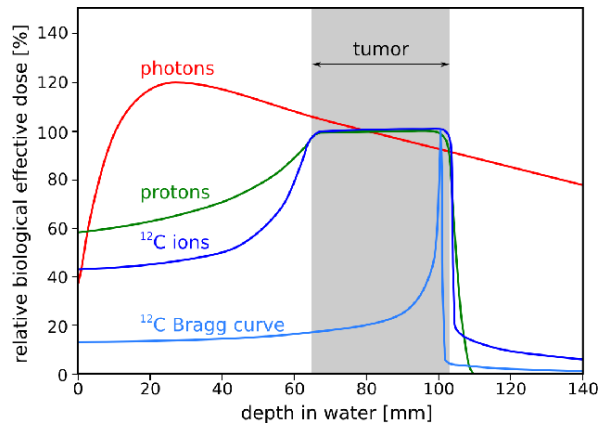


Figure 1.1: Schematic illustration of the depth distributions of the biological effective dose for photon, proton, and carbon ion beams of therapeutically used energies. The superposition of proton and carbon ion beams of different energies creating a spread-out-Bragg-peak covering the distal tumor extension is illustrated. Reprinted from Gwosch (2012).

inelastic interactions between projectile and target nuclei the number of primary particles is reduced and secondary fragments evolve. The fragmentation of target nuclei predominantly results in slow ions with short ranges. In contrast to that, projectile fragments are highly energetic. For carbon ion beams, the projectile fragmentation causes a spectrum of hydrogen, helium, lithium, beryllium, and boron ions, travelling together with the primary carbon ions in forward direction and thus contaminating the beam. Most of the projectile fragments have a longer range in tissue than the primary particles due to their lower mass and charge number but similar velocity. This is the reason for the characteristic dose tail behind the Bragg peak in the carbon ion depth dose distribution (see Figure 1.1). Moreover, the fragments have a different biological effectiveness compared to the primary particles (Chu (2006)). For these reasons, it is important to know the complex radiation spectrum resulting from a primary beam in a given situation, including evolving ion species and energy-loss characteristics as a function of depth in matter, in order to understand the biological effects of the irradiation and enable a precise therapy planning.

Previously, mainly rather bulky and complex experimental set-ups have been used for investigations of nuclear fragmentation processes. Figure 1.2 shows an illustration of an exemplary measurement set-up. Most of the measurements were based on a combination of particle energy-loss and residual energy information, partially combined with time-of-flight measurements for determination of the particle velocities (e.g. Golovkov et al. (1997) or Gunzert-Marx et al. (2008)). In such approaches, the distal extension of the scintillators used for the determination of the particle energy has to be large enough to completely stop the particles. For example, in Matsufuji et al. (2003) a scintillator with a length of 300 mm was used. Moreover, distances between target

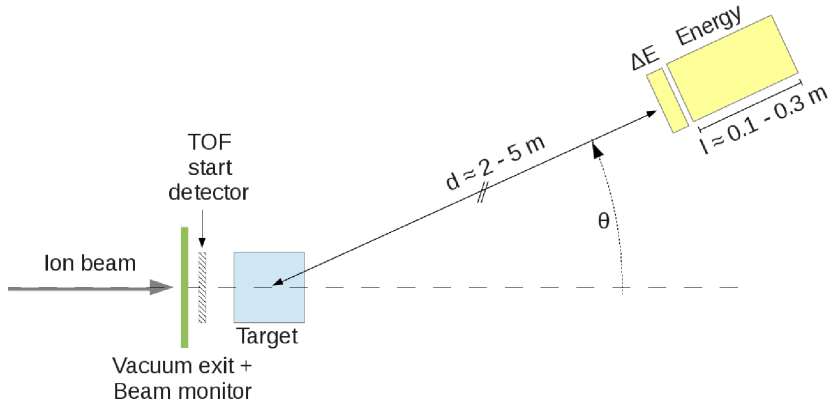


Figure 1.2: Schematic illustration of a typical measurement set-up used previously for nuclear fragmentation studies in therapeutic ion beams (e.g. Matsufuji et al. (2003) or Gunzert-Marx et al. (2008)). Two detection systems were used to gain information on particle energy-loss characteristics and the residual particle energy. In addition, the particle velocity was determined by time-of-flight (TOF) measurements. To gain a high resolution, large distances between target materials and detectors were required.

materials and the detectors of up to several meters are required for high resolution time-of-flight-measurements, which make the devices rather difficult to handle in clinical facilities. For this reason, up to now ion spectroscopic measurements have only been performed in limited combinations of projectile species and energies. Concerning target materials and geometries, measurement data are mainly available for water and only for restricted angles from the beam axis. Overall, the amount of accessible data is low.

The aim of the work presented in this thesis is to develop a novel method for ion spectroscopy in therapeutic ion beams. The main requirement is to use an easy to handle experimental set-up, offering the possibility to obtain a large number of measurements for a wide range of projectile species, projectile energies, target materials and target geometries. Furthermore, the set-up should enable acquiring information on fragmentation processes directly within therapy relevant situations, e.g. in water tanks or closely behind other tissue-equivalent phantoms. For this reason, the pixelated detector Timepix (Llopart et al. (2007)) based on semiconductor technology is employed. This small^a detector has a 300 μm thick silicon sensor. Its high spatial resolution enables the detection of single particles. Having originally been designed for photon beam applications, up to now experiences of the detector's use in ion beams are very limited (e.g. Jakubek et al. (2008); Granja et al. (2011); Pinsky et al. (2011)).

Against the described background, the thesis is structured as follows: In the next chapter, the physical background for interactions of ions in matter is described. While Chapter 3 gives an overview on previous studies on nuclear fragmentation in therapeu-

^aOverall size of detector and read-out: 150 x 50 x 20 mm³.

1 Introduction

tic ion beams, in Chapter 4 the physical and biological aspects of nuclear fragmentation with clinical impact are explained. The materials and methods used for the work presented in this thesis are described in Chapter 5, while the experiments and results are shown in Chapters 6 and 7. The thesis comprises three main contributions. In the first contribution, presented in Sections 6.1 and 7.1, the response of the Timepix detector to ions of therapeutic energies is characterized. Based on the obtained results, suitable detector settings as well as parameters for the evaluation of the detector signal are specified. The second contribution is a study of the detector's potential for energy-loss measurements in therapeutic ion beams. The experimental set-up and applied beam parameters are described in Section 6.2, while the results are shown in Section 7.2. Finally, studies of ion spectra were performed with the Timepix detector. An initial experiment used for the assignment of the detector signal to different ion species was conducted before verifying the applicability of the method and studying various combinations of beam parameters, target materials and measurement geometries. Information on these measurements is given in Section 6.3, while the corresponding results are presented in Section 7.3. The findings are discussed in Chapter 8, where in addition an outlook on future work is given, and summarized in Chapter 9, which also contains conclusions.

2 Physical Background: Interactions of Ions with Matter

In this chapter, the processes taking place upon traversal of ions of therapeutic energies^a through matter will be discussed. In the following, all ion species heavier than protons will be referred to as heavy ions.

Energetic charged particles penetrating matter interact with the electrons and nuclei of the atoms of the target material. In these interactions, the charged particles deposit energy inside the medium and therefore slow down. The energy-loss of charged particles is a gradual process. In each interaction, generally only a small fraction of the particle energy is transferred to the medium. At particle energies above 10 keV/u, the ion energy-loss is dominated by inelastic collisions of the ions with the atomic electrons causing ionization or excitation of the atoms. Quantities related to these so called 'electronic interactions' are summarized in Section 2.1.

Elastic scattering of ions, in contrast, mainly occurs from atomic nuclei. This process is less frequent compared to the electronic interactions and in general only small amounts of energy are transferred. However, it results in a lateral spread of ion beams traversing media. This so called Multiple Coulomb Scattering is discussed in more detail in Section 2.2.1. Furthermore, fragmentation processes occur due to inelastic nuclear reactions of the projectile ions with target nuclei. For heavy ions, the collisions can lead to a shearing of nucleons in the overlapping zone from both interacting nuclei and result in projectile and target fragments of reduced mass. The fragmentation processes cause a reduction of the number of primary particles in the beam and the production of secondary ions. For protons, only target fragmentation may occur. The basic principles of fragmentation processes are described in Section 2.2.2.

Other possible processes due to interactions of ions and matter are the emission of Cherenkov radiation and Bremsstrahlung. They are however of no relevance for ion beams in therapeutic energy ranges and will therefore not be further discussed in this work.

^aTypically, ion energies of up to approximately 220 MeV for protons and up to 430 MeV/u for carbon ions are used in particle therapy.

2.1 Electronic Interactions

2.1.1 Energy-Loss

The energy-loss of charged particles in matter can be described by the stopping power S , defined as the mean energy-loss dE of a particle per path length dx

$$S = - \left(\frac{dE}{dx} \right). \quad (2.1)$$

The minus sign in Equation 2.1 indicates that the energy is lost by the particle and defines the stopping power as a positive quantity (Sigmund (2004)).

In principle, the stopping power is made up of several contributors. However, at ion energies typically used in radiotherapy, electronic stopping due to inelastic collisions of the ions with the target electrons dominates the energy-loss. Only at very low projectile energies (≤ 10 keV/u) elastic collisions of the ions with target nuclei make a significant contribution to the energy-loss. Although these interactions dominate the stopping process within the last few μm of the particle path, the corresponding dose contribution can be neglected (Elsässer et al. (2009); Schardt et al. (2010)). For this reason, in the following only the electronic energy-loss will be discussed.

For ions, the mean electronic energy-loss per unit path length, also referred to as electronic stopping power S_{el} , can be well described by the Bethe-Bloch-formula (Bethe (1930); Bloch (1933); Fano (1963); Ziegler (1999))

$$S_{el}(E) = - \left(\frac{dE}{dx} \right) = \frac{2 \pi e^4}{m_e c^2} N_A \frac{Z}{A} \frac{z^2}{\beta^2} \rho \left[2 \ln \left(\frac{2 m_e c^2 \beta^2}{I (1 - \beta^2)} \right) - 2 \beta^2 - \delta - 2 \frac{C}{Z} \right], \quad (2.2)$$

where E is the kinetic particle energy, e the charge of an electron, m_e the electron rest mass, c the speed of light, N_A Avogadro's number, Z and A the atomic number and the atomic weight of the target material, ρ the density of the target material, z the charge of the projectiles, $\beta = v/c$ the velocity of the projectiles divided by the speed of light and I is the mean excitation potential of the target atoms.

The last two terms in Equation 2.2 describe correction factors to the original Bethe-Bloch-formula. The shell correction C was introduced for incoming particles with velocities in the order of or even smaller than the orbital velocity of the electrons bound in atoms. In this case, the electrons in the atoms can no longer be considered stationary with respect to the incoming particle. Therefore, the particle may capture electrons from the target, which partially neutralize the charge of the ion and thus lower the stopping power. For protons in the energy range of 1 - 100 MeV the shell correction can amount to up to 6% of the stopping power (Ziegler (1999)). The density correction δ accounts for polarization effects along the particle trajectory in the target due to the electric field of the incoming particle. The polarization shields electrons far from the particle path from the full electrical field intensity. Therefore, collisions

with outer electrons contribute less to the total energy-loss than initially predicted by the Bethe-Bloch formula. This effect is mainly important for high particle energies and depends on the density of the traversed material (Leo (1994)). For example, in photographic emulsion, a deviation of about 1% was found for protons of 1000 MeV due to the density effect (Ziegler (1999)). As the effect decreases for lower energies, it is of minor importance for therapeutically used energy ranges.

At non-relativistic energies the electronic stopping is dominated by the factor $1/\beta^2$. Therefore, the particle energy-loss increases with decreasing particle velocity. In this energy range, most ion species exhibit distinct energy-loss-curves. This characteristic can be exploited for particle identification. For very low particle energies (velocities comparable to or below velocity of atomic electrons), the energy-loss reaches a maximum before decreasing sharply (see explanations for shell correction above, Leo (1994)).

2.1.2 Energy-Loss Straggling

While the Bethe-Bloch equation (2.2) describes the mean energy-loss of particles in an absorber, the energy-loss of a single particle in a certain absorber thickness may be different due to the statistical fluctuations in the number of collisions and the energy transferred in each collision. The probability distribution for the energy-loss of a particle in an initially mono-energetic beam depends on the number of interactions and thus on the absorber thickness. Therefore, the theoretical calculations of this distribution differ in their regions of applicability. The discriminating parameter k is the ratio between the mean energy-loss $\overline{\Delta E}$ of the particle in the absorber and the maximum energy transfer in a single collision W_{max}

$$k = \frac{\overline{\Delta E}}{W_{max}}. \quad (2.3)$$

Ignoring the logarithmic term in the Bethe-Bloch equation (2.2) and the correction factors, the mean energy-loss can be approximated by (Leo (1994))

$$\begin{aligned} \overline{\Delta E} \simeq \xi &= 2\pi r_e^2 m_e c^2 N_A \frac{Z}{A} \frac{z^2}{\beta^2} \rho x \\ &= 2\pi \left(\frac{e^2}{4\pi \epsilon_0 m_e c^2} \right)^2 m_e c^2 N_A \frac{Z}{A} \frac{z^2}{\beta^2} \rho x \\ &= 0.1535 \frac{\text{MeV cm}^2}{\text{g}} \frac{Z}{A} \frac{z^2}{\beta^2} \rho x, \end{aligned} \quad (2.4)$$

2 Physical Background: Interactions of Ions with Matter

where r_e is the classical electron radius^a. The maximum energy transfer in a single collision for an incident particle of mass M is given by (Leo (1994))

$$W_{max} = \frac{2 m_e c^2 (\beta\gamma)^2}{1 + 2 \frac{m_e}{M} \sqrt{1 + (\beta\gamma)^2} + \left(\frac{m_e}{M}\right)^2}, \quad (2.5)$$

where $\gamma = 1/\sqrt{1 - \beta^2}$. For $M \gg m_e$ Equation 2.5 becomes

$$W_{max} \simeq 2 m_e c^2 (\beta\gamma)^2. \quad (2.6)$$

Generally, an absorber is considered thin for $k \leq 0.01$ and thick for $k > 10$, although for $k > 1$ the distribution already begins to approach the Gaussian limit described in the following (Leo (1994)).

For thick absorbers in which a high number of interactions take place, the energy-loss distribution is in first approximation Gaussian (Leo (1994)):

$$f(\Delta E) \sim \exp\left(\frac{-(\Delta E - \overline{\Delta E})^2}{2\sigma^2}\right), \quad (2.7)$$

where ΔE is the energy-loss in the absorber, $\overline{\Delta E}$ is the mean energy-loss in the absorber and σ is the standard deviation of the distribution. For non-relativistic heavy particles, the standard deviation depends only on the penetrated absorber thickness x , the density ρ , the atomic number Z and the atomic weight A of the absorber. It can be approximated by (Leo (1994))

$$\sigma_0^2 = 4\pi N_A r_e^2 (m_e c^2)^2 \rho \frac{Z}{A} x = 0.1569 \rho \frac{Z}{A} x \text{ [MeV}^2\text{]}. \quad (2.8)$$

For relativistic particles, the formula can be extended to (Leo (1994))

$$\sigma^2 = \frac{(1 - 0.5\beta^2)}{1 - \beta^2} \sigma_0^2. \quad (2.9)$$

For absorbers which are thin compared to the particle range and where the number of collisions is small, the possibility of a large energy transfer in a single collision can no longer be neglected. For $k \leq 0.01$ the energy-loss distribution is described by the Landau theory (Landau (1944)) using the following assumptions (Leo (1994)):

- The energy transferred in a collision is sufficiently large. Thus the electron binding energy is negligible, i.e. the electrons can be treated as free and small energy transfers from distant collisions can be ignored.
- The maximum permitted energy transfer is infinite.
- The decrease in the particle velocity is negligible.

^a $r_e = \frac{e^2}{4\pi\epsilon_0 m_e c^2} = 2.818 \cdot 10^{-15} \text{m}$ (Kuchling (2004), p. 551)

The Landau distribution f_L is given by (Landau (1944), Leo (1994))

$$f_L(x, \Delta E) = \frac{\Phi(\lambda)}{\xi}, \quad (2.10)$$

with

$$\Phi(\lambda) = \frac{1}{\pi} \int_0^\infty e^{(-y \ln y - \lambda y)} \sin(\pi y) dy, \quad (2.11)$$

and

$$\lambda = \frac{1}{\xi} \cdot [\Delta E - \xi \cdot (\ln \xi - \ln \epsilon + 1 - C_E)], \quad (2.12)$$

where C_E is the Euler constant equal to 0.5772 and

$$\ln \epsilon = \ln \frac{(1 - \beta^2) I^2}{2m_e c^2 \beta^2} + \beta^2. \quad (2.13)$$

The position of the peak in the Landau distribution defines the most probable energy-loss ΔE_p , as shown in Figure 2.1. It is given by (Meroli et al. (2011))

$$\Delta E_p = \xi \left[\ln \frac{2m_e c^2 \beta^2 \gamma^2}{I^2} + \ln \frac{\xi}{I} + 0.2 - \beta^2 - \delta \right], \quad (2.14)$$

where δ is the density correction discussed in Section 2.1.1. ΔE_p is located at a lower value compared to the mean energy-loss $\overline{\Delta E}$ obtained from the Bethe-Bloch equation (2.2). Although events in which very high amounts of energies are transferred are rare, their possibility is reflected in a long tail towards high energies in the energy-loss probability distribution, leading to an asymmetric form (see Figure 2.1).

For all k the Vavilov theory can be applied. This theory generalizes the Landau theory by taking into account the correct expression for the maximum allowable energy transfer (Leo (1994)) and the spin of the incident particle (Meroli et al. (2011)). The formalism describing the Vavilov theory can only be solved numerically. It reduces to the Landau distribution for $k \rightarrow 0$ and approximates a Gaussian form for $k \rightarrow \infty$.

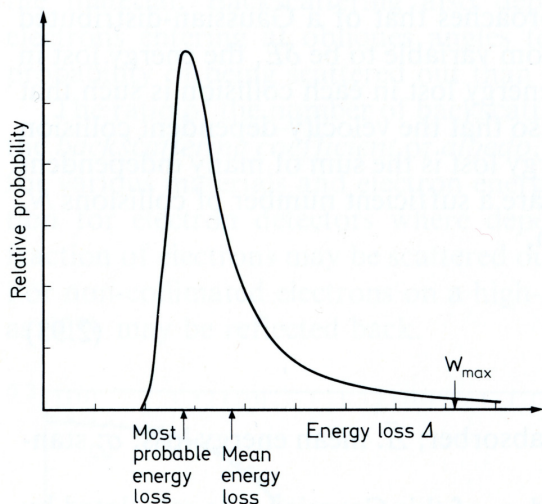


Figure 2.1: Typical energy-loss distribution in a thin absorber (Landau distribution). Reprinted from Leo (1994).

Further modifications to the theories of Landau and Vavilov were presented to include binding effects of the atomic electrons and consider the atomic shell structure (Blunck and Leisegang (1950); Shulek et al. (1966)). The resulting distribution is broader compared to the original Vavilov distribution and the peak position is usually increased by a small amount.

2.1.3 Particle Range and Range Straggling

The particle range R describes how far particles penetrate an absorber before losing all their energy, i.e. stopping completely. It depends on the particle type and energy as well as on the absorber material (Leo (1994)).

In the continuous slowing down approximation (CSDA) the mean travelled path length R is given by the integration over the inverse of the stopping power from the initial kinetic particle energy $E_{initial}$ to zero

$$R(E) = - \int_{E_{initial}}^0 \left(\frac{dE}{dx} \right)^{-1} dE. \quad (2.15)$$

In general, the projected particle range R_p in an absorber is smaller than the total path length R of a particle's trajectory due to effects of multiple scattering resulting in a zigzag path of the particle through the absorber (see Section 2.2.1). The difference between the two quantities is described by the projected-range correction, also called *detour factor*, given by R_p/R , which is ≤ 1 (ICRU73 (2005)). Equation 2.15 can therefore only approximate the projected particle range R_p when effects of multiple scattering can be neglected. For a given particle range, the range straggling and therefore the detour factor is smaller the heavier the ions are. Therefore, Equation 2.15 is more likely to be valid for the projected particle range of heavy charged particles like carbon ions, compared to protons.

In addition to effects of multiple scattering, statistical fluctuations of energy-loss lead to differences in the range for particles of the same species and initial energy. This effect is known as range straggling. In an ensemble of particles of the same species and initial energy, the statistical distribution of ranges is in a first approximation Gaussian shaped and thus centered on a mean value. This mean range corresponds to the thickness of the medium at which about half of the incident particles are absorbed (Leo (1994)). The variance of the range straggling is directly related to the variance of the energy-loss straggling (see Section 2.1.2). Furthermore, inhomogeneity in the density of penetrated tissue can contribute to range straggling.

2.1.4 Dose

The macroscopic quantity dose can be considered the most important physical measure in radiation therapy. The absorbed dose D describes the mean amount of energy dE

deposited by ionizing radiation in a mass element dm_X of the absorber material X :

$$D = \frac{dE}{dm_X} \left[1\text{Gy} = 1 \frac{\text{J}}{\text{kg}} \right]. \quad (2.16)$$

Knowing the stopping power for ions of charge Z and energy E in water and the ion fluence F , the dose-to-water can be determined by

$$D_{\text{ion,H}_2\text{O}}(E, Z, F) = F \cdot \left[\frac{dE}{dx}(Z, E) \right]_{\text{H}_2\text{O}} \cdot \rho_{\text{H}_2\text{O}}^{-1} \left[1\text{Gy} = 1 \frac{\text{J}}{\text{kg}} \right]. \quad (2.17)$$

2.1.5 Linear Energy Transfer

The linear energy transfer (LET) is defined as

$$LET = \frac{dE}{dl} \left[\frac{\text{J}}{\text{m}}, \frac{\text{keV}}{\mu\text{m}} \right], \quad (2.18)$$

where dE is the kinetic energy transferred by the charged particle to secondary electrons and dl is the path length of the particle in the medium. The restricted linear energy transfer (LET_Δ) of a charged particle characterizes the ionization density on a microscopic level. In this case, only secondary electrons with energy below a maximum kinetic energy Δ are considered. These electrons deposit their energy locally, along the particle trajectory. The unrestricted $LET_{\Delta=\infty}$ is equal to the stopping power S discussed in Section 2.1.1.

The LET is an indirect measure for the number of ionizations due to the particle per unit path length in the medium. It is often used to quantify effects of ionizing radiation, for example on a biological sample or in a radiation detector (Leroy and Rancoita (2011)). For the same particle velocity, the energy transferred to secondary electrons increases with increasing particle charge. For the same residual particle range, the energy-loss of carbon ions is about 25 times higher than for protons (ICRU49 (1999); ICRU73 (2005)).

2.2 Nuclear Interactions

2.2.1 Multiple Coulomb Scattering

Charged particles traversing matter experience repeated elastic scattering caused by the Coulomb field of the target nuclei, so called Coulomb scattering. Neglecting spin effects and screening, the cross section for a single interaction is given by the Rutherford formula

$$\frac{d\sigma}{d\Omega} = \left(\frac{1}{4\pi\epsilon_0} \frac{zZe^2}{4E} \right)^2 \cdot \frac{1}{\sin^4\left(\frac{\Theta}{2}\right)}, \quad (2.19)$$

2 Physical Background: Interactions of Ions with Matter

where z and Z are the charge of the projectile and target nucleus, respectively, E is the kinetic energy of the projectile and Θ is the deflection angle. While the vast majority of these collisions result in a small angular deflection of the particles, the cumulative effect of many small angle scattering processes results in a net deflection of the projectiles from their original direction (Leo (1994)). This effect is also known as Multiple Coulomb Scattering and described by the formalism of the Molière theory (Molière (1948); Bethe (1953)). In general, for a large number of collisions, the resulting distribution of particle directions is roughly Gaussian for small deflection angles. For larger deflection angles, the resulting distribution is similar to the angular distribution obtained from Rutherford scattering. For the Gaussian approximation for small deflection angles, the standard deviation is given by an empirical formula (Highland (1975); Gottschalk et al. (1993))

$$\sigma_{\Theta}[\text{rad}] = \frac{14.1 \text{MeV}}{pv} z \sqrt{\frac{d}{L_{rad}}} \left[1 + \frac{1}{9} \log_{10} \left(\frac{d}{L_{rad}} \right) \right], \quad (2.20)$$

where d is the penetration depth and z , p , and $v = \beta c$ are the projectile charge, momentum and velocity, respectively. In this approach, the absorber material is characterized by its radiation length L_{rad} (values for particular materials can be found e.g. in Tsai (1974)).

From Equation 2.20 and the data given in Tsai (1974) the following consequences can be derived (Schardt et al. (2010)):

- At the same thickness normalized to density (in units of g/cm^2), targets containing heavy elements cause a larger angular spread than targets of light elements.
- For heavy charged particles the angular spread is initially small (for a thin target in the order of 1 mrad), but increases significantly towards lower energies due to the pv term in the denominator.
- For beams of protons and carbon ions with the same residual range in water, the angular spread of protons is more than three times higher than the angular spread of carbon ions.

2.2.2 Fragmentation

Besides the interactions of the projectile nuclei with the atomic target electrons and scattering off target nuclei described in the previous sections, nuclear fragmentation processes occur along the particle trajectory. Although having a much smaller probability than the previously described interactions, nuclear fragmentation processes lead to significant effects on the radiation field, especially for heavy projectiles, high projectile energies and large penetration depths.

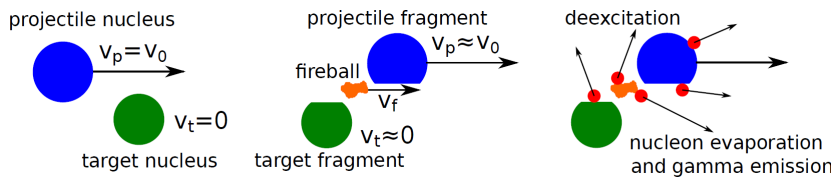


Figure 2.2: Schematic illustration of the abrasion-ablation model describing peripheral collisions of high energetic nuclei. Reprinted from Gwosch (2012).

For geometrical reasons, peripheral collisions are the most frequently occurring reactions (Gunzert-Marx et al. (2008); Schardt et al. (2010)). This process, in which the projectile particles lose nucleons is described by the abrasion-ablation model (Serber (1947)), which is illustrated in Figure 2.2. In the first step of the interaction process, the collision between the incident particle and the target nucleus causes a shearing of nucleons in the overlapping zone (abrasion). These nucleons are called participants. The time frame of the interaction is approximately equivalent to the time the projectile needs to traverse the target nuclei (10^{-23} s, Gunzert-Marx (2004)). Typically, only a few nucleons are abraded. As they are highly excited they are also referred to as fireball (Gunzert-Marx (2004)). Containing nucleons from both, the projectile and the target nuclei, the fireball travels with an intermediate velocity. At the same time, the spectator nucleons in the outer zone are only slightly affected. The projectile-fragment of reduced charge and mass proceeds travelling with almost the same velocity and direction as the incident projectile, while the target-fragment can be in good approximation considered to stay at rest.

In the second step of the interaction process, the remaining excited projectile and target fragments as well as the fireball de-excite in cascades by evaporation of nucleons or light clusters (ablation) (Gunzert-Marx (2004)). Furthermore, γ -rays are emitted. The time frame of the de-excitation processes is 10^{-21} s to 10^{-16} s (Kraft (2000)). While the nucleons emitted from the projectile fragments and the fireball appear forward peaked due to the high velocity of the projectile fragment and the fireball, respectively, nucleons evaporated from the target fragments are emitted isotropic and have lower velocities. Thus, the nucleons evaporated from the target fragment deposit their energy locally, while the nucleons evaporated from the projectile fragment, the projectile fragment itself and the fireball enhance the dose besides the intrinsic particle trajectory. The projectile fragments contribute to the dose deposition until they are either stopped or undergo further nuclear reactions (Gunzert-Marx (2004)).

Fragmentation processes in irradiations with heavy ions result in both projectile and target fragmentation. Non-elastic interactions of protons, in contrast, lead to the production of target fragments only. A certain fraction of the emerging secondary radiation, such as heavy nuclear recoils or short-range inelastic secondaries is absorbed

locally (Pedroni et al. (2005)). Therefore, the kinetic energy is deposited at the point of the nuclear collision. Moreover, there are secondary products with long range, hence depositing dose beyond the interaction location, and secondary neutral particles.

In the following chapter an overview of previous studies investigating nuclear fragmentation in therapeutically relevant ion beams is presented. Aspects of nuclear fragmentation which are important for heavy ion beam therapy will be discussed in more detail in Chapter 4.

3 Previous Studies on Nuclear Fragmentation in Therapeutic Ion Beams

Initial Nuclear Physics Experiments The first studies on high energy interactions between nuclei were performed in the 1940s and thus well before high energy heavy ion beams became available in accelerator laboratories. Observations of cosmic-ray nuclear interactions with photographic emulsion (Freier et al. (1948)) have given a prospect of the physics of interactions between relativistic nuclei (Goldhaber and Heckman (1978)). In the early 1970s, the availability of relativistic, heavy ion beams ($E > 0.1$ GeV/u, $A \geq 4$) at different accelerator laboratories, like the Princeton Particle Accelerator (Princeton, NJ, USA), Lawrence Berkeley Laboratory (Berkeley, CA, USA), Saclay (France) and the Joint Institute for Nuclear Research (Dubna, Russia) enabled to study these interactions in more detail.

First Medical Physics Experiments In the same decade, first studies dedicated to biomedical applications were performed at the Princeton Particle Accelerator (Schimmerling et al. (1971)). The secondary particle production in interactions of nitrogen ions of 3.9 GeV with polyethylene was investigated. By means of time-of-flight measurements, transmitted nitrogen ions could be clearly separated from lighter fragments with higher velocities than the initial ions. At the Lawrence Berkeley Laboratory (LBL) BEVALAC accelerator, Maccabee and Ritter (1974) studied the attenuation of ^{16}O beams of up to 250 MeV/u in water and the build-up of B-, C- and N-fragments.

Investigations of ^{20}Ne beams More than 25 years after the first application of He ions for therapy (in 1957 at Berkeley, Ma and Lomax (2012)), Schimmerling et al. developed a large and complex beam spectrometer “to provide complete characterization of the relativistic heavy ion beams used for medical therapy and biology experiments at the Lawrence Berkeley Laboratory BEVALAC” (Schimmerling et al. (1983)). The spectrometer consisted of a variable thickness absorber, a time-of-flight (TOF) telescope, and a multi-element detector array mounted on a movable frame. It allowed to measure the charge, the fluence, the angular distribution, and in a restricted range also the mass

3 Previous Studies on Nuclear Fragmentation in Therapeutic Ion Beams

of the primary particles and the fragments as a function of depth in tissue. Detailed characterizations of ^{20}Ne beams ($E=670\text{ MeV/u}$) used for patient treatments at LBL BEVALAC between 1975 and 1992 (Schimmerling et al. (1989); Schardt et al. (2010)) were performed. Another, much simpler approach was used by Llacer et al. (Llacer (1984), Llacer (1990a)) at the LBL BEVALAC. The employed solid-state telescope consisted of a thin silicon detector for linear-energy-transfer (LET, see Section 2.1.5) measurements and a thick germanium detector to measure the residual particle energy (Llacer (1984)). The device enabled the identification of particle charge and was designed to allow fast on-line assessment of beam characteristics, like LET, separately for each ion species. Analysis of ^{20}Ne beams ($E=670\text{ MeV/u}$) in different water depths were presented in Llacer (1990b). A large number of low-LET particles has been determined. Although many hydrogen and helium ions were detected, due to their low LET it was found that “they contribute very little to the total LET of the beam” and their “distribution to the dose was seen to be small, but their contribution did become more significant beyond the Bragg peak” (Llacer (1990b)).

Comparison of Projectile Ion Species In the 1990s, extensive fragment spectra measurements for projectile ions between ^{10}B and ^{20}Ne were performed at GSI (Gesellschaft für Schwerionenforschung, Darmstadt, Germany) using a large-area position-sensitive ionization chamber combined with a plastic-scintillator telescope (Schall et al. (1996)). The particle energies ranged from 200 to 670 MeV/u. Fragmentation was mainly investigated in thick water targets (up to 25.5 cm), but also in carbon, Lucite, polyethylene, and aluminum. The attenuation of primary particles in water as well as the build-up of fragments with $5 \leq Z \leq 10$ were used to obtain mean free path lengths and corresponding total and partial charge-changing cross sections. A relatively high charge changing cross section was obtained for ^{14}N , while the value for ^{12}C was found to be very low. In continuation of these studies, Golovkov et al. analyzed longitudinal and transverse momentum distributions of projectile fragments ($Z=1$ to $Z=5$) produced by a ^{12}C -beam ($E=270\text{ MeV/u}$) in thick water absorbers (Golovkov et al. (1997)). Deviations of these momentum distributions from model predictions were reported.

The HIMAC Experiments Similar experimental approaches like at GSI, using combinations of energy-loss measurements, time-of-flight-measurements, and detectors to determine the residual particle energies, were used at HIMAC (Heavy Ion Medical Accelerator in Chiba) in Japan by Kurosawa et al. (1999), by Zeitlin et al. (2007) and by Matsufuji et al. (2003), among others. Fragmentation and neutron production of He-ions ($E=100\text{ MeV/u}$) in various thick targets were investigated (Kurosawa et al. (1999)). In the study of Matsufuji et al., Poly(MethylMethAcrylate) (PMMA) was used as a tissue-like target, based on the results from previous studies showing that

“the stopping power and the total nuclear reaction cross sections of PMMA against carbon ions are proportional to those of water to high accuracy all over this relativistic energy domain” (Matsufuji et al. (2003)). Moreover, fragment fluence distributions in different material depths were retrieved for various projectiles ranging from ^4He to ^{40}Ar . The measurement of LET spectra allows to calculate the fractions of dose deposited by the different ion species. In a second study, investigations on the spatial distribution of fragments produced from a therapeutic ^{12}C -ion beam ($E=290\text{ MeV/u}$) in water were presented (Matsufuji et al. (2005)). Deflections of the fragments exceeding the effect of multiple scattering estimated by the Molière theory were observed. The deviations could be explained by a momentum transfer at the point of nuclear reaction.

Focusing on Carbon Ion Beams Also at GSI investigations on ion fragmentation were continued in the 2000s, now focusing on carbon ion beams, which were used there for patient treatment between 1997 and 2005. Measured energy spectra and angular distributions of light charged particles and fast neutrons produced in interactions of carbon ions ($E=200\text{ MeV/u}$) in water were published (Gunzert-Marx (2004); Gunzert-Marx et al. (2008)). A further comprehensive study on reactions of incident ^{12}C -ions ($E=200\text{ MeV/u}$ and $E=400\text{ MeV/u}$) at six different depths in a water phantom was presented in Haettner (2006) and Haettner et al. (2006). The results include energy- and angular distributions, fragment yields, and build-up curves for secondary fragments with charge $Z = 1 - 5$, as well as attenuation studies of the primary projectile ions. Exemplary, angular distributions measured behind 15.9 and 31.2 cm thick water targets are shown in Figure 3.1. The results obtained in this study were later used to benchmark the Monte Carlo transport code FLUKA (Mairani (2007)).

Lower carbon ion energies (95 MeV/u) were investigated at GANIL (Grand Accélérateur National d’Ions Lourds, France) for thick tissue equivalent targets and angles of up to 70 degrees (Braunn et al. (2011)) and for thin targets (Dudouet et al. (2013)), while the fragmentation of ^{12}C -ions of 62 MeV/u on a thin carbon target ($d/\rho=104\text{ }\mu\text{g cm}^{-2}$)

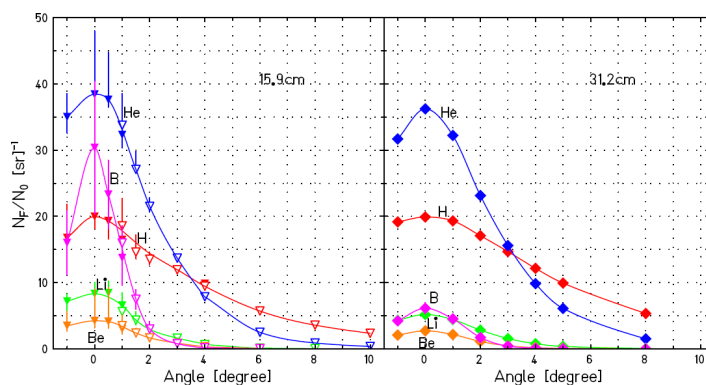


Figure 3.1: Angular distributions of different fragments of a ^{12}C -ion beam ($E=400\text{ MeV/u}$) obtained behind 15.9 and 31.2 cm thick water targets. Reprinted from Haettner (2006).

3 Previous Studies on Nuclear Fragmentation in Therapeutic Ion Beams

was investigated at INFN (Istituto Nazionale di Fisica Nucleare, Italy) (De Napoli et al. (2012)). The measured cross sections were used to validate nuclear reaction models of the Monte Carlo code GEANT4 and it was found that the GEANT4 prediction models need to be improved at intermediate energies (De Napoli et al. (2012)).

The FIRST Experiment While most of the measurements performed in the past are related to yields or total cross sections, differential cross section measurements are rare (Golosio et al. (2011)). The FIRST (Fragmentation of Ions Relevant for Space and Therapy) experiment at the SIS (Schwerionensynchrotron) accelerator of GSI is dedicated to fill in some of these lacks by measuring double differential cross sections for light ions and in the energy range used for hadron therapy (Golosio et al. (2011); Pleskac et al. (2012); Agodi et al. (2012)). The experimental set-up consists of various detection systems, partly specifically designed and built for this experiment. The overall size of the set-up is approximately $10 \times 6 \text{ m}^2$. First data were taken in 2011 using ^{12}C -ions of 400 MeV/u on an 8 mm thick carbon target and a 0.5 mm thick gold target. By the time of writing this thesis, a detailed data analysis of this experiment has not yet been published.

Passive Detection Systems Currently, the overall amount of experimental data available on nuclear fragmentation processes in therapeutic ion beams is small. All of the studies discussed previously in this chapter use active detection systems. They have in common that the employed set-ups are rather large and complex. Due to their high demands on experimental space, equipment and time for the set-up, the flexibility of the experiments is limited. There are also approaches using smaller set-ups. However, all of them are based on passive (offline) detection systems. Examples are measurements based on nuclear track detectors (Golovchenko et al. (1999); Mrázová et al. (2010)) or nuclear emulsion films (De Lellis et al. (2011)). The sensitive component has to be exchanged for each alteration of the experimental set-up. Moreover, these methods require post-irradiation processing for the data acquisition. This makes the measurements highly time-consuming. Therefore, these techniques are not suited to acquire data with high statistics and in a wide phase-space.

Approach Introduced in this Work As described in Chapter 1, the aim of the work presented in this thesis is to develop a novel approach for fragmentation analysis in therapeutic ion beams, which allows filling some of the existing gaps. The use of the silicon pixel detector Timepix as an active detection system, which is at the same time small and easy to handle, offers a highly flexible experimental set-up. The developed ion spectroscopic method is intended to allow measurements in a wide phase-space concerning projectile species, projectile energies, target materials and target geometries.

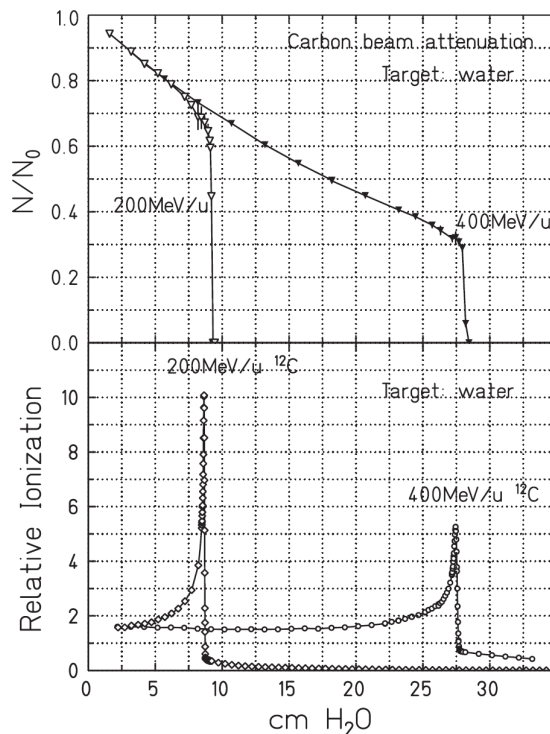
4 Physical and Biological Aspects of Nuclear Fragmentation with Clinical Impact

Nuclear fragmentation processes of ion beams in tissue, as described in Section 2.2.2, are of particular importance in the clinical application of ion beams, since they directly influence the biological effects of the irradiation field and therefore the clinical outcome of the therapy. In this chapter, the effects of nuclear fragmentation processes with clinical impact are discussed in more detail. While in Section 4.1 physical aspects of nuclear fragmentation in heavy ion radiotherapy are illustrated, in Section 4.2 differences in proton radiotherapy are shortly addressed. In Section 4.3 the concept of relative biological effectiveness is introduced and its relation to nuclear fragmentation is described.

4.1 Physical Aspects of Nuclear Fragmentation in Heavy Ion Radiotherapy

Impact of Nuclear Fragmentation on the Particle Field Nuclear fragmentation processes influence the composition and the angular distribution of the irradiation field. The projectile fragmentation leads to an attenuation of the primary particle flux and a build-up of lower-charged fragments (see descriptions in Section 2.2.2). The relevance of this effect increases with tissue penetration depth. For a carbon ion beam with a range of 16 cm in water only 52% of the primary ions reach the Bragg peak (Scharadt et al. (2010)). In Figure 4.1 two examples for carbon ion attenuation measurements in water are shown. The emerging projectile fragments have a lower charge and therefore different energy-loss characteristics compared to the primary particles (see descriptions of energy-loss in Section 2.1.1). Furthermore, the lighter ions show wider angular distributions compared to the primary ions due to multiple Coulomb scattering, as explained in Section 2.2.1.

Figure 4.1: The top plot shows the attenuation of carbon ion beams ($E_{\text{initial}}=200$ and 400 MeV/u) in water. The bottom plot illustrates the corresponding Bragg curves. The lines are shown to guide the eyes. Reprinted from Haettner (2006).



Impact of Nuclear Fragmentation on the Dose Delivery The fraction of dose deposited by fragments increases with depth. Figure 4.2 illustrates the contributions of primary particles and secondary or higher order fragments to the relative ionization in dependence of the water depth for the example of a carbon ion beam with an initial energy of 330 MeV/u. Considering this effect in therapy planning is important, since the radio-biological dose of an ion beam depends not only on the physical dose, but also on the beam composition regarding the nuclear charge and the energy of the particles (Gunzert-Marx (2004)). The underlying processes will be discussed in Section 4.3.

While the primary particles stop in the Bragg peak, the projectile fragments can have sufficient energy to pass beyond. As described in Section 2.2.2, they have a reduced charge and mass but proceed travelling with almost the same velocity and direction as the incident particles. For particles of the same velocity the range approximately scales with A/Z^2 (Schardt (2007)). Therefore, at a given particle velocity, lower charged ions have longer ranges in matter. For this reason, the secondary projectile fragments cause the characteristic dose tail behind the Bragg peak in heavy-ion depth-dose-distributions, as depicted in Figure 4.2. The heavier the projectile ions are, the larger is in general the dose delivered in the tail region (normalized to the dose delivered by the primary ions at the proximal end of the spread-out-Bragg-peak (SOBP)) (Chu et al. (1993)). For neon-ions the dose directly behind the distal end of the SOBP can be as large as 30% of the target dose. For carbon ions, in comparison, the effect is less pronounced with doses behind the distal end of the SOBP of 10-20% of the SOBP-plateau value (Amaldi and Kraft (2005)).

4.1 Physical Aspects of Nuclear Fragmentation in Heavy Ion Radiotherapy

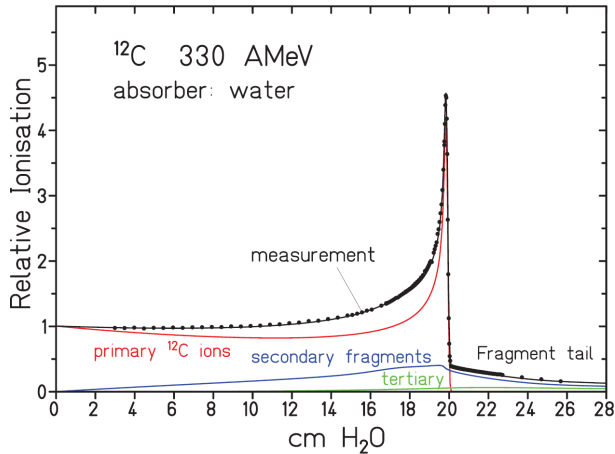


Figure 4.2: Depth dose distribution of a carbon ion beam ($E_{\text{initial}}=330 \text{ MeV/u}$) in water. The measurement was performed at GSI. The measurement data (dots) are compared to model calculations by Sihver et al. (1993) (solid lines). The dose contributions due to primary ions, and secondary and tertiary fragments are indicated. Reprinted from Schardt (2007).

Impact on the Choice of the Ion Species In order to minimize the negative aspects of nuclear fragmentation, using an ion species with a small probability for projectile fragmentation processes, i.e. a small charge changing cross section in tissue, is beneficial for clinical use. In Schall et al. (1996) a comparative study of the charge changing cross sections for beams of ^{10}B , ^{12}C , ^{14}N , ^{16}O , and ^{20}Ne in water was presented. For all ion species, similar energy per nucleon values were evaluated. While for ^{14}N -beams a relative high probability for reactions changing the charge was obtained, it was found to be about 1.2 times lower for ^{12}C -beams. Moreover, the value for ^{12}C -beams was even lower than the value obtained for ^{10}B . These findings indicate influences of shell-structure effects in the reactions (Schardt et al. (2010)) and can be understood when regarding the structure of the ^{12}C -nuclei. Each ^{12}C -nuclei is built of six protons and six neutrons. Corresponding to Pauli's principle, these 12 nucleons fill three energy levels. Each level is occupied by two protons with antiparallel spin and two neutrons with antiparallel spin. Therefore, the spins compensate and the overall spin is zero. Due to the even atomic and mass numbers the nuclei have a high binding energy and are very stable leading to favorable conditions of ^{12}C -ion beams for therapeutic use in the treatment of tumors located deep in the human body (Schall et al. (1996)).

Beneficial Implications of Nuclear Fragmentation: In-Vivo Imaging An advantage of nuclear fragmentation processes is the possibility to use the reaction products for in-situ verification measurements of the treatments. Currently, the only clinically available method are tissue activation measurements using the technique of positron emission tomography (PET) (Enghardt et al. (2004); Parodi et al. (2008)). In this method, information carried by β^+ -emitters is exploited to gain information on the beam delivery and dose deposition in the patient. The β^+ -emitters are for example ^{11}C - and ^{10}C -fragments produced in ablation processes of single neutrons from the primary ^{12}C -projectiles. Furthermore, methods based on the analysis of emitted prompt gamma quanta (Min et al. (2006); Testa et al. (2008); Bom et al. (2012); Smeets et al.

(2012)) and secondary charged particles were proposed (Amaldi et al. (2010); Henriquet et al. (2012); Agodi et al. (2012)) and investigated in initial studies (Gwosch et al. (2013)).

4.2 Physical Aspects of Nuclear Fragmentation in Proton Radiotherapy

Also in irradiations of matter with protons non-elastic interactions occur, leading to an attenuation of the primary proton flux. A fraction of the emerging target fragments is absorbed locally at the point of the nuclear collision, e.g. heavy nuclear recoils or low energetic secondary ions with short ranges (Pedroni et al. (2005)). They might however have a higher relative biological effectiveness than the primary protons (see explanations in the next section). Furthermore, secondary products with long range depositing kinetic energy further downstream of the interaction point are created, as well as neutral particles, which can also have relatively long ranges before being absorbed. They offer the main dose contribution behind the Bragg peak in proton irradiations. In total, the dose contribution to the patient by secondary neutrons is however small (less than 0.5%, Chu et al. (1993)).

4.3 Relative Biological Effectiveness

As described in Section 4.1, the same amount of physical dose can lead to different biological effects, depending on the type of radiation depositing the energy. This applies even if all other irradiation conditions are fixed. To quantify the so called biological effective dose, the concept of relative biological effectiveness (RBE) can be employed (ICRU30 (1979)). The RBE describes the ratio of a reference photon dose D_γ (typically ^{60}Co photon radiation) and a corresponding ion dose D_I leading to an identical biological effect in tissue (Friedrich et al. (2010)):

$$RBE = \frac{D_\gamma}{D_I} \Big|_{\text{Iso-effect}} . \quad (4.1)$$

The biologically effective dose of an ion beam can be determined by multiplying the physically absorbed dose with the RBE-factor. The unit of the RBE-weighted dose is Gy (RBE).

The differences in the biological response between photon and particle radiation can be explained by differences of the energy transfer mechanisms. While in photon irradiations moderate doses are distributed over a wide area, e.g. the whole cell nucleus, for particle radiation high doses are deposited in localized areas, like small parts of the cell nucleus (Kraft (1999)). Therefore, more complex lesions are created with increasing

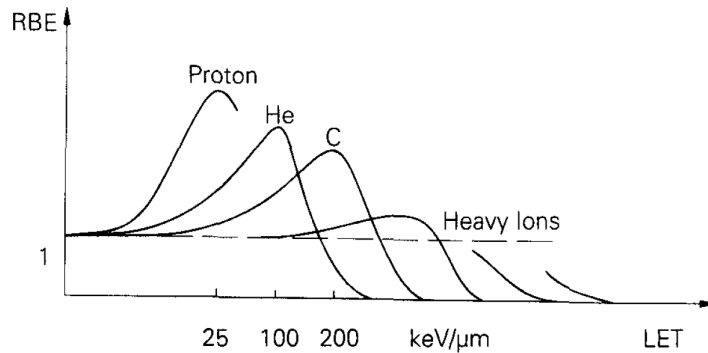


Figure 4.3: Dependence of the RBE on the LET and the ion species. Reprinted from Kraft (1999).

linear energy transfer (LET), which are more difficult to repair (for the definition of LET see Section 2.1.5). This results in an enhanced biological effect and therefore in an RBE value large than one.

Moreover, there is also a dependence of the RBE on the atomic number of the projectiles. This dependence is also correlated to the LET of the particles. As shown in the example in Figure 4.3, from low to intermediate LET values the RBE increases with increasing LET and therefore with decreasing particle energy. The reason is a higher energy concentration within the particle tracks, which is a result of the increasing LET itself and the simultaneous decreasing track diameter due to the lower particle energy^a (Scholz (2006)). Consequently, the ionization density is higher leading to more complex and hence difficult to repair damages. These correlations are however only valid up to a certain LET value. For higher LET values, there is a saturation effect as the additional dose is delivered to cells, which are already lethally damaged. At the same time, a smaller number of ions are required to achieve an equivalent dose deposition, resulting in a lower hitting probability. These effects lead to a drop of the RBE (Scholz (2006); Schardt et al. (2010)), as depicted in Figure 4.3.

The LET-value corresponding to the maximum RBE depends on the ion species. For heavier ions the maximum is shifted towards higher LET values, while at the same time the maximum achievable RBE value decreases (Kraft (1999)). At a given LET, heavier ions have larger energies. Consequently, for heavier ions the volume over which the energy is distributed is larger resulting in lower RBE values.

Protons of therapeutically used energies exhibit comparably low LET values over almost their entire range and are therefore sparsely ionizing. A modest increase of the RBE value with depth in the spread-out-Bragg-peak can be observed (Paganetti (2002)). Close to the distal end of the SOBP however a clear rise of the effective dose

^aThe track diameter is determined by the range of the most energetic electrons ejected. Since the electron energy is directly correlated to the projectile energy, lower energetic projectiles lead to smaller track diameters (Kraft (1999)).

can be noticed. Nonetheless, the use of a generic clinical RBE value of 1.1 is currently considered to be appropriate and is generally used for all positions along the depth dose curves, for all dose levels per fraction and in all tissues (Paganetti (2002); Choi and Kang (2012)).

In heavy-ion therapy, the situation is more complex due to large variations of the LET in depth. Relatively low LET values are found in the entrance channel, while the values are increased in more distal regions. The heavier the particle is the higher is the LET towards the end of the particle range and therefore the ionization density (Amaldi and Kraft (2005)).

Carbon ions are therefore sparsely ionizing in the entrance region and densely ionizing in the Bragg peak area. Consequently, an increase of the RBE by a factor of two to three is found in the distal SOBP compared to the entrance region (Jäkel (2007)). Figure 4.4 illustrates the track structures for a proton and a carbon ion in the Bragg peak (residual energy: 1 MeV/u). The higher ionization density around the carbon ion track is clearly visible. Even heavier ions already start to get densely ionizing in the entrance channel. Therefore, the elevated RBE is extended to healthy tissue in front of the target volume (Amaldi and Kraft (2005)) leading to an unfavorable dose distribution.

Local Effect Model (LEM) The RBE depends in general on various additional parameters like tissue- or cell-type, the biological endpoint, the fractionation scheme, or the deposited dose. It can be measured in biological in-vitro or in-vivo experiments. Due to the described complex dependencies of the RBE in the mixed radiation field, in addition to the measurements, biophysical modeling is required for carbon ion therapy

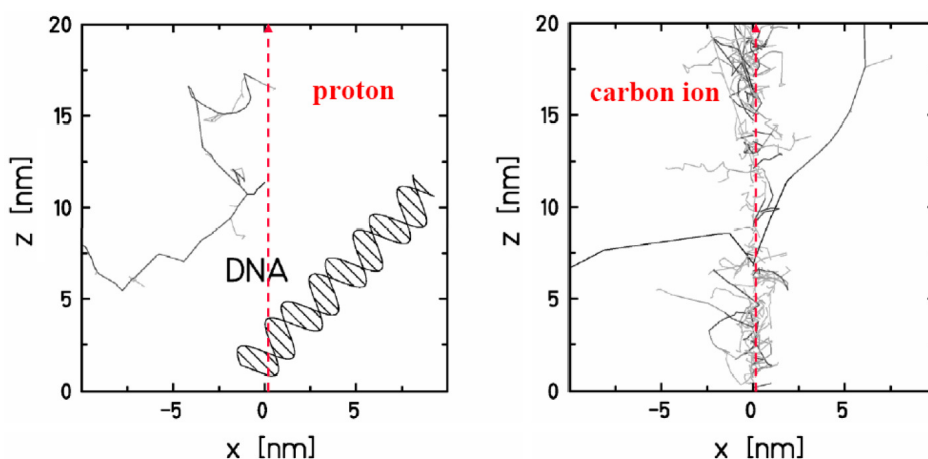


Figure 4.4: Structures of a proton (left) and a carbon ion track (right) in the Bragg peak. For comparison of sizes, a schematic representation of a DNA molecule is shown. The higher density of secondary electrons around the carbon ion track leads to a higher number of clustered DNA damages. Reprinted from Amaldi and Kraft (2005).

treatment planning. Several approaches exist and are used in the different facilities world-wide. One approach is using the local effect model (LEM) developed at GSI (Gesellschaft für Schwerionenforschung, Darmstadt, Germany). This model predicts the RBE values in each position in the treatment field based on three parameters: the photon dose-response curve of the system, i.e. the x-ray sensitivity of the tissue, the physical dose distribution around single ion tracks, and the size of the cell nucleus as the sensitive target (Scholz and Kraft (1994); Schardt et al. (2010)). The basic assumption of the model is that “the biological effect of irradiation is entirely determined by the spatial local dose distribution inside the cell nucleus” (Schardt et al. (2010)), independent of the radiation quality. Using amorphous track structure models, the local dose in the different ion tracks in the cell nucleus can be calculated for small subvolumes. For each of these subvolumes, the effectiveness of the particle can be determined by comparison with data of x-ray experiments. By integration of the results over the entire cell nucleus the biological damage can finally be extrapolated (Schardt et al. (2010)).

5 Materials and Methods

The materials and methods used for the studies presented in this thesis are described in the following sections. In the first part, details on the radiation facilities where the measurements were performed are given (see Section 5.1). In the second part of the chapter (Section 5.2) the characteristics of the Timepix detector are presented, while in the third part (Section 5.3) the measurement phantoms used in the studies are described. The final section summarizes information on the software employed for the data acquisition, processing and evaluation (see Section 5.4).

5.1 Radiation Facilities

In this section, the radiation facilities where the measurements for this work have been carried out are described. The main part of the investigations was performed employing therapeutic proton and carbon ion beams at the Heidelberg Ion-Beam Therapy Center described in Section 5.1.1. Additional experiments were carried out in low energetic ion beams, as present in the mixed ion spectra evolving from therapeutic carbon ion beams in tissue. Measurements with low energetic protons and deuterons were performed at the van de Graaff-accelerator of the Czech Technical University in Prague, while investigations in lithium ion beams were carried out at the Tandem accelerator at the Maier-Leibnitz-Laboratory in Garching near Munich. Detailed information about these accelerators is given in Section 5.1.2.

5.1.1 The Heidelberg Ion-Beam Therapy Center (HIT)

The Heidelberg Ion-Beam Therapy Center (HIT) in Heidelberg, Germany, was the first hospital-based facility in Europe providing radiotherapy with proton and carbon ion beams. The center was built in 2005 and started its clinical operation with the treatment of the first patient in late 2009 (Combs et al. (2010)). Since then, more than 1600 patients have been treated (status: July 25th, 2013)^a. For patient treatment, two treatment rooms with fixed, horizontal beam lines are available, while a third treatment room is equipped with a heavy ion gantry allowing irradiation from 360

^aPersonal communication with HIT personnel.

5 Materials and Methods

degrees (Haberer et al. (2004)). An additional room with a horizontal beamline is dedicated to quality assurance measurements and experiments for preclinical research.

In each room an isocenter is defined. At the horizontal beamlines, the isocenter is a selected point in a specific distance from the beam application monitoring system (see descriptions below). The isocenter is labeled by three intersecting lasers, allowing to reproducibly position objects at this point. In patient treatments typically the tumor volume is positioned in the isocenter.

A schematic illustration of the beam acceleration and delivery system at HIT is shown in Figure 5.1. Particle acceleration is accomplished using a combination of a linear accelerator for pre-acceleration of the ions and a synchrotron. The synchrotron design allows acceleration of ions from protons to oxygen (Haberer et al. (2004)). Currently two ion species, protons and carbon ions, are employed clinically, while oxygen ion beams are available in dedicated experimental campaigns.

The acceleration of ions in the synchrotron is not continuous, but carried out in bunches of ions. Each particle acceleration phase takes about five seconds and is followed by a beam extraction phase with a maximum duration of also five seconds. Each extraction phase is referred to as a spill. The ion beam is thus not continuous in time but has a characteristic spill structure.

Protons with energies of 48 to 221 MeV are available, while the energy range for carbon ions is 89 to 430 MeV/u. For both ion species these energies correspond to particle ranges in water of 20-300 mm (Haberer et al. (2004)). For each ion species 255 predefined energy steps are available. A change of the energy step can be performed in between two subsequent synchrotron cycles.

For beam delivery to the patient, an active volume scanning system is implemented at HIT. The system is based on the possibility to actively change the beam energy given by the use of a synchrotron, as described above, and a raster scanning technique (Haberer et al. (1993)). In this technique, narrow, pencil-like beams are scanned over the lateral extensions of the target volume to enable a homogeneous dose coverage. At HIT, the ion beams are focused by quadrupole magnets creating the required narrow pencil-beams. Six different beam spot widths are available for each ion type and energy step. The full-width half-maximum (FWHM) values range between 4 and 20 mm, depending on the particular particle type and energy (Krämer et al. (2000)). The beams are approximately normal distributed in terms of fluence, i.e. the number of ions irradiated to a given position, and energy (Telsemeyer (2012)). With the help of two pairs of dipole magnets, lateral deflection of the pencil beams is possible. The scanner magnets are placed about 7 m upstream from the isocenter, allowing quasi-parallel beam scanning. The area which can be covered by the pencil beams in the isocenter is 200 x 200 mm² large. In a typical irradiation, the distance between the beam spots is 2 mm (Krämer et al. (2000)).

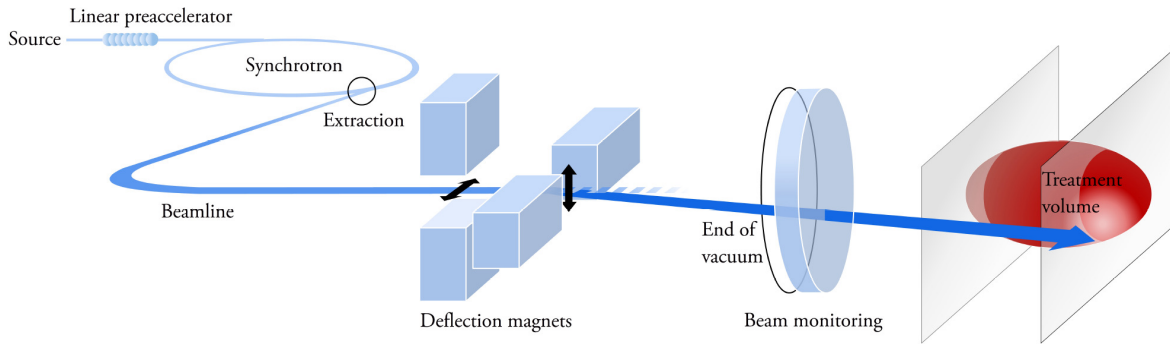


Figure 5.1: Schematic illustration of the beam acceleration and delivery system at the Heidelberg Ion-Beam Therapy Center. Reprinted from Huber (2011)

For the beam intensity, i.e. the number of particles delivered per time unit, 15 logarithmically spaced settings are defined (Parodi et al. (2012)). For carbon ions, values between $2 \cdot 10^6$ ions/s and $5 \cdot 10^8$ ions/s are available, while the proton intensities are increased by a factor of 40 to compensate for their lower stopping power. Consequently, for both ion species similar dose rates are reached.

After acceleration, the particles leave the vacuum tube through a vacuum exit window and pass a so called beam application monitoring system (BAMS). This system is used to control the application of each irradiation spot. It consists of multi-wire proportional chambers (MWPCs) which examine online the beam spot size and position, and transmission ionization chambers (ICs) monitoring the ion fluence. Furthermore, at each irradiation place a ripple filter is available. This passive device is typically used in carbon ion beams. It broadens the energy spread of the beam. Consequently, the Bragg peak in the carbon ion depth dose distribution is widened, and smooth spread-out Bragg peaks (SOBPs) can be created without requiring too small energy steps (Weber and Kraft (1999)).

5.1.2 Van-de-Graaff Accelerators at IEAP in Prague and at MLL in Garching

Van-de-Graaff accelerators are electrostatic particle accelerators. The electrostatic field is created by a van-de-Graaff generator, which uses a moving belt to accumulate electrical charge and therewith create the static electrical field. The potential difference can reach up to several MV.

Measurements in beams of low energetic protons and deuterons were performed at the van-de-Graaff accelerator of the Institute of Experimental and Applied Physics of the Czech Technical University in Prague (IEAP, CTU in Prague). This accelerator delivers continuous beams of light ions with beam currents of 0.5 to 10 μ A. In addition,

lower intensities in the order of $10^5 \text{ cm}^{-2} \text{ s}^{-1}$ can be achieved by scattering the particles. Protons and deuterons are provided in an energy range of 0.3 to 2.5 MeV and ^4He in an energy range of 1 to 5 MeV. Furthermore, fast neutrons are available from deuterium-deuterium or deuterium-tritium reactions. The experiments are performed in vacuum chambers with a vacuum level of $10^{-5} \text{ mbar}^{\text{a}}$.

Additional measurements were performed in beams of ^7Li at the Tandem van-de-Graaff accelerator at the Maier-Leibnitz-Laboratory (MLL) in Garching near Munich. In Tandem accelerators, the accelerating voltage is used twice, exploiting a midway change of the ion charge by stripping off electrons. The maximum achievable energy for protons is 25 MeV (Reinhardt et al. (2011)). For ions with higher charge a higher energy is achievable by removing more than one electron in the stripping process. The energy resolution at the MLL Tandem accelerator is in the order of 10^{-4} (Reinhardt et al. (2011)). Continuous beams with currents of up to 0.1 mA can be produced (Weber and Herlitzius (2010)). The measurements presented in this work were performed at an irradiation site equipped with a Kapton vacuum exit window of 50 μm thickness and 10 mm diameter, allowing accomplishing measurements in air (Reinhardt et al. (2013)).

5.2 The Timepix Detector

The Timepix detector (Llopart et al. (2007)) is a hybrid semiconductor pixel detector which was developed within the framework of the Medipix collaboration^b at CERN (European Organization for Nuclear Research). Timepix is an evolution of the Medipix2 chip (Llopart et al. (2002)). The detectors share many features and physical dimensions, e.g. the same active area or pixel size. Both detectors are based on the quantum counting principle, but they have different functionalities on the level of the single pixel. The Medipix2 chip offers the possibility to select an energy window, with the upper and the lower threshold being adjustable pixelwise with 3 bits. On the one hand, this feature offers a uniform performance over the whole pixel matrix, on the other hand it allows selecting and investigating only events in a certain energy range. The Timepix detector, in contrast, has only a single, lower energy threshold, which can be adjusted pixelwise with 4 bits to ensure the uniform performance of the pixel matrix. Furthermore, the lower threshold allows reducing the background signal by suppression of electronic noise or dark current of the sensor (Leroy and Rancoita (2011)). The Timepix device offers the additional feature of a high frequency external reference clock. The clock allows to measure the arrival time of ionizing radiation in the sensitive detector volume or the amount of charge detected. In this section, the detector design

^aInformation taken from <http://aladdin.utef.cvut.cz/projekty/VdG/>, accessed in April 2013.

^b<http://medipix.web.cern.ch/medipix/>, accessed: April 16th, 2013.

and principle of operation of the Timepix detector are described along with characteristics being of special interest for the operation of the detector in charged particle beams, namely the charge sharing effect and the calibration of the detector in terms of deposited energy.

5.2.1 Detector Design and Principles of Operation

The detector consists of a sensor layer which is flip-chip bump-bonded to the Timepix read-out chip (Llopart et al. (2007)). Figure 5.2 shows a schematic illustration of this bump-bonding architecture. The chip is designed to detect either positive or negative charge input. It can therefore be utilized with various sensor materials (e.g. Si, CdTe, GaAs) and thicknesses (Leroy and Rancoita (2011)). In the device used in this work, a 300 μm thick crystalline silicon layer is used as sensor. The size of the active area is approximately $1.4 \times 1.4 \text{ cm}^2$. The detector chip is equipped with a single common electrode on one side and a matrix containing 256×256 electrodes (65536 pixels), each with an area of $55 \times 55 \mu\text{m}^2$ on the other side (Jakubek (2009b)). Figure 5.3 shows a schematic illustration of the sensitive detector layer, the electrodes and the read-out electronics of a single pixel.

Ionizing radiation penetrating the sensitive volume creates free charge carriers (electron-hole pairs). In the detector used for this work, a reverse bias voltage is applied to the sensor electrodes in order to create a depleted volume and collect the free charge carriers (holes) and transfer them towards the read-out electrodes (Jakubek (2009b)).

Each front side electrode (pixel) contains its own read-out circuit, consisting of an analog part with a signal preamplifier and a discriminator as well as a digital counter integrated on the Timepix read-out chip. The discriminator contains a single energy threshold, which can be adjusted pixelwise. The detector signal is read-out in frames (images) of a given frame duration called acquisition time, which can be chosen arbitrarily. Any ionizing radiation creating free charge carriers arriving at the readout

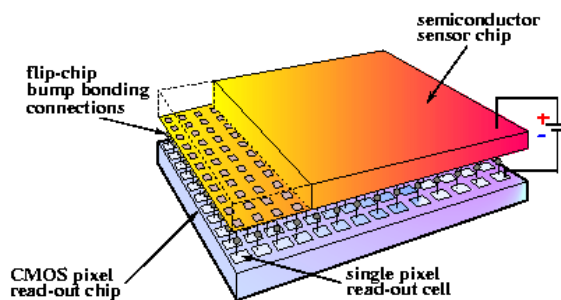


Figure 5.2: Schematic illustration of the hybrid design of the Timepix detector. Reprinted from Anton et al. (2009).

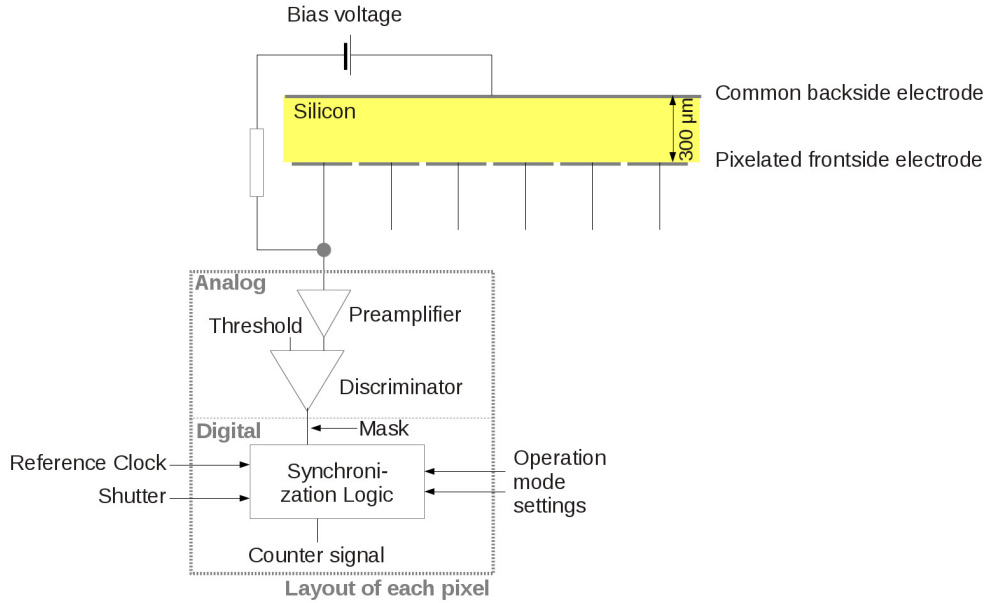


Figure 5.3: Schematic illustration of the Timepix detector showing the radiation sensitive sensor and the read-out electronics in a single pixel.

electrode within this preselected time interval is registered. A globally applied shutter signal is used to control the beginning and the end of the frame time. The data in each pixel is integrated in a 14-bit counter with a dynamic range of 11810 counts (Llopart et al. (2007)). During the frame time the pixel counters are incremented by the external reference clock depending on the mode in which the pixel is operated (Llopart et al. (2007); Anton et al. (2009)).

Each pixel can be operated independently in one of the following four different operation modes illustrated in Figure 5.4 (Llopart et al. (2007); Plackett et al. (2009)). The operation modes are:

- **Medipix mode (counting mode):** The counter is incremented by one each time the output of the preamplifier passes the preset threshold. In this mode, the number of ionizing particles registered in the pixel within the duration of a particular frame can be counted.
- **Timepix mode (time mode):** The counter is started when the amplifier output first passes the threshold and is then incremented continuously with one count per clock cycle until the end of the measurement frame. In this manner, the time of the first signal detection in the pixel is recorded.
- **Time-over-threshold (TOT)-mode (energy mode):** While the amplifier output is above threshold, the counter is incremented continuously by one count per clock cycle. Since the recorded time-over-threshold is correlated to the am-

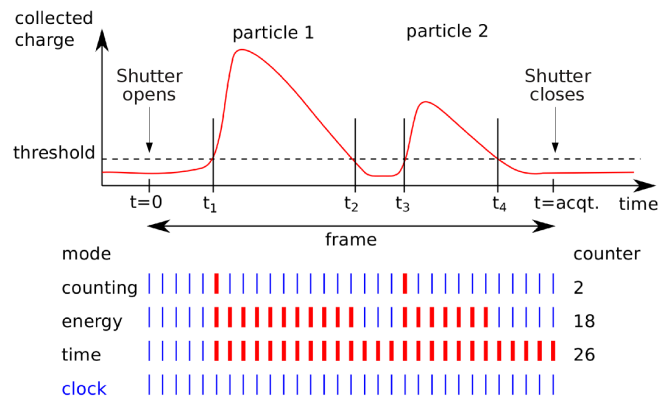


Figure 5.4: Illustration of the different operation modes of the Timepix detector. The operation modes are explained in the text. Reprinted from Gwosch (2012).

plitude of the collected charge, in this mode the pixel value is a measure of the energy deposited in the pixel during the time the shutter is open.

- **Masked mode:** The pixel shutter is not opened. This mode can be used to mask pixels, e.g. pixels known to be malfunctioning.

Read-out of the information stored in the counter is performed for the whole detector after the shutter closes, i.e. after the end of the frame duration. The dead time connected to the frame read-out procedure is in the order of 10 ms. In all working modes, the depth of the counter is restricted to 11810 counts. This is a particular limitation in Timepix mode and for the detector being operated at high clock frequencies (Plackett et al. (2009)).

The detector is fully operated and read out via the USB^a-based FITPix interface (Kraus et al. (2011)). Figure 5.5 shows a picture of the Timepix detector and the FITPix interface employed in this work. The interface contains a field-programmable gate array (FPGA) circuit, providing a control unit communicating with a PC through USB 2.0 and a control unit communicating with the Timepix or other detectors of the Medipix family. The maximum possible readout speed is 90 frames per second (Kraus et al. (2011)). The FITPix interface also provides the bias voltage for the sensor in a range from 5 to 100 V. It has a compact size of 62 x 50 x 20 mm³. For operation of the detector there is no need for any additional equipment, except for a standard personal computer. This makes the Timepix detector highly flexible and portable and enables its use in many set-ups and geometries or even within phantoms.

The data acquisition software package Pixelman (Turecek et al. (2011)) provides control and read-out of the Timepix detector via the FITPix interface. It enables on-line visualization and analysis of the detector signal. Further details on the Pixelman software are given in Section 5.4.

^aUniversal Serial Bus

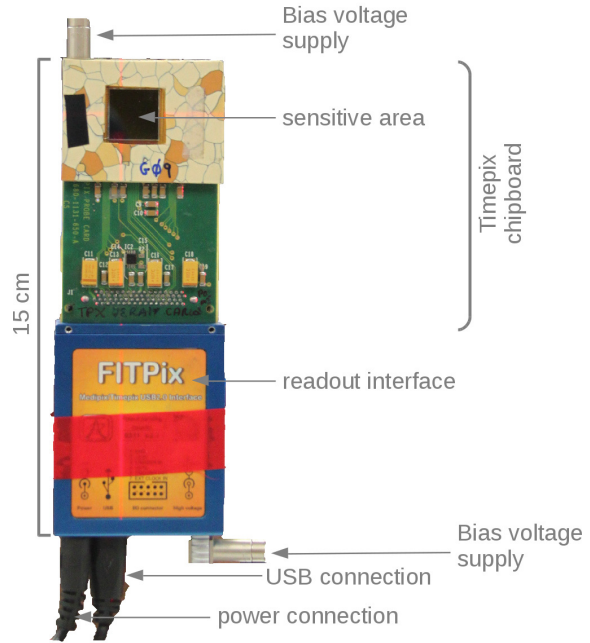


Figure 5.5: The Timepix detector used in this work and the FITPix read-out interface.

5.2.2 Charge Sharing Effect

Semiconductor materials have a small band gap between the electronic conduction band and the valence band. Therefore, a certain energy is needed to excite an electron from the valence into the conduction band. In case of silicon, this energy amounts to 1.12 eV (Leroy and Rancoita (2011)). After an excitation, a positively charged hole is left in the valence band and a free electron in the conduction band.

Upon irradiation of a silicon detector with ionizing particles, the charged particles gradually deposit their energy in the silicon in multiple interactions (see descriptions in Section 2.1). Consequently, electrons are excited from the valence to the conduction band and many charge carriers are released. Depending on the polarity, an externally applied field forces either the positive (holes) or the negative (electrons) charge carriers towards the read-out electrode. The drift velocity of the charge carriers is determined by their polarity and the applied electric field. In silicon the electron mobility is given by $\mu_e = 1350 \text{ cm}^2 \text{ V}^{-1} \text{ s}^{-1}$ and the hole mobility by $\mu_h = 450 \text{ cm}^2 \text{ V}^{-1} \text{ s}^{-1}$ (Leroy and Rancoita (2011)).

On their way to the electrode, the free charge carriers are subject to the so called charge sharing effect. This term describes the spread of the charge cloud during the collection process. Consequently, the charge is collected by several adjacent pixels of the read-out electrode, forming a so called pixel cluster (Jakubek (2009b)). Figure 5.6 illustrates the charge sharing effect.

The charge sharing effect mainly takes place due to electrostatic repulsion and charge diffusion (Jakubek (2009b)). It strongly depends on the deposited energy, the applied bias voltage, i.e. the strength of the electric field determining the speed of charge col-

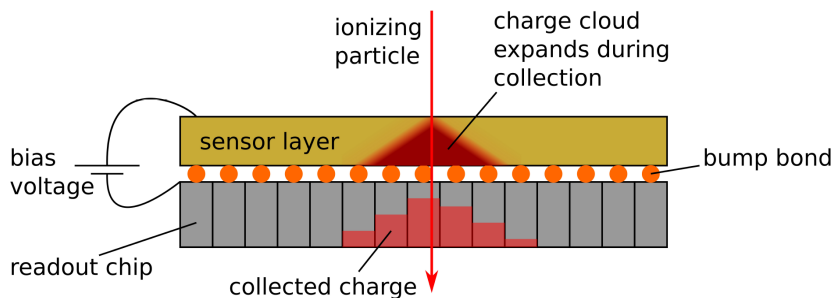


Figure 5.6: Illustration of the Timepix detector set-up and the charge sharing effect. Recent findings on induced charge are not considered. Reprinted from Gwosch (2012).

lection, and the thickness of the depleted zone in the sensitive detector volume. For a 300 μm thick Timepix silicon sensor the voltage for full depletion is about 20-25 V (Leroy and Rancoita (2011)). While diffusion and drift processes, being the dominant process responsible for the charge sharing for X-rays, are well-known (Jakubek (2009b)), further effects have to be taken into account for charged particles, which lead to dense carrier tracks in the silicon (Leroy and Rancoita (2011)). Due to the very high energy deposition, the free charge carriers can locally distort the externally applied electric field.

Figure 5.7 shows the lateral spread of clusters produced by α -particles of 5.4 MeV in a Medipix2 detector with a 300 μm thick silicon sensor as a function of the applied bias voltage. With the sensitive detector layer being the same as used for the Timepix device in this work, the obtained results can be directly transferred. The charge column created by the α -particles is 28 μm long and has an initial radius of about 1 μm . The curve shown in Figure 5.7 can be divided into four regions which can be explained as follows (Campbell et al. (2008); Leroy and Rancoita (2011)):

- The **initial increase** is due to the onset of the depleted volume and diffusion in the comparably long collection time at low bias voltages.
- In the region of the **first decrease** funneling starts to contribute to the charge sharing. The charge column approaches the depleted area and the electric field near the depleted area is modified. Charge carriers inside the column are funneled towards the collecting electrodes, decreasing the charge carrier concentration inside the column and hence the lateral diffusion.
- The **second increase** occurs when the depleted region reaches the particle track. More of the diffusing charge is pulled by the electric field to the electrode. Consequently the charge at the edges of the clusters can pass the threshold and the cluster size increases.

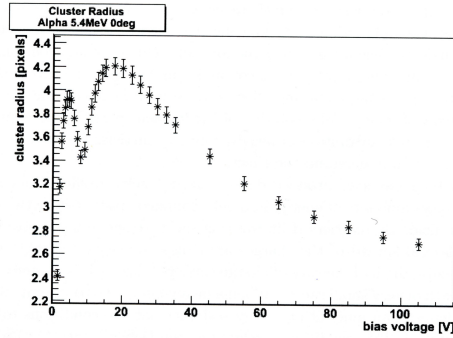


Figure 5.7: Illustration of the lateral spread of the charge for α -particles of 5.4 MeV in a Medipix2 detector with a 300 μm thick silicon sensor. The average cluster radius is shown as a function of the applied bias voltage. Reprinted from Leroy and Rancoita (2011).

- When the entire particle track is included in the depleted region a **second decrease** can be observed. Due to the increasing strength of the applied electrical field charge collection is faster, there is less time for diffusion and the cluster size decreases, while the total amount of collected charge is maximal.

For protons and heavy charged particles of therapeutic energies no detailed studies of the lateral cluster spread have been published. While the explanations given by Campbell et al. (2008) and described above only hold for charged particles with low energies, hence stopping within the first μm of the sensitive detector layer, the influences can be largely different for particles traversing the whole sensor thickness.

For measurements with the Timepix detector, the amount of charge collected in each pixel can be measured in energy-operation mode. Ideally, the overall charge released by a particle can be revealed by summation of all fractional charge, i.e. adding up the signal of all pixels in the cluster. The measurements may however be distorted by various influences, as discussed in Section 5.2.3. In addition, as described in Section 5.2.1, the charge in a particular pixel is only registered when it is above the defined threshold. Some pixels, e.g. at the outer rim of the cluster, may collect charge too small to be recorded. This charge is therefore lost. As a consequence, the overall charge in the cluster was found to be often lower than the correct value (Jakubek (2009a)). On the other hand, for high energy depositions in the sensitive detector layer there are pixels showing a signal due to induced charge, as discussed in the next paragraph. This artificial signal can wrongly increase the overall cluster signal.

Induced Charge Recent investigations^a have shown that the initial increase and first decrease of the cluster spread with increasing bias voltage are moreover influenced by an effect which can be referred to as 'Induced Charge'. For ionizing radiation

^aPersonal communication with J. Jakubek, IEAP, CTU in Prague.

depositing large amounts of charge in the sensor layer the released drifting charge carriers cause the induction of an electrostatic charge with opposite polarity in the conductive pixel electrodes (i.e. negative charge is induced in the case of hole collection). The charge integrating preamplifiers connected to the respective pixels collect this induced charge. Due to its polarity, the output signal of the amplifier does not cross the threshold and the discriminator output is inactive. However, the feedback capacitors in the preamplifier are charged with the inverted signal. After all drifting charge carriers have been collected by the respective pixels, the induced charge in the pixel electrodes is redistributed to maintain a zero potential on the metallic contacts. This results in an equal charge signal but with opposite polarity added to the preamplifier feedback capacitors (i.e. positive polarity for hole collection). Therefore, the overall integrated induced charge should be zero. However, after creation of the induced charge stored in the feedback capacitor and during the drifting process the feedback capacitors are slowly discharged and thus a part of the previously stored induced charge is 'forgotten'. Therefore, after full recollection of the induced charge a non-zero signal results. Moreover, it has the same polarity as the signal of the drifting charge and is therefore added to the overall signal in the pixel. The effect is of special importance for a high energy deposition in the detector. The induced signal is more pronounced for low bias voltages, as in their case the charge collection process is slower and therefore larger parts of the induced charge are 'forgotten' during the drifting time. The lateral range of influence of this effect can easily exceed the area of pixels collecting drifting charge due to charge sharing. It can therefore result in a rim of pixels with low, artificial signal arranged around the actual charge cluster and in an increase of the overall cluster size and signal.

Influence of Radiation Damage The dynamics of charge collection are moreover influenced by radiation damage the detector experiences. Already very small changes of the sensor properties due to irradiation affect the cluster size significantly (Platkevic et al. (2013)). This effect can be assigned to a lower resistivity of the damaged compared to undamaged sensor material. Therefore, the electric field inside the damaged zone is lower. Consequently, the charge collection is slower and there is a larger diffusion of charge carriers in the damaged detector zones. Below the damaged area on contrary the electric field is stronger compared to the electric field in undamaged regions (Jakubek et al. (2013)). Depending on the bias voltage, these variations in the electric field strength can lead to an increase or a decrease of the cluster sizes in the damaged detector regions. Radiation damage also influences the charge collection efficiency, as is discussed in the next section.

5.2.3 Influences on the Charge Collection Efficiency

The charge collection efficiency (*CCE*) describes the ratio of the collected charge Q to the initially deposited charge Q_0 (Leroy and Rancoita (2011))

$$CCE = \frac{Q}{Q_0}. \quad (5.1)$$

It depends on various parameters, like the point where a free charge has been created, the charge mobility, the externally applied electrical field (bias voltage), trapping or recombination of charge carriers. Both, trapping and recombination are related to defects in the sensor material. Possible defects in the crystal lattice are for example impurities or vacancies. They can be a result of the manufacturing process of the sensor or radiation damage. Trapping and recombination reduce the lifetime of free charge carriers and lead to a loss of charge in the collection process.

For the Timepix detector, influences of radiation damage on the charge collection have been investigated (Jakubek et al. (2013); Platkevic et al. (2013)). The charge collection efficiency was found to decrease with the extent of the radiation damage. This can be partly corrected for by a recalibration of the detector (Platkevic et al. (2013)). More information on the detector calibration is presented in the next section. On the other hand, radiation damage can increase the detector noise and influence other electrical properties.

The distortion of energy-loss measurements due to recombination or trapping are also referred to as quenching. Further possible parameters altering the measurements are signal loss in the read-out electronics or an overflow of the counter (artificial quenching). The quenching probabilities of the Timepix detector in therapeutic ion beams have not been explicitly studied before. In this work, these probabilities are partially investigated. The corresponding experiments and results are presented in Sections 6.1, 6.2, 7.1, and 7.2, respectively.

5.2.4 Detector Calibration for Energy Measurements

The energy-mode allows to measure the charge collected by the individual pixels (see Section 5.2.1). To convert the collected charge to the corresponding energy values, a calibration is needed (Jakubek et al. (2008)). Each of the 65536 pixels of the Timepix detector uses its own analog circuit and therefore needs to be separately energy calibrated.

For the calibration procedure developed by the Institute of Experimental and Applied Physics of the Czech Technical University in Prague (Jakubek et al. (2008), Jakubek (2009a), Jakubek et al. (2011)), discrete X-ray radiation of known energies is used. Two radioactive sources (^{55}Fe emitting γ -quanta of 5.9 keV and ^{241}Am emitting γ -quanta of 59.5 keV) and many different fluorescent materials emitting characteristic X-rays

(Fe: 6.4 keV, Cu: 8.0 keV, Zr: 15.8 keV, Mo: 17.5 keV, Cd: 23.2 keV, In: 24.2 keV) are employed (Jakubek et al. (2008)). The fluorescence is initiated by a tungsten X-ray tube.

In order to be able to correlate the signal of a pixel to the measured energy, only events in which the complete charge released by the particle was collected by a single pixel are used. For this reason, only single-pixel clusters are considered in the calibration procedure. All events in which the charge released by a particle creates a signal in two or more pixels, e.g. due to hitting the border between two pixels or charge sharing, are not regarded. In an improved calibration method, the charge lost due to leakage to adjacent pixels is estimated by simulations and the energy calibration is corrected accordingly (Jakubek (2009b)).

At least three energy spectra are used for the calibration. For each pixel, the signal spectrum obtained for a known particle energy is fitted by a Gaussian. Subsequently, an individual calibration curve is computed for each pixel in another fitting process. The energy response of each pixel is modeled by a surrogate function depending on four parameters:

$$TOT(E) = a \cdot E + b - \frac{c}{E - t}. \quad (5.2)$$

Pixels which are found to be malfunctioning during the calibration procedure are set to masked mode and are disregarded in subsequent measurements.

Figure 5.8 shows exemplary calibration curves for 20 randomly chosen detector pixels. Large variations between the individual calibration curves can be seen.

In the low energy range the surrogate functions are non-linear. However, since they are linear in the higher energy region (starting at approximately 10 keV), an extrapolation can be used to measure energy values higher than the highest value used in the calibration procedure. The linear extrapolation is well applicable for energies of

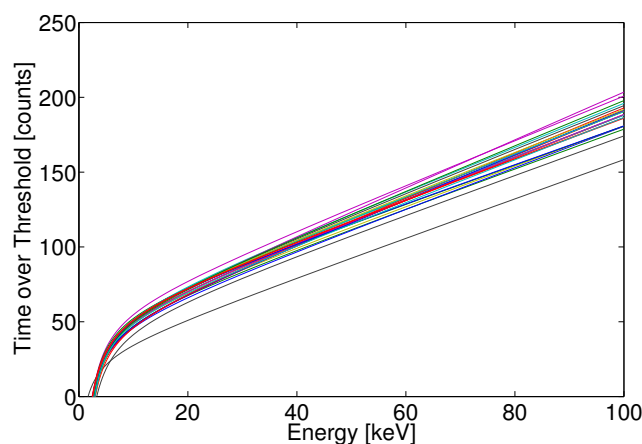


Figure 5.8: Examples for the calibration curves of 20 randomly chosen pixels of the Timepix detector used in this work.

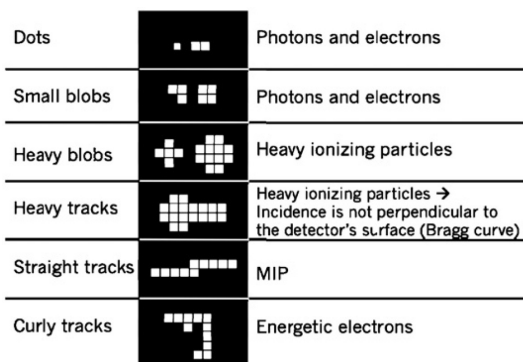
up to 900 keV (Jakubek (2010)). For even higher energies, the pixel electronics start to behave non-linearly, thus distorting the energy measurement. In this energy region, the pixel response was found to be drastically increased. For even higher charge collected in a pixel, the response of the pixel electronic chain gradually saturates (Granja et al. (2011)), leading to a decrease of the pixel signal for increasing energies. Consequently, the charge clusters show a dip in the center, where the highest amount of charge is collected. For very high amounts of charge collected in a pixel and high bias voltage, the pixel signal can become nearly zero. This effect can be partly reduced by applying a sufficiently low bias voltage.

5.2.5 Single Particle Detection in Ion Beams with the Timepix Detector

For ionizing charged particles depositing energies above the preset threshold, detectors of the Medipix2-type show detection efficiencies close to 100% (Bouchami et al. (2011b)). Being based on the same sensor type, the same applies for the Timepix detector used in this work. This can be explained by the high stopping power of ions on the one hand, and the high density and purity of the sensor material combined with only small losses of charge carriers on the other hand. Together with the high spatial resolution of the detector, the detection of individual ions is possible. Moreover, even for low energetic electrons single particles can be detected.

In the studies of Holy et al. (2008) and Bouchami et al. (2011a) the possibility to differentiate between different types of irradiation by the pattern they introduce in Medipix2 detectors were investigated. A correlation between specific types of ionizing radiation and the obtained geometrical features of the clusters (the cluster shapes) was described (see Figure 5.9). Electrons with kinetic energies in the keV range have random trajectories as they undergo multiple scattering within the detector layer leading to clusters in the form of curly tracks. Low energetic photons are detected in an indirect procedure, based on the release of low energetic electrons. The related tracks are small, often expanding to only a few pixels. Higher energetic photons lead to clusters similar

Figure 5.9: Examples for different cluster shapes generated by different types of radiation in the Medipix2 detector. Reprinted from Bouchami et al. (2011a).



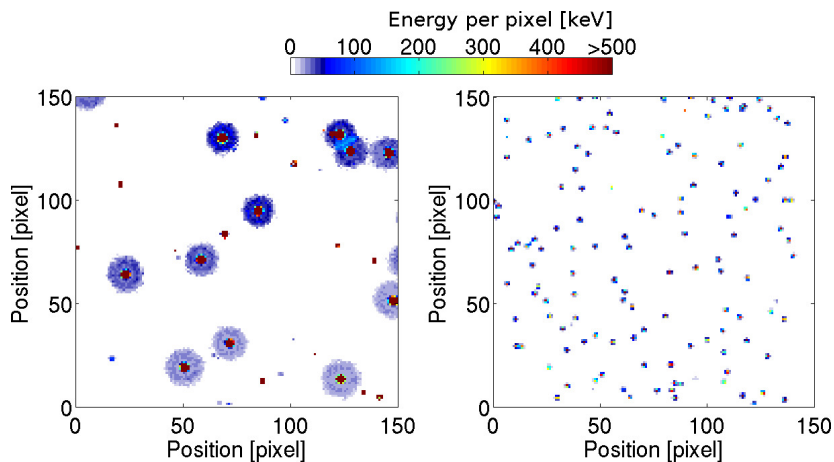


Figure 5.10: Timepix detector signal in a carbon ion beam of $E_{\text{initial}} = 89$ MeV/u (left) and a proton beam of $E_{\text{initial}} = 48$ MeV (right). The color bar indicates the energy registered per pixel. A region of the sensitive area of 150×150 pixels is shown.

to small blobs. For heavy charged particles the cluster shape strongly depends on the incident angle of the particle on the sensor and on the ion energy. Low energetic, heavy ionizing particles, like alpha particles with short ranges, produce round blobs. For perpendicular hits, also higher energetic heavy charged particles typically appear as large blobs, while non-perpendicular incident heavy charged particles result in heavy tracks. For minimum ionizing particles (MIP) straight thin tracks are obtained.

The presented classification does however not allow distinguishing between different ion species. In this work, the Timepix detector is used in energy-mode thus enabling to enhance the information given by the cluster shape by the information contained in the cluster signal. In Figure 5.10 examples for the Timepix detector signal in mono-energetic carbon ion and proton beams are shown. The detector was operated in energy-mode and the primary beam direction was perpendicular to the detector surface. In both cases, the signal clusters due to individual ions are clearly separated. A distinct difference in terms of size, signal and shape between the clusters induced by the two ion species can be seen. These differences are also obvious in the direct comparison of cluster size and cluster signal distributions for the two ion species depicted in Figure 5.11. They build the basis for the approach of ion spectroscopy with the Timepix detector investigated in this work.

In particular, the cluster quantities used for characterization of the clusters are defined as

- **Cluster size:** The number of pixels in the cluster, i.e. the number of directly or diagonally neighboring pixels with a non-zero signal (a signal above the preset threshold).

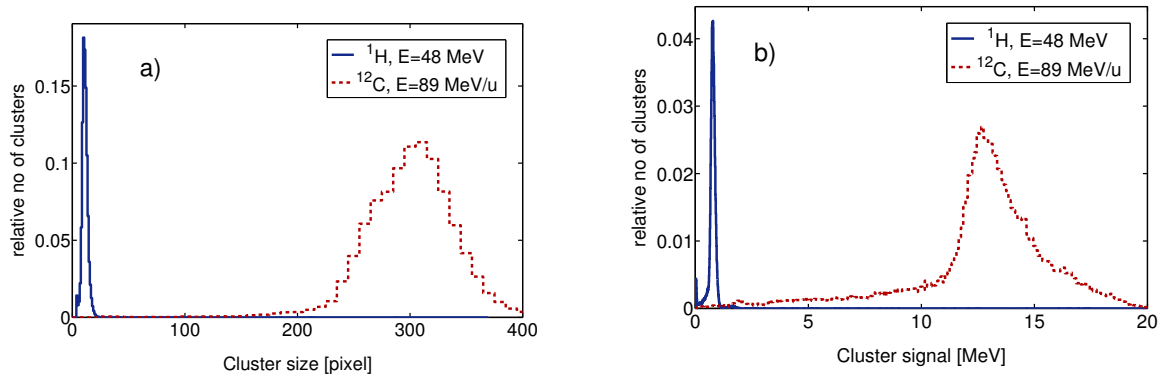


Figure 5.11: Distribution of cluster sizes (a) and cluster signals (b) for measurements in a carbon ion beam of $E_{\text{initial}} = 89 \text{ MeV/u}$ and a proton beam of $E_{\text{initial}} = 48 \text{ MeV}$. A clear difference between the cluster parameters for the two ion species can be seen.

- **Cluster signal:** The sum of the pixel TOT(time-over-threshold)-values of all pixels in the cluster. For energy-calibrated data this value is correlated to the energy deposited in the sensor by the particle creating the cluster. In this case, the cluster signal is given in eV.
- **Mean cluster signal:** The average cluster signal per pixel, for energy-calibrated data given in eV.
- **Cluster height:** The maximum pixel value in the cluster, for energy-calibrated data given in eV.
- **Cluster roundness:** The ratio between the diameter d of the circle having the same area as the respective cluster and the distance D_{max} between the two pixels in the cluster with the largest distance to each other (Opalka et al. (2012), see Figure 5.12)^a. This parameter ranges between 0 and 1 and is equal to 1 for a cluster with an ideal circular shape.
- **Cluster position:** The signal weighted center of mass of the cluster.

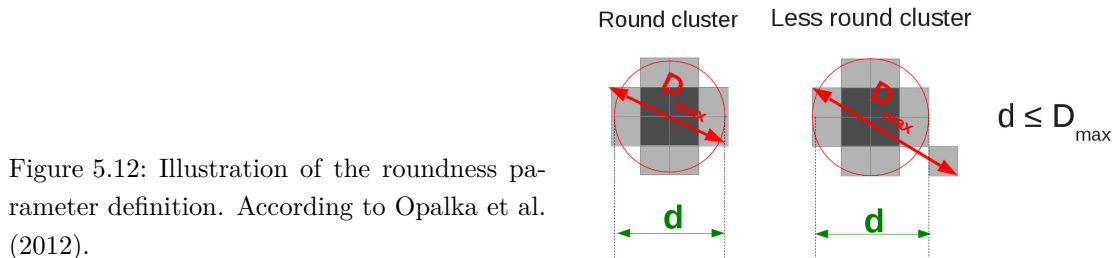


Figure 5.12: Illustration of the roundness parameter definition. According to Opalka et al. (2012).

^aPlease note that in Opalka et al. (2012) the distance between the centers of the two pixels with the largest distance to each other was used for the calculation of the roundness parameter, while in this work the distance between the respective outer pixel rims was considered.

5.3 Phantoms Used for the Measurements

For the measurements presented in this work, homogeneous phantoms with simple geometries were used.

The used **PMMA^a phantom** (PTW, Freiburg, Germany) comprises multiple individual slabs with a size of 30 x 30 cm² and thicknesses of 1, 2, 5, or 10 mm, respectively. The tolerance of the thickness for each slab is 0.1 mm (PTW Freiburg). The slabs can be combined arbitrarily, so that any total thickness between 1 mm and 30 cm can be created. The water-equivalent path length (WEPL)^b of PMMA was determined by Jäkel et al. (2001) to 1.165. This value could be verified for the slab phantom used in this work^c. For measurements in which even larger PMMA thicknesses were required, additional PMMA blocks with thicknesses between 5 and 8 cm and sufficiently large lateral dimensions were used.

The employed **steel phantom** has a cylindrical form with a diameter of 160 mm and a thickness of 30.1±0.1 mm. Its WEPL was determined in a measurement with a peakfinder (PTW, Freiburg, Germany) to be 5.63±0.02. A schematic drawing and an image of the peakfinder set-up at HIT are shown in Figure 5.13. In this measurement, the depth dose distribution of a carbon ion beam ($E_{\text{initial}}=380.97$ MeV/u) in water was determined. In a second measurement, the steel phantom was placed in front of the peak finder and the measurement was repeated. The difference in the obtained peak positions is equivalent to the water-equivalent thickness (WET) of the phantom. By division of the WET-value with the thickness of the phantom, the WEPL was calculated. The obtained value was found to agree within the limits of accuracy to the value published for steel by Jäkel (2006).

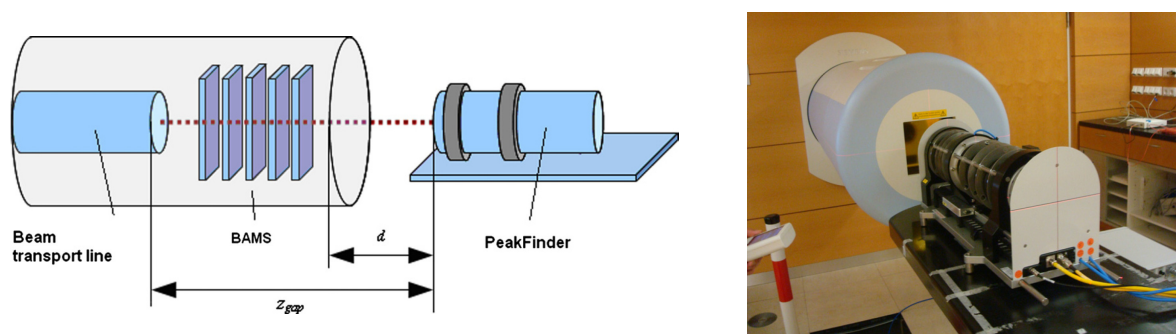


Figure 5.13: Schematic drawing (left) and image (right) of the peakfinder set-up at the horizontal beamline at HIT. Both reprinted from Sánchez-Parcerisa et al. (2012).

^aPoly(MethylMethAcrylate)

^bThe water-equivalent path length is a measure for the ratio of the range of ions in a given material to the range of identical ions (same particle species and initial energy) in water.

^cPersonal communication with S. Brons, HIT.

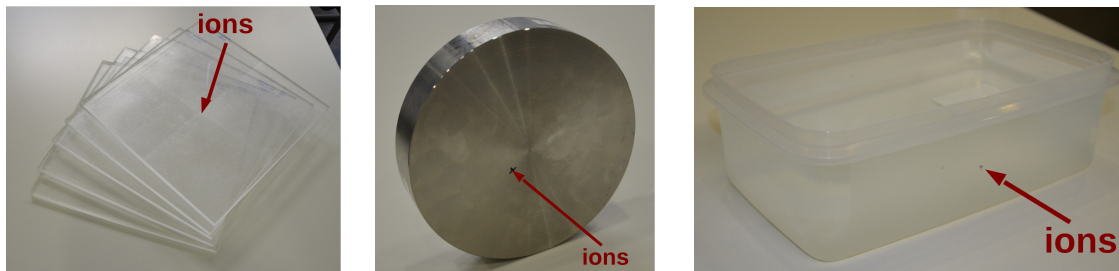


Figure 5.14: The phantoms used for the measurements. Left: PMMA slabs, each 10 mm thick. Center: Steel plate, 30.1 mm thick. Right: Water tank filled with distilled water, 158 mm thick.

Furthermore, a small **water tank** was used. It is made of plastic material and has a wall thickness of 2 mm. The width of the water tank in beam direction is 158 mm. For the measurements it was filled with distilled water.

Table 5.1 summarizes the main properties of the employed phantoms, while images of them are shown in Figure 5.14.

Table 5.1: Density and water-equivalent-path-length (WEPL) of the phantom materials used in this work.

Material	Density $\left[\frac{g}{cm^3}\right]$	WEPL
Water	1	1
PMMA	1.18	$(1.165 \pm 0.013)^a$
Steel	8.1	$(5.63 \pm 0.02)^b$

5.4 Software Used for Data Acquisition, Processing, and Evaluation

5.4.1 Data Acquisition with Pixelman

For the acquisition of data with the Timepix detector the Pixelman software was used. Pixelman is a multi-platform software package running on Microsoft Windows, Linux and Mac OS X operating systems. Pixelman is written in C++ and has a Java graphical user interface. It has a flexible modular architecture and the functionality can be further extended by software plug-ins. The most important modules are hardware libraries communicating with the detector through a variety of readout interfaces, the Medipix Control Library, which handles all connected detector devices and provides

^aData taken from Jäkel et al. (2001).

^bOwn measurement.

5.4 Software Used for Data Acquisition, Processing, and Evaluation

synchronized access to them, and the Pixelman manager for plugin management, synchronization and communication between the plugins as well as access of the plugins to the Control Library (Turecek et al. (2011)). Pixelman enables to fully control the Timepix detector, i.e. to set all detector parameters. In addition to the detector itself, also other devices, like stepper motors can be controlled by the Pixelman software. These devices can be managed by C++ plugins which can also be used for data processing or experiment control. For communication between the C++ core and the Java based part a Java wrapper is used. A Java manager loads and initializes the Java plugins, which can extend the Pixelman functionality in the same way as C++ plugins (Turecek et al. (2011)). Figure 5.15 shows a screenshot of the Pixelman Java graphical user interface.

For the measurements presented in this work, each measurement frame was written to an individual plain text file, listing the positions and values of pixels showing a signal above the preset threshold. In order to exclude measurement frames from the analysis which were taken during the time the beam was off, only frames showing a significant signal were considered in the evaluation.

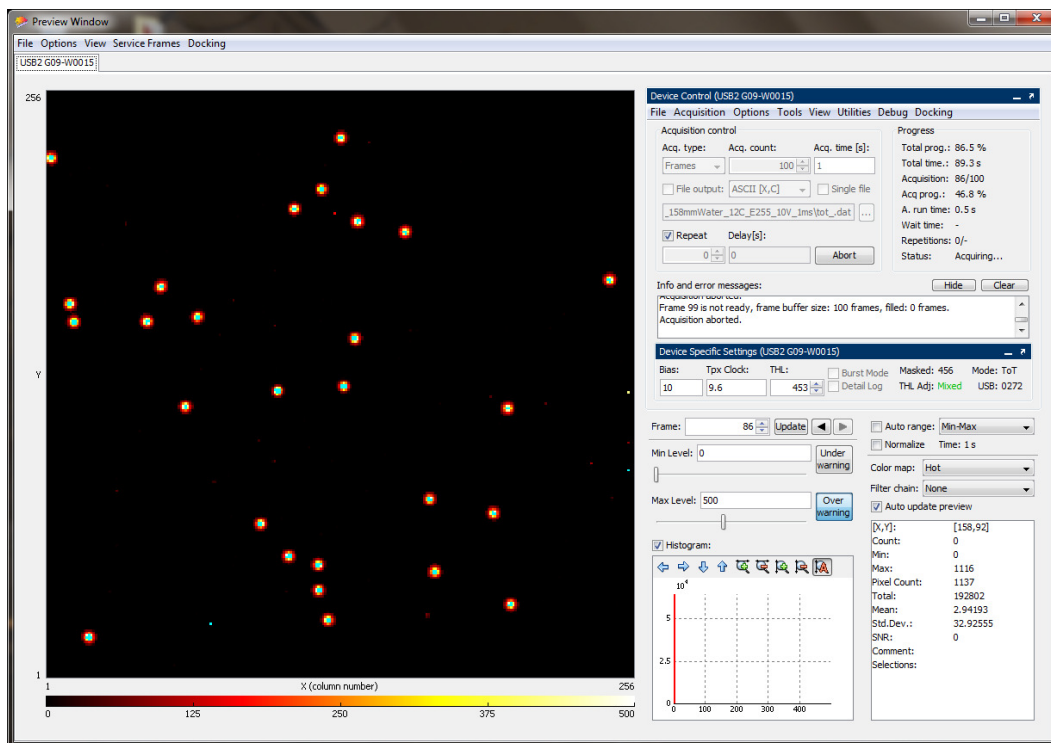


Figure 5.15: Screenshot of the Java graphical user interface of Pixelman during detection of α -particles emitted by a ^{241}Am -source. The detector is operated in time over threshold-mode. The panel on the top right allows to define the measurement parameters and monitor the measurement progress. The panel on the left shows the current measurement frame online. The parameters for this display can be adjusted with the panel on the bottom right.

5.4.2 Data Processing and Evaluation with Matlab

For the processing of the data, self-written routines implemented in the Matlab software (Mathworks, Nattick, MA, USA) were used. Subroutines written in C++ were integrated to speed up time consuming calculations. The signals created by individual ions were extracted from the data by considering all directly or diagonally adjacent pixels within a frame showing a non-zero signal as a cluster. From the pixel values within each cluster, the cluster properties like size, signal or height were derived as described in Section 5.2.5 .

For the further evaluation of the cluster properties one- and two-dimensional histograms showing the distributions of the clusters in different parameters were used.

5.4.3 libamtrack

libamtrack^a (Greulich et al. (2010)) is an open source library (under GNU General Public License 3) for amorphous track modeling. It is intended to facilitate the application and numerical comparison of different track structure models. libamtrack is written using ANSI C. Being designed as a shared library, it can be accessed from different software toolkits and programs. libamtrack provides computational routines for the prediction of detector response to proton and heavy charged particle beams as well as auxiliary physics routines.

In this work, libamtrack version 0.5.2. was used to compute the energy of an ion after traversing a slab of material and therefore to estimate the energy-loss in the respective material. The energy-loss is determined using the Bethe-equation for calculating the stopping power (see Section 2.1.1 for more details) and a continuous-slowng-down-approach, meaning that the material is divided into many thin slabs and the energy-loss in each slab is calculated individually.

^aHosted at <http://libamtrack.dkfz.org>.

6 Experiments

In this chapter, the experiments performed for the work presented in this thesis are described. The corresponding results are presented in Chapter 7, which features the same substructure. The experiments are divided into three main parts. In the first part, the detector response to therapeutic ion beams is characterized. The corresponding experiments are described in Section 6.1, while the results are presented in Section 7.1. The potential applicability of the detector for energy-loss measurements in therapeutic ion beams is investigated in the second part (Sections 6.2 and 7.2). The third part contains descriptions (Section 6.3) and results (Section 7.3) of the performed ion spectroscopy measurements.

6.1 Characterization of the Detector Response in Therapeutic Ion Beams

The Timepix detector was originally designed for X-ray imaging applications. The investigations presented in this work are the first detailed studies on the detector response to therapeutic ion beams. In the following paragraphs, an overview of the studies performed to investigate dependencies of the detector signal in therapeutic proton and carbon ion beams on the detector settings and the applied evaluation parameters is given. The standard detector settings and evaluation parameters derived in these studies are introduced. They are summarized in Table 6.1, while detailed information on their determination are presented in Section 7.1. Descriptions of the corresponding experiments can be found in Sections 6.1.1 to 6.1.6.

For the measurements, most detector parameters were set to the same values as were used in the detector calibration procedure in order to keep its applicability (see Section 5.2.4 for explanations of the procedure). Unless otherwise noted, this applies also to the frequency of the external reference clock ($f_{\text{standard}}=9.6$ MHz, see Table 6.1).

At first, influences of the acquisition time setting and the bias voltage applied to the sensitive detector layer were investigated, as described in Sections 6.1.1 and 6.1.2. Both values can be varied within certain limits without influencing the detector calibration. Based on the results presented in Sections 7.1.1 and 7.1.2, the **acquisition time and bias voltage values** presented in Table 6.1 were defined as the standard settings.

6 Experiments

Table 6.1: Summary of standardly used detector settings and evaluation parameters, as determined in the experiments presented in this section.

Parameter	Protons	Carbon Ions
Clock Frequency	9.6 MHz	
Acquisition Time (t_{acq})	1 ms	
Bias Voltage (V_{bias})	10 V	
Min. Cluster Size (A_{cluster})	4 pixels	30 pixels
Min. Cluster Roundness ($\text{roundness}_{\text{cluster}}$)	0.6625	0.7375
Height of Roundness Determination	5% of cluster height	10% of cluster height

Using them, the distributions of cluster sizes measured in carbon ion and proton beams covering the complete energy range available at HIT were studied with the methodology presented in Section 6.1.3. Not all clusters observed in an irradiation are due to the ion species under investigation. Sources of smaller clusters, e.g. induced by secondary radiation, were analyzed. To exclude them from the further analyses, **constraints on the minimum required cluster size** were determined for measurements in both, proton and carbon ion beams, as depicted in Table 6.1.

The dependencies of the cluster parameters on the angle between the incident particle and the detector surface were investigated as described in Section 6.1.4. The incident particle angle directly influences the path length of the ion in the sensitive detector volume and therefore also the cluster shape and the deposited energy. For most investigations presented in this work, only clusters due to ions traversing the detector perpendicularly were considered in the analysis. To exclude clusters due to ions traversing the detector at a significantly larger angle, **constraints on the minimally required cluster roundness** were determined separately for protons and carbon ions (see Table 6.1 and Sections 6.1.4 and 7.1.4).

The uniformity of the detector response in terms of cluster size, signal and height (see Section 5.2.5 for definitions) over the sensitive area was analyzed, as described in Section 6.1.5. Moreover, changes in the detector response were monitored over a time frame of 16 months. To do so, cluster size and signal distributions obtained in different measurement campaigns were analyzed and compared as described in Section 6.1.6.

All experiments were performed at the horizontal beam line at HIT, dedicated to quality assurance measurements. Unless otherwise noted, for all measurements described in this chapter the detector was placed in the isocenter, with its surface aligned perpendicularly to the beam axis. A schematic drawing of the set-up is shown in Figure 6.1. No additional material was placed in front of the detector. The incident beam

6.1 Characterization of the Detector Response in Therapeutic Ion Beams

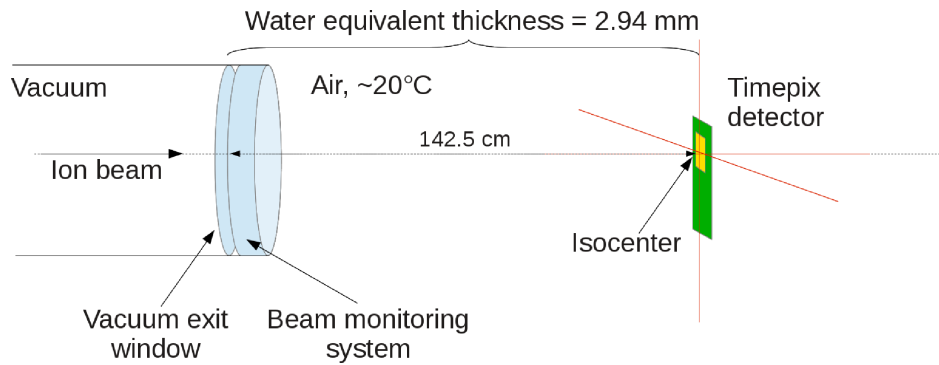


Figure 6.1: Schematic drawing of the standardly used measurement set-up. The detector is placed in the isocenter with its surface aligned perpendicularly to the beam axis. No material is placed in front of the detector.

therefore only experienced stopping and scattering in the vacuum exit window, the beam application monitoring system (see Section 5.1.1) and in the air between beam exit window and isocenter ($142.5 \text{ cm}^{\text{a}}$). In total, the material traversed by the particles has a water-equivalent thickness of 2.94 mm.

For both ion species and all investigated energies, unless otherwise noted, the largest available beam foci were chosen to reduce the probability of clusters containing the overlapping signal of two or more particles. Since this was often not sufficient, the beam intensities were set to values far below the minimum levels standardly used at HIT (10^6 s^{-1} for carbon ion beams and 10^8 s^{-1} for proton beams, see Section 5.1.1). To achieve the lower values, manual tuning of the accelerator was needed. The used beam intensities are out of the measurement range of the beam monitoring chambers. For this reason, no exact values can be given here. Moreover, for such low beam intensities no measurement of the ion fluence is possible.

6.1.1 Influence of the Acquisition Time on the Measured Signal

The detector acquisition time is an important parameter, especially for the determination of the cluster signal, which is a quantity related to the energy deposited in the sensitive detector layer by an ionizing particle. To measure the full signal, the acquisition time has to be long enough to cover the entire time span the amplifier output is above threshold. This applies for each pixel in the cluster. For particles with high energy transfer, longer acquisition times are needed to acquire the full signal as compared to measurements of radiation with a lower energy deposition in the sensitive detector layer. However, for a given beam intensity, longer acquisition times also lead to a higher probability of clusters containing overlapping signals of two or more ions.

^aPrivate communication with O. Jäkel and S. Brons, HIT.

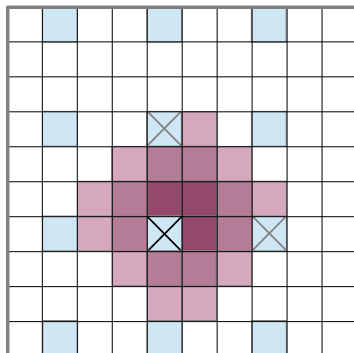


Figure 6.2: Schematic illustration of a cluster detected in mixed measurement mode. Pixels operated in Timepix mode are labeled as blue squares. The given cluster (purple squares) comprises three pixels operated in Timepix mode (marked with X). The value of the Timepix-pixel situated closest to the energy-weighted center of mass of the cluster (black X) is considered as the particle arrival time.

Investigations in Energy Mode In order to study the dependency of the detector signal on the acquisition time, the distributions of cluster size and cluster signal for acquisition times of 0.75, 1, 1.25, 2, and 5 ms, respectively, were analyzed. The investigated acquisition time range was chosen according to results of previous measurements. Carbon ion beams of 89 and 430 MeV/u and proton beams of 48 and 221 MeV were investigated. For both ion species, these energies represent the lowest and highest initial energies available at HIT. All detector pixels were operated in energy-mode (also called time over threshold- or TOT-mode). The detector bias voltage was set to the standard value of 10 V. Only clusters passing the standard constraints on minimally required cluster size and roundness were considered in the analysis (for further information see Sections 6.1, 6.1.3 and 6.1.4). High energetic protons result in the smallest ion-induced clusters. In their case, also clusters with a size of only three pixels were included in the cluster size analysis to demonstrate that their number is low. For the cluster signal analysis, the standard constraint on the minimally required cluster size of four pixels was applied. The obtained cluster size and cluster signal distributions are compared.

Investigations with Simultaneous Energy and Time Measurements A mixed measurement mode enables enhanced investigations by providing time- and energy-loss-related information for the clusters. In this mode, a fraction of pixels distributed regularly over the detector area is operated in Timepix mode. These pixels register the time the first signal is detected in the respective pixel. All remaining pixels are operated in energy-mode. In this way, a simultaneous acquisition of the cluster signal value and the time the respective ion is registered is possible. This operation mode therefore allows to study arrival time related effects of the measured cluster signal. In Figure 6.2 a schematic illustration of the described mixed measurement mode is shown.

6.1 Characterization of the Detector Response in Therapeutic Ion Beams

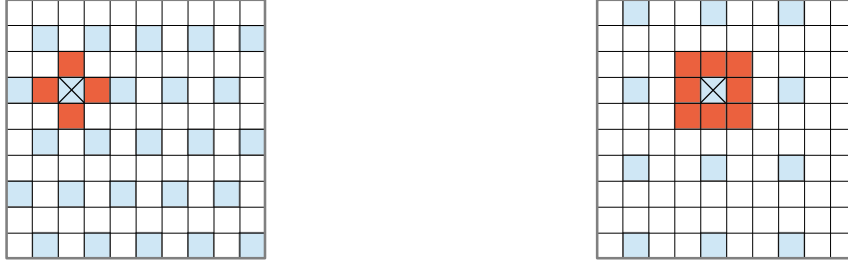


Figure 6.3: Schematic illustration of the distribution of pixels operated in Timepix mode (blue squares) and energy mode (white squares) over the detector area. The graph on the left shows the distribution for measurements in which one out of four pixels was operated in Timepix mode, while in the graph on the right one out of nine pixels is operated in Timepix mode. The red squares indicate the pixels used for derivation of the pseudo energy value of the pixel marked with a black cross.

Studies in the described mode were performed for a proton beam ($E_{\text{initial}}=48$ MeV) and carbon ion beams of $E_{\text{initial}}=89$, 271, and 430 MeV/u, covering the primary energy range available at HIT. For the measurement of carbon ions of $E_{\text{initial}}=89$ MeV/u one out of four pixels was operated in Timepix-mode, while for all other measurements one out of nine pixels was operated in Timepix-mode. The other pixels were operated in energy-mode. Figure 6.3 illustrates the distribution of pixels operated in Timepix- and energy-mode over the detector area. To determine the arrival time of an ion, the time-related information in the respective cluster is stored. Subsequently, a pseudo energy value is calculated for the pixels operated in Timepix mode by determining the mean signal value of the surrounding pixels operated in energy mode, as depicted in Figure 6.3. Subsequently, for each cluster the energy-weighted center of mass is determined. Each cluster is assigned the value of the Timepix-pixel situated the closest to its center of mass as arrival time.

Due to the limited counter depth of the detector (maximum value: 11810 counts) at a given clock frequency, the dynamic range for measurements in Timepix-mode is limited. For a clock frequency of 9.6 MHz, a signal overflow of the counter occurs for detector acquisition times longer than 1.23 ms. To perform studies in mixed operation mode at longer acquisition times, the clock frequency has to be reduced. For measurements at an acquisition time of 5 ms, a clock frequency of 1.92 MHz was chosen to avoid signal overflow, resulting however in a coarser time resolution. Since the standardly used detector calibration was obtained at a clock frequency of 9.6 MHz, the pixel values obtained in measurements with a clock frequency of 1.92 MHz have to be multiplied by a factor of five before converting them into energy values. The applicability of the described procedure to recalculate pixel values obtained at lower clock frequencies is analyzed by comparing the cluster signal distributions obtained in this manner with corresponding cluster signal distributions obtained in measurements with standard clock frequency and in which all pixels were operated in energy-mode.

Investigations for Different Threshold Values In the studies described before, irregularities in the detector response were observed. To further investigate them, the detector response was investigated for different internal pixel threshold values. The internal threshold was risen for all pixels in five steps by approximately 5, 7, 8, 9, and 13 keV, respectively. The effects on the cluster size, cluster signal and cluster height distributions are studied.

6.1.2 Influences of the Bias Voltage on the Measured Signal

The bias voltage applied to the sensitive detector layer determines the thickness of the depletion zone and the speed of charge collection (see descriptions in Section 5.2). In this thesis, effects of the bias voltage on the detector response to therapeutically used ion beams are analyzed. The investigated bias voltages cover the complete range available for Timepix (5 to 100 V). The acquisition time was set to the standard value of 1 ms. The parameters of clusters induced by carbon ion beams of 89 and 430 MeV/u and proton beams of 48 and 221 MeV, being the lowest and highest respective energies available at HIT, are studied in dependence of the applied bias voltage. The investigated parameters are the size, signal and height of the clusters. In addition, dependencies of the mean cluster sizes and cluster signals on the bias voltage are analyzed. Furthermore, profiles through the center of mass of the clusters were established for carbon ions of 89, 271 and 430 MeV/u and for protons of 48, 143 and 221 MeV. Changes in the profiles for different bias voltages are expected, since the bias voltage influences the speed of charge collection and consequently the diffusion of the charge carriers in the sensitive detector layer. For the study, the average values of 1000 clusters were used. The profiles obtained for different bias voltages are compared.

For the lowest beam energies (carbon ions of 89 MeV/u and protons of 48 MeV), only clusters passing the standard constraints on cluster size and cluster roundness (see Sections 6.1, 6.1.3 and 6.1.4 for details) were considered in the analysis. For carbon ions and protons of higher initial energies, the corresponding clusters are smaller due to the lower energy deposition. In combination with a high detector bias voltage the cluster size is further reduced. Therefore, applying the standard constraints on the minimum required cluster size would lead to a removal of clusters although they were induced by the ions under study. For this reason, for the evaluation of data obtained in carbon ion beams of 271 and 430 MeV/u the minimally required cluster size was reduced from 30 to 20 and 15 pixels, respectively, after dedicated studies. For protons of 143 and 221 MeV, no constraint on the minimally required cluster size was applied. Furthermore, also no constraint on the minimally required cluster roundness was used, as this parameter is of limited applicability for very small clusters (1 to 3 pixels).

6.1.3 Investigations of Small Clusters

In addition to the clusters due to primary protons and carbon ions, smaller clusters were observed in the experiments. Based on the observation that the number of such small clusters per measurement frame is correlated to the number of primary ions detected, two possible sources of these small clusters were investigated: secondary radiation from the beamline and detector noise. To further examine the possible sources, measurements with ^{12}C -ion beams performed with the standard measurement set-up depicted in Figure 6.1 were compared to

- a) measurements in which the detector was placed 3 cm aside of the beam axis, therefore registering no more primary particles, and
- b) measurements in which the ripple filter was brought into the beam path, expected to increase the number of secondary particles detected.

The relative numbers of small clusters observed in these measurements are analyzed.

Since the small clusters are not induced by the ions under study, they should be excluded in measurements intended to analyze characteristics of the ions themselves and the corresponding detector response. In order to do so, a constraint on the minimal cluster size has been introduced. To estimate suitable parameters, the cluster size distributions measured in carbon ion beams of 89 and 430 MeV/u and in proton beams of 48 and 221 MeV, corresponding to the lowest and highest initial energies available at HIT, were investigated using standard values for the detector acquisition time, bias voltage and the roundness constraint (see Table 6.1). No constraint on the minimally required cluster size was applied.

6.1.4 Angular Dependency of the Detector Signal

The dependency of the detector signal on the incident angle of the particles was studied with proton and carbon ion beams of intermediate energies available at HIT (carbon ions: $E_{\text{initial}}=271$ MeV/u, protons: $E_{\text{initial}}=143$ MeV). For these investigations, the standardly used measurement set-up shown in Figure 6.1 was taken as the reference position. The detector was then rotated around the horizontal axis going through the center of its sensitive area. Defining the rotation angle as the angle between beam direction and sensitive detector layer (see illustration in Figure 6.4), the following angles were studied:

- for carbon ions: $\alpha = 90, 85, 80, 70, 45,$ and 10 degrees,
- for protons: $\alpha = 90, 85, 80, 70, 60,$ and 45 degrees.

Exemplary measurement frames for the different incident particle angles are analyzed. Moreover, the cluster signal distributions obtained for the different angles are compared quantitatively. The maximum positions of these distributions are studied

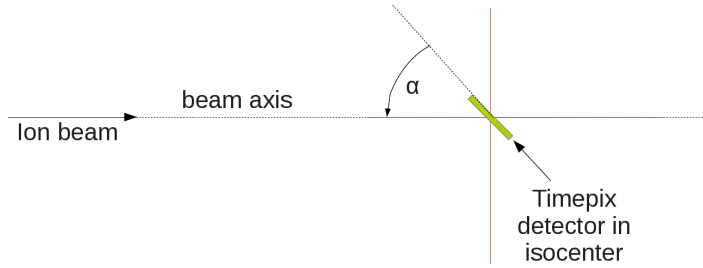


Figure 6.4: Schematic drawing of the measurement set-up used for studies of the angular dependency of the detector signal including an illustration of the definition of the angle between beam axis and detector (α). View from top. The detector was placed in the isocenter. The angle between detector surface and beam axis was varied. No material was placed in front of the detector.

in dependence of the rotation angle. For these analyses no constraint on the minimum required cluster roundness was applied, while standard values were used for the minimally required cluster size.

Dependence of the Cluster Roundness Parameter on the Incident Particle Angle

The measurements at different angles were further used to study the dependence of the cluster roundness parameter on the incident particle angle. The cluster roundness distributions obtained at different angles were compared quantitatively. Differences of the cluster roundness distributions for the roundness parameter being defined at different levels relative to the cluster height were studied in order to determine the level at which the best discrimination between small and large incident particle angles is possible. Based on this analysis, standard values for a constraint on the minimally required cluster roundness were defined. This constraint can be applied for measurements in which only particles traversing the detector perpendicularly shall be included in the evaluation. As a side effect, the cluster roundness constraint also enables to exclude clusters containing the signal of more than one ion, however only if the distance between the individual ion tracks is large enough to deform the cluster shape.

6.1.5 Uniformity of the Detector Response over the Sensitive Area

Possible variations of the detector response in terms of cluster size, cluster signal and cluster height (see Section 5.2.5 for definitions) over the sensitive area were studied. For the measurements, the standard set-up shown in Figure 6.1 was used. The detector was irradiated with carbon ion beams of 89, 271, and 430 MeV/u and proton beams of 48, 143, and 221 MeV, covering the respective energy ranges available at HIT. The detector acquisition time was set to the standard value of 1 ms, while the bias voltage was varied between the standard value of 10 V and a lower (5 V) and higher respective value (15 V). For the evaluation of the measured signal, standard constraints for the

minimally required cluster size and cluster roundness were used. In this kind of study, a high statistic is needed to reduce the statistical uncertainty of the mean cluster parameter in each position. For this reason, the detector pixels were binned in groups of four-by-four, thus decreasing the spatial resolution by a factor of four, in order to enhance the statistics per bin. All clusters with centroid positions in the area of a bin were assigned to this bin. The average size, signal and height of all clusters belonging to the respective bin were calculated. Using these values, 2-dimensional maps showing the distributions of average cluster size, cluster signal and cluster height over the sensitive detector layer were created. Dependencies of these maps on the initial ion energy and the applied detector bias voltage are studied.

6.1.6 Investigations of Detector Response Changes with Time

Possible changes of the detector response with time, e.g. due to effects of radiation damage, were investigated. The detector response to carbon ion beams of 89 and 430 MeV/u and proton beams of 48 and 221 MeV was studied repeatedly over a time frame of 16 months. The measurement set-up and beam parameters described in the previous section were used for all measurement campaigns. However, the energy response of the detector was recalibrated for the measurements performed after 10 and 16 months. To analyze the data obtained after 0, 4, 10, and 16 months, histograms of the integral cluster size and signal distributions are used. Furthermore, 2-dimensional maps showing the distributions of average cluster size, cluster signal and cluster height over the sensitive detector layer obtained as described in the previous section are compared.

6.2 Energy-Loss Measurements

The potential applicability of the Timepix detector for direct particle energy-loss measurements in therapeutic ion beams was investigated. Therefore, the correlation of the cluster signal values with the expected energy-loss of the particles in the detector was examined. The experiments and analytical methods employed for this study are described in this section, while the results are presented in Section 7.2.

6.2.1 Measurements of the Mean Energy-Loss Free-in-Air and in Vacuum

The detector response to several ion species (Z between 1 and 8) was studied either free in air or in vacuum. All of the studied ion species are of relevance in ion beam therapy, either as currently used or potential primary ions (protons, carbon ions, oxygen

ions) or as secondary fragments. Due to the differences in their track structures, the ion species exhibit different ionization densities resulting in variations in the particular recombination effects. To investigate and compare influences of these ion species related effects on particle energy-loss measurements, different ion species were included in the study.

Moreover, particles of high and low initial energies were used, since mixed spectra resulting from projectile and target fragmentation processes include both kinds of ions. In general, the investigated beams can be divided into two categories:

- Proton, carbon and oxygen ion beams with initial energies in therapeutically used ranges were employed. These particles have enough energy to traverse the sensitive layer of the detector and deposit only a fraction of their initial energy there. Such particles are in the following considered as **crossing particles**.
- Measurements in proton, deuterium, and lithium ion beams of energies below 5 MeV/u were performed. These ions stop in the sensitive detector layer and deposit all their remaining energy there. In the following they are considered as **stopping particles**.

For evaluation, the cluster signal distributions are analyzed and compared. In addition, the mean cluster signal values are compared to mean energy-loss values calculated with the software package libamtrack (see Section 5.4.3 for more information). In the calculations, the energy-loss of the ions in materials in front of the detector was considered. For this purpose, for measurements performed at HIT the material of the beamline (vacuum exit window and beam application monitoring system) was modeled as a slab of water with an equivalent radiologic thickness ($\text{WET}_{\text{beamline}}=1.47 \text{ mm}^{\text{a}}$). Furthermore, an air layer of 1.425 m in front of the detector was included in the calculation. For measurements at other accelerators, the materials in the beam path considered in the calculations are described in the respective paragraphs.

High Energy Protons (Crossing) Measurements in high energy proton beams were performed at HIT using the measurement set-up depicted in Figure 6.1. Proton beams with energies of 48, 55, 70, 94, 143, and 221 MeV, covering the complete range of primary proton energies available at HIT, were investigated. The standard detector bias voltage of 10 V was used. In addition, for protons of 48, 143, and 221 MeV also measurements at a bias voltage of 22 V were examined. For this bias voltage the sensitive detection layer is fully depleted and the cluster signal in proton measurements was found to be increased to a stable level (see Section 7.1.2). For the other detector settings and evaluation procedures the standard parameters were applied (see Section 6.1).

^aPersonal communication with O. Jäkel and S. Brons, HIT.

Low Energy Protons and Deuterium (Stopping) Measurements in low energy proton ($E=0.55$ and 1 MeV/u) and deuterium beams ($E=1$ MeV/u) were performed at the van-de-Graaff accelerator of the Institute of Experimental and Applied Physics of the Czech Technical University in Prague (see Section 5.1.2 for further information on the accelerator). The experiment was performed in a vacuum chamber to avoid energy-loss of the ions in materials in front of the detector (e.g. in air or a vacuum exit window). Narrow ion beams (width: 3 mm) were used for the irradiations.

Since the primary particle fluence is in the order of 10^{12} s^{-1} and therefore very high, for measurements with the detector placed directly in the beam it is not possible to separate the individual clusters. To avoid this situation, the beam was directed onto a thin gold foil and the backscattered ions were registered, as depicted in the schematic drawing of the measurement set-up shown in Figure 6.5. The energy of the backscattered ions can be calculated with the Rutherford backscattering formula (Oura et al. (2003))

$$E_1 = a \cdot E_0, \quad (6.1)$$

with

$$a = \left(\frac{m_1 \cdot \cos \Theta_1 + \sqrt{m_2^2 - m_1^2 (\sin \Theta_1)^2}}{m_1 + m_2} \right)^2, \quad (6.2)$$

where m_1 is the mass of the projectile, m_2 is the mass of the target nucleus and Θ is the scattering angle of the projectile. Equation 6.2 is valid for $m_1 < m_2$ (Oura et al. (2003)).

For the measurement, the detector was placed at an angle of 19.7° from the beam axis. With $m_{\text{proton}}=1.0073$ u, $m_{\text{deuterium}}=2.0141$ u and $m_{\text{gold}}=196.97$ u this results in a factor $a=0.9997$ for protons and $a=0.9994$ for deuterium. As in both cases the difference in energy between the original and the backscattered ions is smaller than

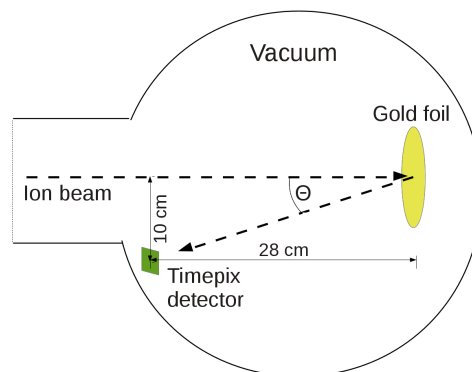


Figure 6.5: Schematic drawing of the measurement set-up used at the van-de-Graaff accelerator for measurements in low energy proton and deuterium beams. The incident ions are directed to a gold foil. The detector is placed at an angle $\Theta=19.7^\circ$ from the beam axis and registers the backscattered ions.

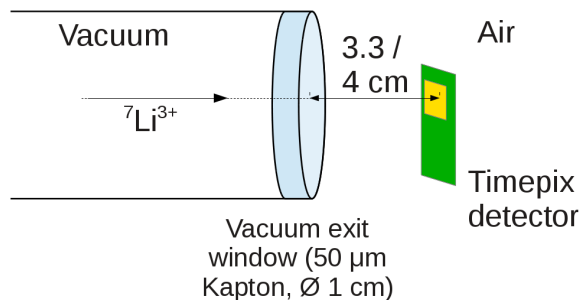


Figure 6.6: Schematic drawing of the measurement set-up used at the Tandem van-de-Graaff accelerator for measurements in lithium ion beams. The incident ions leave the vacuum through a 50 μm thick kapton foil. The detector is placed at a distance of 3.3 cm (in case of $E_{\text{initial}}=5.65 \text{ MeV/u}$) or 4 cm (in case of $E_{\text{initial}}=4.51 \text{ MeV/u}$), respectively, from the kapton foil with its surface being aligned perpendicularly to the beam axis.

0.1%, the energies of the backscattered ions were considered to be equivalent to the initial projectile energies.

Due to their low energies, the protons and deuterium ions stop in the sensitive detector layer. Therefore, the deposited energy is equivalent to the rest energy of the ions when entering the detector. The measured cluster signal values were compared to these expected values. Measurements were performed at detector bias voltages of 10 and 22 V for the reasons described above, while all other detector settings and evaluation parameters were set to standard values.

Low Energy Lithium Ions (Stopping) To analyze the detector response to low energy lithium ions, measurements were performed at the Tandem van-de-Graaff accelerator of the Maier-Leibnitz-Laboratory (MLL) in Garching near Munich. Initial particle energies of 4.51 and 5.65 MeV/u were used. The measurement set-up is depicted in Figure 6.6. The distance between the vacuum exit window and the detector amounted to 4 cm for the lower investigated lithium energy and to 3.3 cm for the higher particle energy, respectively. The standard detector settings and evaluation parameters determined in ${}^{12}\text{C}$ -ion beams were employed.

As the lithium ions stop in the sensitive detector layer, the deposited energy is equivalent to the rest energy of the ions when entering the detector. To determine the theoretical value of the rest energy, the energy-loss of the ions in the kapton foil used as vacuum exit window was calculated employing the tables of ICRU73 (2005). The subsequent energy-loss in air was calculated using libamtrack.

High Energy Carbon Ions (Crossing) The measurements in high energy carbon ion beams were performed at HIT using the standard measurement set-up depicted in Figure 6.1. Ion beams with initial energies of 89, 102, 130, 175, 271, and 430 MeV/u

were investigated, covering the complete primary energy range available at HIT. For all detector settings and for the evaluation the standard parameters were applied. Furthermore, for carbon ion beams of 89, 271, and 430 MeV/u, the cluster signal distributions obtained at bias voltages of 10 and 22 V were analyzed and compared (see explanations on the choice of bias voltage above).

High Energy Oxygen Ions (Crossing) Measurements in high energy oxygen ions were performed at HIT employing the standard measurement set-up. Oxygen ions of 127, 321, and 421 MeV/u were investigated. They cover the primary oxygen energy range currently available at HIT. Standard values determined for ^{12}C -ions were used for the detector settings and evaluation parameters.

6.2.2 Energy-Loss Straggling - Comparison of Measurements and Calculations

While in the evaluations of the experiments described above (Section 6.2.1), the mean cluster signal values are compared to the calculated or theoretical mean energy-loss, in Section 7.2.2, the shapes of the obtained cluster signal distributions are compared to calculated energy-loss distributions. Only measurements for ions crossing the detector were considered in the analysis, since for ions stopping in the detector no energy-loss straggling exists. To calculate the distributions, the CERN ROOT software package *TMath::Vavilov* (Rotondi and Montagna (1990)) was used. The input parameters for the routine are the parameters k and β . As explained in detail in Section 2.1.2, k describes the ratio between the mean energy-loss value $\overline{\Delta E}$ for a particle in an absorber and the maximum possible energy transfer in a single collision W_{max} . The factor k was calculated according to Equation 2.3 using Equations 2.4 and 2.5 for the calculation of $\overline{\Delta E}$ and W_{max} , respectively. The parameter β relates to the velocity and therefore the energy of the incident particles (see Section 2.1.2 for more information). To determine the energy of the ions when entering the detector, the energy-loss in the beam path was calculated using libamtrack and the parameters described in Section 6.2.1. Using the residual particle energy obtained in this manner, β was calculated as (Leroy and Rancoita (2011))

$$\beta = \sqrt{1 - \frac{1}{\gamma^2}}, \quad (6.3)$$

with

$$\gamma = \left(\frac{E_k}{mc^2} \right) + 1, \quad (6.4)$$

where E_k is the kinetic energy and m is the mass of the incident ion. The output of the *TMath::Vavilov*-routine is a frequency distribution over the parameter λ . Using λ in Equations 2.12 and 2.13 the frequency distribution of the energy-loss values was

calculated. Values for the mean excitation potential of the target material were taken from Leo (1994), p. 26.

While the mean energy-loss of the ions in the beam path (beam line and air in front of the detector) was calculated using libamtrack and considered in the calculation for the energy-loss straggling, influences of preceding energy-loss straggling in these materials was not included in the calculation. It has to be kept in mind, that this procedure neglects possible sources for energy-loss straggling in the detector and might thus result in an underestimation of the width of the calculated distribution.

High Energy Protons The cluster signal distributions measured in proton beams of $E_{\text{initial}}=48, 55, 70, 94, 143,$ and 221 MeV are compared to the corresponding calculated energy-loss distributions. The full-width-half-maximum (FWHM) values of the measured and calculated distributions are evaluated quantitatively.

High Energy Carbon Ions For carbon ions, the cluster signal distributions measured for $E_{\text{initial}}=89, 102, 130, 175, 271,$ and 430 MeV/u are compared to the corresponding calculated energy-loss distributions. Like for protons, additionally the full-width-half-maximum (FWHM) values of the measured and calculated distributions are compared.

High Energy Oxygen Ions For oxygen ions, cluster signal distributions measured for particle energies of $127, 321,$ and 421 MeV/u are analyzed in the same way as described for carbon ions.

6.2.3 Measurements in Different Material Depths

The detector response to carbon ions slowed down in PMMA blocks of different thicknesses was evaluated. The measurement set-up used for the experiment is shown in Figure 6.7. The detector was aligned with the isocenter and kept in a fixed position throughout the experiment. The PMMA phantom was placed in front of the detector in a distance of 12 mm. To change the thickness of the phantom, additional PMMA was added in front of the phantom.

Carbon ions with an initial energy of 271 MeV/u (corresponding to a medium energy available at HIT) were used. They were slowed down by a phantom made of PMMA blocks of $5, 10, 11, 12,$ and 12.7 cm thickness in beam direction, resulting in measurements in the plateau and the Bragg peak area. Measurements without phantom in front of the detector were performed for reference. In Section 7.2.3, the measured cluster signal distributions are analyzed. In addition, the measured mean cluster signal is compared to the calculated mean energy-loss. For the calculation libamtrack was used. The deceleration of the ions in the phantom and in the material in the beam path upstream the phantom was considered. For the vacuum exit window and the beam

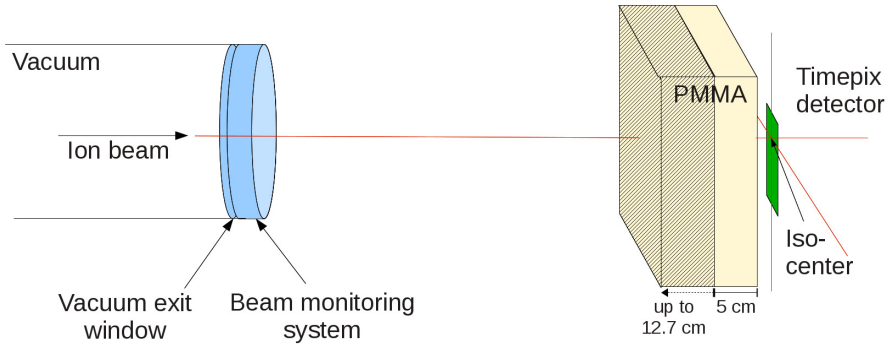


Figure 6.7: Schematic drawing of the set-up used for measurements in different material depths. The detector is placed in the isocenter with its surface aligned perpendicularly to the beam axis. PMMA phantoms of different thickness are placed in front of the detector at a fixed distance of 12 mm.

application monitoring system a water-equivalent thickness of 1.47 mm was assumed (see above). In addition, an up to 1.425 m thick air layer in front of the detector was considered. For simplification, no effects of straggling or scattering were considered in the calculations. For the thickest phantom no more primary particles are expected to be detected. However, many lighter particles resulting from fragmentation of the carbon ions in the phantom are expected to reach the detector due to their longer range in tissue.

6.3 Ion Spectroscopy

In order to study the possibility of ion spectroscopy measurements with the Timepix detector, several experiments were performed, as described in Sections 6.3.1 to 6.3.4. Before, in the following paragraphs, details on the applied detector settings and evaluation parameters are given.

Based on the results of the experiments dedicated to study the Timepix detector properties in ion beams and described in the previous sections, the operation parameters of the detector for the ion spectroscopy experiments were chosen as following:

- The detector acquisition time was set to 1 ms.
- A comparison of ion spectroscopy measurements performed at $V_{\text{bias}}=10$ and 22 V (see Appendix E) revealed a bias voltage of 10 V to be better suited for the given purpose. Therefore, this bias voltage was used for the measurements.
- The minimum size of clusters to be included in the analysis was set to the value which was found beneficial for protons, being the ion species expected to create the smallest ion induced clusters in mixed ion fields. ($A_{\text{cluster}} \geq 4$ pixels, see Section 7.1.3 for details).

- Applying a constraint on the minimum cluster roundness is important in ion spectroscopy measurements, e.g. to exclude the signal of ions traversing the detector at large angles and therefore resulting in a larger cluster size and cluster signal than expected for the given ion species. Although, in general, also these clusters provide interesting information, the identification approach used in this work cannot yet reasonably treat them.

For mixed ion fields, the roundness constraint must be chosen carefully. On the one hand small clusters, which for geometrical reasons tend to have smaller roundness values, induced by e.g. high energy protons should not be excluded from the comparison. This could however be the case when the constraint found beneficial for carbon ion measurements is used universally. On the other hand, for the reasons described above, large clusters due to e.g. heavy ions traversing the detector not perpendicularly should not be included in the analysis, as might happen when using the constraint found beneficial for proton measurements as a general constraint.

To account for this situation, a cluster size dependent roundness constraint was used. A linear interpolation between the values found beneficial for protons and carbon ions was used for the evaluation of ion spectroscopy measurements. The interpolation was applied for clusters with sizes between 6 pixels, being the most probable cluster size for the proton irradiation studied for determination of the respective roundness constraint, and 120 pixels, being the most probable cluster size for the carbon ion irradiation studied for determination of the roundness constraint. In this range, both, the roundness value itself, as well as the relative height of roundness determination were interpolated linearly, as depicted in Figure 6.8. For clusters which are 4 or 5 pixels large the standard proton constraint was applied, while for clusters larger than 120 pixels, the standard carbon ion constraint was used.

Approach to Ion Spectroscopy in this Work The approach to ion spectroscopy presented in this work is based on the investigation of the parameters cluster size and cluster signal. For the evaluation, 2-dimensional histograms showing the distributions of these two parameters are used. An example for a histogram obtained from a measurement in a mixed irradiation field resulting from fragmentation of carbon ions in a PMMA phantom is shown in Figure 6.9. Several areas showing concentrations of clusters are visible. To correlate these areas to the different ion species between ^1H and ^{12}C , the development of the distribution for measurements in changing material depths was studied as described in Section 6.3.1. The identification was verified by comparing measurements of the carbon ion fragmentation in a water phantom to an analogous study based on an established method for ion spectroscopy. The measurement set-up

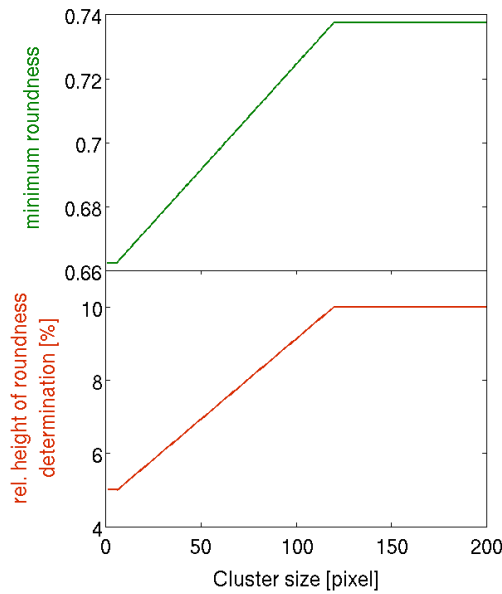


Figure 6.8: Illustration of the cluster size dependent roundness constraints applied for ion spectroscopy measurements. The values for the relative height of the roundness determination and the minimum roundness are depicted in dependence of the cluster size.

and parameters used for this experiment are presented in Section 6.3.2. Finally, the developed ion spectroscopy method was applied in two measurements: a study of lateral fragment distributions behind a PMMA phantom (see Section 6.3.3) and a study of fragmentation in different materials (see Section 6.3.4). For both studies, the detector was placed directly behind the phantoms, therefore enabling to gain information on ion spectra close to the interaction location, what was not possible with the previous electronic methods for ion spectroscopy measurements (see Section 3 for further details on previous methods).

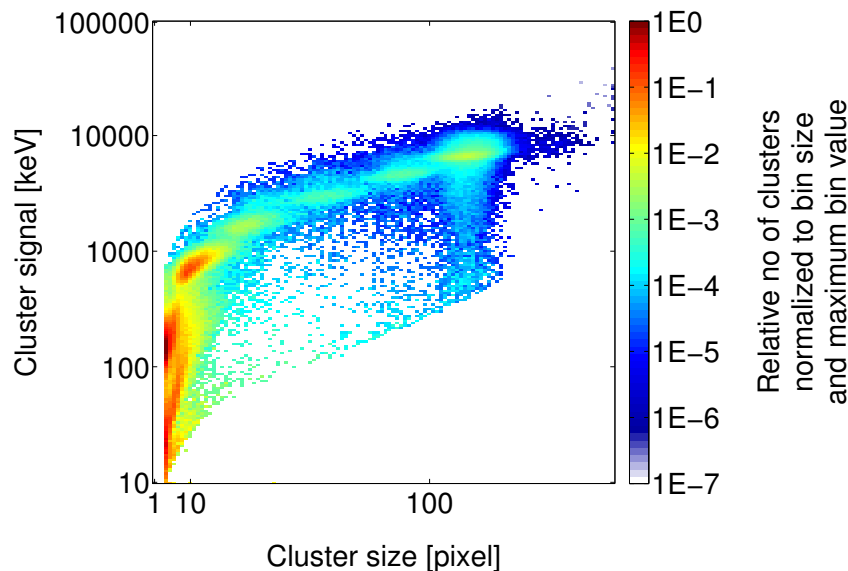


Figure 6.9: 2-dimensional histogram showing the distributions of cluster signal and cluster size for a mixed radiation field resulting from fragmentation of carbon ions ($E_{\text{initial}}=271$ MeV/u) in a 145 mm thick PMMA phantom. Several areas showing concentrations of clusters are visible.

6.3.1 Identification of Ion Species by Measurements in Different Material Depths

In the 2-dimensional histograms of cluster size and cluster signals (see example in Figure 6.9) derived from measurements in mixed radiation fields several areas showing concentrations of clusters can be seen. In order to assign them to the different particle species a comparison between measurements in different PMMA depths was performed using a fixed primary carbon ion energy and exploiting that for a given velocity lighter ions have longer ranges in tissue (the range scales with A/Z^2 , see Section 4.1 for further explanations).

The experimental set-up used for the measurements is depicted in Figure 6.10. The detector was placed perpendicular to the beam in the isocenter. A PMMA phantom was placed in front of the detector. The distance between phantom and detector amounted to 15.1 cm. A carbon ion pencil beam ($E_{\text{initial}}=271 \text{ MeV/u}$) was directed onto the phantom. At this beam energy the particle range in PMMA is approximately 12.4 cm. To study fragmentation products in the Bragg peak area and far behind the peak, the thickness of the PMMA phantom was varied between 11.8 and 44.8 cm. To be able to detect single particles and to avoid overlaps of their signal in the detector, the beam intensity was adjusted, depending on the thickness of material in front of the detector.

For evaluation of the measurements, the detector signal was studied in dependence of the PMMA depth. In addition, the measurements described in Section 6.2.3, originally intended for energy-loss studies, were included in the ion spectroscopy study. In particular, three measurement positions in front of the Bragg peak (PMMA depths of 0, 5, and 10 cm) were investigated.

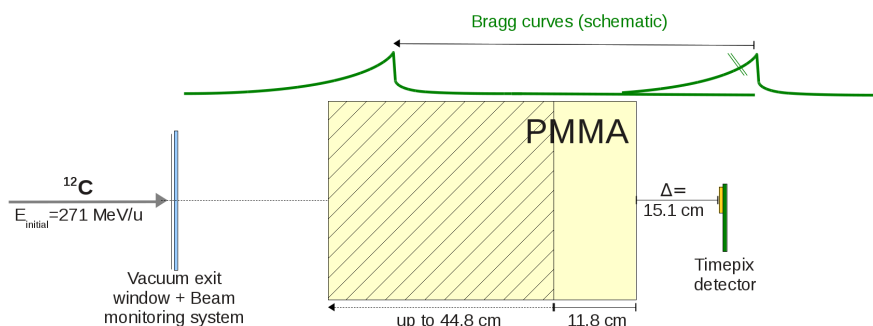


Figure 6.10: Schematic illustration of the measurement set-up used for identification of the ion species, view from top, not to scale. The curves on top illustrate schematically the position of the Bragg peak for the thinnest PMMA phantom used (11.8 cm) and the largest PMMA thickness (44.8 cm).

6.3.2 Verification of the Identification

In order to enable a direct verification of the identification of ion species derived from the experiment described in the previous section, the fragmentation of carbon ion in water was studied in analogy to a measurement presented in literature (Haettner (2006)). The target and beam parameters were chosen as close as possible to the parameters described in Haettner (2006). In Table 6.2 the measurement parameters are compared to the parameters of the reference measurement. The measurement set-up is depicted in Figure 6.11. The 15.8 cm thick phantom was placed close to the beam application monitoring system (BAMS) at the end of the HIT beam tube. In this way, the lateral scattering of primary ions in front of the detector was reduced. The distance between the BAMS and the center of the water tank was 25 cm. The detector was placed in a large distance behind the phantom ($\Delta=250$ cm). To study the fragmentation spectra at different angles, the lateral detector position was varied between 0 and 30.4 cm, corresponding to angles between 0° and 7° . For irradiation, carbon ion beams of $E_{\text{initial}}=400$ MeV/u with a nominal width (FWHM) of 3.5 mm were used. The beam intensity was adjusted, depending on the lateral detector position, to be able to detect single particles and to avoid overlaps of their signal in the detector.

For evaluation, the 2-dimensional histograms showing the distribution of cluster size and cluster signal are analyzed. The relative numbers of hydrogen, helium, lithium, beryllium and boron fragments detected at angles of 2° , 4° , and 6° from the beam axis are compared to according data presented in Haettner (2006).

6.3.3 Application I: Lateral Fragment Distributions

Among the most important applications of the ion spectroscopy approach investigated in this work is the study of lateral distributions of secondary fragments in or behind targets. To reduce the influence of scattering of the ions behind the target, in the example presented in this work, the detector was placed at a short distance (5 cm)

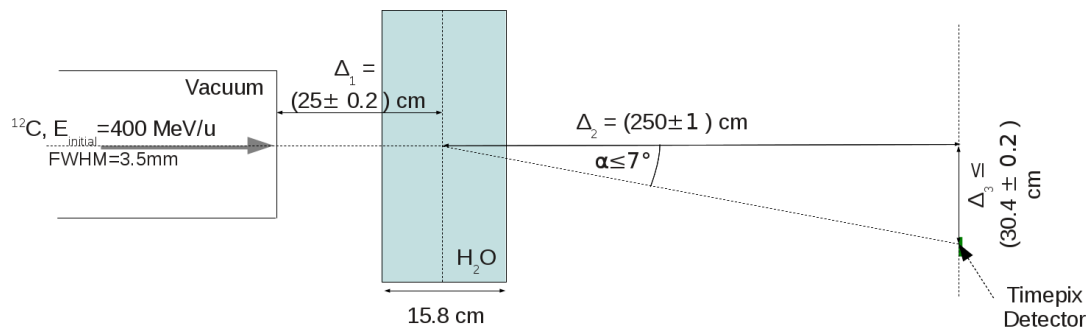


Figure 6.11: Schematic illustration of the measurement set-up used for the study of lateral fragment distributions behind water. (View from top, not to scale.) The parameters were chosen in analogy to a measurement presented in Haettner (2006).

6 Experiments

Table 6.2: Comparison of experimental settings and parameters used for the measurements described in Section 6.3.2 and the reference measurement presented in Haettner (2006)

Parameter	This Work	Reference
Ion Species	^{12}C	^{12}C
Energy	400 MeV/u	400 MeV/u
Beam Width (FWHM)	3.5 mm	approx. 4 - 5 mm
Phantom Material	H_2O	H_2O
Phantom Width	15.8 cm	15.9 cm
Phantom Walls	2 mm plastic	2 mm PMMA
Distance BAMS to Phantom Center	(25 ± 0.2) cm	n.a.
Distance Phantom Center to Detector	(250 ± 1) cm	287 - 294 cm

behind a PMMA phantom. Thus, the fragment distribution could be studied close to the interaction points.

The experimental set-up used for the measurement is shown in Figure 6.12. The detector was placed in the isocenter, perpendicular to the beam axis. A 12.7 cm thick PMMA phantom was placed in a distance of 5 cm in front of the detector. The irradiation was performed with a thin carbon ion pencil beam with a nominal width (FWHM) of 4.3 mm. The beam energy of 271 MeV/u was chosen such that the Bragg peak was located about 3 mm in front of the distal end of the PMMA phantom. Therefore, only secondary radiation was leaving the phantom. To cover a wide lateral area, the detector was shifted sideways in three steps of 1.2 ± 0.1 cm each (see Figure 6.12). The overall area covered by the sensor amounted to $1.4 \times 5 \text{ cm}^2$.

For the evaluation of the data, the overall area covered by the detector was divided into 16 equally spaced cylindrical bins centered on the beam axis. For each bin, a 2-dimensional histogram showing the distribution of the clusters in terms of size and signal was generated. Clusters induced by different ion species were identified according to their energy deposition and cluster size exploiting the results achieved from the experiments described in Section 6.3.1. For each bin, the number of ions detected was normalized to the fractional area of the full circular bin covered by the detector. Moreover, the results were corrected for the difference in primary carbon ions used in the irradiations for the four detector positions. Since for the very low beam intensities required in measurements with the Timepix detector (see explanations in Section 6.1) no direct measurement of the ion fluence is possible, for the correction the number of ions detected in the areas covered by two overlapping detector positions were used for adjustment. In this way, lateral distributions of the ion species can be studied.

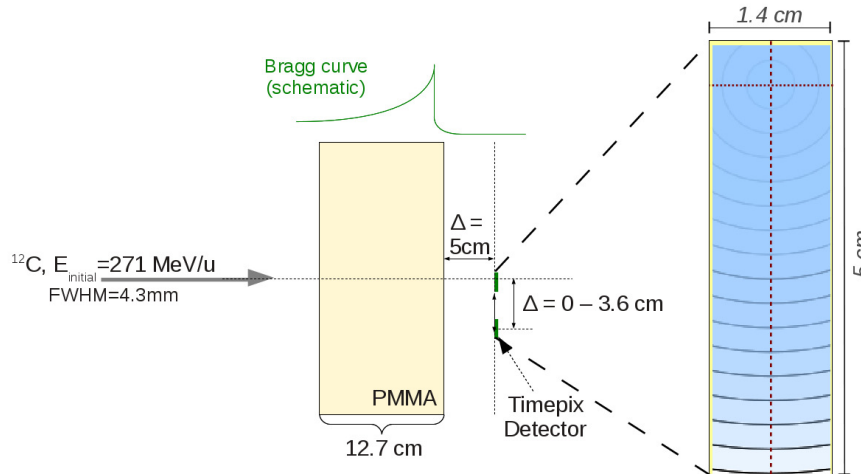


Figure 6.12: Schematic illustration of the measurement set-up used for the study of lateral fragment distributions behind a PMMA phantom. (View from top, not to scale.) The green curve schematically illustrates the Bragg peak position close to the proximal end of the phantom. For evaluation, the overall area covered by the detector was divided into 16 cylindrical bins, equally spaced around the beam axis, as depicted on the right. The red cross illustrates the isocenter location.

6.3.4 Application II: Fragmentation in Different Materials

Another interesting question to be answered by a new generation of ion spectroscopy techniques is the study of ion spectra resulting from fragmentation in different materials. Currently, the data used in ion beam therapy treatment planning systems is based on measurements of fragmentation in water. Ideally, this data would be complemented by fragmentation data for human tissues and implant materials. In this work, the fragmentation of carbon ions in PMMA (being similar to water but easier to handle) and steel (used in implants) phantoms is investigated. Both phantoms have the same water-equivalent thickness of 169 mm. The experimental set-up used for the measurements is shown in Figure 6.10. For all measurements, the Timepix detector was placed in the isocenter perpendicular to the beam axis. In the first set-up (I), a PMMA phantom of 145 mm thickness in beam direction was placed in front of the detector. The distance between phantom and detector amounted to 5.5 cm. The phantom was irradiated by carbon ions of the highest energy available at HIT ($E_{\text{initial}}=430 \text{ MeV/u}$). The PMMA thickness and the ion energy were chosen such that the detector position is well in front of the Bragg peak. For the second set-up (II), the PMMA phantom was replaced by a 30.1 mm thick steel phantom, which has an equivalent radiologic thickness. The same beam parameters as used for set-up (I) were chosen. In this way, in both measurements the detector was placed in the same position relative to the Bragg peak, as depicted in Figure 6.10. The relative fractions of ion species measured behind the different materials are compared. To verify the water-equivalent thickness

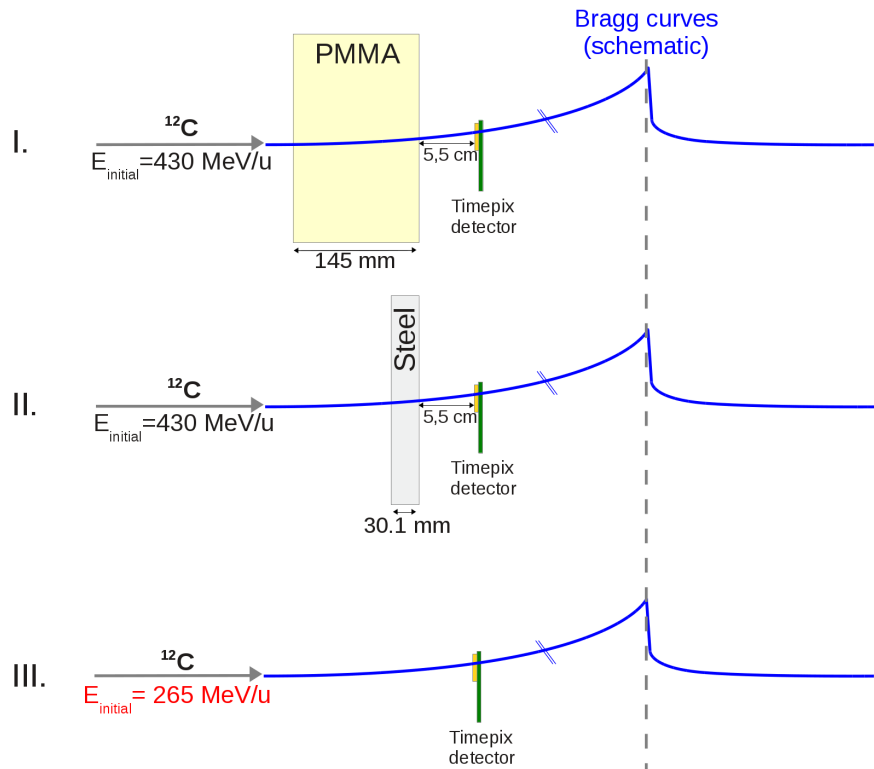


Figure 6.13: Schematic illustration of the measurement set-up used for the study of fragmentation in different materials, view from top, not to scale. The blue curves schematically illustrate the Bragg peak position.

of the phantoms, in a third irradiation (III), no phantom was placed in front of the detector. Carbon ions of reduced energy ($E_{\text{initial}}=265 \text{ MeV/u}$) were used. This energy is supposed to be equivalent to the residual energy of the carbon ions behind the phantoms in measurements (I) and (II). In this way, again an equivalent detector position relative to the Bragg peak as in the two previous set-ups should be achieved. The cluster parameter distributions measured in the three different set-ups are compared.

7 Results

In this chapter, the results obtained in the experiments described in Chapter 6 are presented. Both chapters feature the same substructure in order to facilitate reading.

7.1 Characterization of the Detector Response in Therapeutic Ion Beams

In the work presented in this thesis, the response of the Timepix detector to therapeutic ion beams is studied in detail for the first time. While the response to low energetic ion beams stopping in the sensitive detector layer has been investigated before, for particles crossing the complete sensor layer many detector properties are so far unknown. For this reason, the dependency of the measurement results on various detector settings and evaluation parameters is studied, following the methodologies described in Section 6.1. A further aim of the investigations is to find suitable parameters for the energy-loss and ion spectroscopy measurements presented in Sections 7.2 and 7.3. For this reason, the results presented in this section are of direct relevance for the further experiments. Therefore, short discussions of the findings are included throughout the section.

7.1.1 Influence of the Acquisition Time on the Measured Signal

Investigations in Energy Mode As described in Section 6.1.1, proton and carbon ion beams with the lowest and the highest energies available at HIT were used to investigate the dependency of the detector response on the acquisition time, i.e. the duration of one measurement frame. Figure 7.1 shows the cluster size and cluster signal distributions measured in a proton beam of $E_{\text{initial}}=48$ MeV, obtained with the standard measurement and evaluation parameters depicted in Table 6.1. For all acquisition times, the cluster sizes observed most frequently are 10 and 11 pixels. In the cluster size distributions, only minor differences for acquisition times of 0.75, 1, 1.25, and 2 ms can be seen. In comparison to them, for $t_{\text{acq}}=5$ ms, the cluster size distribution is shifted towards lower values. The cluster signal distributions show a distinct peak around the most frequent cluster signal of approximately 760 keV. The relative number of clusters in the peak increases with increasing acquisition time. At the same time, the relative number of clusters showing a signal below 600 keV decreases. Most of these clusters are due to

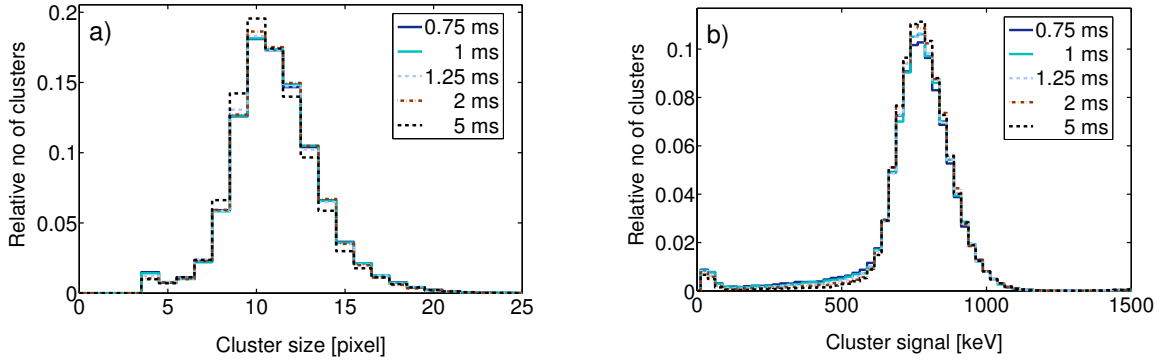
${}^1\text{H}$, $E_{\text{initial}}=48$ MeV

Figure 7.1: Cluster size (a) and cluster signal (b) distribution for different detector acquisition times. The distributions are normalized to their areas. For all distributions, the statistical uncertainty in the highest bin is less than 1.5%. Further settings: $V_{\text{bias}}=10$ V, $A_{\text{cluster}} \geq 4$ pixel, $\text{roundness}_{\text{cluster}} > 0.6625$ at 5% of cluster height.

particles arriving towards the end of the frame duration. In this case, the remaining measurement time is shorter than the time the preamplifier signal is above threshold. Therefore, not the complete signal can be digitized, resulting in a lower cluster signal value. The relative number of affected clusters decreases with increasing acquisition time. Moreover, a high number of clusters with signals below 100 keV was observed. These clusters are due to secondary radiation, as shown in Section 7.1.3.

The cluster size and cluster signal distributions for protons of an initial energy of 220 MeV are displayed in Figure 7.2. For these high energy protons, the clusters are smaller than for the lower proton energy studied before. The cluster size obtained most

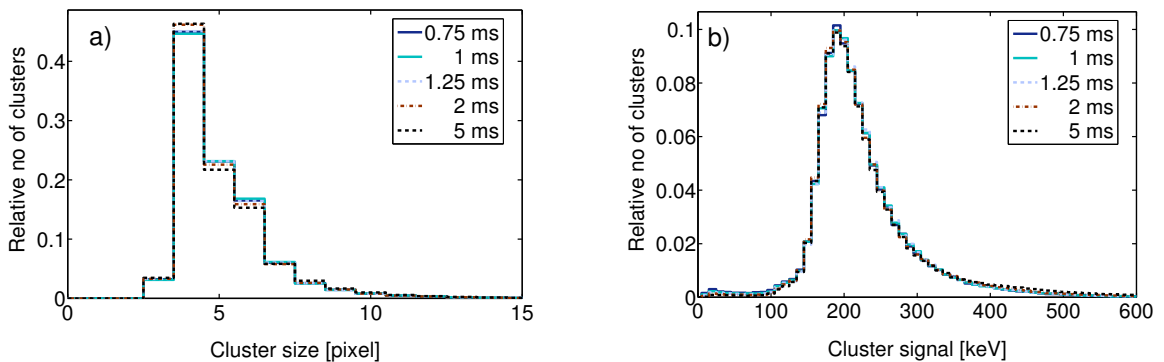
 ${}^1\text{H}$, $E_{\text{initial}}=220$ MeV

Figure 7.2: Cluster size (a) and cluster signal (b) distribution for different detector acquisition times. The distributions are normalized to their areas. For all distributions, the statistical uncertainty in the highest bin is less than 1%. Further settings: $V_{\text{bias}}=10$ V, $A_{\text{cluster}} \geq 4$ pixel, $\text{roundness}_{\text{cluster}} > 0.6625$ at 5% of cluster height. In the cluster size distribution also clusters with a size of 3 pixels are shown to demonstrate that their number is low.

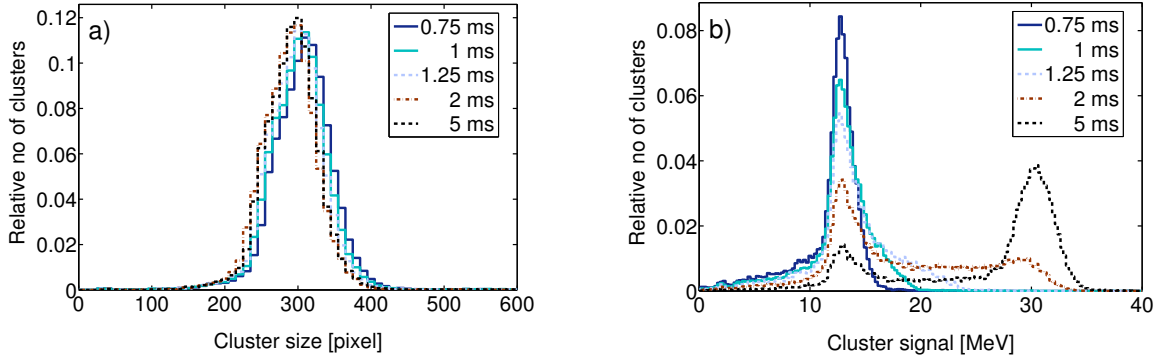
^{12}C , $E_{\text{initial}}=89 \text{ MeV/u}$ 

Figure 7.3: Cluster size (a) and cluster signal (b) distribution for different detector acquisition times. The distributions are normalized to their areas. For all distributions, the statistical uncertainty in the highest bin is less than 3.5%. Settings: $V_{\text{bias}}=10 \text{ V}$, $A_{\text{cluster}} \geq 30 \text{ pixel}$, $\text{roundness}_{\text{cluster}} > 0.7375$ at 10% of cluster height.

frequently is four pixels. Only minor differences in the cluster size distributions were observed for all studied acquisition times.

Also in the cluster signal distribution only minor differences were obtained. For all acquisition times the bin showing the most frequent cluster signal is centered at 190 keV.

The situation found in carbon ion beams is largely different. For $E_{\text{initial}}=89 \text{ MeV/u}$ distinct differences in the cluster size distributions can be seen (see Figure 7.3). For increasing acquisition times, the cluster size distributions are shifted towards lower values. The reason for this finding could not be clarified.

Also the cluster signal distributions show distinct differences for different acquisition times. At $t_{\text{acq}}=0.75 \text{ ms}$ one peak centered at approximately 13 MeV can be seen. For higher acquisition times, this peak is still visible, while more and more clusters with an essentially higher signal appear. For $t_{\text{acq}}=5 \text{ ms}$, a second peak is found at signal values of around 30 MeV, while the relative number of clusters in the first peak is significantly decreased. Like in the measurement in low energetic proton beams, the relative number of clusters showing very low signal (below 10 MeV) decreases with increasing acquisition time, as the probability for a particle arriving towards the end of the measurement frame is decreased.

Similar results were obtained for carbon ion beams of $E_{\text{initial}}=430 \text{ MeV/u}$, as shown in Figure 7.4. While the differences in the cluster size distributions for the different acquisition times are only small, again a second peak was obtained in the cluster signal distribution for long acquisition times.

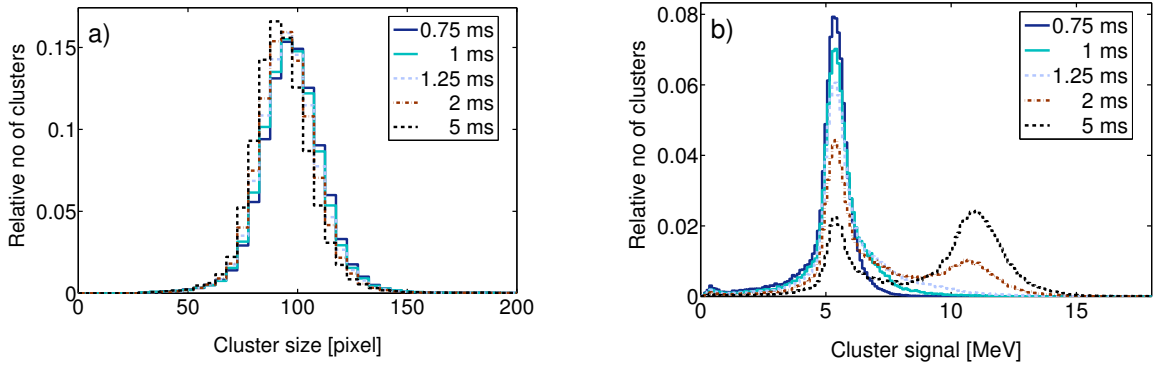
^{12}C , $E_{\text{initial}}=430 \text{ MeV/u}$


Figure 7.4: Cluster size (a) and cluster signal (b) distribution for different detector acquisition times. The distributions are normalized to their areas. For all distributions, the statistical uncertainty in the highest bin is less than 2.5%. Further settings: $V_{\text{bias}}=10 \text{ V}$, $A_{\text{cluster}} \geq 30 \text{ pixel}$, $\text{roundness}_{\text{cluster}} > 0.7375$ at 10% of cluster height.

Investigations with Simultaneous Energy and Time Measurements To investigate the reason for the second peak observed in the cluster signal distributions for carbon ion measurements at higher acquisition times, further measurements were performed in mixed detector operation mode (see Section 6.1.1 for explanations). Exemplary, the results for carbon ions of $E_{\text{initial}}=89 \text{ MeV/u}$ are shown in Figure 7.5. In Plot a), the two-dimensional distribution of the cluster size and the arrival time is shown. For most clusters sizes between 200 and 400 pixels were observed, independent of the particle arrival time. In the distribution of the cluster signal and the cluster size shown in Figure 7.5 b), two areas with a high number of events can be seen. Both areas correspond to the same cluster size but different cluster signal. These results are consistent with the one-dimensional distribution of the cluster signal for the same carbon ion energy shown in Figure 7.3. The graph in Figure 7.5 c) shows the distribution of the cluster signal and the arrival time of the corresponding particle during the frame duration. A clear correlation can be seen. For particles arriving during approximately the first half of the measurement time a stable cluster signal distribution centered around approximately 30 MeV is visible (region 1). This stable regime is followed by a transition (region 2) to a second stable regime at a signal of approximately 13 MeV (region 3). The clusters in this second stable regime are due to particles arriving during approximately the last fifth of the frame duration. For particles detected towards the very end of the measurement frame (region 4), the time-over-threshold of the preamplifier signal exceeds the remaining acquisition time. As a consequence, a part of the cluster signal cannot be digitized and is cut. The closer to the end of the measurement frame a particle is detected, the higher is the fraction of the signal which is cut off. This is reflected in the cluster signal distribution approaching

7.1 Characterization of the Detector Response in Therapeutic Ion Beams

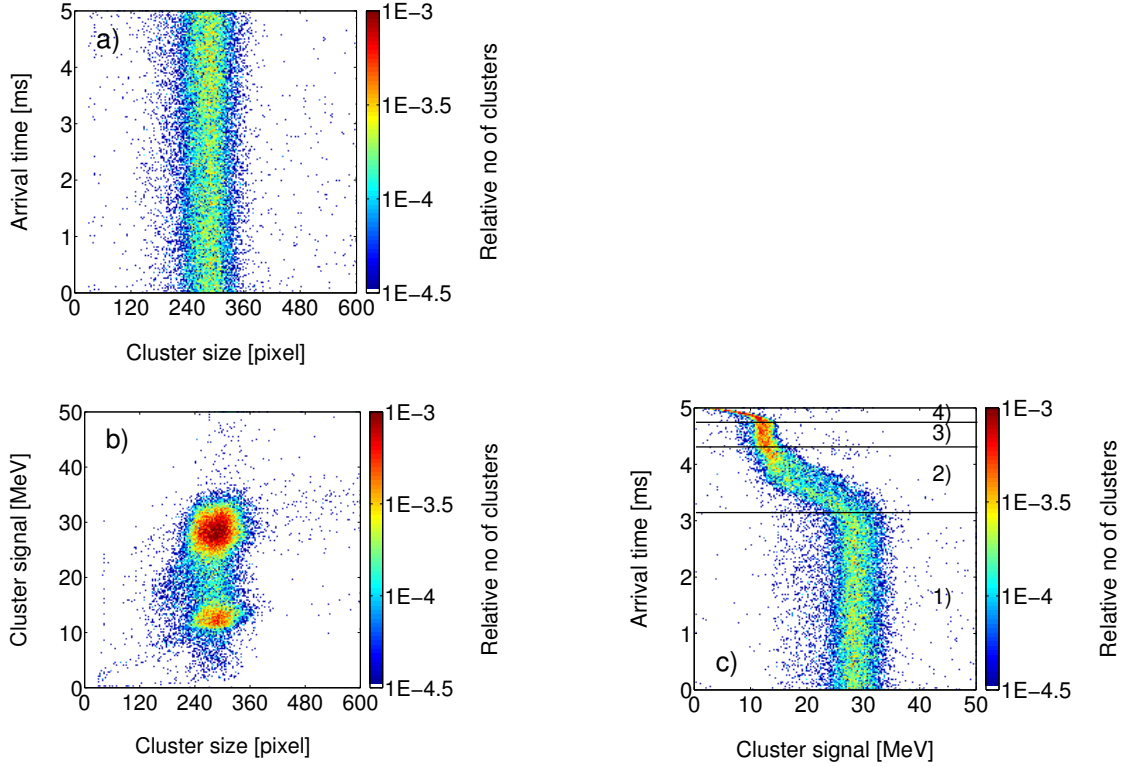


Figure 7.5: Investigation of cluster properties for measurements of a ^{12}C -ion beam of $E_{\text{initial}}=89\text{ MeV/u}$. Two dimensional distributions of particle arrival time and cluster size (a), cluster signal and cluster size (b), and cluster signal and arrival time (c) obtained in mixed detector operation mode are shown. One out of four pixels was operated in Timepix-mode. A reduced clock frequency of 1.92 MHz was used. Further settings: $t_{\text{acq}}=5\text{ ms}$, $V_{\text{bias}}=10\text{ V}$, $A_{\text{cluster}} \geq 30\text{ pixel}$, $\text{roundness}_{\text{cluster}} > 0.7375$ at 10% of cluster height.

a value of zero for events detected at the very end of the measurement frame. The approximations needed in order to evaluate the results obtained in mixed operation mode are further examined in Appendix A.

Similar results were obtained for carbon ions of $E_{\text{initial}}=271\text{ MeV/u}$ and $E_{\text{initial}}=430\text{ MeV/u}$ for the measurements in mixed operation mode. A possible explanation for the dependence of the cluster signal on the particle arrival time are overshoots in the preamplifier output due to oscillations in the pixel electronics. Figure 7.6 illustrates this theory^a. Ideally, after all charge collected by a pixel has been processed the preamplifier output should be zero. The overshoot theory however describes oscillations of the pixel electronics, which can cause a second rise of the preamplifier output above the threshold, the so called overshoot. Consequently, the pixel value does not only consist of the signal corresponding to the collected charge itself but additionally of a fake overshoot signal.

^aThe theory was developed in collaboration with P. Soukup and J. Jakůbek, IEAP, CTU in Prague. The effect has not been described before for the Timepix detector.

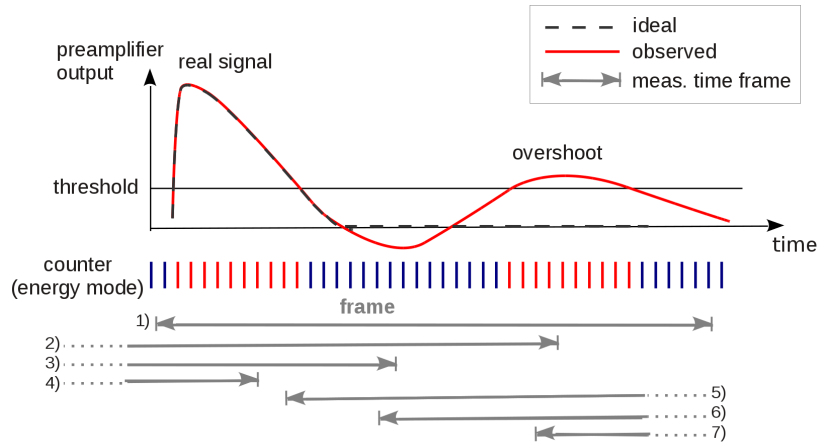


Figure 7.6: Illustration of the overshoot in the preamplifier output as a proposed explanation for the particle arrival time dependence of the detector signal. The ideal waveform and the waveform explaining the observations are depicted. The arrows illustrate the start and end of the acquisition time for seven different cases. Further explanations are given in the text.

The overshoot can have different influences on the measured cluster signal, depending on the time a particle is detected relative to the start and the end of the acquisition time and on the duration of the acquisition time itself. For a sufficiently long acquisition time with respect to the time the preamplifier output is above threshold (including the initial signal and the overshoot signal), the following situations can be distinguished (see illustrations in Figure 7.6, as well as illustrations in Figure 7.5 for situations 1) to 4) and in Figure 7.7 for situations 5) to 7)):

- 1) **The particle arrives early in the acquisition time:** The remaining frame time is long enough to collect the full time-over-threshold-signal, including both the initial real signal and the overshoot signal. The obtained cluster signal is therefore larger than the real signal corresponding to the energy deposited by the particle.
- 2) **The particle arrives in the middle of the acquisition time:** The remaining frame time is long enough to collect the full real signal. The acquisition however ends during the time-over-threshold of the overshoot signal. The overshoot signal is therefore not fully digitized. The obtained cluster signal is larger than the initial signal of the particle but not as large as the cluster signal in situation 1). The cluster signal further decreases the later the particle arrives. This situation corresponds to the transition phase.
- 3) **The particle arrives even later in the acquisition time:** The remaining frame time is long enough to cover the full time-over-threshold of the real signal. The acquisition time ends before the overshoot signal rises above the threshold. The overshoot signal is therefore not measured. For this situation, the measured cluster signal corresponds only to the signal due to the particle itself. It is therefore the preferable situation for the determination of the charge released by a particle.

- 4) **The particle arrives at the end of the acquisition time:** The remaining frame time is too short to cover the full time-over-threshold of the initial particle. The measured signal is therefore smaller than the initial particle signal. The signal is cut more, the later in the acquisition time the particle arrives.
- 5) **The particle arrives during the detector dead-time, shortly before the start of the measurement frame:** A part of the real signal plus the complete overshoot signal are collected within the acquisition time. As the signal is already above threshold at the beginning of the acquisition time, the corresponding particle arrival time is 0 ns.
- 6) **The particle arrives during the detector dead-time, within an intermediate time before the start of the measurement frame:** The frame starts after the real signal has decayed but before the overshoot signal rises above the threshold. Therefore the cluster signal corresponds to the overshoot signal alone.
- 7) **The particle arrives during the detector dead-time, long before the start of the measurement frame:** By the time the measurement starts, the overshoot signal is already above threshold. Only a part of the overshoot signal is measured. The particle arrival time is 0 ns.

For situations 5), 6) and 7), the obtained clusters are much smaller compared to situations 1) to 4). This is due to the fact that carbon ion clusters have a large rim of relatively low signal due to induced charge (see exemplary frame in Figure 5.10), which is not affected by the oscillation effects. Therefore, only the pixels in the center of the clusters are influenced by the oscillation effects. For the analysis shown in Figure 7.5 only clusters with sizes larger than 30 pixels were considered. Consequently, clusters corresponding to situation 5), 6), and 7) are not visible. For comparison, Figure 7.7 shows the same measurements as Figure 7.5, however now including all clusters with sizes larger than 4 pixels. Clusters of type 5) and 7) are assigned an arrival time value of 0 ns and are therefore hard to recognize in Figure 7.7 a) and c). The region containing clusters of type 6) is however clearly visible. In the two dimensional distribution of the cluster signal and the cluster size (Plot b), the small clusters of type 5) to 7) can be seen. It is however difficult to differentiate between the three types. In general, the longer before the start of the acquisition time a particle arrives, the smaller is the corresponding cluster signal. In order to understand the two-dimensional distribution of cluster size and the arrival time shown in Figure 7.7 a), it has to be considered that high energetic secondary electrons can lead to clusters with similar small sizes as clusters of type 5) to 7). These electrons are detected throughout the acquisition time. For time values of approximately 1.5 ms and below, additionally clusters of type 6) are detected, leading to a higher relative number of small clusters in this time period.

To demonstrate that for lower pixel values no overshoot signal is registered, a similar analysis as presented in Figure 7.5 was performed for proton beams ($E_{\text{initial}}=48 \text{ MeV}$)

7 Results

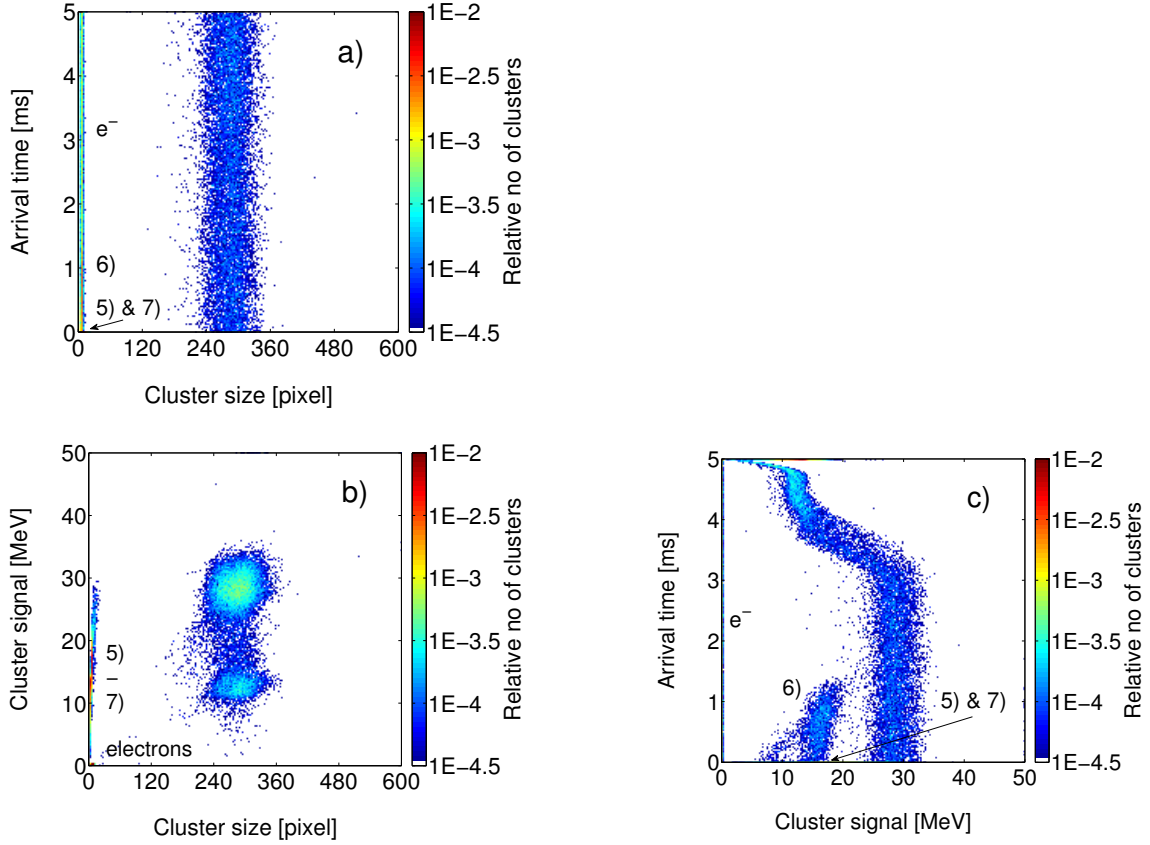


Figure 7.7: Measurements in mixed detector operation mode. Investigation of cluster properties for measurement of a ^{12}C -ion beam of $E_{\text{initial}}=89\text{ MeV/u}$. Two dimensional distributions of arrival time and cluster size (a), cluster signal and cluster size (b), and cluster signal and arrival time (c) are shown. One out of four pixels was operated in Timepix mode. A reduced clock frequency of 1.92 MHz was used. Further settings: $t_{\text{acq}}=5\text{ ms}$, $V_{\text{bias}}=10\text{ V}$, $A_{\text{cluster}} \geq 4\text{ pixel}$, $\text{roundness}_{\text{cluster}} > 0.7375$ at 10% of cluster height. Please note that in comparison to Figure 7.5 also clusters with a size between 4 and 30 pixels were included in the analysis.

depositing less energy in the sensor. In the measurement, one out of nine pixels was operated in Timepix mode. The two dimensional distributions of cluster size, cluster signal and arrival time are presented in Figure 7.8. No dependence of the cluster size on the arrival time of the corresponding particle can be seen. However, in Plot b) two areas with a high number of events are visible. The area corresponding to lower cluster signal values is induced by the approximations needed in order to evaluate the results obtained in mixed detector operation mode. Further investigations are shown in Appendix A. Over a wide range of arrival times, also no dependence of the cluster signal on the arrival time can be seen. Only for particles arriving at the very end of the acquisition time smaller cluster signals are observed (see descriptions of situation 4) above). These findings show that for low pixel values no overshoot effect is observed. However, overshoots which stay below the threshold could possibly exist.

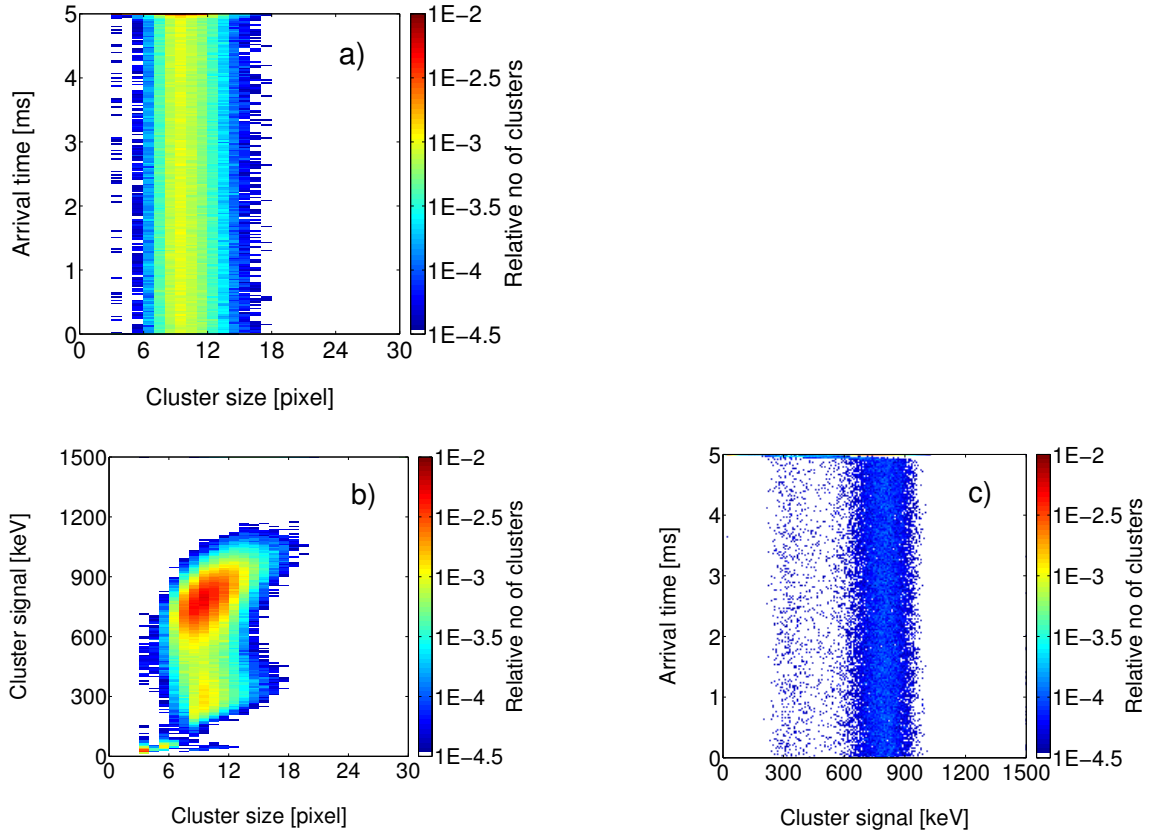


Figure 7.8: 2-dimensional distributions of arrival time and cluster size (a), cluster signal and cluster size (b) and cluster signal and arrival time (c) obtained in mixed detector operation mode. Each 9th pixel was operated in Timepix-mode. ^1H -beam of $E_{\text{initial}}=48$ MeV. A reduced clock frequency of 1.92 MHz was used. Further settings: $t_{\text{acq}}=5$ ms, $V_{\text{bias}}=10$ V, $A_{\text{cluster}} \geq 4$ pixel, $\text{roundness}_{\text{cluster}} > 0.7375$ at 10% of cluster height.

Investigations for Different Threshold Values A further proof of the overshoot theory was obtained by changing the internal threshold values of the pixels. The standard threshold was increased in six steps by approximately 5, 7, 8, 9, and 13 keV, respectively. The obtained cluster size, cluster signal and cluster height distributions are shown in Figure 7.9. The cluster size distributions are shown in Plot a). An increase of the threshold leads to a decrease of the cluster size, since for higher threshold values the signal of many pixels in the cluster rim does no longer reach the threshold. At the same time, the cluster size distribution is considerably narrower for higher threshold values. For the cluster signal distributions shown in Plot b), also a clear change of the obtained values can be seen. While for low threshold values two separate peaks are observed, for higher thresholds only one peak is obtained. In this case, the overshoot signal does not exceed the threshold value, as it was also assumed for the measurements in proton beams. The distributions of cluster heights are shown in Figure 7.9 c) (see Section 5.2.5 for the definition of the cluster height parameter). For all but the lowest thresholds two separate peaks are obtained in the distribution. While the first peak is

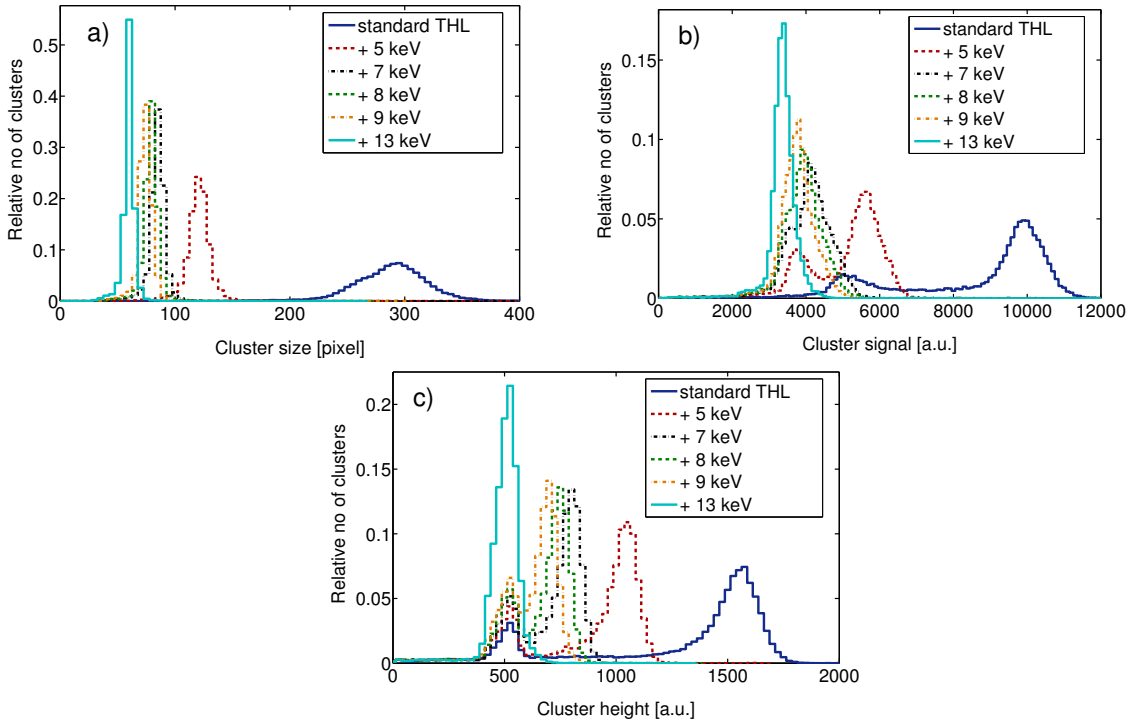
$^{12}\text{C}, E_{\text{initial}}=89 \text{ MeV/u}$


Figure 7.9: Cluster size (a), signal (b) and height (c) distributions obtained in energy-mode. Different threshold values were applied to the minimum required signal of a pixel in order to be registered. The distributions are normalized to their areas. For all distributions, the statistical uncertainty in the highest bin is less than 3.6%. A reduced clock frequency of 1.92 MHz was used. Further settings: $t_{\text{acq}}=5 \text{ ms}$, $V_{\text{bias}}=10 \text{ V}$, $A_{\text{cluster}} \geq 30 \text{ pixel}$, $\text{roundness}_{\text{cluster}} > 0.7375$ at 10% of cluster height.

at approximately the same position for all threshold values, the second peak is shifted towards lower cluster height values, the higher the threshold is set. This is because the higher the threshold is set, the shorter the overshoot signal stays above threshold. For an increase of the threshold value by 13 keV only one peak is obtained. In this case, the real particle signal crosses the threshold, while the overshoot signal stays below. Moreover, from the cluster height measurements it can be seen that the preamplifier waveform of the real particle signal rises and falls much steeper than the overshoot signal. For this reason, the position of the first peak is hardly changed for different threshold values. The findings confirm the proposed overshoot theory.

Consequences for Further Measurements To reduce the number of clusters showing an artificially increased signal due to overshoot effects, shorter acquisition times are beneficial. However, the shorter the acquisition time is chosen, the higher is the relative fraction of particles arriving towards the end of the acquisition time. Due to insufficient time for digitization the signal of the corresponding clusters is cut. As a compromise between the two effects, for further measurement an acquisition time of 1 ms was used.

7.1.2 Influences of the Bias Voltage on the Measured Signal

Experiments to study the dependency of the detector signal on the applied bias voltage were performed as described in Section 6.1.2, gaining the results shown in this section.

Measurements in Proton Beams For protons, the cluster signal distributions measured in beams of $E_{\text{initial}}=48$ MeV and 221 MeV for bias voltages between 5 and 100 V were investigated, thus covering the complete proton energy range available at HIT and the complete bias voltage range available for the detector. The results are presented in Figure 7.10. For further information on the employed detector settings and constraints see Section 6.1. In Plot a) the results for $E_{\text{initial}}=48$ MeV are shown. Besides the main peak centered at approximately 800 keV a small second peak centered at approximately 1600 keV can be seen in all distributions. This second peak displays the signal of clusters containing the overlapping signal of two particles. An additional peak in the distributions is observed for very small cluster signals. It can be assigned to secondary radiation which is further analyzed in Section 7.1.3. The cluster signal distributions for $E_{\text{initial}}=221$ MeV are shown in Plot b). Also for this ion energy, besides the main peak centered at approximately 200 keV a second area showing a high number of events with higher cluster signal can be seen. In this area, which is not separated from the main peak, on the one hand clusters showing a high signal due to energy-loss statistics (see further investigations in Section 7.2) and on the other hand clusters containing overlapping signals of two particles are displayed. Their number is particularly high since no constraints were applied on the minimum cluster roundness, for reasons discussed in Section 6.1.2.

For both energies, the cluster signal distributions show a clear dependence on the detector bias voltage. The position of the distributions is shifted towards higher cluster signals for increasing bias voltage, while the width of the main peak in the distributions does not change significantly. In Figure 7.10 c) the corresponding weighted mean values of the cluster signal distributions are displayed in dependence of the bias voltage. For the determination of the mean values only histogram bins in the main peak were considered ($E_{\text{initial}}=48$ MeV: cluster signal between 150 and 1250 keV, $E_{\text{initial}}=221$ MeV: cluster signal between 50 and 400 keV). Furthermore, a constraint on the bin height relative to the maximum bin height in the distribution required in order to be included in the analysis of 10% ($E_{\text{initial}}=48$ MeV) or 20% ($E_{\text{initial}}=220$ MeV), respectively, was set. In this way, the signal of clusters due to particles arriving at the end of the acquisition time, clusters containing overlapping signal of two or more particles, signal influenced by oscillation effects in the detector electronics (in the case of ^{12}C -ions, see previous chapter), and signal due to secondary radiation is excluded from the analysis. To allow for a direct comparison of the results, for both energies studied the weighted mean values were normalized to the value obtained for $V_{\text{bias}}=22$ V.

Protons

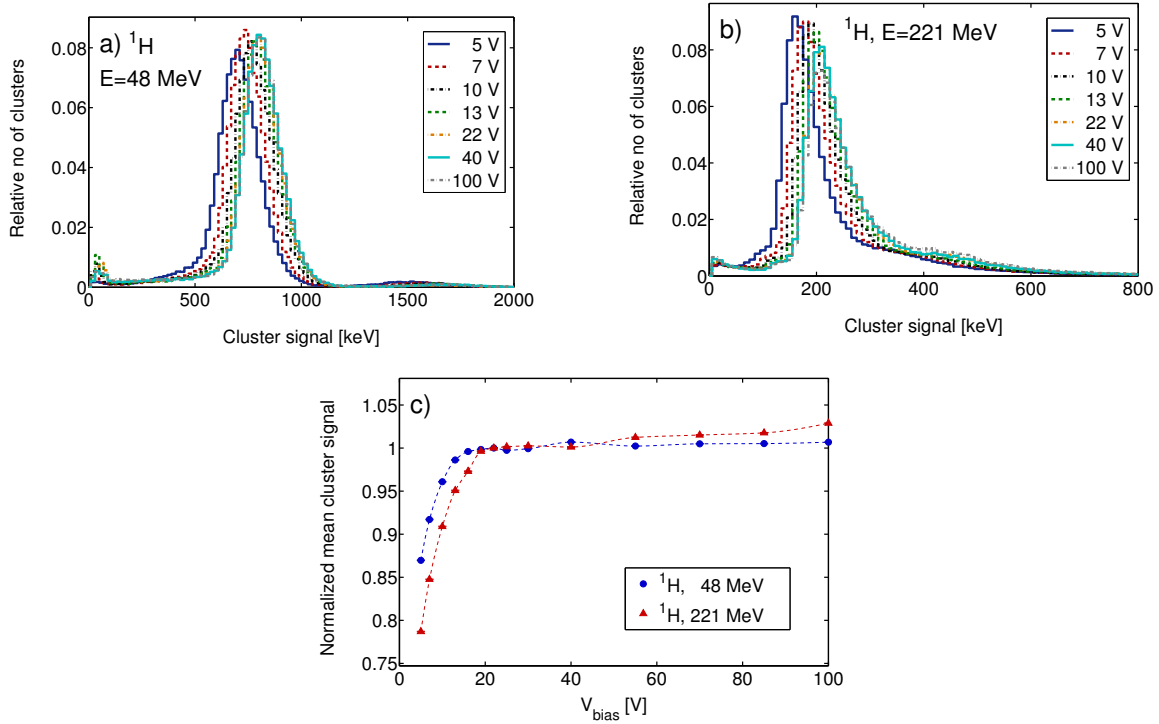


Figure 7.10: a) and b) Cluster signal distributions for protons of the lowest and highest energy available at HIT for different detector bias voltages. The distributions are normalized to their areas. For all distributions the statistical uncertainty in the highest bin is below 1.5%. c) Normalized mean cluster signal in dependence of the bias voltage. Splines are shown to guide the eye. The statistical uncertainties are smaller than the symbol sizes. Further settings: $t_{\text{acq}}=1$ ms, 48 MeV: $A_{\text{cluster}} \geq 4$ pixels, $\text{roundness}_{\text{cluster}} > 0.6625$ at 5% of cluster height; 221 MeV: No constraints on cluster size and roundness for clusters to be analyzed.

For low bias voltage values, the weighted mean value increases with increasing bias voltage. This can be assigned to a growing depletion width in the silicon sensor resulting in a higher charge collection efficiency. In the non-depleted zone, the electric field is weak. Consequently, the charge collection from that zone is slow and there is more time for diffusion or recombination of the charge carriers, resulting in signal loss. The detector is fully depleted for $V_{\text{bias}}=20\text{-}25$ V (see Section 5.2.2). For higher bias voltage values, variations in the obtained weighted mean signal are smaller. The direct comparison of the results shows that for protons of $E_{\text{initial}}=48$ MeV the mean cluster signal stabilizes at a lower bias voltage than for protons of $E_{\text{initial}}=220$ MeV. A possible explanation are influences of induced charge adding artificial signal at low bias voltage (see Section 5.2.2). The artificial signal partly compensates for signal lost due to recombination. With the artificial signal being higher the higher the initial energy deposition in the sensitive volume is, its impact is stronger for low proton energies.

This effect is also important to understand the dependence of the mean cluster size

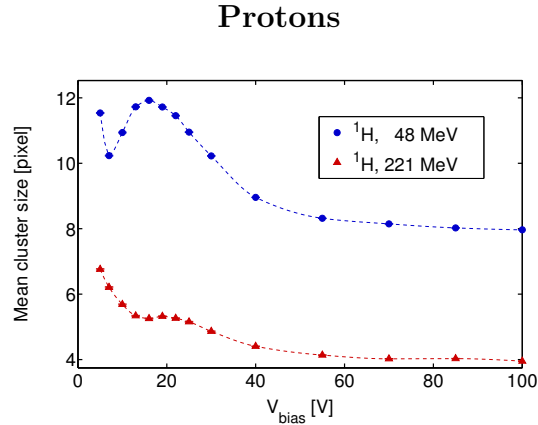


Figure 7.11: Mean cluster size in dependence of the bias voltage. Splines are shown to guide the eye. The statistical uncertainties are smaller than the symbol sizes. Further settings: $t_{\text{acq}}=1$ ms, 48 MeV: $A_{\text{cluster}} \geq 4$ pixels, $\text{roundness}_{\text{cluster}} > 0.6625$ at 5% of cluster height; 221 MeV: No constraints on cluster size and roundness for clusters to be analyzed.

on the bias voltage displayed in Figure 7.11. For protons of $E_{\text{initial}}=48$ MeV an initial decrease of the obtained mean cluster size is followed by an increase resulting in a maximum value at a bias voltage of approximately 19 V. At even larger bias voltages the mean cluster size again decreases. The initial decrease can be assigned to the effect of induced charge which is most prominent at low bias voltage values and leads to a signal in pixels which do not collect any charge. The second increase is presumably related to the decreasing width of the non-depleted sensor zone with increasing bias voltage. Since the non-depleted zone is formed at the side of the sensor opposing the electrodes, charge carriers released in this area show the widest spread due to diffusion. For a low bias voltage, a part of these charge carriers is however lost due to recombination. The higher the bias voltage is the smaller is the non-depleted zone and the more charge carriers from this area are collected by the electrodes. Due to the wide spread of these charge carriers, the mean cluster size increases with increasing bias voltages. The second decrease of the mean cluster size for a bias voltage above approximately 19 V is dominated by the increasing strength of the electric field leading to a faster charge collection and therefore reduced time for diffusion processes. For protons of $E_{\text{initial}}=221$ MeV the mean cluster size decreases with increasing bias voltage, indicating the increasing strength of the electric field to be the dominating effect in the charge collection process.

Also the cluster height distributions for protons shown in Figure 7.12 depict a clear dependence on the applied detector bias voltage. With increasing bias voltage the cluster height distributions are shifted towards higher values. At the same time the shape of the distributions changes significantly. While for a low detector bias voltage an approximately symmetrical distribution is observed, with increasing bias voltage the distribution is increasingly asymmetric with a higher fraction of clusters showing

Protons

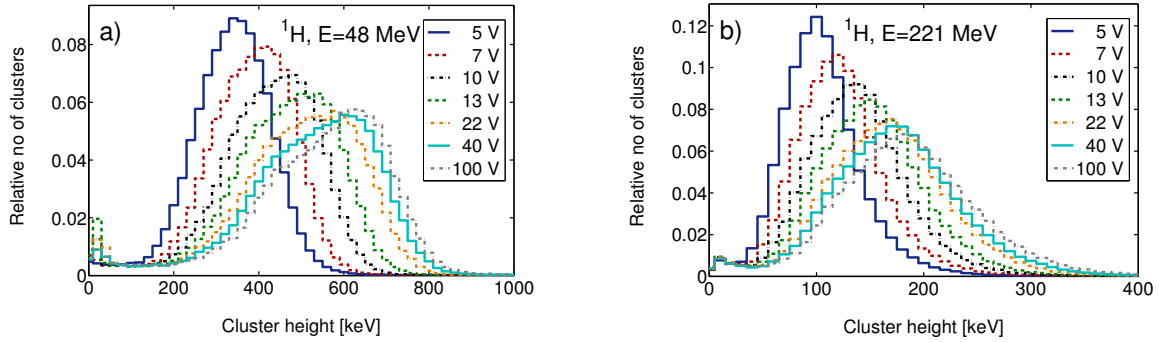


Figure 7.12: Cluster height distributions for protons at different detector bias voltages. The distributions are normalized to their areas. For all distributions the statistical uncertainty in the highest bin is below 2.5%. Further settings: $t_{\text{acq}}=1$ ms, a) $A_{\text{cluster}} \geq 4$ pixels, $\text{roundness}_{\text{cluster}} > 0.6625$ at 5% of cluster height; b) No constraints on cluster size and roundness for clusters to be analyzed.

relatively high maximum values. These findings can be explained by a change in the distribution of the signal over the cluster pixels. While at low bias voltages the probability for the main part of the signal being concentrated in only one or two pixels of the cluster is relatively low due to an increased influence of charge sharing processes, the probability increases with increasing bias voltage. At the same time, there are still clusters for which the main part of the signal is distributed over more pixels, e.g. for particles registered at the border between two pixels. Consequently, these clusters show smaller cluster height values. Their relative number is however decreasing with increasing bias voltage. Consequently, with increasing bias voltage the shape of the cluster height distribution gets broader and is expanded towards higher cluster heights. The clusters with very small heights (below 40 keV) can be assigned to secondary radiation (see Section 7.1.3).

Cluster Profiles for Proton Measurements In addition to studying the cluster size, signal and height separately, profiles through the clusters allow understanding correlations between the parameters. The profiles for different initial proton energies and bias voltages are shown in Figure 7.13. For each measurement, profiles through the centers of mass of 1000 clusters were established and averaged. For all investigated energies, the height of the profiles increases with increasing bias voltage due to an increasing charge collection efficiency and decreased diffusion of the charge carriers. At low bias voltage values the clusters are approximately Gaussian shaped, while at higher bias voltage values the main part of the signal is concentrated to only one or a few pixels. In addition, there is a rim of pixels around this central part showing small signal values.

Protons

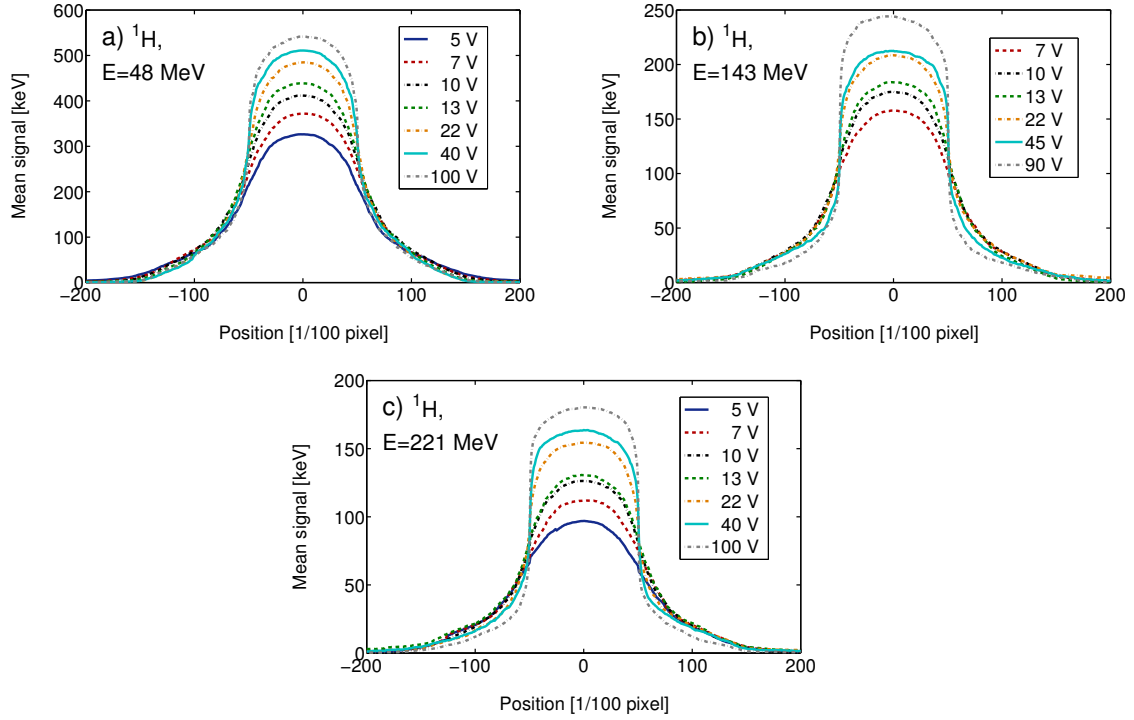


Figure 7.13: Average profiles over 1000 clusters for free in air measurements in ^1H -beams of different initial energies and for different detector bias voltages. Further settings: $t_{\text{acq}}=1$ ms, a) $A_{\text{cluster}} \geq 4$ pixels, $\text{roundness}_{\text{cluster}} > 0.6625$ at 5% of cluster height; b) and c) No constraints on cluster size and roundness for clusters to be analyzed.

Measurements in Carbon Ion Beams In contrast to protons, the cluster parameters for carbon ions of therapeutically used primary beam energies show largely different dependencies on the bias voltage. Figure 7.14 shows the cluster signal distributions for measurements in carbon ion beams of $E_{\text{initial}}=89$ MeV/u (a) and $E_{\text{initial}}=430$ MeV/u (b). While for both energies at a bias voltage between 5 and 22 V the distributions show one peak, at a bias voltage of 45 V a second peak can be observed. The origin of this second peak was found to be related to the position on the detector where the respective clusters were registered. The findings were however not studied in detail.

While for carbon ions of $E_{\text{initial}}=89$ MeV/u the cluster signal distributions show decreasing values for an increasing detector bias voltage, for $E_{\text{initial}}=430$ MeV/u the distributions are in an approximately constant position up to $V_{\text{bias}}=13$ V. For a higher bias voltage also for this ion energy the distributions show decreasing values. The related weighted mean values of the cluster signal distributions displayed in Figure 7.14 c) show the same tendencies. For the determination of the mean values a constraint on the minimum required bin height for a bin to be included in the analysis relative to the maximum bin height in the distribution of 15% was set (see explanations above). To allow for a direct comparison between the studied energies, the mean cluster signal

Carbon ions

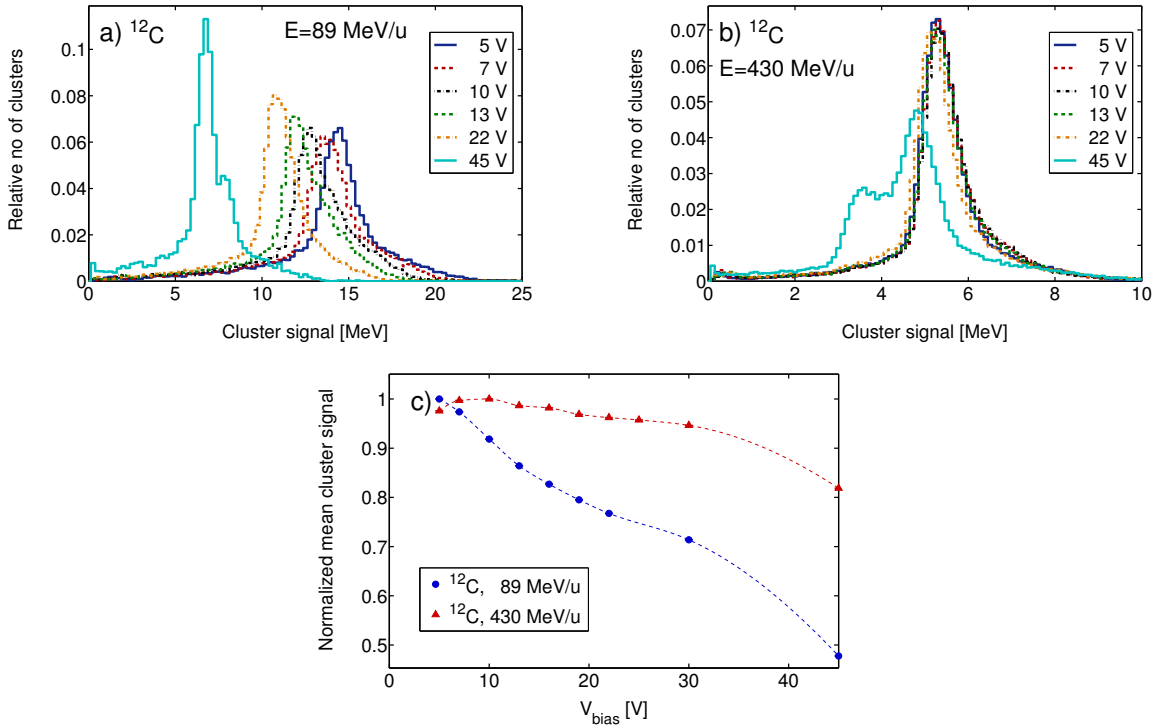


Figure 7.14: a) and b) Cluster signal distributions for ^{12}C -ions of the lowest and highest energy available at HIT at different detector bias voltages. The distributions are normalized to their areas. For all distributions the statistical uncertainty in the highest bin is below 2.9%. c) Normalized mean cluster signal in dependence of the bias voltage. Splines are shown to guide the eye. The statistical uncertainties are smaller than the symbol sizes. Further settings: $t_{\text{acq}}=1\text{ ms}$, $\text{roundness}_{\text{cluster}}>0.7375$ at 10% of cluster height, 89 MeV/u: $A_{\text{cluster}} \geq 30$ pixels, 430 MeV/u: $A_{\text{cluster}} \geq 15$ pixels.

values were normalized to the maximum value obtained for the respective energy.

The observation of decreasing cluster signal values with increasing bias voltage are consistent with saturation of the detector response in pixels registering very high signals. The higher the bias voltage is the larger is the part of the cluster signal concentrated to the central pixels. Therefore, the saturation effects are more influential at higher bias voltages. For carbon ions of $E_{\text{initial}}=89\text{ MeV/u}$ the relative decrease in the mean cluster signal with increasing bias voltage is larger (more than 50% for $V_{\text{bias}}=45\text{ V}$ compared to $V_{\text{bias}}=5\text{ V}$) than for $E_{\text{initial}}=430\text{ MeV/u}$ (approximately 15% in the same range). This can be explained by the lower energy deposition in the detector for carbon ions of $E_{\text{initial}}=430\text{ MeV/u}$ and therefore a smaller influence of saturation effects.

The saturation effects are also reflected in the cluster height distributions shown in Figure 7.15. For carbon ions of $E_{\text{initial}}=89\text{ MeV/u}$ (Plot a)), the cluster height distributions are shifted towards lower values for increasing bias voltages. Moreover, the cluster height distributions show a distinct falling edge. To understand the reason for this falling edge, the course of the detector calibration function for very high input

signal has to be considered. While standardly a linear course of the calibration curve for energies above 10 keV is assumed, new studies have indicated that these assumption is only valid for energies of up to 900 keV (see Section 5.2.4). Above, the calibration curve was found to drastically increase before decreasing due to saturation of the response of the pixel electronic chain. Recently, the course of the calibration function for very high input signal was tested qualitatively using a LED diode which was placed directly on the detector surface^a. The qualitative course of the curve observed in these measurements is illustrated in Figure 7.16. Considering these findings, the falling edge in the cluster height distributions can be correlated to the point where the calibration curve starts to drop. Due to variations of the calibration curves between pixels, the falling edge is however not sharp but shows a certain extension. Moreover, the position of the falling edge depends on the bias voltage, indicating a dependence also of the calibration curve in this high energy region on the bias voltage.

At the same time, also clusters with height values above the value corresponding to the falling edge position in the respective cluster height distribution were observed, what is not possible with respect to the calibration curve shown in Figure 7.16. In a further study, the corresponding clusters were found to be induced by ions arriving at the beginning of the measurement frames. The signals and heights of these clusters are likely to be influenced by overshoots in the preamplifier output described in the previous section. The findings indicate, that in this case the course of the calibration curve shown in Figure 7.16 is only of limited validity.

The falling edges can also be seen in the cluster height distributions for carbon ions of $E_{\text{initial}}=430$ MeV/u (see Figure 7.15 b)). However, different dependencies on the bias voltage were observed. For a bias voltage between 5 and 22 V the cluster height

Carbon ions

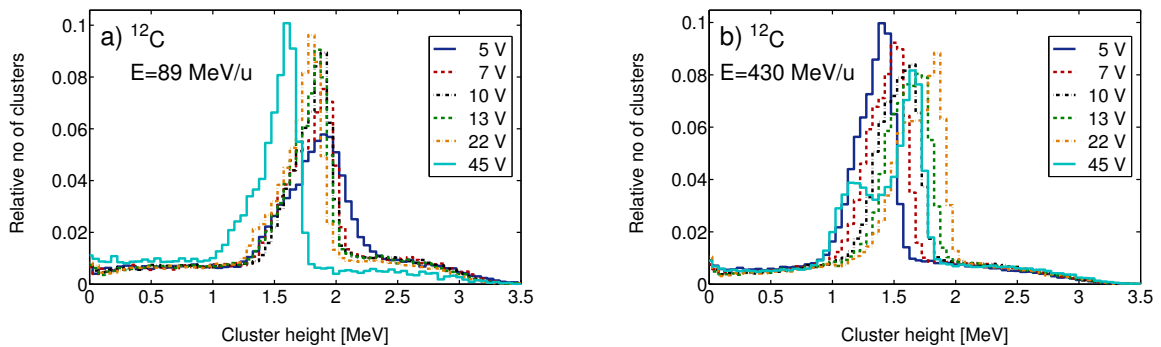


Figure 7.15: Cluster height distributions for ^{12}C -ions at different detector bias voltages. The distributions are normalized to their areas. For all distributions the statistical uncertainty in the highest bin is below 3.1%. Further settings: $t_{\text{acq}}=1$ ms, $\text{roundness}_{\text{cluster}}^{\text{min}} > 0.7375$ at 10% of cluster height, a) $A_{\text{cluster}} \geq 30$ pixels, b) $A_{\text{cluster}} \geq 15$ pixels.

^aPersonal communication with J. Jakubek, IEAP, CTU in Prague.

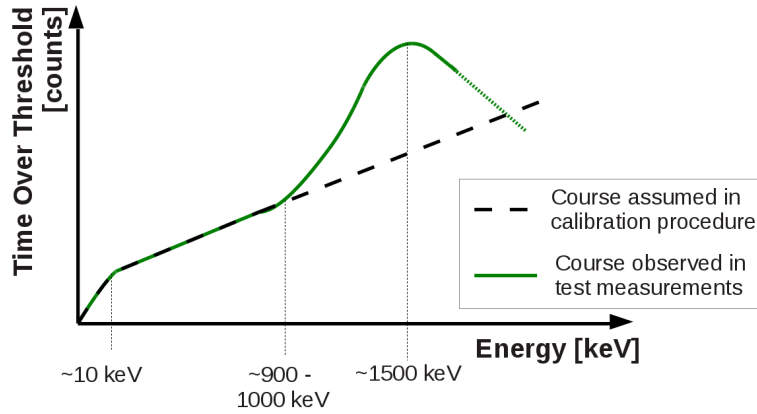


Figure 7.16: Schematic course of the calibration curve for very high input signals. A white LED diode placed directly on the detector surface was used for the investigations. For comparison also the course of the function currently assumed for the calibration procedure is illustrated.

distributions are shifted towards higher values with increasing bias voltage. At the same time also the positions of the falling edges are shifted towards higher values. For a bias voltage of 45 V, in contrast, the cluster height distribution and the falling edge are in turn shifted towards smaller values. While the shifts in the positions of the cluster height distribution allow to conclude that saturation effects for this ion energy are only of importance for bias voltages above 22 V, the observation of falling edges also at lower bias voltages cannot be brought into agreement with this theory.

The weighted mean values of the cluster size distributions are shown in Figure 7.17. For carbon ions of $E_{\text{initial}}=89 \text{ MeV/u}$ an initial increase between $V_{\text{bias}}=5$ and 7 V followed by a subsequent decrease of the mean cluster sizes can be seen. For carbon ions of $E_{\text{initial}}=430 \text{ MeV/u}$ the clusters are much smaller. Also in their case the sizes initially increase up to a bias voltage of 13 V and subsequently decrease. Besides effects of the non-depleted zone in the sensor volume it needs to be considered that the cluster sizes are largely influenced by the effect of induced charge due to the high energy deposition of the carbon ions in the sensitive volume. While the first effect leads to an increase of the cluster size with the bias voltage, the latter effect decreases with increasing bias voltage, in turn resulting in smaller cluster sizes. Due to the large rim of the clusters caused by induced charge, charge sharing due to diffusion of the charge carriers itself is assumed to have no influence on the measured overall size of the clusters.

Cluster Profiles for Carbon Ion Measurements The average cluster profiles obtained for the different carbon ion energies are shown in Figure 7.18. For all energies, the central part of the clusters gets narrower with increasing bias voltage. This observation is consistent with decreasing diffusion of the charge carriers in the sensitive detector layer. The higher the electric field strength, the shorter is the time for diffusion of free

Carbon ions

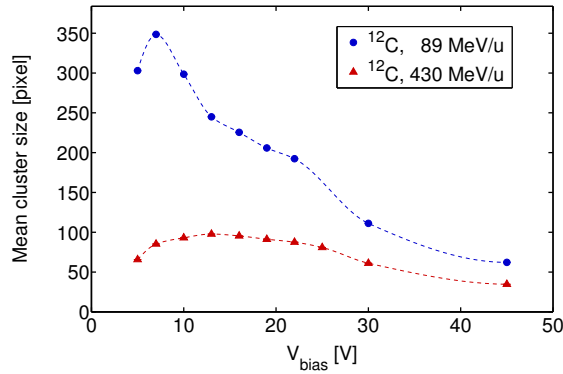


Figure 7.17: Mean cluster size in dependence of the bias voltage. Splines are shown to guide the eye. The statistical uncertainties are smaller than the symbol sizes. Further settings: $t_{\text{acq}}=1$ ms, $\text{roundness}_{\text{cluster}}>0.7375$ at 10% of cluster height, 89 MeV/u: $A_{\text{cluster}} \geq 30$ pixels, 430 MeV/u: $A_{\text{cluster}} \geq 15$ pixels.

charge carriers before being collected at the read-out electrode. In addition, significant differences between the ion energies and for the different bias voltages can be seen. For carbon ions of $E_{\text{initial}}=89$ MeV/u the profiles show a dip in the center for bias voltages of 7 V and above. The signal in the center of this dip decreases with increasing bias voltage. The concentration of the charge in the central pixels for higher bias voltages leads to a decrease of the signal of these pixels due to saturation effects. At the same time the height of the rim to both sides of the dip decreases with increasing bias voltage. This can possibly be explained by averaging effects between saturated and non-saturated pixels in the establishing procedure for the cluster profiles. The higher the saturation in the center of the clusters is, the more likely the values in the rim are to be reduced. However, the decrease in the cluster rim is also consistent with the dependency of the decrease in the falling edge of the cluster height distributions on the bias voltage, which itself cannot be explained by averaging effects. For an ion energy of 271 MeV/u the central dip is almost vanished and the height of the profiles increases with increasing bias voltages up to a value of about 22 V. Similar results can be observed for the highest initial carbon ion energy investigated. Again, the findings are consistent with the dependency of the falling edge in the cluster height distributions on the bias voltage.

Consequences for Further Measurements As described in the previous paragraphs, the influences of the bias voltage on the signal measured in proton and carbon ion beams of therapeutically used energies are complex. For protons, the decreasing width of the non-depleted sensor zone for an increasing bias voltage has the largest influence on the cluster size and cluster signal. To achieve an as high as possible charge collec-

Carbon ions

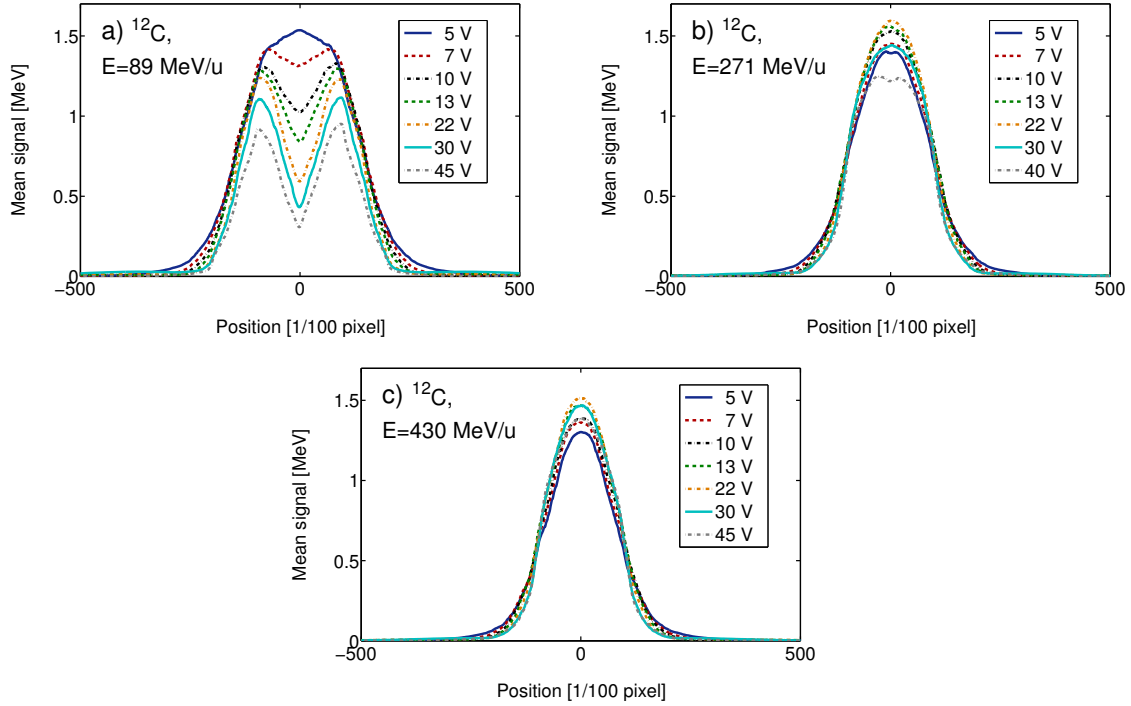


Figure 7.18: Average profiles over 1000 clusters for free in air measurements in ^{12}C -ion beams of different initial energies covering the complete energy range available at HIT for different detector bias voltages. Further settings: $t_{\text{acq}}=1 \text{ ms}$, $\text{roundness}_{\text{cluster}}>0.7375$ at 10% of cluster height, a) $A_{\text{cluster}} \geq 30$ pixels, b) $A_{\text{cluster}} \geq 20$ pixels, c) $A_{\text{cluster}} \geq 15$ pixels. (See Section 6.1.2 for further explanations on the choice of A_{cluster} .)

tion efficiency, for measurements in proton beams of therapeutically used energies the detector should be operated at a bias voltage of 20-25 V, resulting in a fully depleted sensor. However, for carbon ion beams depositing higher energies in the sensor, the effect of the non-depleted sensor zone was found to be overlain by saturation effects. They result in a decrease of the cluster signal for increasing bias voltages due to the concentration of the signal to less pixels. Based on these results, no bias voltage level optimal for all ion species and energies, as for example present in mixed ion fields resulting from fragmentation of primary carbon ions, can be determined. Therefore, for the energy-loss measurements presented in Section 7.2 measurements for bias voltages of 10 and 22 V are compared, while for the ion spectroscopy measurements presented in Section 7.3 the bias voltage is chosen considering the aspect of a better separability between ion species.

7.1.3 Investigations of Small Clusters

In the experiments, in addition to the clusters induced by primary proton and carbon ions, smaller clusters were observed. Although the relative number of the small clusters is significant, their contribution to the overall detected signal is low. It amounts to less than 0.6% for free-in-air measurements of primary carbon ion beams and to less than 2.9% for primary proton beams of the energy range available at HIT. In this section, the sources of these small clusters are analyzed.

Free-in-Air Measurements in Carbon Ion Beams In Figure 7.19 the cluster signal and cluster size values observed in measurements of carbon ions of $E_{\text{initial}}=89$ and 430 MeV/u are shown. For the evaluation of the measurements, no constraints on the minimum required cluster size or roundness were applied in order to study unbiased distributions. In the distributions, three distinct regions can be seen. The clusters in the first region labeled with ' ^{12}C ' can be assigned to the primary ions. The corresponding clusters are relatively large (on average approximately 300 pixels for $E_{\text{initial}}=89$ MeV/u and 100 pixels for $E_{\text{initial}}=430$ MeV/u) and show signal values of on average approximately 13,000 keV ($E_{\text{initial}}=89$ MeV/u) or 5,500 keV ($E_{\text{initial}}=430$ MeV/u).

In the second region labeled 'detector artefacts' in Figure 7.19, clusters due to overshoots in the preamplifier output, which can lead to small clusters with high signals (see explanations in Section 7.1.1) are displayed. As their origin is known, they were excluded for the further investigations of the small clusters of unknown origin displayed in the region labeled '?', which have an overall signal value below 1000 keV. To do so, a constraint on the maximum mean cluster signal of 200 keV was used.

For clusters in the third region ('?'), the relative number of clusters per measurement frame was found to be strongly correlated to the number of primary ions detected.

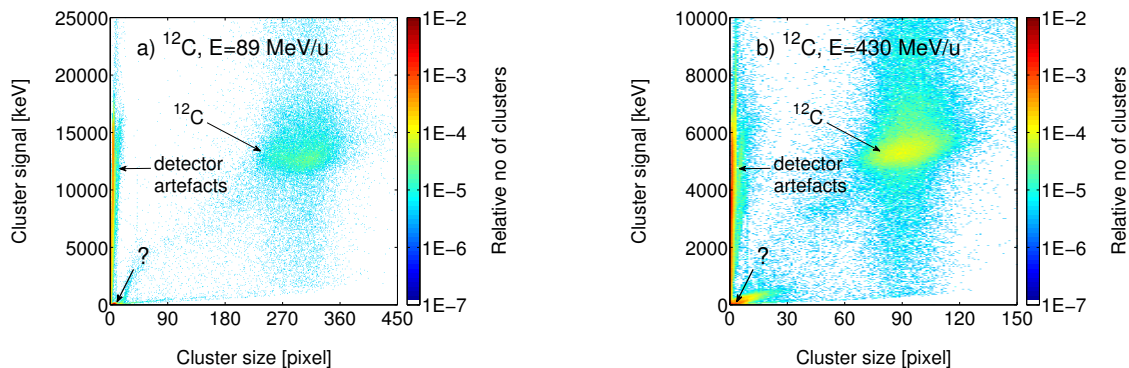


Figure 7.19: 2-dimensional distribution of cluster signal and size for free-in-air measurements of ^{12}C -ion beams of the lowest (a) and highest (b) energy available at HIT. Besides clusters due to initial ^{12}C -ions and known detector artefacts, additional clusters with small size and at the same time low signal can be seen (marked with '?'). Detector settings: $V_{\text{bias}}=10$ V, $t_{\text{acq}}=1$ ms. No constraints were applied on size or roundness of the clusters.

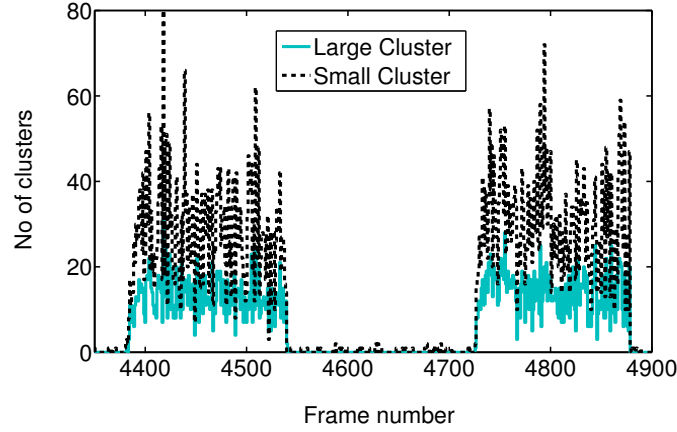


Figure 7.20: Number of small clusters ($A < 30$ pixel) and large clusters ($A \geq 30$ pixel) detected in 550 subsequent measurement frames for free-in-air measurements in a ^{12}C -ion beam of $E_{\text{initial}} = 89$ MeV/u. The number of small clusters is strongly correlated to the number of large clusters detected. The spill structure of the beam at HIT can be recognized. In the spill pause, a low number of small clusters is detected. Detector settings: $V_{\text{bias}} = 10$ V, $t_{\text{acq}} = 1$ ms. No constraints were applied on the roundness of the clusters.

Exemplary, the number of small and large clusters detected in 550 subsequent measurement frames for measurements in a ^{12}C -ion beam of $E_{\text{initial}} = 89$ MeV/u are depicted in Figure 7.20. In the spill pause, a low number of small clusters is detected, while no large clusters are observed. Based on these findings, two possible sources of the small clusters with low signal values are conceivable:

- 1) The clusters are due to secondary radiation produced in the beam path.
- 2) The clusters are due to detector effects provoked by the primary particles.

To study the two possibilities, measurements of ^{12}C -ion beams performed with the standard measurement set-up depicted in Figure 6.1 are compared to

- a) measurements in which the detector was placed 3 cm aside of the beam axis, therefore registering no more primary particles (nominal beam width (FWHM): 3.4 mm),
- b) measurements in which the ripple filter was brought into the beam path, expected to increase the number of secondary particles detected.

Measurements beside Beam Axis While the distribution of clusters measured in a carbon ion beam of $E_{\text{initial}} = 430$ MeV/u on the beam axis is presented in Figure 7.19 b), the results obtained beside the beam axis are shown in Figure 7.21 a). In this measurement, no clusters which can be assigned to primary carbon ions or detector artefacts known to be caused by primary carbon ions (see Section 7.1.1 for details) can be seen. However, small clusters with small signal are still visible. In Figure 7.21 b) the cluster signal distributions for measurements on and beside the beam axis are compared quantitatively. For both measurements, similar distributions of clusters with signals of up to approximately 300 keV can be seen. While in the measurement on the beam

7.1 Characterization of the Detector Response in Therapeutic Ion Beams

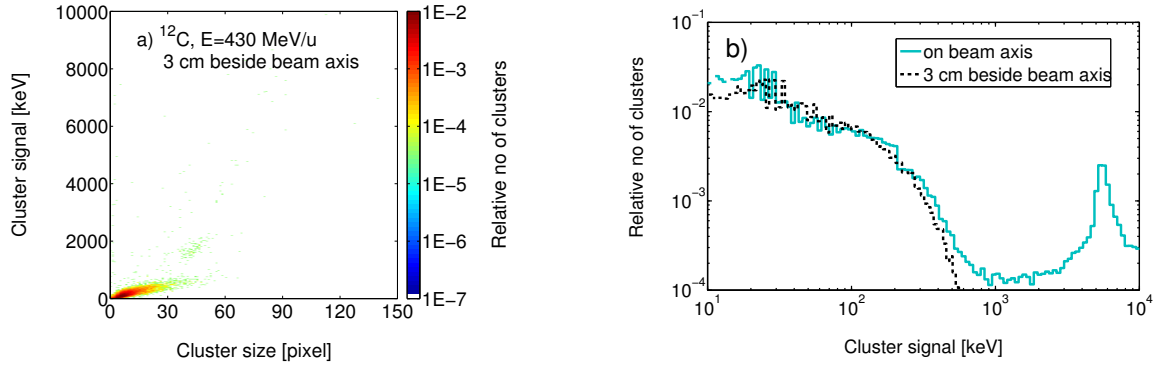


Figure 7.21: a) 2-dimensional distribution of cluster signal and cluster size for free-in-air measurements of a ^{12}C -ion beam of $E_{\text{initial}}=430$ MeV/u and FWHM=3.4 mm. The detector was placed 3 cm beside the beam axis. Only clusters with small size and signal are visible. b) Comparison of cluster signal distributions in measurements on the beam axis and 3 cm beside the beam axis. The distributions were normalized to the number of clusters with signal between 10 and 100 keV and to the bin size. Detector settings: $V_{\text{bias}}=10$ V, $t_{\text{acq}}=1$ ms. No constraints were applied on size or roundness of the clusters.

axis also higher values were obtained, for the measurement beside the beam axis the number of clusters with signal values above 500 keV is negligible. These findings show that the small clusters under investigation are also registered in measurements in which no primary particles reach the detector. They therefore argue against possibility 1) but for possibility 2) indicating secondary radiation originating from the beam line to be the source of the small clusters. Due to increased scattering for light particles, the secondary radiation is more likely to be registered in the measurement beside the beam axis than the primary carbon ions.

Comparison of Measurements With and Without Ripple Filter Inserting additional material in the beam path is expected to enhance the production of secondary radiation. Therefore, for ^{12}C -ion beams of $E_{\text{initial}}=271$ and 430 MeV/u, measurements with and without the ripple filter in the beam path were compared. The cluster size and cluster signal distributions are shown in Figure 7.22. All distributions are normalized to the number of primary particles detected. In the cluster size distributions, a shift of the position of the peaks corresponding to primary carbon ions (cluster size larger than 40 pixels) can be seen for measurements with and without ripple filter. Since the measurements were performed in different campaigns, these differences can be assigned to changes in the detector response over time (see Section 7.1.6 for further details). For both investigated ion energies, the relative number of clusters smaller than 30 pixels and clusters with a signal below 800 keV is increased for measurements with the ripple filter in the beam path. These findings are consistent with secondary radiation being the reason for the observed small clusters.

7 Results

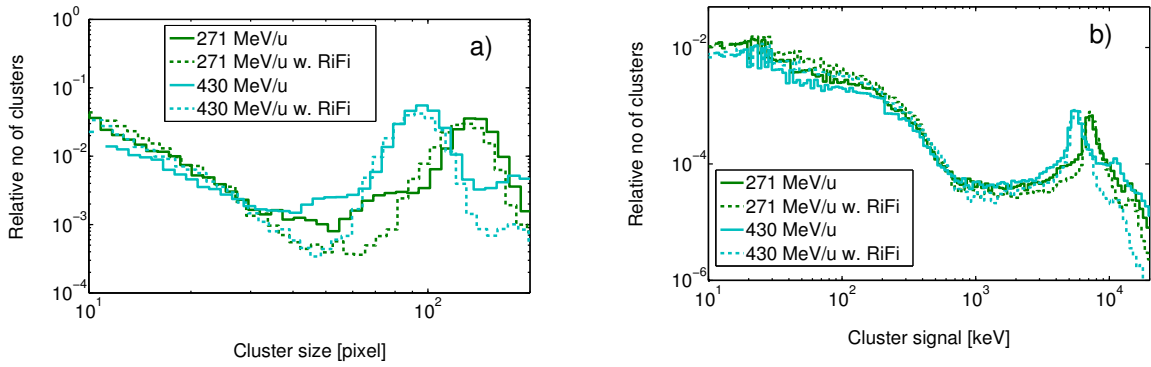


Figure 7.22: Distributions of cluster size (a) and cluster signal (b) for free-in-air measurements of ^{12}C -ions. Measurements without ripple filter (RiFi) in the beam line are compared to measurements with ripple filter. The distributions are normalized to the number of primary carbon ions detected. Detector settings: $V_{\text{bias}}=10\text{ V}$, $t_{\text{acq}}=1\text{ ms}$. No constraints were applied on size or roundness of the clusters.

Discussion of Possible Radiation Types While both studies indicate secondary radiation to be the source of small clusters, they do not give any information on the kind of secondary radiation detected. However, there are several points arguing for electrons to cause the small clusters:

- A relative high number of small clusters is detected (for measurements in ^{12}C -ion beams of $E_{\text{initial}}=89\text{ MeV/u}$ with the standard measurement set-up approximately 2.21 small clusters per primary carbon ion were detected).
- In proton measurements a lower relative number of small clusters (approximately 0.1 small clusters per primary proton) was detected compared to measurements in carbon ion beams.
- The higher the initial ion energy, the lower is the number of small clusters per large cluster detected (^{12}C -ions: 2.21 for $E_{\text{initial}}=89\text{ MeV/u}$, 0.56 for $E_{\text{initial}}=430\text{ MeV/u}$; protons: 0.11 for $E_{\text{initial}}=48\text{ MeV}$, 0.09 for $E_{\text{initial}}=221\text{ MeV}$).
- The higher the initial ion energy the higher is the signal of the small clusters and the relative contribution to the overall energy detected (^{12}C -ions: 0.4% for $E_{\text{initial}}=89\text{ MeV/u}$, 0.6% for $E_{\text{initial}}=430\text{ MeV/u}$; protons: 0.9% for $E_{\text{initial}}=48\text{ MeV}$, 2.9% for $E_{\text{initial}}=221\text{ MeV}$).

Comparison of Cluster Size Distributions Obtained With Standard Constraints

To exclude the small clusters, including both the analyzed secondary radiation and for heavier ions also the detector artefacts due to overshoots in the preamplifier output (see Section 7.1.1), from the analysis of clusters induced by primary particles, a constraint on the minimally required cluster size can be used. To determine suitable values for this

7.1 Characterization of the Detector Response in Therapeutic Ion Beams

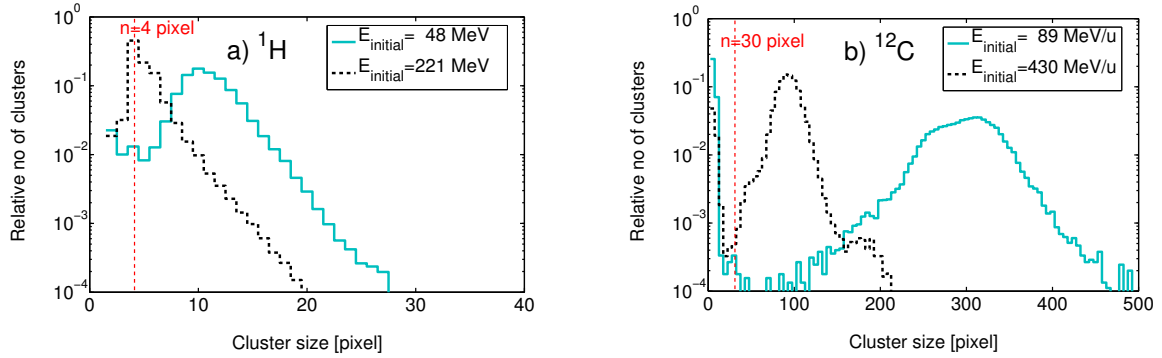


Figure 7.23: Distribution of cluster sizes for protons (a) and carbon ions (b) of the lowest and highest respective energies available at HIT. The statistical uncertainty in the highest bin is below 1.1% for all measurements. The values used as minimum cluster size constraints in further measurements are indicated by red lines. Settings: $V_{\text{bias}}=10\text{ V}$, $t_{\text{acq}}=1\text{ ms}$, a) $\text{roundness}_{\text{cluster}} > 0.6625$ at 5% of cluster height, b) $\text{roundness}_{\text{cluster}} > 0.7375$ at 10% of cluster height, no constraint on minimum cluster size.

constraint, the cluster size distributions for carbon ions with initial energies of 89 and 430 MeV/u and for protons of 48 and 221 MeV were measured using standard values for the detector settings and the roundness constraint. A comparison of the distributions (see Figure 7.23) demonstrates a minimum cluster size of 4 pixels to be a suitable constraint for measurements in proton beams, while for carbon ion measurements a cluster size of at least 30 pixels is suitable. Nonetheless, a certain number of clusters due to secondary radiation with sizes large than the constraints might still be included in the analysis.

7.1.4 Angular Dependency of the Detector Signal

The angle between the incident particle and the detector directly influences the path length of the ion in the sensitive layer and consequently the cluster shape and the deposited energy. For this reason, the dependency of the detector signal on the incident particle angle on the sensitive layer was studied in free-in-air measurements. The results obtained in the measurements described in Section 6.1.4 are presented in the following.

Figure 7.24 shows examples for measurement frames obtained in proton beams of $E_{\text{initial}}=143\text{ MeV}$ at incident particle angles on the detector of 90° (perpendicular incidence) and 45° . Clear differences in the cluster shapes depending on the incident particle angle can be seen. For particles traversing the detector approximately perpendicularly the clusters are small and their shape is in good approximation round. In contrast to that, at an incident angle of about 45° the clusters are larger and all of them are elongated in the same direction. Additionally, in both example frames clusters with a size of only one pixel can be seen. Possible sources of these clusters were analyzed in Section 7.1.3.

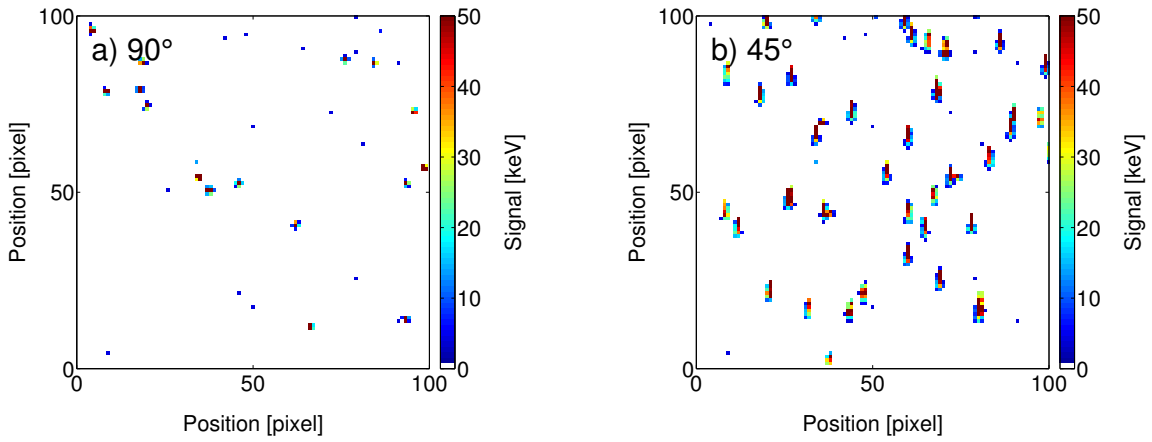
^1H , $E_{\text{initial}}=143$ MeV

Figure 7.24: Example frames for a) particles traversing the detector approximately perpendicularly, and b) an initial particle angle on the detector of 45° . Cut-outs of the example frames of 100×100 pixels are shown. Detector settings: $t_{\text{acq}}=1$ ms, $V_{\text{bias}}=10$ V.

Figure 7.25 a) shows a comparison of the cluster signal distributions obtained at incident particle angles of 90° , 85° , 80° , 70° , 60° , and 45° . To quantify the differences in the distributions, in Figure 7.25 b) the most frequent cluster signal value of each distribution is plotted in dependence of the incident particle angle. The longer ion path through the sensitive detector layer at smaller angles results in a higher energy deposition. Therefore, the most frequently obtained cluster signal values increase for decreasing initial particle angles on the detector. Furthermore, at an incident particle angle of 45° the cluster signal distribution is significantly wider compared to the

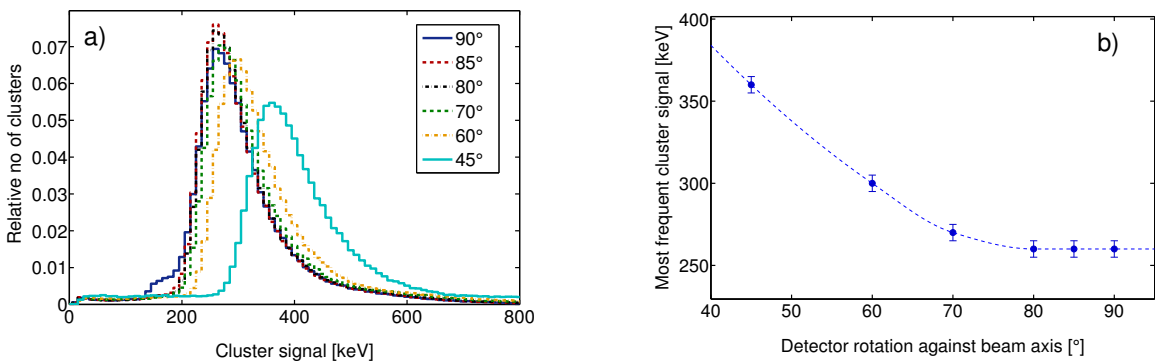
 ^1H , $E_{\text{initial}}=143$ MeV

Figure 7.25: a) Cluster signal distributions for different initial particle angles. b) The position of the cluster signals obtained most frequently (largest bins in a)) in dependence of the initial particle angle. The spline is shown to guide the eye. Settings: $t_{\text{acq}}=1$ ms, $V_{\text{bias}}=10$ V, $A_{\text{cluster}} \geq 4$ pixel, no constraint on the minimum required cluster roundness.

7.1 Characterization of the Detector Response in Therapeutic Ion Beams

distributions obtained at smaller angles. The underlying process is an increased energy-loss and range straggling due to the increased path length of the ions in the sensitive detector layer and the resulting higher number of interaction processes.

The deviations between the most frequent cluster signals for ions traversing the detector at angles of 70° and above compared to ions traversing the detector perpendicularly are less than 4%. Therefore, including clusters due to ions traversing the detector at these angles in the evaluation of experiments with initially perpendicular incident particles influences the obtained cluster signal distributions only little. Influences on the cluster signal distributions for particles with incident angles smaller than 70° are accordingly larger.

A possible parameter to distinguish between particles traversing the detector at different angles is the cluster roundness. Its applicability to discriminate between ions with small and large incident angles on the detector was studied by comparing the cluster roundness distributions obtained at angles of 90° , 70° , and 45° . The cluster roundness (see Section 5.2.5 for the definition) was determined at different height levels relative to the overall cluster height. For example, for the roundness determination at a cluster height of 5% only pixels showing a signal of at least 5% of the cluster height were considered, while for the roundness determination at a cluster height of 0% all cluster pixels were used to determine the cluster roundness. The roundness values determined at cluster heights of 0%, 5%, 7.5% and 10% are shown in Figure 7.26. The results demonstrate that already for a roundness determination at 0% cluster height a good separation between incident particle angles on the detector of 70° and 45° based on the cluster roundness parameter is possible. The separation further improves when the roundness parameter is determined at a cluster height of 5%, while no additional improvement was obtained for determinations at cluster heights of 7.5% and 10%. For the roundness parameter being determined at a relative cluster height of 5% and for an incident particle angle of 45° only 5.9% of the clusters show a roundness value larger than 0.6625, while for an incident particle angle of 70° 7.6% of the clusters show a roundness value smaller than 0.6625. Based on these results, determining the roundness at a relative height of 5% of the cluster height and using a roundness constraint of 0.6625 (see Figure 7.26, b)) was defined as the standard roundness constraint in proton measurements.

An analogous study was performed in carbon ion beams of $E_{\text{initial}}=271$ MeV/u. Figure 7.27 shows example frames obtained in measurements at different primary particle angles on the detector. The large clusters induced by carbon ions can be recognized well. For particles traversing the detector perpendicularly (a), the clusters have an in good approximation round shape. The pixels in the center of the clusters show high signals, while the signal in the rim around this center caused by induced charge (see Section 5.2.2) is relatively small. For an incident particle angle of 70° (b) no significant

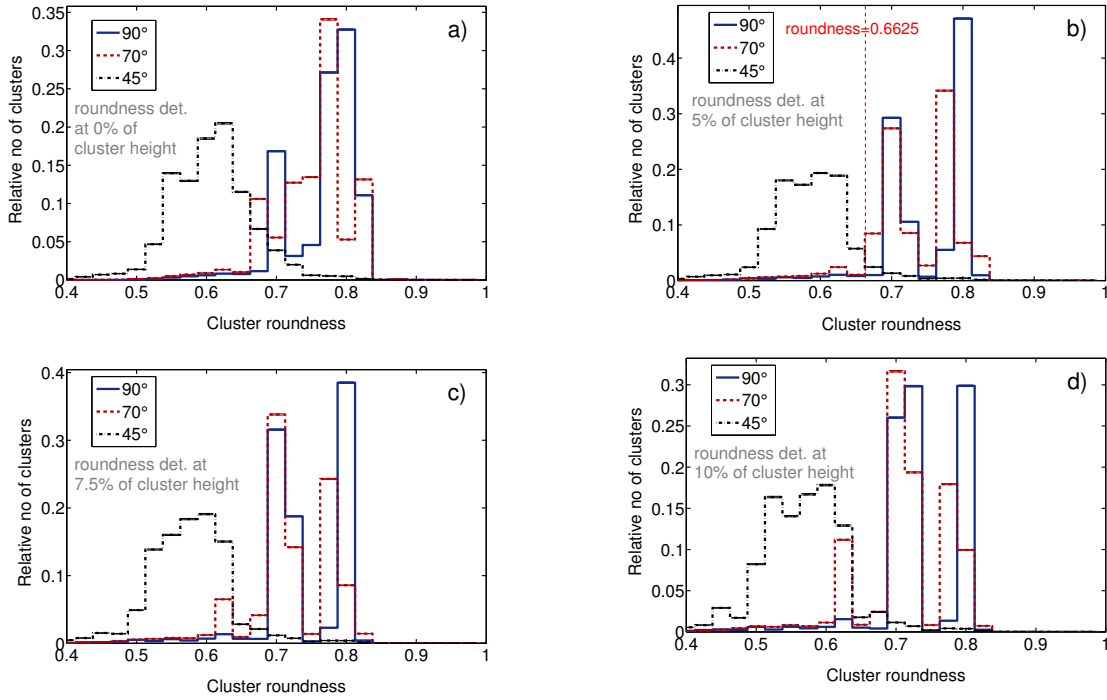
^1H , $E_{\text{initial}}=143$ MeV

Figure 7.26: Cluster roundness distributions for different incident particle angles on the detector. The cluster roundness was obtained considering a) all pixels in the clusters, or only pixels showing a signal of at least 5% (b), 7.5% (c) or 10% (d) of the cluster height (corresponding to the maximum pixel value in the cluster). The statistical uncertainties are negligible. Settings: $t_{\text{acq}}=1$ ms, $V_{\text{bias}}=10$ V, $A_{\text{cluster}} \geq 4$ pixel, no constraint on the minimum required cluster roundness.

difference in the cluster shape can be seen. Also for particles traversing the detector at an angle of about 45° (c) the overall cluster shape is approximately round. However, when regarding only the pixels with high signals in the center of the clusters, an elongation in horizontal direction is clearly visible. This elongation becomes even more distinct for an incident particle angle of 10° (d). For this very small incident particle angle also the low signal rim around the cluster center shows an elongated shape. The influence of the incident particle angle on the cluster signal distribution is shown in Figure 7.28 a). For incident particle angles of 70° and above, the cluster signal distributions show only small differences to the distributions obtained for particles traversing the detector approximately perpendicular (90°). For a quantitative comparison, the cluster signals measured most frequently were analyzed as a function of the incident particle angle as shown in Figure 7.28 b). The deviations between the most frequent cluster signals for ions traversing the detector at angles of 70° and above compared to ions traversing the detector perpendicularly are less than 11%. For smaller incident particle angles the obtained cluster signal distributions shown in Figure 7.28 a) show clearly increased values. This is due to the increased path length of the ions in the

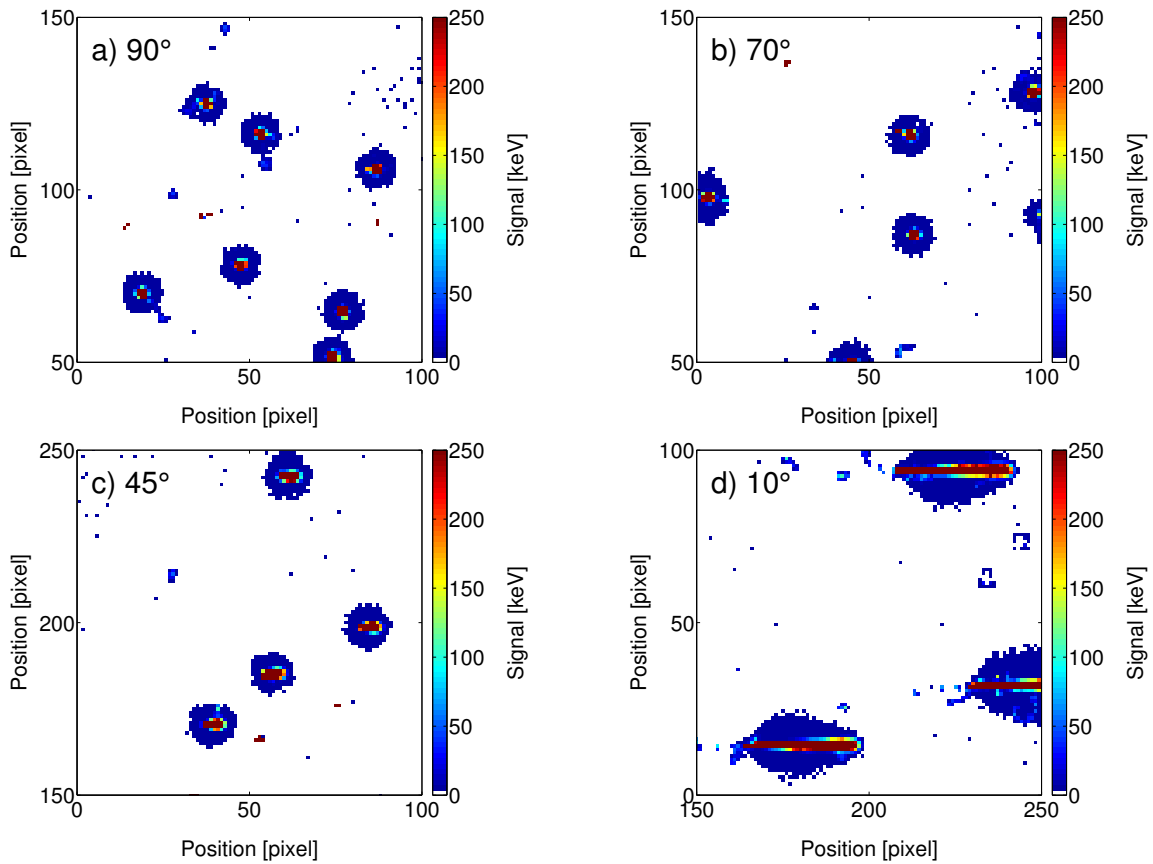
^{12}C , $E_{\text{initial}}=271 \text{ MeV/u}$ 

Figure 7.27: Example frames for a) particles traversing the detector approximately perpendicularly, b) an incident particle angle of 70° , c) 45° and d) 10° . Cut-outs of the example frames of 100×100 pixels are shown. Detector settings: $t_{\text{acq}}=1 \text{ ms}$, $V_{\text{bias}}=10 \text{ V}$.

sensitive detector layer and the resulting higher energy deposition. Moreover, for incident particle angles below 45° the obtained cluster signal distributions are significantly wider compared to the distribution obtained at 90° , presumably due to an increased energy-loss straggling. The described effects become even more significant at very small incident particle angles (10°).

Like for protons, also for carbon ions the influence of the initial particle angle on the corresponding cluster roundness distributions was studied. As already visible in Figure 7.27, the overall shape of the clusters is less influenced by the incident particle angle than is the shape of the central area of the cluster with high pixel values. For this reason, the cluster roundness was calculated at different heights, relative to the overall cluster height, as shown in Figure 7.29. The best discrimination from all studied cases can be achieved when determining the roundness at 10% and 15% of the cluster height (Figure 7.29, c and d). For a determination of the roundness at 10% of the cluster height and for an incident particle angle of 45° only 4.7% of the clusters show a roundness value

7 Results

^{12}C , $E_{\text{initial}}=271 \text{ MeV/u}$

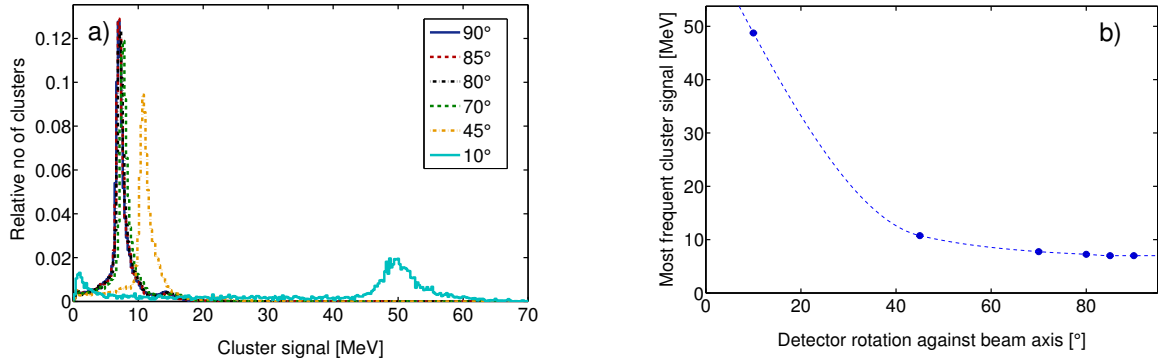


Figure 7.28: a) Cluster signal distributions for different initial particle angles. b) The position of the cluster signals obtained most frequently (largest bins in a)) in dependence of the initial particle angle. The spline is shown to guide the eye. Uncertainties are smaller than the symbol sizes. Settings: $t_{\text{acq}}=1 \text{ ms}$, $V_{\text{bias}}=10 \text{ V}$, $A_{\text{cluster}} \geq 30 \text{ pixel}$, no constraint on the minimum required cluster roundness.

^{12}C , $E_{\text{initial}}=271 \text{ MeV/u}$

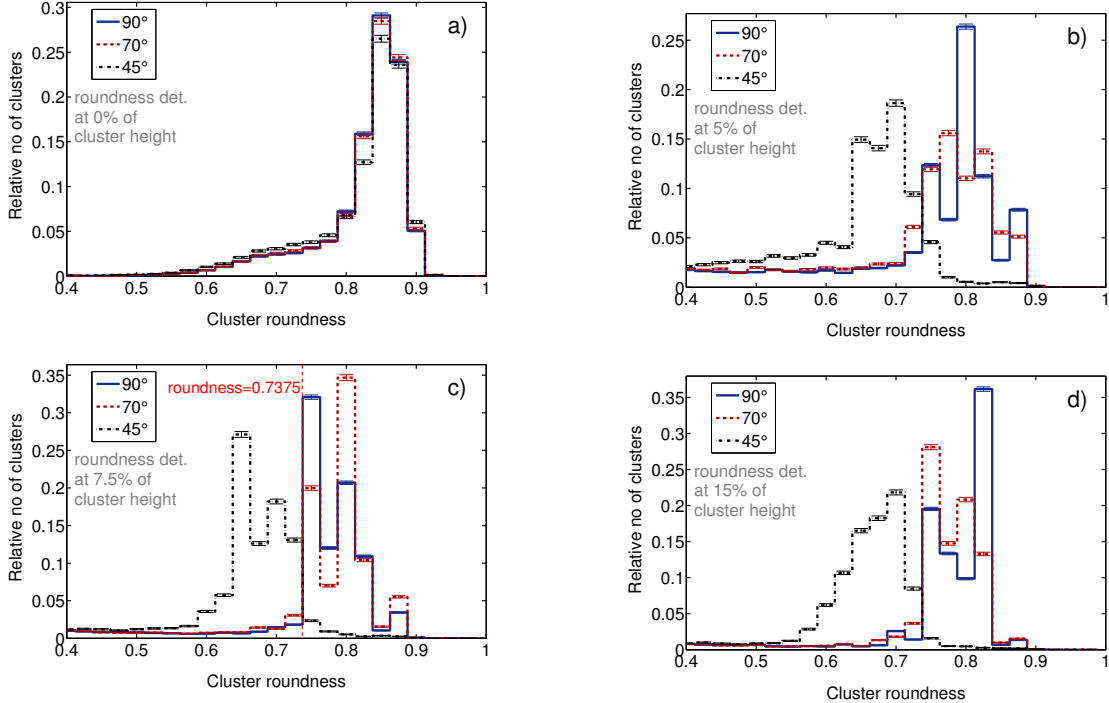


Figure 7.29: Cluster roundness distributions for different incident particle angles on the detector. The cluster roundness was obtained considering a) all pixels in the clusters, or only pixels showing a signal of at least 5% (b), 10% (c), or 15% (d) of the cluster height (corresponding to the maximum pixel value in the cluster). The error bars represent the statistical uncertainties. Settings: $V_{\text{bias}}=10 \text{ V}$, $t_{\text{acq}}=1 \text{ ms}$, $A_{\text{cluster}} \geq 30 \text{ pixel}$, no constraint on the minimum required cluster roundness.

larger than 0.7375, while for an incident particle angle of 70° 20.8% of the clusters show a roundness value smaller than 0.7375. According to these results, a cluster roundness value of 0.7375 offers a good separation between incident particle angles of 70° and 45° . Consequently, the minimally required cluster roundness parameter was set to 0.7375 when determining the cluster roundness at 10% of the cluster height.

7.1.5 Uniformity of the Detector Response over the Sensitive Area

Possible variations of the detector response over the sensitive area were analyzed in order to understand dependencies of the cluster parameters size, signal and height on the detector position registering the corresponding particle. The methodology is described in detail in Section 6.1.5. While in the following only selected results are discussed, an overview of all results obtained in this study can be found in Appendix B.

To discuss the results, a numbering scheme for different detector regions is used in this section, as depicted in Figure 7.30.

Region 1: Undamaged Sensor Area Region 1 corresponds to sensor material which did not suffer from radiation damage ('healthy sensor material'). Nonetheless, in some measurements an inhomogeneity can be observed in this region. The inhomogeneity has a tree ring-pattern, which can be assigned to an inhomogeneous distribution of dopants originating from the crystal growth process (Jakubek et al. (2012)). The variations in dopant concentration result in an inhomogeneous shape of the depletion volume and affect the intensity of the local electric field.

For carbon ion beams, the structure of the tree ring-pattern can be observed in the cluster size distributions for measurements at a low detector bias voltage ($V_{\text{bias}}=5\text{ V}$) and high initial particle energies ($E_{\text{initial}}=271$ and 430 MeV/u). The corresponding

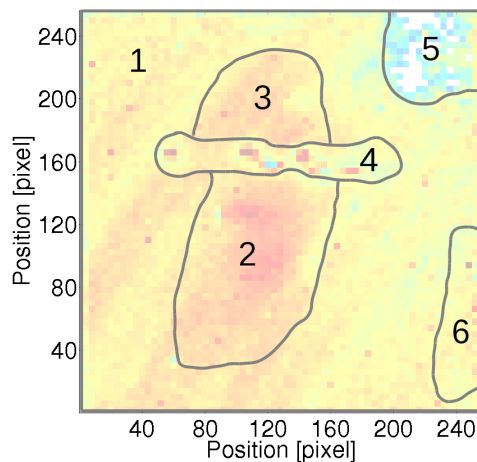


Figure 7.30: Map showing the numbering scheme for different detector regions.

Cluster size distributions

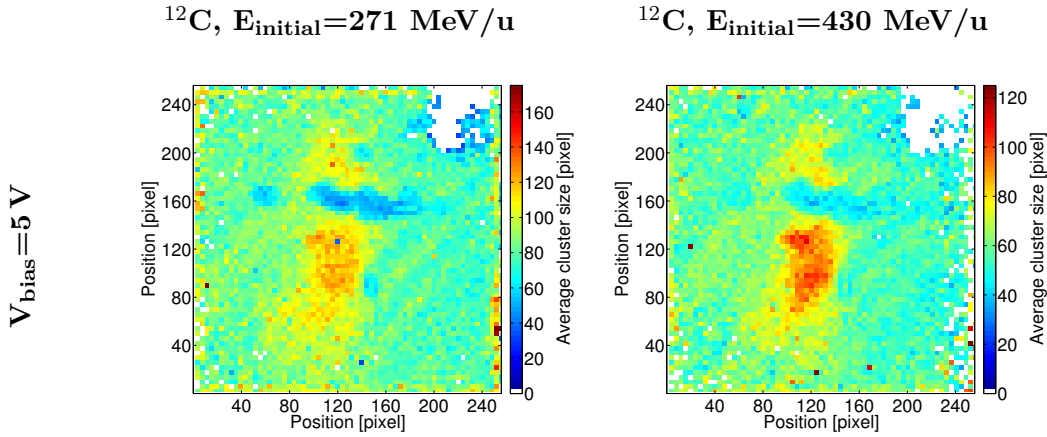


Figure 7.31: Distributions of average cluster size over the sensitive detector area. The scales were chosen to enable recognition of the effects described in the text. Further settings: $t_{\text{acq}}=1$ ms, $A_{\text{cluster}} \geq 30$ pixel, $\text{roundness}_{\text{cluster}} > 0.7375$ at 10% of cluster height.

detector maps showing the distributions of the mean cluster size over the sensitive detector area are displayed in Figure 7.31. No effect can be seen in the corresponding cluster signal and cluster height distributions. Also in the cluster size distributions for higher bias voltages and in all distributions obtained for the lowest carbon ion energy investigated no inhomogeneity over region 1 was observed.

For protons the described effect is more distinct (see Figure 7.32). At $E_{\text{initial}}=48$ MeV it largely influences the cluster size distributions for $V_{\text{bias}}=5$ and 10 V. For $V_{\text{bias}}=10$ V variations between the mean cluster sizes over region 1 are in the order of 20%. Moreover, for $V_{\text{bias}}=5$ V also the cluster signal distribution shows a diagonal pattern (see Figure 7.32), indicating influences of the dopant concentration on the charge collection efficiency. No effect can be seen in the cluster size and cluster signal distributions obtained at higher bias voltages, as well as in the cluster height distributions. For protons of $E_{\text{initial}}=143$ and 221 MeV the tree ring-pattern is less dominant but clearly visible in the cluster size distribution obtained at $V_{\text{bias}}=5$ V (see Figure 7.33). At higher bias voltages and in the cluster signal and height distributions no effect of the inhomogeneous dopant distribution is visible.

Regions 2 & 3: Radiation Damage Type I In regions 2 and 3 the sensor was damaged by an unknown radiation source. The effect of this damage is of particular importance in the cluster size distributions obtained in low energetic carbon ion beams which exhibit especially large cluster sizes. Smaller clusters are found in the damaged compared to the surrounding undamaged detector region (see Figure 7.34). The difference between the mean cluster sizes is in the order of 40%.

7.1 Characterization of the Detector Response in Therapeutic Ion Beams

^1H , $E_{\text{initial}}=48 \text{ MeV}$

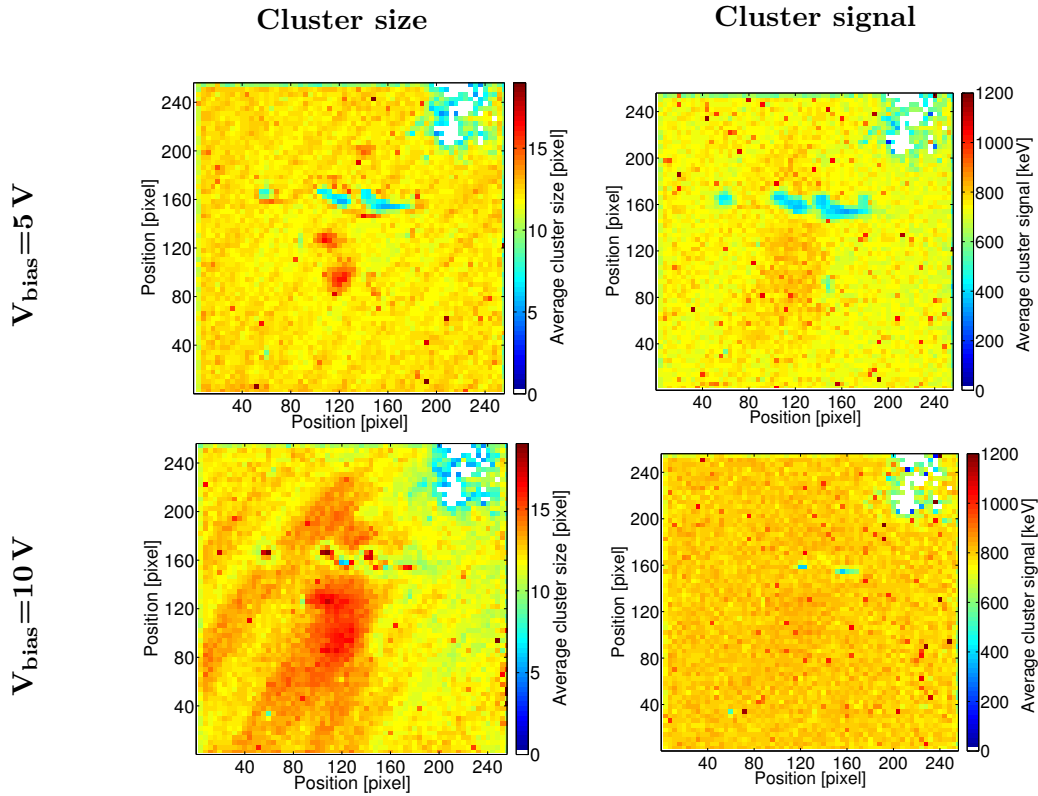


Figure 7.32: Distributions of average cluster size and average cluster signal over the sensitive detector area. The scales were chosen to enable recognition of the effects described in the text. Further settings: $t_{\text{acq}}=1 \text{ ms}$, $A_{\text{cluster}} \geq 4 \text{ pixel}$, $\text{roundness}_{\text{cluster}} > 0.6625$ at 5% of cluster height.

Cluster size distributions

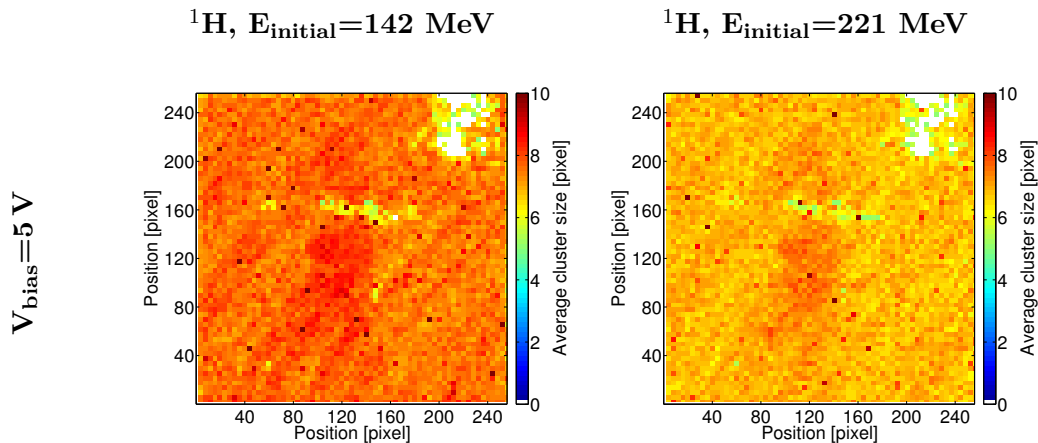


Figure 7.33: Distributions of average cluster size over the sensitive detector area. The scales were chosen to enable recognition of the effects described in the text. Further settings: $t_{\text{acq}}=1 \text{ ms}$, $A_{\text{cluster}} \geq 4 \text{ pixel}$, $\text{roundness}_{\text{cluster}} > 0.6625$ at 5% of cluster height.

Cluster size distributions

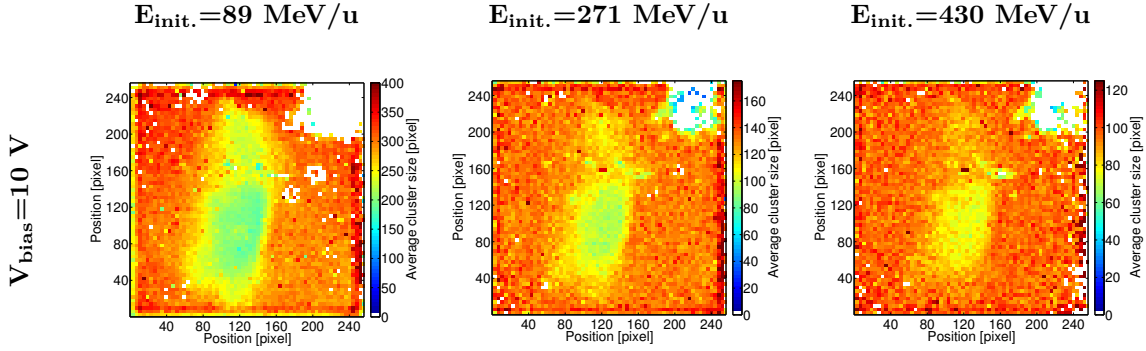


Figure 7.34: Distributions of average cluster size over the sensitive detector area for different carbon ion energies. The scales were chosen to enable recognition of the effects described in the text. Further settings: $t_{\text{acq}}=1$ ms, $A_{\text{cluster}} \geq 30$ pixel, $\text{roundness}_{\text{cluster}} > 0.7375$ at 10% of cluster height.

Also for medium and high energetic carbon ion beams, the effects of radiation damage in region 2 and 3 are clearly visible in the cluster size distributions (see Figure 7.34). While for $E_{\text{initial}}=271$ MeV/u the difference between the mean cluster sizes is also in the order of 40%, for $E_{\text{initial}}=430$ MeV/u the clusters in the damaged region are about 25% smaller than in the surrounding area.

For these energies also dependencies on the detector bias voltage were studied (see Figure 7.35). For $V_{\text{bias}}=5$ V larger average clusters are found in the damaged compared to the surrounding undamaged detector region. The difference between the mean cluster sizes is in the order of 60%. In contrast, for $V_{\text{bias}}=15$ V the clusters in the damaged areas are smaller than in the undamaged area. In this case, the difference between the mean cluster sizes in the two areas is in the order of 40%.

Cluster size distributions

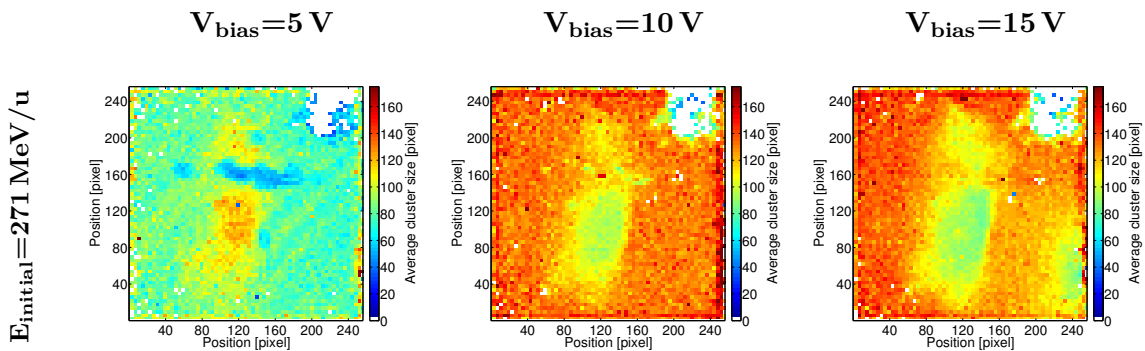


Figure 7.35: Distributions of average cluster size over the sensitive detector area for different bias voltages. The scales were chosen to enable recognition of the effects described in the text. Further settings: $t_{\text{acq}}=1$ ms, $A_{\text{cluster}} \geq 30$ pixel, $\text{roundness}_{\text{cluster}} > 0.7375$ at 10% of cluster height.

7.1 Characterization of the Detector Response in Therapeutic Ion Beams

The difference between the cluster size in damaged and undamaged detector areas is influenced by several effects. An explanation for changes of the cluster size in areas affected by radiation damage caused by particles only partly penetrating the sensor is given in Jakubek et al. (2012): Due to the radiation damage, the material resistivity in the damaged regions is decreased and the electric field inside of the damaged zone is lower. Therefore, the time for charge diffusion is increased leading to a wider spread of the charge. At the same time the intensity of the electric field below the damaged layer is increased. Consequently the time for charge diffusion is decreased and the spread of charge is smaller than in corresponding layers in healthy sensor areas. Depending on the applied bias voltage the described effects can result in smaller or larger clusters in damaged compared to undamaged detector regions. Moreover, for low energetic carbon ions the cluster size is largely influenced by the effect of induced charge. This effect itself depends on the applied bias voltage. Due to the complicated interplay of the various effects it is beyond the scope of this thesis to explain the observed behavior of cluster sizes in the damaged and undamaged detector area in detail. In the corresponding mean cluster signal and cluster height distributions no distinct dependencies on the detector area can be seen.

For measurements in proton beams of $E_{\text{initial}}=48$ MeV, an increased cluster size is found in regions 2 and 3 for $V_{\text{bias}}=5$ and 10 V (see Figure 7.32). The difference between the mean cluster sizes in damaged and undamaged area can however not be quantified, as the undamaged area itself shows an inhomogeneous cluster size distribution as discussed in the previous section. At $V_{\text{bias}}=15$ V no distinct difference between the cluster size in regions 2 and 3 and in the surrounding area was observed for the low proton energy studied. In the corresponding cluster signal distributions, an about 10-20% increased value is found in regions 2 and 3 at $V_{\text{bias}}=5$ V, while for higher bias voltages and in the cluster height distributions no distinct influences of the damage in these areas can be seen. Similar results were obtained for protons of $E_{\text{initial}}=143$ and 221 MeV.

Regions 4: Radiation Damage Type II In region 4, the sensor suffered radiation damage in several spots from a proton beam of 4.9 MeV. The range of these protons in silicon amounts to 210 μm . In a previous study employing an X-ray source (Jakubek et al. (2012)), the charge collection efficiency was found to be equivalent to zero inside this damaged layer, while it was partly degraded below. Moreover, while the detector was found to behave normally in the damaged region for high bias voltages, a larger influence was obtained at lower bias voltages.

In the measurements performed in carbon ion beams, influences of the radiation damage in region 4 are most distinct in the cluster size distributions obtained for $E_{\text{initial}}=$

Cluster signal distributions

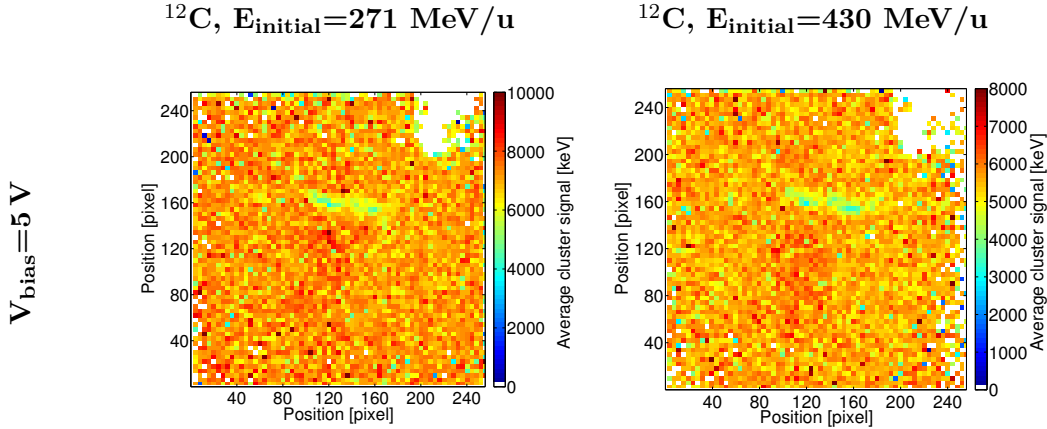


Figure 7.36: Distributions of average cluster signals over the sensitive detector area. The scales were chosen to enable recognition of the effects described in the text. Further settings: $t_{acq}=1$ ms, $A_{cluster} \geq 30$ pixel, $roundness_{cluster} > 0.7375$ at 10% of cluster height.

271 and 430 MeV/u and $V_{bias}=5$ V. These distributions are shown in Figure 7.31. The clusters in the damaged area are on average about 40% smaller than in the surrounding healthy sensor. Moreover, they are about 60% smaller than the clusters observed in regions 2 and 3. These findings indicate a difference in the radiation damage the sensor suffered in regions 2 and 3 compared to region 4. Also in the corresponding cluster signal distributions decreased values are obtained in region 4 (see Figure 7.36). The difference is in the order of 40%. For higher bias voltages influences of the radiation damage in region 4 are less significant. In proton beams the radiation damage in region 4 largely influences the obtained cluster size, signal and height distributions. Exemplary, the results obtained for $E_{initial}=48$ MeV are shown in Figure 7.37. While for low bias voltages the cluster size, signal and height were found to be decreased in region 4, the situation is more complex at higher bias voltages. At $V_{bias}=10$ V the average cluster size is larger than in the surrounding area, while the cluster signal and height were found to be decreased. At $V_{bias}=15$ V influences of the damage in region 4 on the cluster size and cluster signal distributions are very small, while for the cluster height distributions again decreased values were obtained. Similar findings were obtained in proton beams of $E_{initial}=142$ and 221 MeV (see Appendix B).

Region 5: Mechanical Damage In addition to the radiation damage, the detector suffered from mechanical damage in region 5^a. Due to the radiation damage, some pixels in this area give a wrong signal. To avoid these signals to be included in the measurements, the respective pixels are set to masked mode (see Section 5.2.1 for further explanations).

^aPersonal communication with C. Granja, IEAP, CTU in Prague.

7.1 Characterization of the Detector Response in Therapeutic Ion Beams

In all measurements, no regular clusters with centers of mass located in region 5 were observed. Therefore, the corresponding area in the cluster parameter distributions is blank. The extension of the blank area is correlated to the average cluster size in the surrounding sensor (region 1) for the respective measurement and detector parameters. The larger these clusters are the larger is the observed blank area.

Region 6: Unknown Effect For measurements in carbon ion beams of $E_{\text{initial}}=271 \text{ MeV/u}$ and $V_{\text{bias}}=15 \text{ V}$ an additional effect was observed in the obtained cluster size distribution. In region 6 the average cluster sizes are smaller than in the surrounding area (see Figure 7.35). No distinct effect of this area was observed in the cluster signal or cluster height distributions or for any of the other measurements.

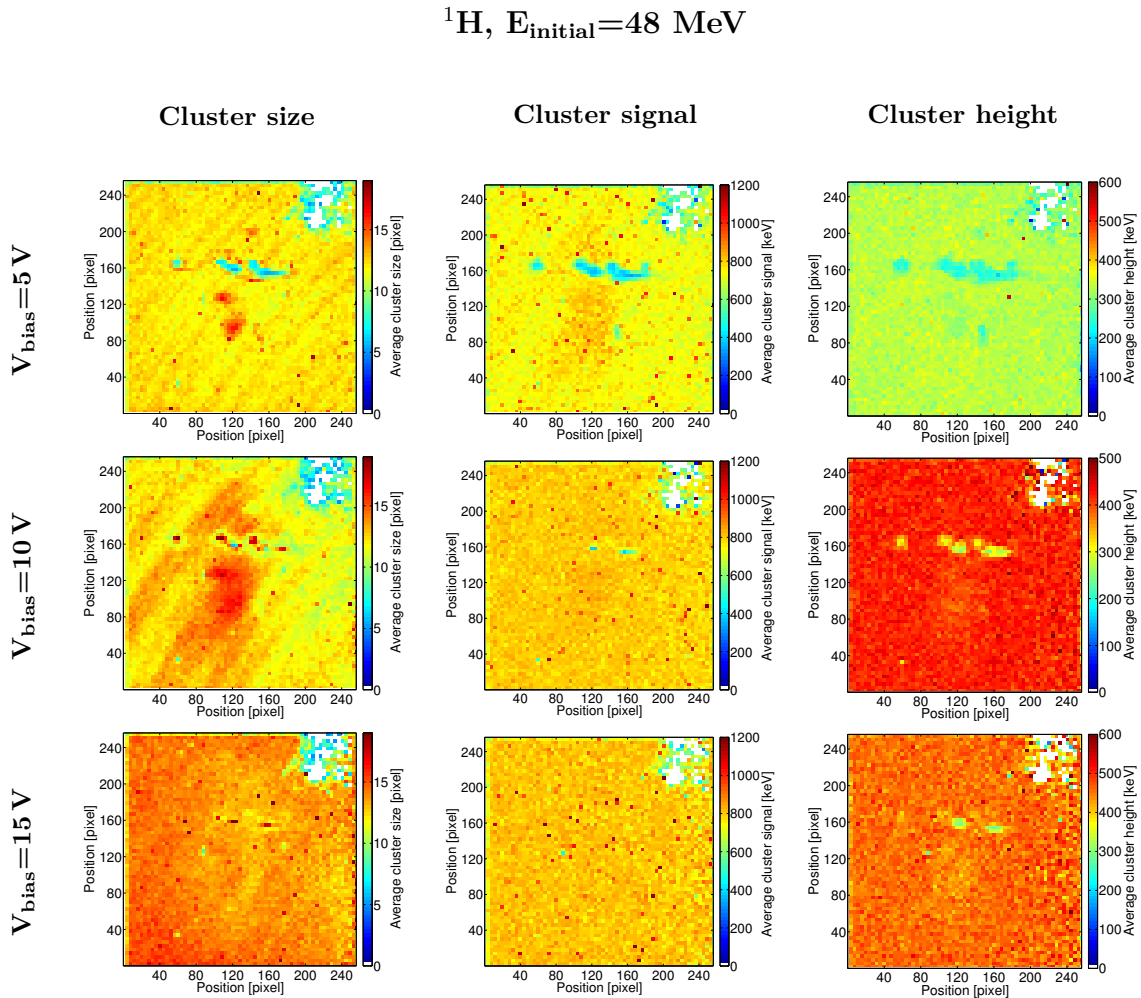


Figure 7.37: Distributions of average cluster size, cluster signal and cluster height over the sensitive detector area for different detector bias voltages. The scales were chosen to enable recognition of the effects described in the text. Further settings: $t_{\text{acq}}=1 \text{ ms}$, $A_{\text{cluster}} \geq 4 \text{ pixel}$, $\text{roundness}_{\text{cluster}} > 0.6625$ at 5% of cluster height.

Consequences for Further Measurements With exception of region 4, the detector response over the sensitive area in terms of cluster signal and cluster height is not influenced by damages of the sensor material. Since the area of region 4 is relatively small, only minor influences on the cluster signal distributions studied for the energy-loss measurements presented in Section 7.2 are expected. Influences of the damages on the cluster size distributions are however large. This needs to be considered in Section 7.3, where besides information on the cluster signal also the cluster size parameter is studied for discrimination between different ion species.

7.1.6 Investigations of Detector Response Changes with Time

Possible changes of the detector response over time, e.g. due to radiation damage in the sensor material, were studied as described in Section 6.1.6. Table 7.1 gives an overview of the ion species and energies studied in four campaigns between October 2011 and January 2013.

Cluster Signal Distributions The cluster signal distributions obtained for measurements in carbon ion beams are shown in Figure 7.38. Table 7.2 lists the corresponding mean cluster signal values and the mean variances. While for carbon ion beams of $E_{\text{initial}}=89 \text{ MeV/u}$ the deviation between the cluster signal distributions obtained in October 2011 and January 2012 are small (the difference in the mean cluster signal is below 0.6%) for the measurement performed in July 2012 a shift of the distribution towards lower values was observed. The corresponding mean cluster signal value is 7.4% smaller than the value obtained in January 2012.

Thereupon, to correct for possible changes in the sensor material, a recalibration of the detector was performed. When applying the new calibration matrices, the signal values of the July 2012 measurements are still lower compared to the previous campaign, the deviation is however decreased to -5.6%. For the measurement performed

Table 7.1: Overview of ion species and energies studied in measurement campaigns to observe changes of the detector response with time.

	^{12}C		^1H	
	89 MeV/u	430 MeV/u	48 MeV	221 MeV
October 2011	✓	✓	x	x
January 2012	✓	✓	✓	✓
July 2012	✓	x	✓	x
January 2013	✓	✓	✓	✓

7.1 Characterization of the Detector Response in Therapeutic Ion Beams

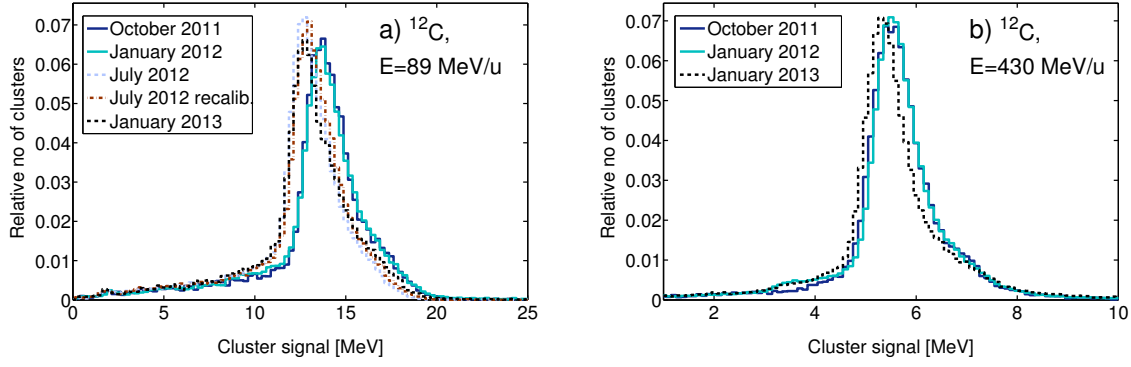


Figure 7.38: Cluster signal distributions obtained at different dates for ^{12}C -ion beams. The distributions are normalized to their areas. For all distributions, the statistical uncertainties in the highest bin are less than 2.9%. Settings: $V_{\text{bias}}=10\text{ V}$, $t_{\text{acq}}=1\text{ ms}$, $A_{\text{cluster}} \geq 30\text{ pixel}$, $\text{roundness}_{\text{cluster}} > 0.7375$ at 10% of cluster height.

in January 2013 again a new calibration of the pixel response was compiled. However no significant change in the cluster signal distribution compared to the measurement performed in July 2012 could be observed. The relative deviation of the mean cluster signal obtained in this campaign (January 2013) to the measurement in January 2012 is -6.2%. For carbon ion beams of $E_{\text{initial}}=430\text{ MeV/u}$ similar results were obtained, as can be seen in Figure 7.38 b) and Table 7.2.

Also in the measurements with proton beams of 48 and 221 MeV similar results were obtained. The corresponding mean cluster signal values are also displayed in Table 7.2. For proton beams of 48 MeV the deviations to the values obtained in January 2012 are -7.7% (July 2012), -5.1% (July 2012, recalibrated) and -3.8% (January 2013). For the higher energetic proton beam studied ($E_{\text{initial}}=221\text{ MeV}$) a relative deviation of the mean cluster signal of -4.7% was observed in January 2013 compared to the measurement in January 2012.

Table 7.2: Mean positions and standard variances of the cluster signal distributions.

E_{initial}	^{12}C		^1H	
	89 MeV/u	430 MeV/u	48 MeV	221 MeV
	Cluster signal _{mean} [MeV]		Cluster signal _{mean} [keV]	
October 2011	14.05 ± 1.05	5.62 ± 0.40	x	x
January 2012	14.13 ± 1.07	5.64 ± 0.36	812.0 ± 69.5	217.5 ± 29.5
July 2012	13.09 ± 0.90	x	749.6 ± 66.1	x
July 2012 recalib.	13.34 ± 0.92	x	770.4 ± 66.7	x
January 2013	13.26 ± 1.04	5.44 ± 0.36	780.8 ± 67.1	207.2 ± 29.5

7 Results

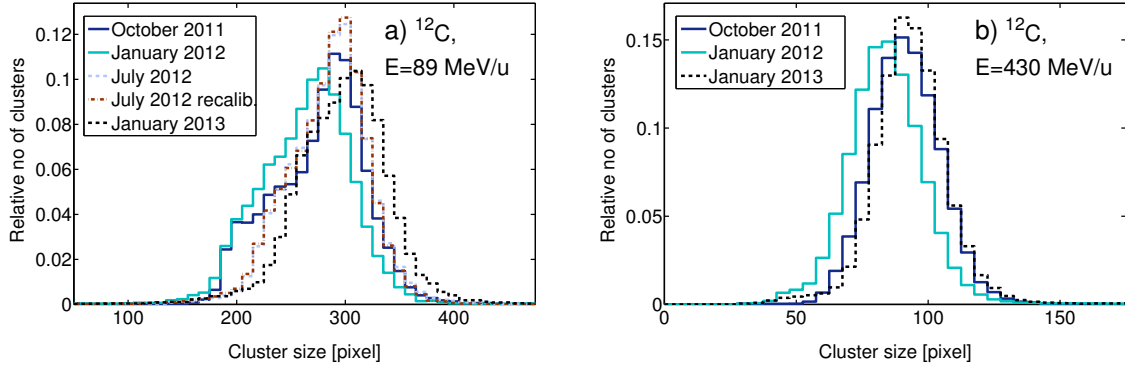


Figure 7.39: Cluster size distributions obtained at different dates for ^{12}C -ion beams. The distributions are normalized to their areas. For all distributions, the statistical uncertainties in the highest bin is less than 3.1%. Settings: $V_{\text{bias}}=10\text{ V}$, $t_{\text{acq}}=1\text{ ms}$, $A_{\text{cluster}} \geq 30\text{ pixel}$, $\text{roundness}_{\text{cluster}} > 0.7375$ at 10% of cluster height.

In summary, the presented results indicate a major change of the detector response between January and July 2012. Changes in the sensitive material can usually be corrected for by recalibrating the detector response. For the device employed in this study, only a partial correction could be achieved upon recalibration. This indicates that the response changes are presumably not solely due to changes in the sensitive material but also influences of changes in the read-out electronics need to be considered.

Cluster Size Distributions The cluster size distributions obtained for measurements in carbon ion beams are shown in Figure 7.39, while in Table 7.3 the corresponding mean cluster sizes and standard variances are listed. Distinct changes of the distributions with time were obtained. For both investigated ion energies the cluster sizes decrease between October 2011 and January 2012, while for later measurements again larger cluster sizes were observed. The largest deviations are found be-

Table 7.3: Mean positions and standard variances of the cluster size distributions.

E_{initial}	^{12}C		^1H	
	89 MeV/u	430 MeV/u	48 MeV	221 MeV
	A_{mean} [pixel]			
October 2011	273.7 ± 35.4	90.8 ± 10.6	x	x
January 2012	263.7 ± 32.3	84.2 ± 10.6	12.2 ± 2.3	4.8 ± 0.8
July 2012	284.5 ± 27.2	x	9.7 ± 1.2	x
July 2012 recalib.	284.5 ± 27.2	x	9.7 ± 1.2	x
January 2013	297.6 ± 29.4	92.7 ± 9.5	10.9 ± 1.7	4.7 ± 0.8

7.1 Characterization of the Detector Response in Therapeutic Ion Beams

tween measurements in January 2012 and January 2013 ($E_{\text{initial}}=89$ MeV/u: 12.9%, $E_{\text{initial}}=430$ MeV/u: 10.1%).

In proton beams of $E_{\text{initial}}=48$ MeV, on average smaller clusters were obtained in July 2012 and January 2013 compared to January 2012. The deviations of the mean cluster sizes listed in Table 7.3 are 20.5% and 10.7%, respectively. For high energetic proton beams only a small decrease of 2.1% in the mean cluster size for measurements in January 2013 compared to measurements in January 2012 was obtained.

Changes of the Uniformity of the Detector Response over the Sensitive Area with Time The changes of the detector response with time are further investigated by studying maps of the cluster parameter distributions over the sensitive area. While in the following only selected results are discussed, an overview of all results obtained in this study can be found in Appendix C.

In Figure 7.40 the cluster signal distributions obtained in carbon ion beams of $E_{\text{initial}}=89$ MeV/u are shown. Measurements were performed in four campaigns be-

Cluster signal distributions for ^{12}C -ions of $E_{\text{initial}}=89$ MeV/u

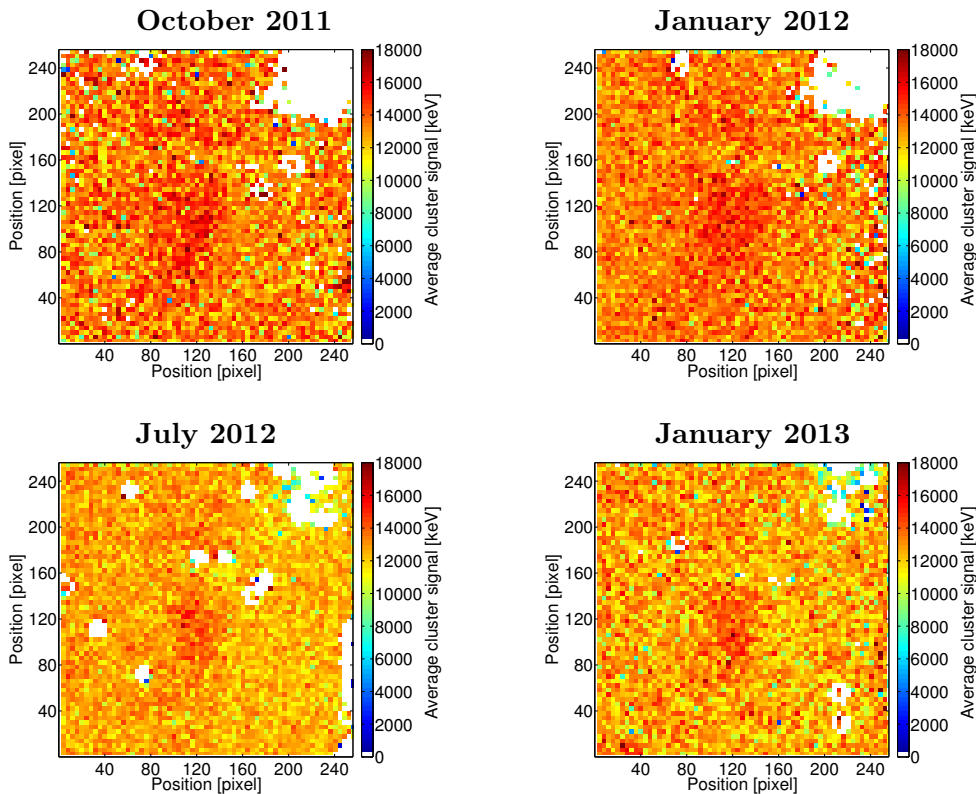


Figure 7.40: Maps showing the distributions of average cluster signal over the sensitive detector area for different measurement dates. The scales were chosen to enable recognition of the effects described in the text. Settings: $V_{\text{bias}}=10$ V, $t_{\text{acq}}=1$ ms, $A_{\text{cluster}} \geq 30$ pixel, $\text{roundness}_{\text{cluster}} > 0.7375$ at 10% of cluster height.

7 Results

tween October 2011 and January 2013. Over the whole detector area a shift of the mean cluster signal towards lower values with time can be seen. This effect is in agreement with the obtained smaller mean cluster signal values for the same measurement campaigns presented in Table 7.2. Furthermore, small circular shaped blank areas were observed, which appear in different positions for the different measurement campaigns. The origin of these areas could not be identified. As described in the previous section, the blank area in the upper right corner of the detector maps corresponds to a region of the sensor which has suffered from mechanical damage.

No regular clusters with centers of mass located in this region are observed. However, the area affected by the mechanical damage gets smaller with time. Also the origin for this effect could not be identified.

Also for higher energetic carbon ion and all investigated proton beams shifts in the mean cluster signals over the whole detector area were observed. Moreover, in all measurements the area affected by mechanical damage was found to get smaller with

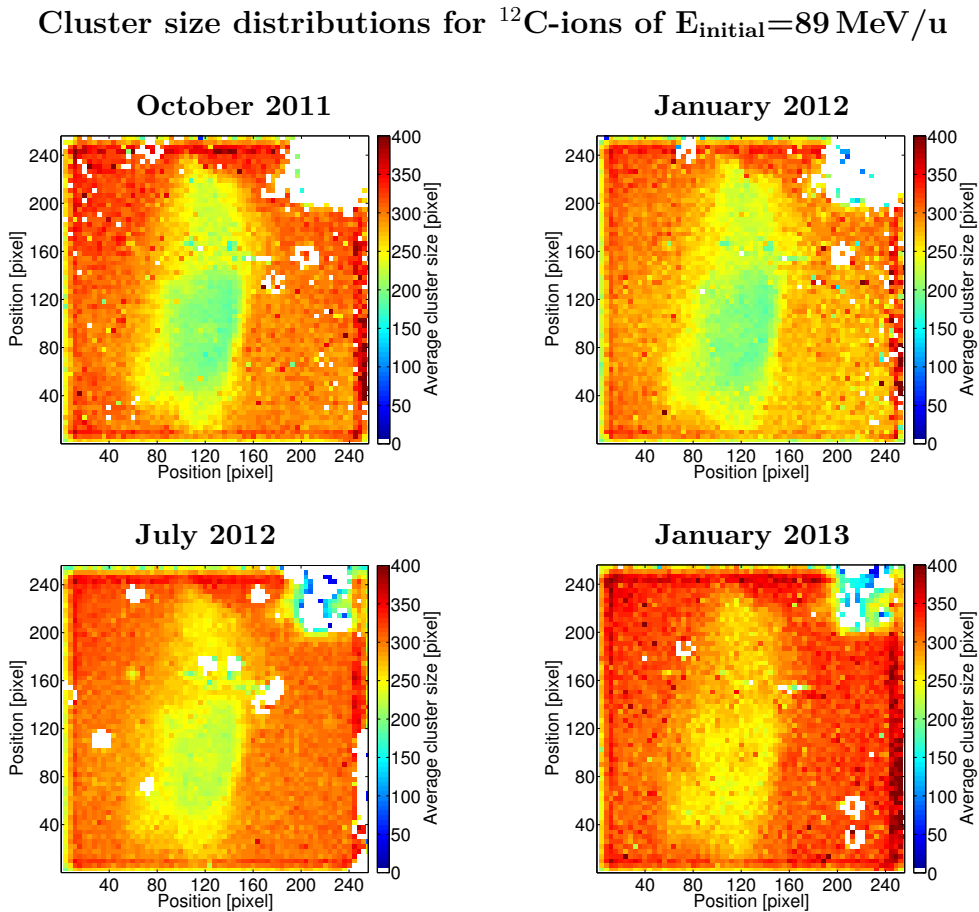


Figure 7.41: Maps showing the distributions of average cluster sizes over the sensitive detector area for different measurement dates. The scales were chosen to enable recognition of the effects described in the text. Settings: $V_{\text{bias}}=10\text{ V}$, $t_{\text{acq}}=1\text{ ms}$, $A_{\text{cluster}} \geq 30\text{ pixel}$, $\text{roundness}_{\text{cluster}} > 0.7375$ at 10% of cluster height.

7.1 Characterization of the Detector Response in Therapeutic Ion Beams

time. No further changes of the uniformity of the cluster signal values over the sensitive area with time were observed.

In the distributions of mean cluster sizes over the sensitive detector area distinct changes with time can be seen. The results for carbon ion beams of $E_{\text{initial}}=89 \text{ MeV/u}$ are shown in Figure 7.41. As discussed for the cluster signal distributions before, also in the cluster size distributions small, circular shaped, blank areas of unknown origin were observed. Moreover, a decrease of the size of the area affected by mechanical damage is clearly visible in the distributions. Differences in the average cluster size between undamaged detector regions and detector regions affected by radiation damage get smaller with time. These changes are consistent with healing of the radiation damages. Parameters influencing the healing process are the time itself, further radiation the detector was exposed to and temperature. Moreover, a change of the cluster size can be seen in the region previously defined as region 6 (lower right corner in the maps). While in this area larger clusters compared to the surrounding region were observed in the measurements of October 2011 and January 2012, in July 2012 no clusters could be detected there. For January 2013, in contrast, especially large mean cluster size values can be seen in this region. For all effects, similar trends were observed for carbon ions of $E_{\text{initial}}=430 \text{ MeV/u}$.

Also in proton beams of $E_{\text{initial}}=48 \text{ MeV}$ changes of the distributions of mean cluster sizes over the sensitive detector area with time could be observed. The distributions are shown in Figure 7.42. While changes in the area influenced by the mechanical damage in the upper right corner and in the areas affected by radiation damage are consistent with the observations made in carbon ion beams, additional effects can be seen in the undamaged detector region. Overall, the cluster size in this area is shifted to

Cluster size distributions for protons of $E_{\text{initial}}=48 \text{ MeV}$

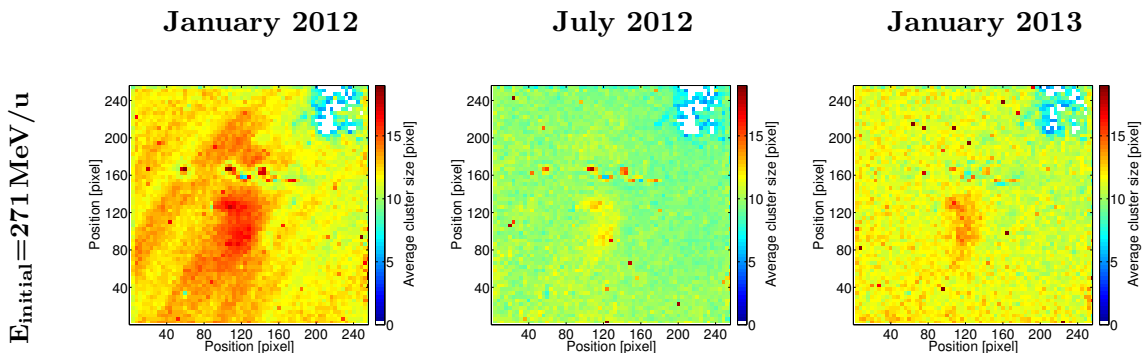


Figure 7.42: Maps showing the distributions of average cluster size over the sensitive detector area for different measurement dates. The scales were chosen to enable recognition of the effects described in the text. Settings: $V_{\text{bias}}=10 \text{ V}$, $t_{\text{acq}}=1 \text{ ms}$, $A_{\text{cluster}} \geq 4 \text{ pixel}$, $\text{roundness}_{\text{cluster}} > 0.6625$ at 5% of cluster height.

smaller values for the measurements in July 2012 compared to January 2012, while in January 2013 again larger clusters were detected. These changes are in agreement with the corresponding mean cluster size values listed in Table 7.3. Moreover, influences of the tree ring-pattern are less prominent in later measurements.

In measurements of higher energetic proton beams in the cluster size distributions the regions influenced by radiation and mechanical damage show similar tendencies as described for low energy proton beams. No further changes of the distribution with time were observed.

7.2 Energy-Loss Measurements

As described in Section 5.2.4, the energy response of the Timepix detector is calibrated in photon beams. No detailed analysis of the detector response to ion beams of therapeutically used energy ranges has been published before. It is therefore unknown, to what extent the calibration curve is also valid for these ions. Therefore, the scope of this section is to investigate the response of the Timepix detector to irradiation with different ion species and energies and to analyze the potential of the detector for direct particle energy-loss measurements on a single ion basis. The experimental set-ups and parameters used for the experiments are described in Section 6.2.

7.2.1 Measurements of the Mean Energy-Loss Free-in-Air and in Vacuum

High Energy Protons (Crossing) The measured cluster signal distributions for proton beams over the whole range of therapeutically used initial energies are presented in Figure 7.43 a). To limit the statistical uncertainties of the measurement, at least 195,000 clusters are included in each distribution. Distinct differences between the distributions obtained at different energy levels can be seen. The lower the initial proton energy is the higher is the mean cluster signal due to the increasing energy deposition in the sensitive detector layer. This finding is in agreement with theoretical expectations according to the Bethe-Bloch-equation. The shapes of the distributions including changes with the initial particle energy are studied in detail in Section 7.2.2.

In Figure 7.43 b) the measured distributions are evaluated quantitatively by comparing the mean cluster signal values to the calculated mean energy-loss. To determine the mean cluster signal values only histogram bins with a height of at least 25% of the maximum bin height in the respective distribution were considered. In this way, clusters due to particles arriving at the end of the measurement frame and therefore having a reduced signal as well as clusters due to secondary radiation passing the size constraint are excluded from the analysis. Deviations between the measured mean cluster signal

High Energy Protons

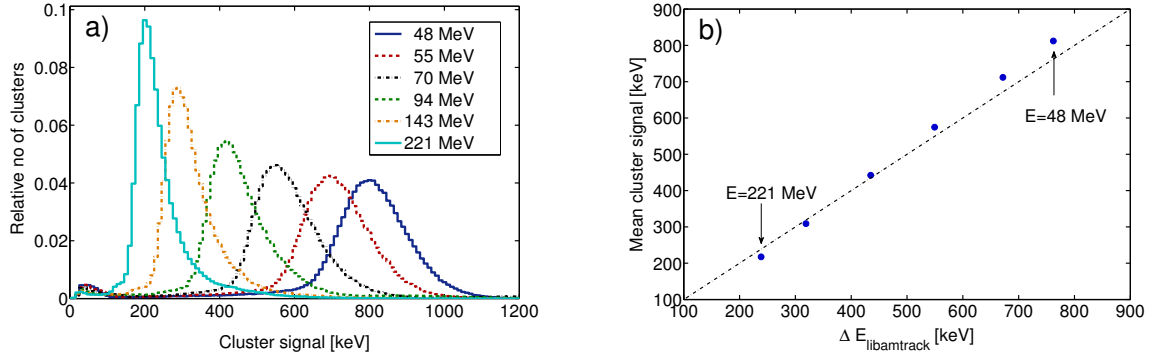


Figure 7.43: a) Cluster signal distributions obtained in proton beams of different initial energies. b) Direct comparison of the mean cluster signal values to calculated energy-loss values. The statistical uncertainties of the mean cluster signal values are smaller than the symbol size. Settings: $t_{\text{acq}}=1$ ms, $V_{\text{bias}}=10$ V, $A_{\text{cluster}} \geq 4$ pixel, $\text{roundness}_{\text{cluster}} > 0.6625$ at 5% of cluster height.

values and the mean energy-loss values calculated with libamtrack are between +6.6% ($E_{\text{initial}}=48$ MeV) and -8.8% ($E_{\text{initial}}=221$ MeV). A tendency for an overestimation of the values in the measurement can be seen towards lower initial proton energies, i.e. higher energy depositions.

In the study presented in Section 7.1.2, the mean cluster signal obtained in proton measurements was found to increase with the bias voltage up to $V_{\text{bias}} \simeq 19$ V. This effect was assigned to an incomplete collection of charge carriers due to recombination in the non-depleted sensor zone, which is, depending on the initial ion energy, partly compensated by induced charge. To test influences of an increased bias voltage on

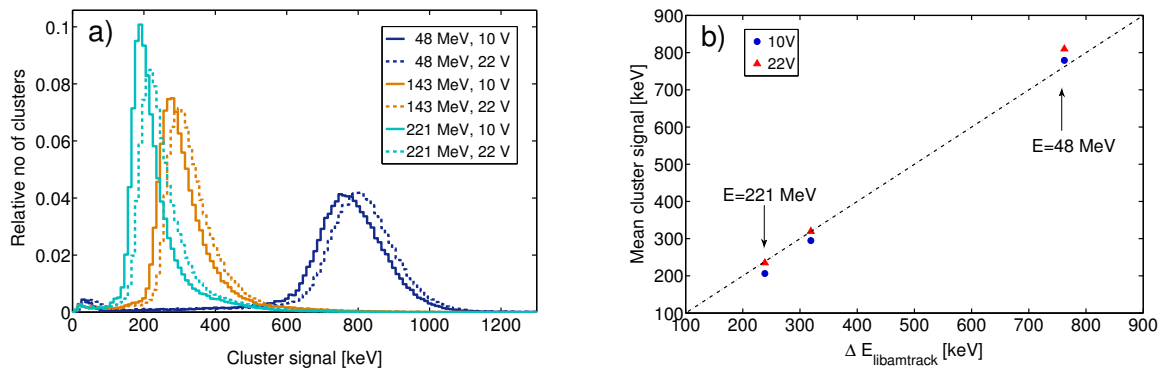
High Energy Protons, different V_{bias} 

Figure 7.44: a) Cluster signal distributions obtained in proton beams of different initial energies at detector bias voltages of 10 and 22 V. b) Direct comparison of the mean cluster signal values to calculated energy-loss values. The statistical uncertainties of the mean cluster signal values are smaller than the symbol size. Further settings: $t_{\text{acq}}=1$ ms, $V_{\text{bias}}=10$ V or 22 V, $A_{\text{cluster}} \geq 4$ pixel, $\text{roundness}_{\text{cluster}} > 0.6625$ at 5% of cluster height.

7 Results

the mean cluster signal in comparison to the calculated mean energy-loss, additional measurements at $V_{\text{bias}}=10$ and 22 V were performed. The obtained cluster signal distributions are shown in Figure 7.44 a). For all investigated energies the cluster signal distributions are shifted to higher values when the detector bias voltage is increased to 22 V. The direct comparison of the obtained mean cluster signals with the calculated mean energy-loss in Figure 7.44 b) shows a deviation of -13.5% at $V_{\text{bias}}=10$ V and of -1.5% at $V_{\text{bias}}=22$ V for high initial proton energies, i.e. small energy-loss values. At the lowest initial energy investigated the deviations are +2.2% for $V_{\text{bias}}=10$ V and +6.3% at $V_{\text{bias}}=22$ V. Please note that the measurements presented in Figure 7.44 were performed in another campaign than the measurements shown in Figure 7.43. Therefore, the results for the same ion energy and detector settings vary (see further investigations on changes of the detector response with time in Section 7.1.6).

Low Energy Protons and Deuterium (Stopping) The cluster signal distributions measured in low energy proton and deuterium beams are shown in Figure 7.45. Plot a) shows the results obtained at a detector bias voltage of 10 V. Distinct peaks were obtained for protons of 0.55 and 1 MeV and for deuterium ions of 0.5 MeV/u. In addition, in all measurements clusters with higher signal can be seen. They contain the overlapping signal of two ions. Furthermore, for all investigated ion species and energies, a high number of clusters with relatively small signal was observed.

A direct comparison of the obtained mean cluster signal values with the theoretically expected energy-loss is shown in Figure 7.45 b). In addition to the measurements shown in Plot a), measurements performed at $V_{\text{bias}}=22$ V are included for comparison. To determine the mean cluster signal values, only bins with a height of at least 25%

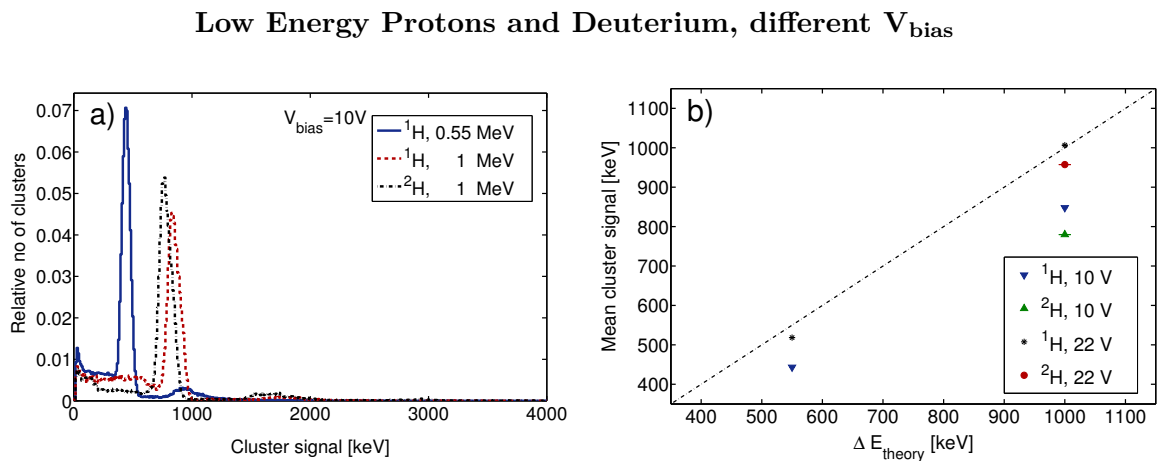


Figure 7.45: a) Cluster signal distributions obtained in ^1H - and ^2H -ion beams of different initial energies. b) Direct comparison of the mean cluster signal values to the theoretical energy-loss values. The statistical uncertainties of the mean cluster signal values are smaller than the symbol size. Settings: $t_{\text{acq}}=1$ ms, $V_{\text{bias}}=10$ V or 22 V, $A_{\text{cluster}} \geq 4$ pixel, $\text{roundness}_{\text{cluster}} > 0.6625$ at 5% of cluster height.

of the maximum bin height in the respective distribution were considered. At a given projectile energy, a smaller deviation can be seen for ^1H - compared to ^2H -ions. For a proton energy of 0.55 MeV/u the deviation between measurement and theory amounts to -19.4%. For the higher proton energy studied (1 MeV) a reduced deviation of -15.2% was obtained, while for ^2H of the same energy the deviation is -22.0%. Moreover, the deviations from the theoretically expected value are smaller at $V_{\text{bias}}=22\text{ V}$ compared to $V_{\text{bias}}=10\text{ V}$ (^1H , 0.55 MeV: -5.7%, ^1H , 1 MeV: 0.6%, ^2H , 1 MeV: -4.3%).

Low Energy Lithium Ions (Stopping) While up to now primary lithium ion beams are of no relevance for patient treatment, they are part of the fragment spectra evolving from irradiations with primary carbon ion beams. Therefore, the detector response to lithium ions was investigated as described in Section 6.2.1. The energy of the ions when entering the detector was calculated to be 3.3 and 4.7 MeV/u, respectively. The measured cluster signal distributions are shown in Figure 7.46 a). For both measurements distinct peaks can be seen. However, there is also a considerable number of clusters showing a relative high signal leading to an extension of the cluster signal distributions towards higher values. The signal of these clusters is most likely influenced by oscillation effects of the detector electronics (overshoot effects) due to the very high energy deposition of the lithium ions. This effect is described in detail in Section 7.1.1. Moreover, in the distributions shown in Figure 7.46 a) clusters with signals smaller than corresponding to the peak area can be seen. These clusters are due to particles arriving at the end of the acquisition time.

The comparison of the obtained mean cluster signal values and the theoretically expected energy-loss is shown in Figure 7.46 b). To determine the mean cluster signal

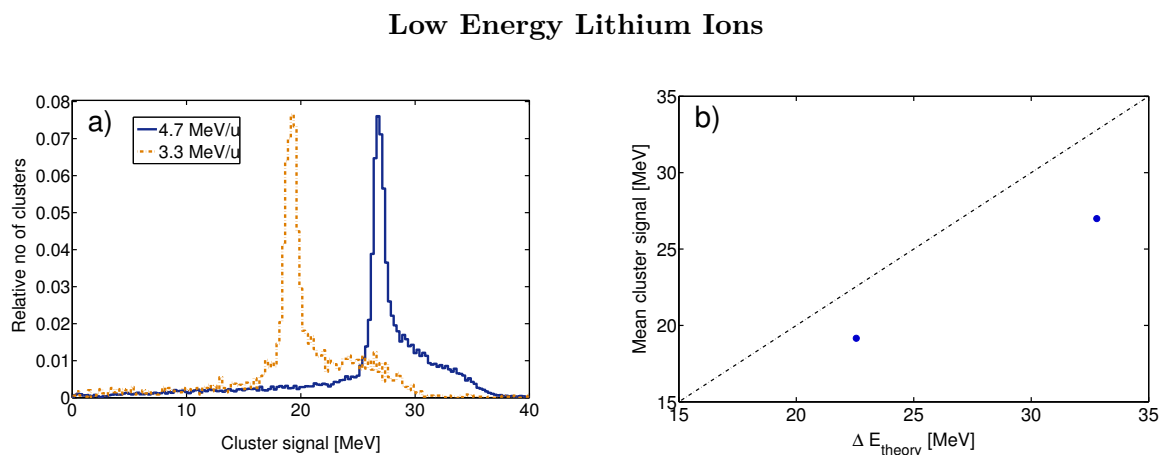


Figure 7.46: a) Cluster signal distributions obtained in ^7Li -ion beams of different initial energies. b) Direct comparison of the mean cluster signal values to calculated energy-loss values. The statistical uncertainties of the mean cluster signal values are smaller than the symbol size. Settings: $t_{\text{acq}}=1\text{ ms}$, $V_{\text{bias}}=10\text{ V}$, $A_{\text{cluster}} \geq 30\text{ pixel}$, $\text{roundness}_{\text{cluster}} > 0.7375$ at 10% of cluster height.

7 Results

values, only bins in the cluster signal distribution with a height of at least 25% of the maximum bin height were considered. In this way, clusters due to particles arriving at the end of the acquisition time and clusters influenced by oscillation effects were excluded from the calculation. For both investigated ion energies the measured mean cluster signal is considerably lower than the expected signal indicating influences of signal quenching in the detector. The deviations amount to -15.0% ($E=3.3$ MeV/u) and -17.7% ($E=4.7$ MeV/u).

High Energy Carbon Ions (Crossing) The detector's capability of energy-loss measurements in carbon ion beams over the complete range of initial energies used therapeutically was studied. The measured cluster signal distributions are presented in Figure 7.47 a). The lower the initial carbon ion energy is, the higher are the cluster signal values due to the increasing energy deposition in the sensitive detector layer. The shape of the cluster signal distributions is studied in detail in Section 7.2.2.

Figure 7.47 b) shows the comparison of the obtained mean cluster signal values with the calculated mean energy-loss. To determine the mean cluster signal values again only bins with a height of at least 25% of the maximum bin height in the respective distribution were considered. For all investigated energy levels, the measured mean cluster signal values are lower than the expected values. The deviation amounts to -6.8% for carbon ions of $E_{\text{initial}}=430$ MeV/u and increases up to -17.6% for carbon ions of $E_{\text{initial}}=89$ MeV/u.

Also for carbon ions, measurements at $V_{\text{bias}}=10$ and 22 V were compared. The study of dependencies of the detector response on the bias voltage presented in Section 7.1.2 showed a decrease of the mean cluster signal with increasing bias voltage for carbon ions of $E_{\text{initial}}=89$ MeV/u, while for $E_{\text{initial}}=430$ MeV/u the mean cluster signal value

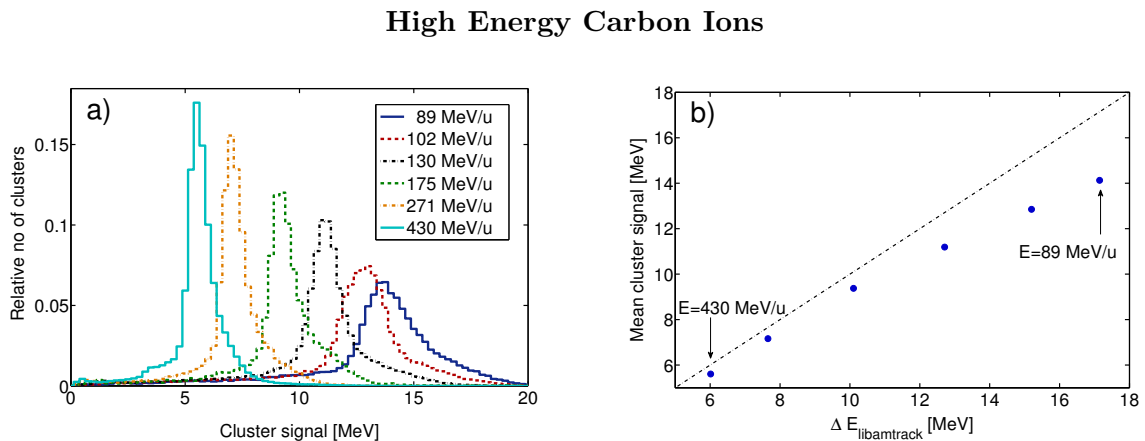


Figure 7.47: a) Cluster signal distributions obtained in ^{12}C -ion beams of different initial energies. b) Direct comparison of the mean cluster signal values to calculated energy-loss values. The statistical uncertainties of the mean cluster signal values are smaller than the symbol size. Settings: $t_{\text{acq}}=1$ ms, $V_{\text{bias}}=10$ V, $A_{\text{cluster}} \geq 30$ pixel, $\text{roundness}_{\text{cluster}} > 0.7375$ at 10% of cluster height.

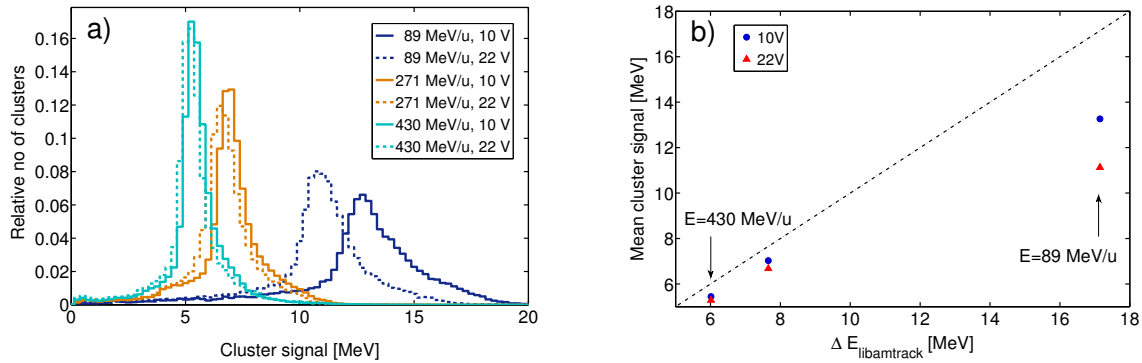
High Energy Carbon Ions, different V_{bias} 

Figure 7.48: a) Cluster signal distributions obtained in ^{12}C -ion beams of different initial energies at detector bias voltages of 10 and 22 V. b) Direct comparison of the mean cluster signal values to calculated energy-loss values. The statistical uncertainties of the mean cluster signal values are smaller than the symbol size. Further settings: $t_{\text{acq}}=1$ ms, $A_{\text{cluster}} \geq 30$ pixel, $\text{roundness}_{\text{cluster}} > 0.7375$ at 10% of cluster height.

was found to increase up to a bias voltage of 10 V and subsequently also to decrease. This effect was assigned to saturation effects.

The cluster signal distributions for $V_{\text{bias}}=10$ and 22 V presented in Figure 7.48 a) show that for all investigated carbon ion energies the cluster signal distributions are shifted towards lower values when the detector bias voltage is increased from 10 to 22 V, what is consistent with the results presented in Section 7.1.2. The direct comparison of the mean cluster signal values to the calculated mean energy-loss in Figure 7.48 b) shows for all investigated energies larger deviations at $V_{\text{bias}}=22$ V. While for $E_{\text{initial}}=271$ and 430 MeV/u the differences are in the order of -10%, a significantly larger difference can be seen for $E_{\text{initial}}=89$ MeV/u. For $V_{\text{bias}}=10$ V the deviation to the calculated mean energy-loss value amounts to -22.7%, while for $V_{\text{bias}}=22$ V it is -35.1%. The presented observations are consistent with signal quenching, which is known to increase with an increasing charge collected by the single pixel, since for a higher bias voltage the signal in the cluster is concentrated to less pixels. Like for protons, also for carbon ions the measurements presented in Figure 7.48 were performed in another campaign than the measurements shown in 7.47. Therefore, the results for the same ion energy and detector settings vary (see further explanations in Section 7.1.6).

High Energy Oxygen Ions (Crossing) In addition to high energy proton and carbon ion beams currently used for patient treatment at HIT, the detector's capability of energy-loss measurements in high energy oxygen ions, as a future candidate for patient treatment, was investigated. The measured cluster signal distributions are shown in Figure 7.49 a). The agreement of the shape of the cluster signal distributions to calculated energy-loss distributions is studied in detail in the next section. When

High Energy Oxygen Ions

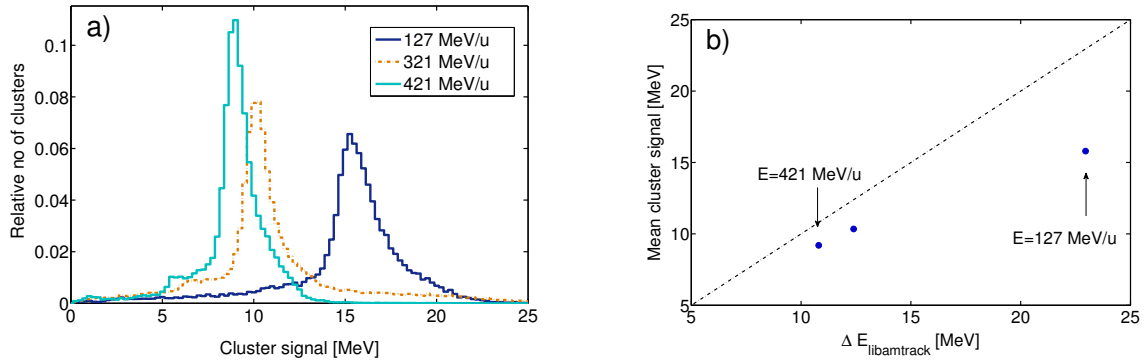


Figure 7.49: a) Cluster signal distributions obtained in ^{16}O -ion beams of different initial energies. b) Direct comparison of the mean cluster signal values to the calculated energy-loss. The statistical uncertainties of the mean cluster signal values are smaller than the symbol size. Settings: $t_{\text{acq}}=1$ ms, $V_{\text{bias}}=10$ V, $A_{\text{cluster}} \geq 30$ pixel, $\text{roundness}_{\text{cluster}} > 0.7375$ at 10% of cluster height.

comparing the mean cluster signal values (determined as described before for carbon ions) to calculated energy-loss values, large deviations of up to -31.2% are obtained, as can be seen in Figure 7.49 b). Therefore, also for oxygen ions, the measurements are largely influenced by signal quenching effects in the detector. These results were anticipated, since for the studied oxygen ions the energy deposition in the detector can be even higher than for the investigated carbon ions.

7.2.2 Energy-Loss Straggling - Comparison of Measurements and Calculations

While in the previous section the mean values of the cluster signal obtained in the measurements were compared to the calculated mean energy-loss, in this section the shape of the measured cluster signal distributions are analyzed. For comparison, calculated energy-loss distributions are used. They were derived as described in Section 6.2.2.

High Energy Protons In Figure 7.50 the measured cluster signal distributions for the lowest and highest investigated proton energy ($E_{\text{initial}}=48$ and 221 MeV) are compared to energy-loss distributions which were calculated according to the Vavilov theory. For the lower energy, the measured distribution is approximately Gaussian shaped, while for the higher energy the distribution resembles a Landau distribution with a tail towards high values. These results are in agreement with expectations from theory (see Section 2.1.2). For both energies, the extension of the measured distributions to lower signal values, compared to the calculated distributions, can be assigned to particles arriving at the end of the acquisition time (see Section 7.1.1) and secondary radiation (see Section 7.1.3). Besides these effects, the general shapes of the measured distribu-

High Energy Protons

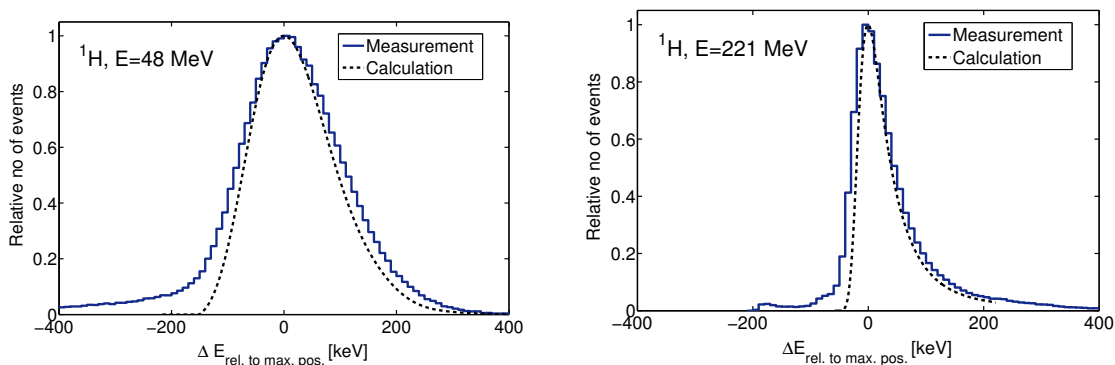


Figure 7.50: Comparison of measured cluster signal distributions and calculated energy-loss distributions (Vavilov theory) for proton beams of the lowest and highest initial energy available at HIT. The distributions are normalized to their maximum values and the positions of the maxima are shifted to zero. Settings: $t_{\text{acq}}=1$ ms, $V_{\text{bias}}=10$ V, $A_{\text{cluster}} \geq 4$ pixel, $\text{roundness}_{\text{cluster}} > 0.6625$ at 5% of cluster height.

tions follow the trends of the calculated distributions. An overview of all investigated energies can be found in Appendix D.

The measured distributions are however systematically wider than the calculated distributions. A quantitative comparison of the full-width-half-maximum values of the measured and calculated energy-loss distributions is shown in Figure 7.51 a). The relative deviations between the widths in dependence of the calculated energy-loss are displayed in Figure 7.51 b). They are between 5.8 and 16.7%. No tendency of the relative deviations with increasing energy-loss in the detector was observed.

High Energy Protons

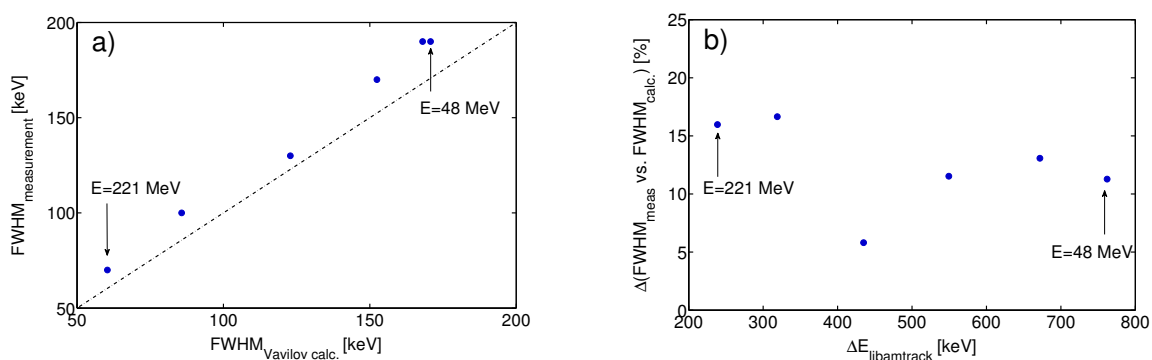


Figure 7.51: a) Quantitative comparison of the full-width-half-maximum of measured cluster signal and calculated energy-loss distributions in the sensitive detector layer for proton beams of different initial energies. The statistical uncertainties of the measured values are smaller than the symbol size. b) Relative deviations between the widths of measured and calculated energy-loss distributions in dependence of the calculated mean energy-loss. Settings: $t_{\text{acq}}=1$ ms, $V_{\text{bias}}=10$ V, $A_{\text{cluster}} \geq 4$ pixel, $\text{roundness}_{\text{cluster}} > 0.6625$ at 5% of cluster height.

High Energy Carbon Ions A similar analysis of the cluster signal distributions as for protons was performed in carbon ion beams. The cluster signal distributions for the lowest and highest investigated energies ($E_{\text{initial}}=89$ and 430 MeV/u) are presented in Figure 7.52. The agreement of the measured distributions with calculations changes with the initial ion energy. For the lower energy studied, the FWHM of the measured distribution is more than two times larger than for the calculated distribution. Several effects can explain the shape of the measured distribution:

- Overshoot effects in the detector electronics (see Section 6.1.1) due to the high energy deposition in the sensitive detector layer can lead to an extension of the distribution towards higher values.
- Particles arriving towards the end of the acquisition time lead to a tail in the cluster signal distribution towards low signals due to insufficient time for digitization of the complete signal. This effect is especially significant for a low particle energy with a high energy deposition in the detector and the corresponding higher cluster signal.
- For the given carbon ion energy, the cluster signal was found to be influenced by energy-loss dependent signal quenching (see Section 7.1.2). In Figure 7.52 the signal quenching is not directly recognizable, as the maxima position of the measured and calculated distributions were superimposed. The comparison of measured and calculated mean energy-loss values in the previous section however showed a significantly decreased value in the measurement.

The cluster signal distribution obtained for the highest carbon ion energy shows a good agreement to the calculated distribution around the most probable energy-loss value (peak area). However, extensions towards low and high cluster signal values can

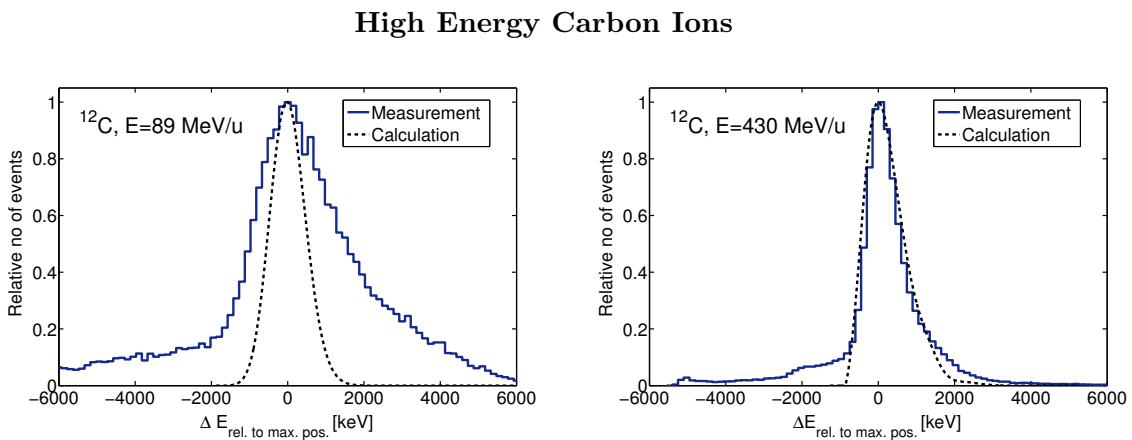


Figure 7.52: Comparison of measured cluster signal distributions and calculated energy-loss distributions for ^{12}C -ion beams of the lowest and highest initial energies available at HIT. Settings: $t_{\text{acq}}=1$ ms, $V_{\text{bias}}=10$ V, $A_{\text{cluster}} \geq 30$ pixel, $\text{roundness}_{\text{cluster}} > 0.7375$ at 10% of cluster height.

High Energy Carbon Ions

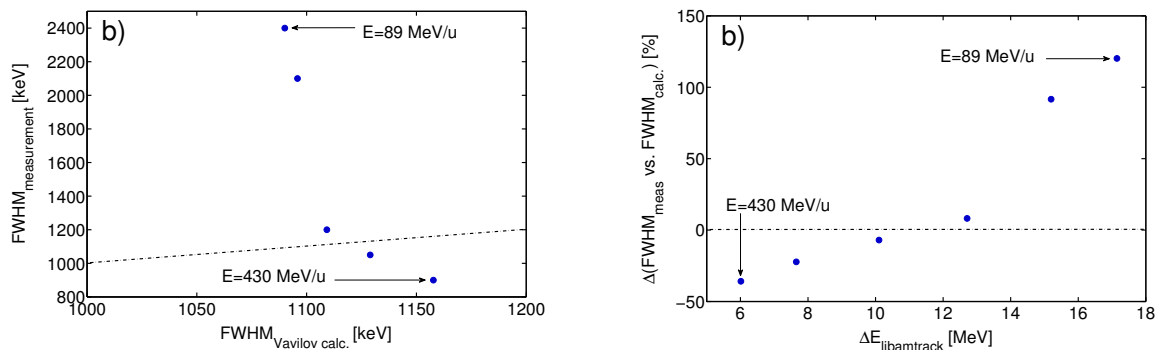


Figure 7.53: a) Direct comparison of the widths (FWHM) of measured cluster signal and calculated energy-loss distributions for ^{12}C -ion beams of different initial energies. The statistical uncertainties of the measured values are smaller than the symbol size. The dash-dotted line marks equal values for $\text{FWHM}_{\text{Vavilov calc.}}$ and $\text{FWHM}_{\text{measurement}}$. b) Relative deviations between the widths of measured and calculated distributions in dependence of the calculated mean energy-loss values. Settings: $t_{\text{acq}}=1\text{ ms}$, $V_{\text{bias}}=10\text{ V}$, $A_{\text{cluster}} \geq 30\text{ pixel}$, $\text{roundness}_{\text{cluster}} > 0.7375$ at 10% of cluster height.

be seen in the measurement. The reasons for the measured low cluster signal values are particles arriving towards the end of the acquisition time, while the high cluster signals are caused by oscillation effects in the detector electronics, as shown in Section 7.1.1. The results for all carbon ion energies studied can be found in Appendix D.

For all investigated carbon ion energies, a quantitative comparison of the measured and calculated FWHM values of the distributions is shown in Figure 7.53 a). Figure 7.53 b) shows the relative deviations between measured and calculated values in dependence of the corresponding calculated mean energy-loss. While for the lowest investigated initial carbon ion energy, i.e. the particles with the highest mean energy-loss, the measured distribution is about 120% wider than the calculated one, for higher initial carbon ion energies the deviations decrease. They approach an agreement at a mean energy-loss value of approximately 11.5 MeV, corresponding to an initial carbon ion energy between 175 and 271 MeV/u. For even higher initial ion energies a narrower distribution is found in the measurements compared to the calculations. The deviations amount to up to -36% for the highest carbon ion energy studied.

High Energy Oxygen Ions For high energy oxygen ion beams the measured cluster signal distributions are compared to calculated energy-loss distributions for three initial energies (127, 321, and 421 MeV/u). The chosen energies cover the whole range of primary oxygen ion energies currently available at HIT. The results shown in Figure 7.54 are similar to the findings in carbon ion beams. Again, the measured distributions show extensions towards low values due to particles arriving towards the end of the acquisition time and towards higher values due to oscillation effects in the pixel electronics.

High Energy Oxygen Ions

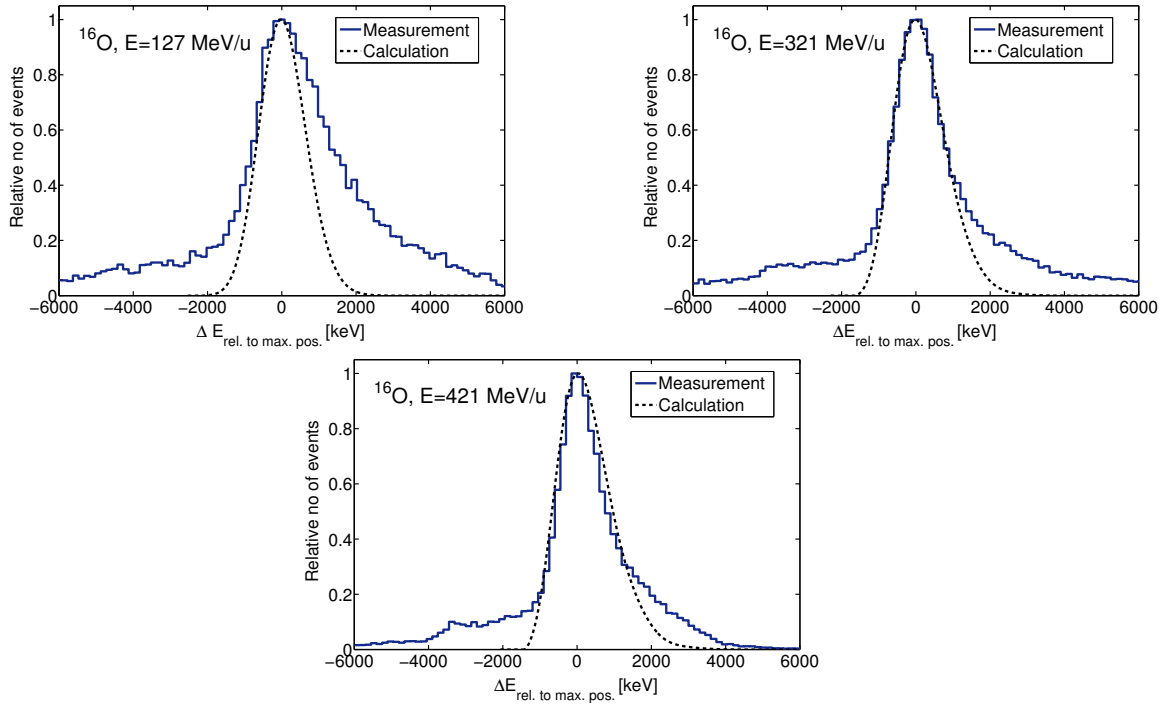


Figure 7.54: Comparison of measured cluster signal and calculated energy-loss distributions for ^{16}O -ion beams of different initial energies. Settings: $t_{\text{acq}}=1$ ms, $V_{\text{bias}}=10$ V, $A_{\text{cluster}} \geq 30$ pixel, $\text{roundness}_{\text{cluster}} > 0.7375$ at 10% of cluster height.

High Energy Oxygen Ions

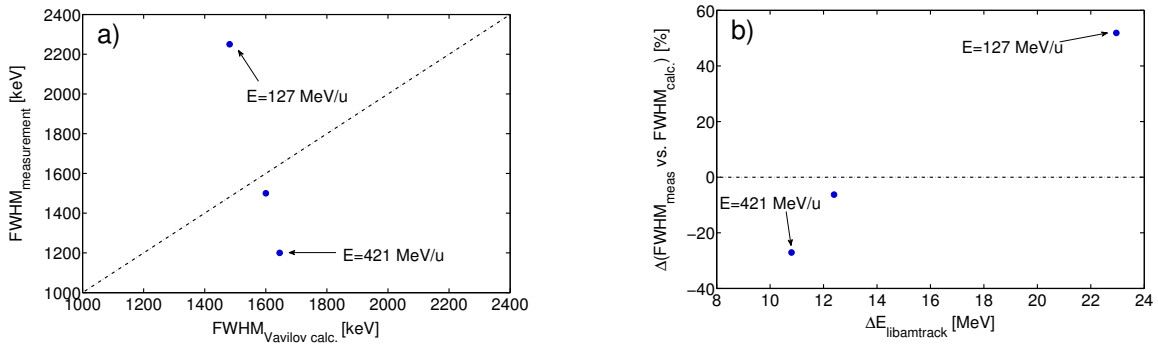


Figure 7.55: a) Quantitative comparison of the widths (FWHM) of measured cluster signal and calculated energy-loss distributions for ^{16}O -ion beams of different initial energies. The statistical uncertainties of the measured values are smaller than the symbol size. b) Relative deviations between the widths of measured and calculated distributions in dependence of the calculated mean energy-loss. Settings: $t_{\text{acq}}=1$ ms, $V_{\text{bias}}=10$ V, $A_{\text{cluster}} \geq 30$ pixel, $\text{roundness}_{\text{cluster}} > 0.7375$ at 10% of cluster height.

While for low initial energies the measured distribution is 51.9% wider than the calculated one (regarding the FWHM), for medium and high initial energies an agreement of the widths within 27% can be seen. The direct comparison between measured and calculated full-width-half-maximum-values is presented in Figure 7.55.

7.2.3 Measurements in Different Material Depths

In addition to the measurements free in air and in vacuum presented in the previous sections, for carbon ion beams measurements were also performed in different phantom (PMMA) depths. In this way, the detector's ability for energy-loss measurements of even slower carbon ions, as present in many fragmentation studies, is tested. The employed set-up and parameter values are described in Section 6.2.3.

An initial carbon ion energy of 271 MeV/u was used. The cluster signal distributions measured behind PMMA blocks of 0, 5, 10, 11, 12, and 12.7 cm were studied. They are shown in Figure 7.56 a). The more material there is in the beam path, the slower the ions are when reaching the detector. Therefore, the thicker the phantom in front of the detector, the higher is the measured mean cluster signal. At the same time, the cluster signal distributions become significantly wider with increasing material depths, due to an increasing effect of energy-loss straggling. Furthermore, the relative number of clusters showing signal values below the main peak increases. Besides clusters due

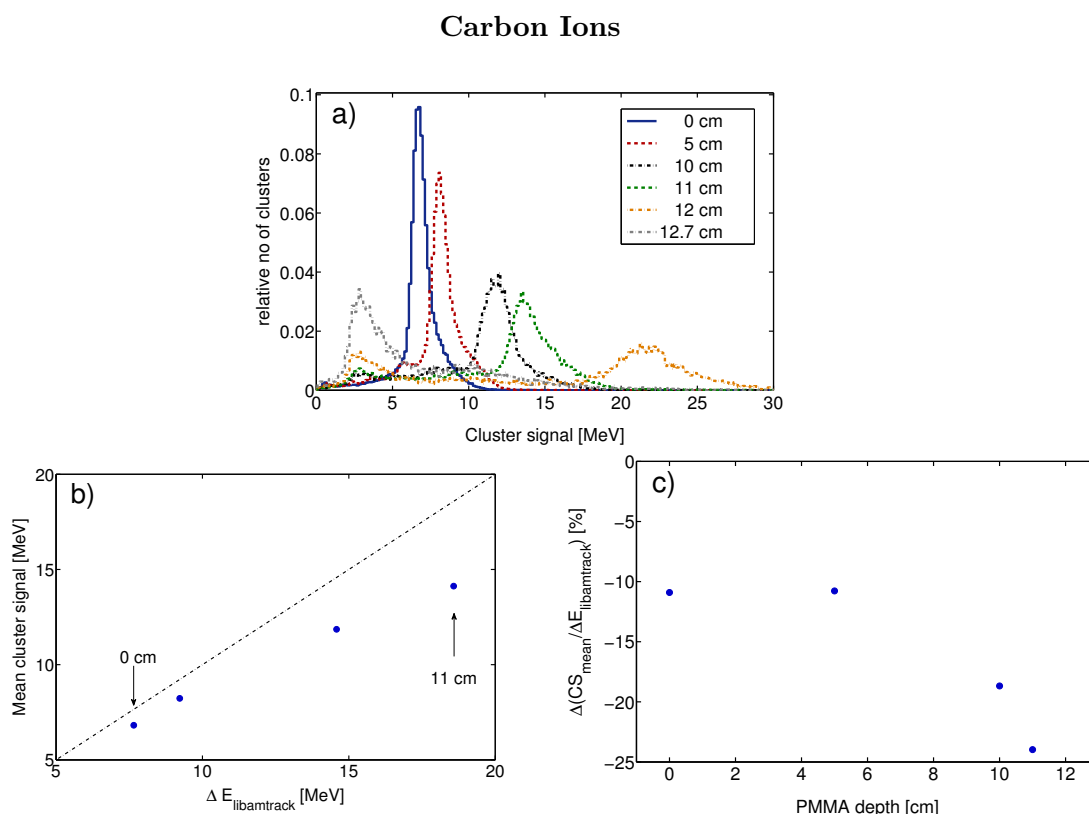


Figure 7.56: a) Cluster signal distributions obtained in ^{12}C -ion beams of $E_{\text{initial}}=271$ MeV/u behind PMMA blocks of different thicknesses. b) Direct comparison of the obtained mean cluster signal (CS_{mean}) values to calculated energy-loss values. The statistical uncertainties are smaller than the symbol size. The measurements behind 120 and 127 mm PMMA were not considered in the analyses (see explanation in the text). c) Relative deviation between measured mean cluster signal and calculated mean energy-loss in dependence of the PMMA depth. Settings: $t_{\text{acq}}=1$ ms, $V_{\text{bias}}=10$ V, $A_{\text{cluster}} \geq 30$ pixel, $\text{roundness}_{\text{cluster}} > 0.7375$ at 10% of cluster height.

7 Results

to carbon ions arriving at the end of the acquisition time (see Section 7.1.1), a part of these clusters is due to high energy secondary target fragments produced in the PMMA. Since the fragments are lighter but still travel with approximately the same velocity, i.e. the same energy per nucleon, as the primary particles, they deposit less energy in the detector than the primary ions (see Section 2.2.2).

To determine the mean cluster signal values, only bins in the distribution with a height of at least 25% of the respective maximum bin height were considered. In this way, signal influenced by ions arriving at the end of the acquisition time and detector artefacts (see Section 7.1.1) as well as secondary electrons (see Section 7.1.3) is excluded from the calculation. Nonetheless, in the vicinity of the Bragg peak the high number of clusters due to secondary particles largely influences the mean cluster signal determination. Therefore, a comparison of the mean cluster signal values to calculated energy-loss values is only possible for material depths of up to 11 cm.

For all investigated positions the measured mean cluster signal is smaller than the expected energy-loss value. The deviations increase from -10.9% in 5 cm PMMA depth to up to -24.0% in 11 cm PMMA depth, as can be seen in Figure 7.56 b) and c). The deviations can be assigned to increased saturation effects with increasing energy deposition in the sensor. Moreover, in the vicinity of the Bragg peak, small deviations in the geometry assumed in the calculations from the experimental set-up can lead to large variances of the energy-loss.

7.2.4 Mean Energy-Loss: Quantitative Comparison of All Measurements

In Figure 7.57 the mean cluster signal values determined as presented in the previous sections (7.2.1 and 7.2.3) are summarized and compared to the corresponding theoretical or calculated energy-loss values. In addition to the measurements presented in this chapter, measurements of proton beams in different PMMA depths are included in the analysis. The values were derived from Schellhammer (2013). The experimental set-up and detector settings used in this work were identical to the measurement in PMMA depths for carbon ion beams presented in the previous section. However, instead of the mean cluster signal, the most probable cluster signal was evaluated. As a reference, the most probable energy-loss values derived from FLUKA Monte Carlo simulations were used in Schellhammer (2013).

Figure 7.57 a) shows the direct comparison between measured and theoretical values for measurements at $V_{\text{bias}}=10\text{ V}$, while Plot b) displays the relative deviations in dependence of the corresponding theoretical energy-loss values. Only for a part of the proton measurements (free-in-air: $E_{\text{initial}}=48\text{--}94\text{ MeV}$ and in up to 11 cm PMMA depth) higher values were obtained in the measurements than in the calculations. For

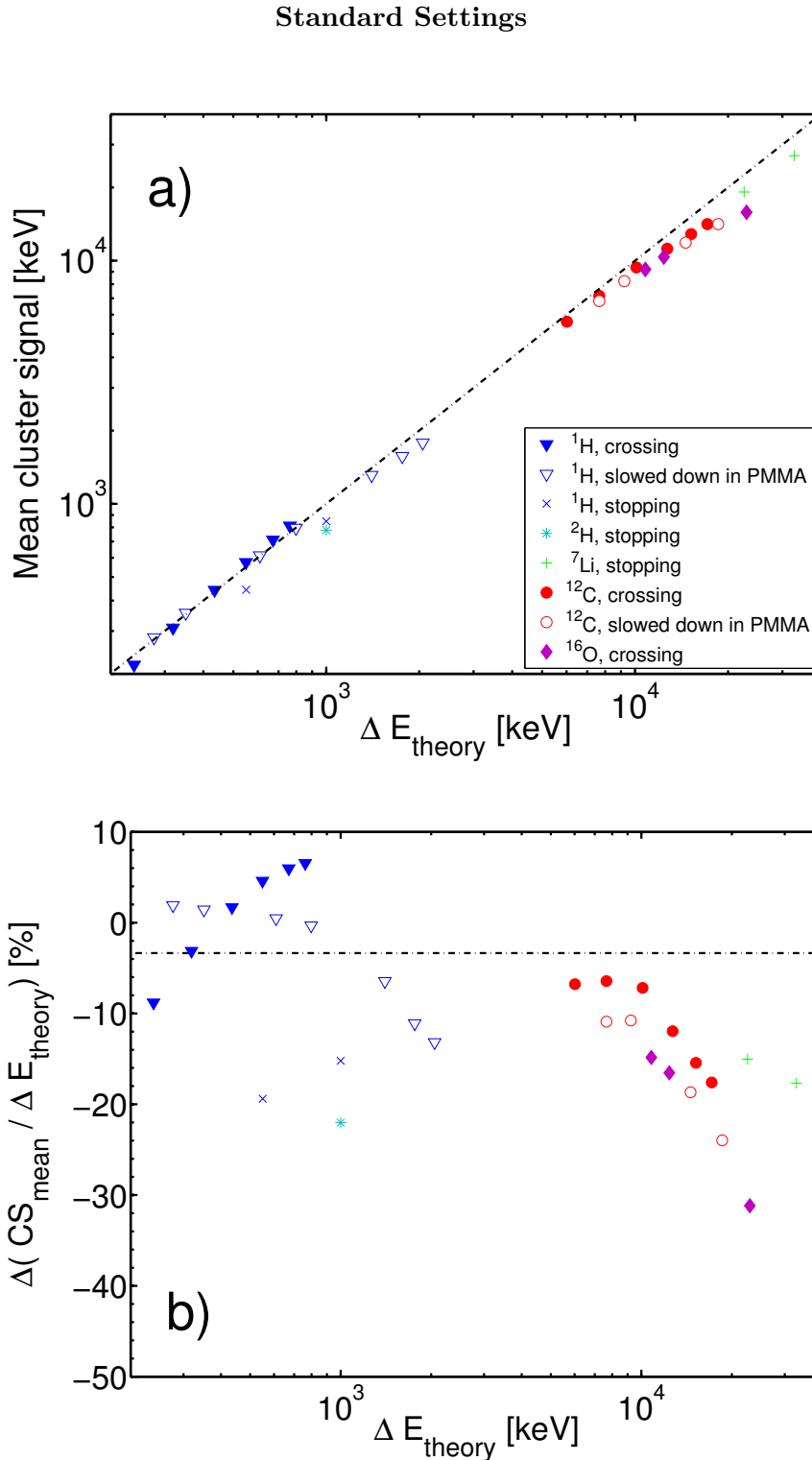


Figure 7.57: a) Quantitative comparison of the measured mean cluster signals to calculated mean energy-loss for all measurements presented in the previous chapters performed at a **detector bias voltage of 10 V**. The statistical uncertainties on the mean cluster signal values are smaller than the symbol sizes. b) Relative deviation between measured and calculated mean cluster signals. Note that the legend in Plot a) also applies for Plot b). The data for ^1H slowed down in PMMA are taken from Schellhammer (2013).

7 Results

all other measurements, the obtained mean cluster signal values are smaller than the energy-loss expected from theory or calculation. Overall the deviations are between +6.6% (^1H , $E_{\text{initial}}=48\text{ MeV}$, free-in-air) and -31.2% (^{16}O , $E_{\text{initial}}=127\text{ MeV/u}$, free-in-air).

For protons stopping in the detector the mean cluster signals show larger deviations from the expected energy-loss than for protons crossing the detector, although the expected energy-loss is in the same range. A possible explanation for these findings is a difference in the influence of the non-depleted sensor zone on the charge collection efficiency for particles traversing the complete sensitive detector layer and particles stopping in it. Also the characteristics of the charge sharing effect described in Section 5.2.2 have different impacts in the two cases and can therefore indirectly influence the cluster signal determination.

For the measurements in carbon ion beams behind PMMA phantoms larger deviations than for the free-in-air measurements were obtained, although the expected energy-loss is in the same range. To understand the effect, the dates of the measurement campaigns have to be considered. The free-in-air measurements (filled circles) were performed in October 2011 and in January 2012, while the measurements in different PMMA depths (open circles) were conducted in July 2012. In between the January and the July 2012 campaigns the detector response was found to have changed significantly (see Section 7.1.6). Therefore, the results presented here are in agreement with the findings presented in Section 7.1.6.

For carbon ion measurements behind PMMA phantoms (open circles, performed in July 2012) and for free-in-air oxygen ion measurements (diamonds, performed in April 2012) similar tendencies of the relative deviations from calculations in dependence of the theoretical energy-loss values can be seen. The measurements in lithium ion beams were performed in between these two campaigns (end of April 2012). However, for lithium significantly smaller deviations from the expected energy-loss values were obtained. These findings indicate a possible dependency of the signal quenching in the detector on the ion species.

For comparison, the mean cluster signal values obtained in measurements at $V_{\text{bias}}=22\text{ V}$ are shown in Figure 7.58 a), while in Plot b) the relative deviations between measured and corresponding theoretical values are displayed. At $V_{\text{bias}}=22\text{ V}$ a lower number of measurement data is available than for $V_{\text{bias}}=10\text{ V}$. For protons and deuterium ions, the deviations between measured and theoretical values tend to be smaller compared to the corresponding measurements at $V_{\text{bias}}=10\text{ V}$. For carbon ion measurements, in contrast, a tendency towards larger deviations can be seen.

A possible explanation for these findings is an influence of the width of the depletion zone in the sensor and of saturation effects. For ions depositing only small amounts of energy, a full depletion of the sensitive detector layer as present at $V_{\text{bias}}=22\text{ V}$ leads

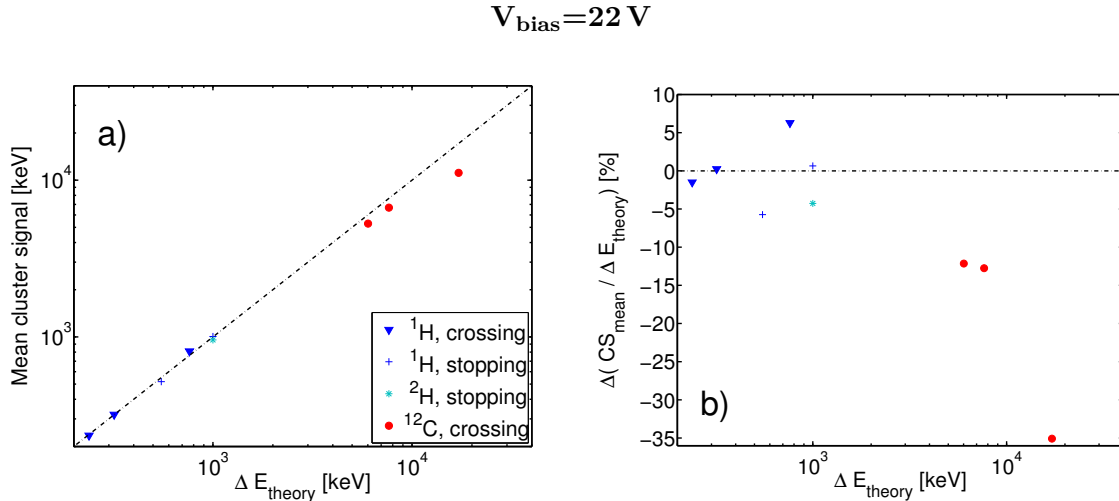


Figure 7.58: a) Quantitative comparison of the measured mean cluster signal to calculated mean energy-loss for the measurements presented in the previous chapters performed at a detector bias voltage of 22 V. The statistical uncertainties on the mean cluster signal values are smaller than the symbol sizes. b) Relative deviation between measured and calculated mean cluster signals. Note that the legend in Plot a) also applies for Plot b).

to an enhanced charge collection efficiency and therefore results in higher mean cluster signal values. However, the overestimation of the mean cluster signal for the lowest proton energy investigated free in air is not influenced by the change of the bias voltage. For carbon ions, in contrast, the mean cluster signals are largely influenced by saturation effects, as presented in Section 7.1.2. Since a higher bias voltage reduces the charge sharing and therefore the number of pixels collecting the signal, the saturation effects are more severe at higher bias voltages resulting in a decrease of the mean cluster signals.

Overall the deviations for measurements at $V_{\text{bias}} = 22 \text{ V}$ are between +6.3% (^1H , $E_{\text{initial}} = 48 \text{ MeV}$) and -35.1% (^{12}C , $E_{\text{initial}} = 89 \text{ MeV/u}$). A direct comparison of the results in Figure 7.57 and 7.58 is however not possible since measurements for the same ion species and energies were performed in different campaigns in between which the detector response is known to have changed significantly (see Section 7.1.6).

7.3 Ion Spectroscopy

In this section, the possibility of performing ion spectroscopy measurements with the Timepix detector is investigated. The methodology of the experiments is described in Section 6.3. For the measurements, the phantoms presented in Section 5.3 were used. The approach to ion spectroscopy presented in this work is based on the evaluation of two parameters of the clusters induced by single ions: the cluster size and the

cluster signal. Both of them are related to the energy deposition of an ion in the sensitive detector layer. 2-dimensional histograms showing the distributions of the clusters in terms of the two parameters obtained from measurements in mixed ion fields are studied. While in the first part of the section, the measurements performed for identification of the different ion species are presented (Section 7.3.1), in the second part this identification is verified (Section 7.3.2). Sections 7.3.3 and 7.3.4 contain examples for possible applications of the presented approach to ion spectroscopy.

7.3.1 Identification of Ion Species by Measurements in Different Material Depths

I: Behind the Bragg Peak As described in Section 6.3, the 2-dimensional histograms of cluster signal and cluster size distributions obtained in a mixed irradiation field show several areas with an increased concentration of clusters. The approach used to identify these areas is based on the knowledge that for a given velocity the lightest ions have the longest range in tissue (the range scales with A/Z^2 , see Section 4.1 for further explanations). Based on this knowledge, measurements in different depths in the area of and behind the Bragg peak were performed. The distributions obtained from measurements behind 118, 121, 129, 198, 348, and 448 mm PMMA, respectively, are shown in Figure 7.59. A clear dependence of the distributions on the material depth can be seen.

Far behind the peak mostly protons are expected to be detected. Based on this knowledge, the high signal area visible in the 2-dimensional histogram obtained from a measurement behind 448 mm PMMA (Figure 7.59 a) can be assigned to clusters which are created by hydrogen ions. Closer to the Bragg peak, at a PMMA depth of 348 mm, a second high signal area is visible in the distribution (Plot b). This area can be assigned to clusters induced by helium ions. In the same way, the area in which the signal of boron ions is displayed can be identified (Plots c and d). Since the range of primary particles of the given initial energy in PMMA is approximately 124 mm, for measurements in 121 mm PMMA depth also a detector signal due to primary particles is expected. Behind 121 mm PMMA a high signal area is observed, which is not obtained at 131 mm, i.e. behind the peak position. This area was consequently assigned to clusters induced by primary carbon ions (Plot e).

Comparing the measurements behind 121 and 118 mm of PMMA (Plots e and f), a change in the cluster size and cluster signal of the carbon ion induced clusters can be recognized. Due to the lower velocity, in larger depth the carbon ions deposit more energy in the detector resulting in larger cluster signal and size. The high number of clusters with similar size but lower signal than clusters in the main carbon ion region (labeled '(x)' in Plot f), can be assigned to primary particles arriving at the end of the

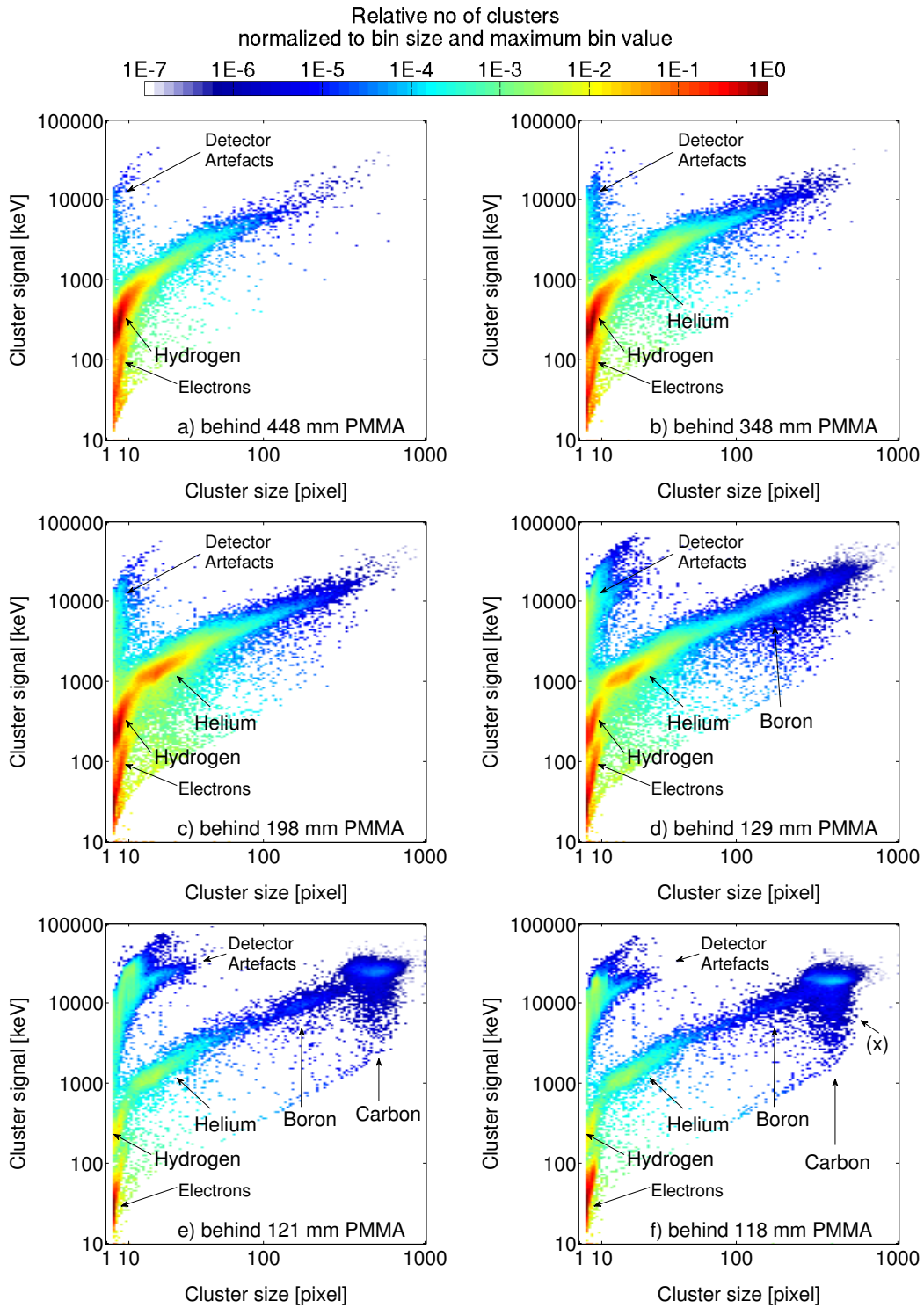
^{12}C , $E_{\text{initial}}=271 \text{ MeV/u}$


Figure 7.59: 2-dimensional histograms showing the distributions of cluster signal and cluster size for measurements in carbon ion beams of $E_{\text{initial}}=271 \text{ MeV/u}$ behind PMMA phantoms of different thicknesses. A clear dependence of the distribution on the material depth (Plot a) - f)) can be seen. Settings: $t_{\text{acq}}=1 \text{ ms}$, $V_{\text{bias}}=10 \text{ V}$, $A_{\text{cluster}} \geq 4 \text{ pixel}$, $\text{roundness}_{\text{cluster}}^{\text{min}}$ as depicted in Figure 6.8.

7 Results

acquisition time (see Section 7.1.1 for further investigations of the effect). This effect is most prominent for carbon ions, since they deposit the largest amount of energy in the detector. For carbon ions arriving very late in the acquisition time, also the size of the corresponding clusters is reduced, leading to a tail of the carbon ion region towards low cluster signal and size.

In Figure 7.59 f), two additional areas of high intensity can be seen. The area labeled 'Electrons' corresponds to secondary electrons (see Section 7.1.3 for further details), while the area labeled 'Detector Artefacts' represents clusters containing left-over signals from particles arriving during the detector dead-time. Their number is particularly high due to the influence of overshoots in the preamplifier output (see Section 7.1.1 for the investigation of this effect). The clusters labeled 'Detector Artefacts' represent an undesired background signal and are of no relevance for further quantitative evaluations. To exclude them from the quantitative analyses, the high average signal per pixel in the clusters can be utilized, using a constraint on the maximum average cluster signal of 200 keV. For illustration, Figure 7.60 shows the histogram for the measurement behind 118 mm PMMA employing this constraint.

In theory, also lithium and beryllium fragments should be detected. According to their charge and mass, energy depositions and ranges in between helium and boron ions are expected. However, for the investigated energy the number of lithium and beryllium ions created in the ^{12}C -fragmentation is about one order of magnitude lower compared to the number of helium ions (Matsufuji et al. (2003), data for fragmentation

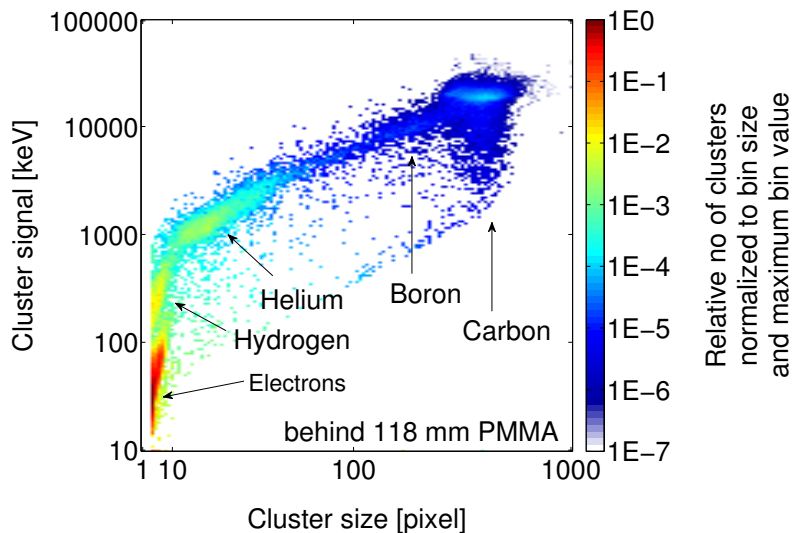


Figure 7.60: 2-dimensional histograms showing the distributions of cluster signal and cluster size for measurements in carbon ion beams of $E_{\text{initial}}=271$ MeV/u behind a 118 mm thick PMMA phantom. The same data as in Figure 7.59 f) is displayed. To exclude detector artefacts from the analysis, a constraint on the maximum average signal of 200 keV was used. Settings: $t_{\text{acq}}=1$ ms, $V_{\text{bias}}=10$ V, $A_{\text{cluster}} \geq 4$ pixel, $\text{roundness}_{\text{cluster}}^{\text{min}}$ as depicted in Figure 6.8.

of ^{12}C , $E_{\text{initial}}=290\text{ MeV/u}$ close to the Bragg peak). To demonstrate that the absence of areas which could be assigned to lithium and beryllium fragments is not caused by an insufficient statistic, for PMMA depths of 118 and 129 mm the measurements were repeated using an at least five times higher number of initial carbon ions. The experimental set-up was the same as for the measurements presented in Figure 7.59. However, the distance between phantom and detector was reduced to 1.6 cm in order to reduce influences of the air between phantom and detector and thus improve the experimental set-up. The corresponding 2-dimensional histograms are shown in Figure 7.61. No distinct areas due to lithium or beryllium ions can be recognized.

II: In Front of the Bragg Peak In addition to the measurements in the Bragg peak area and behind the Bragg peak presented in the previous paragraph, measurements with thinner PMMA phantoms were evaluated. For comparison, a measurement free-in-air was included in the analysis.

The 2-dimensional histograms showing the cluster parameter distributions for the free-in-air measurement and measurements in 5 and 10 cm PMMA depth are shown in Figure 7.62. In the free-in-air measurement presented in Plot a), an area corresponding to primary carbon ions ('Carbon'), areas related to secondary electrons originating from the beam-line and air in front of the detector ('Electron') as well as detector artefacts ('Detector Artefacts') can be identified. In addition, an at least two order of

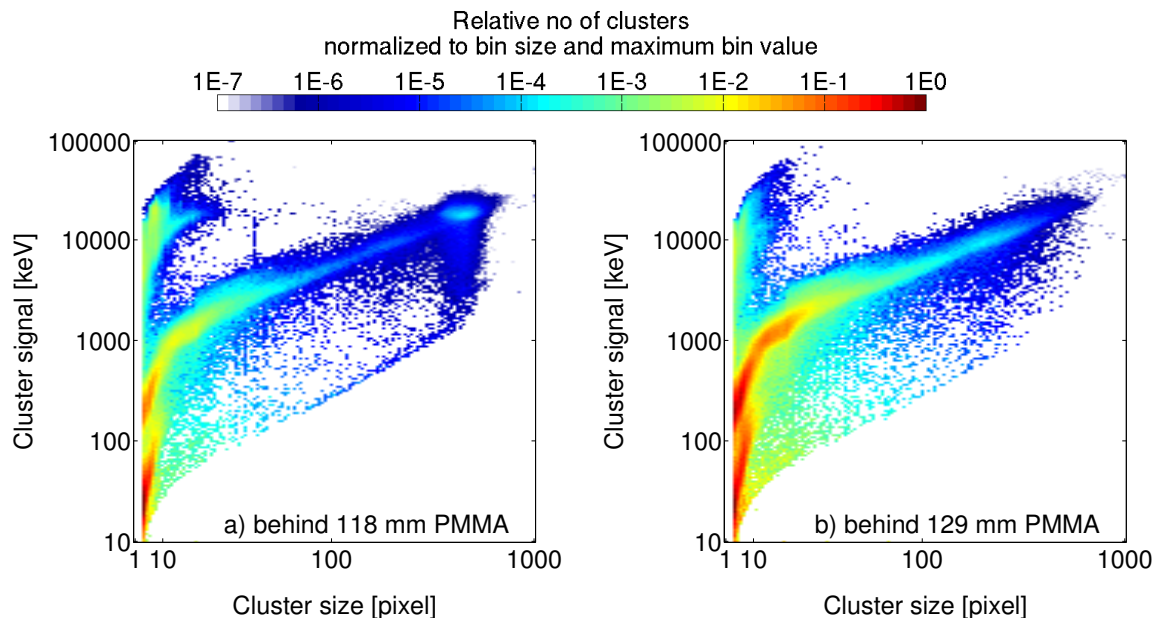


Figure 7.61: 2-dimensional histograms showing the distributions of cluster signal and cluster size for measurements in carbon ion beams of $E_{\text{initial}}=271\text{ MeV/u}$ behind PMMA phantoms of a) 118 mm and b) 129 mm thickness. In comparison to the measurements presented in Figure 7.59 an increased number of initial carbon ions was studied to enhance the statistics. Settings: $t_{\text{acq}}=1\text{ ms}$, $V_{\text{bias}}=10\text{ V}$, $A_{\text{cluster}} \geq 4\text{ pixel}$, $\text{roundness}_{\text{cluster}}^{\text{min}}$ as depicted in Figure 6.8.

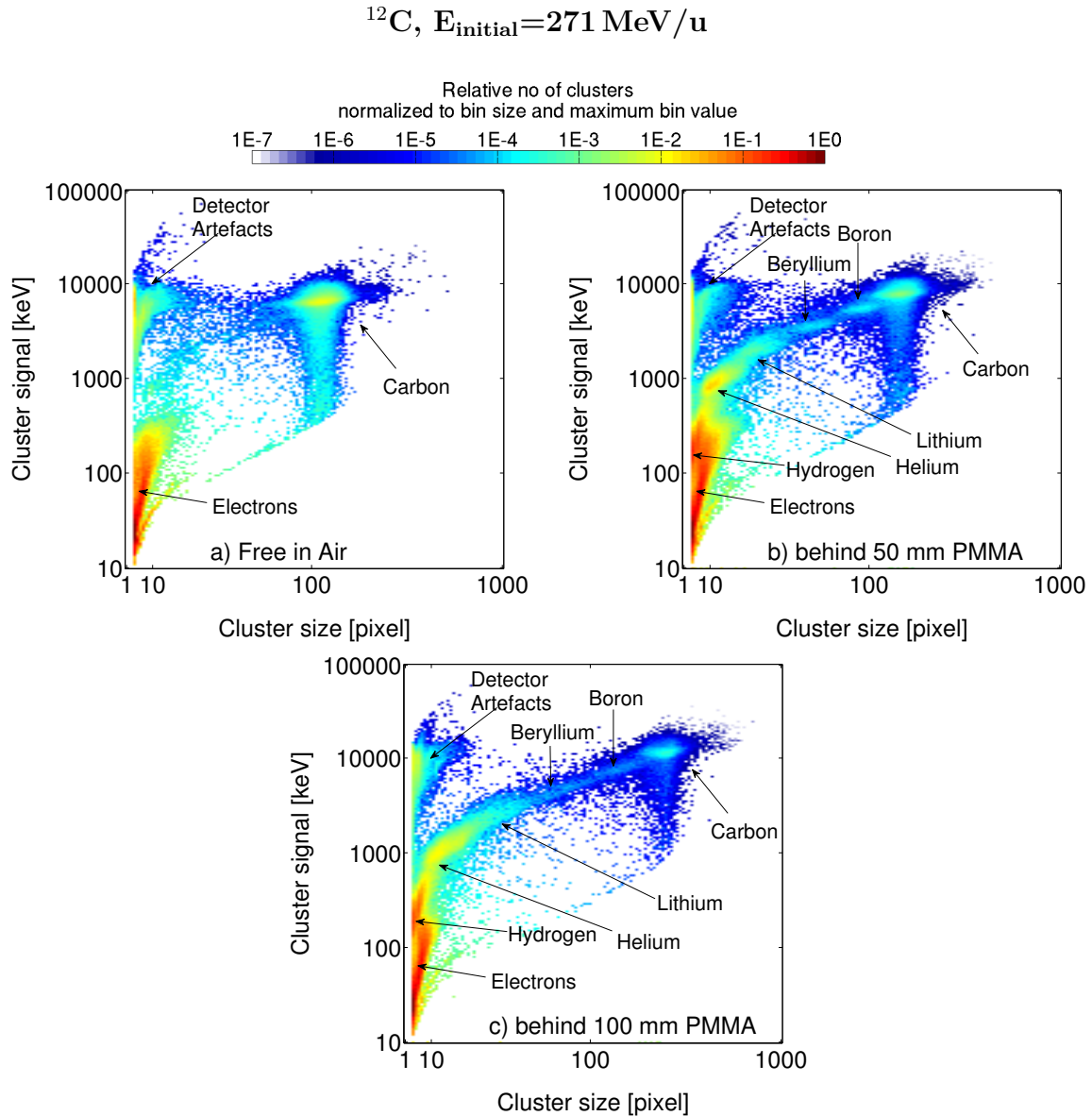


Figure 7.62: 2-dimensional distributions of cluster signal and cluster size for free-in-air measurements (a) and behind 50 mm (b) and 100 mm (c) thick PMMA phantoms. A clear dependence of the distribution on the material depth can be seen. The range of the primary ions in PMMA is 124 mm. Settings: $t_{\text{acq}}=1 \text{ ms}$, $V_{\text{bias}}=10 \text{ V}$, $A_{\text{cluster}} \geq 4 \text{ pixel}$, $\text{roundness}_{\text{cluster}}^{\text{min}}$ as depicted in Figure 6.8.

magnitudes lower number of events is registered in areas where the signal of secondary fragments would be expected. The histogram obtained behind a PMMA phantom of 5 cm thickness (Plot b) shows regions of clusters due to secondary hydrogen, helium, lithium, beryllium and boron fragments, which are clearly distinguishable. In contrast to that, in the measurement in 10 cm PMMA depth (Plot c), the separation of the regions corresponding to secondary lithium, beryllium and boron is not as distinct as in 5 cm PMMA depth (Plot b). A possible explanation is an increasing effect of energy-loss straggling of the secondary particles with increasing material depths, which can cause a smearing of the distribution.

7.3.2 Verification of the Identification

To verify the identification of the ion species presented in the previous section, the fragmentation of a carbon ion beam of $E_{\text{initial}}=400$ MeV/u in a water target was studied. The experimental set-up and beam parameters were chosen as close as possible to a measurement presented in Haettner (2006) (see Section 6.3.2 for details). As described in Section 3, the measurements presented in Haettner (2006) have been used to benchmark the Monte Carlo transport code FLUKA and are therefore relevant in treatment planning for carbon ion beam therapy. The angular distributions of fragments obtained in the experiment by Haettner (2006) are shown in Figure 3.1 (left).

The distributions of clusters in terms of size and signal measured with the Timepix detector are shown in Figure 7.63. On the beam axis (Plot a), regions corresponding to ion species between proton and carbon ions, as well as a region related to secondary electrons, can be identified. The same applies for the measurement at an angle of 2° from the beam axis, shown in Plot b), although the relative number of clusters in the different areas changes. Compared to the measurement on the beam axis, the relative number of primary carbon ions is decreased, while the relative number of secondary fragments increases. At 4° from the beam axis, only very few carbon, boron and beryllium ions are detected, while the relative number of lithium ions is still comparatively high. Also many hydrogen and helium ions, as well as secondary electrons are observed. At an even larger angle of 6° , besides secondary electrons almost exclusively hydrogen and helium ions are detected.

To perform a quantitative comparison of the measurements in this work and the data presented in Haettner (2006), hand-drawn regions of interest for hydrogen, helium, lithium, beryllium and boron induced clusters were identified in the 2-dimensional histograms. For illustration, the regions of interest used for the measurement at an angle of 2° from the beam axis are depicted in Figure 7.64.

For the measurements at angles of 2° , 4° , and 6° from the beam axis the relative numbers of events in the respective regions of interest were determined. The measurement on the central beam axis was not included in the analysis, since the data presented in Haettner (2006) for small angles ($0-2^\circ$) are afflicted with large uncertainties caused by primary carbon ion events screening the fragment data (Haettner (2006)). At an angle of 6° from the beam axis only hydrogen and helium ions were investigated, since the number of heavier fragments is very low (see Figure 7.63 d). In Figure 7.65, for each investigated position the fractions of the different ion species are compared to the reference measurement. Table 7.4 presents the same data. For both ion spectroscopy methods the relative numbers of the fragment species follow similar trends.

The relative fractions for hydrogen, helium, beryllium, and boron fragments estimated using the method presented in this thesis agree with the reference data within the limits of uncertainties (Δ_{ref}), except for the relative fraction of hydrogen at an angle

7 Results

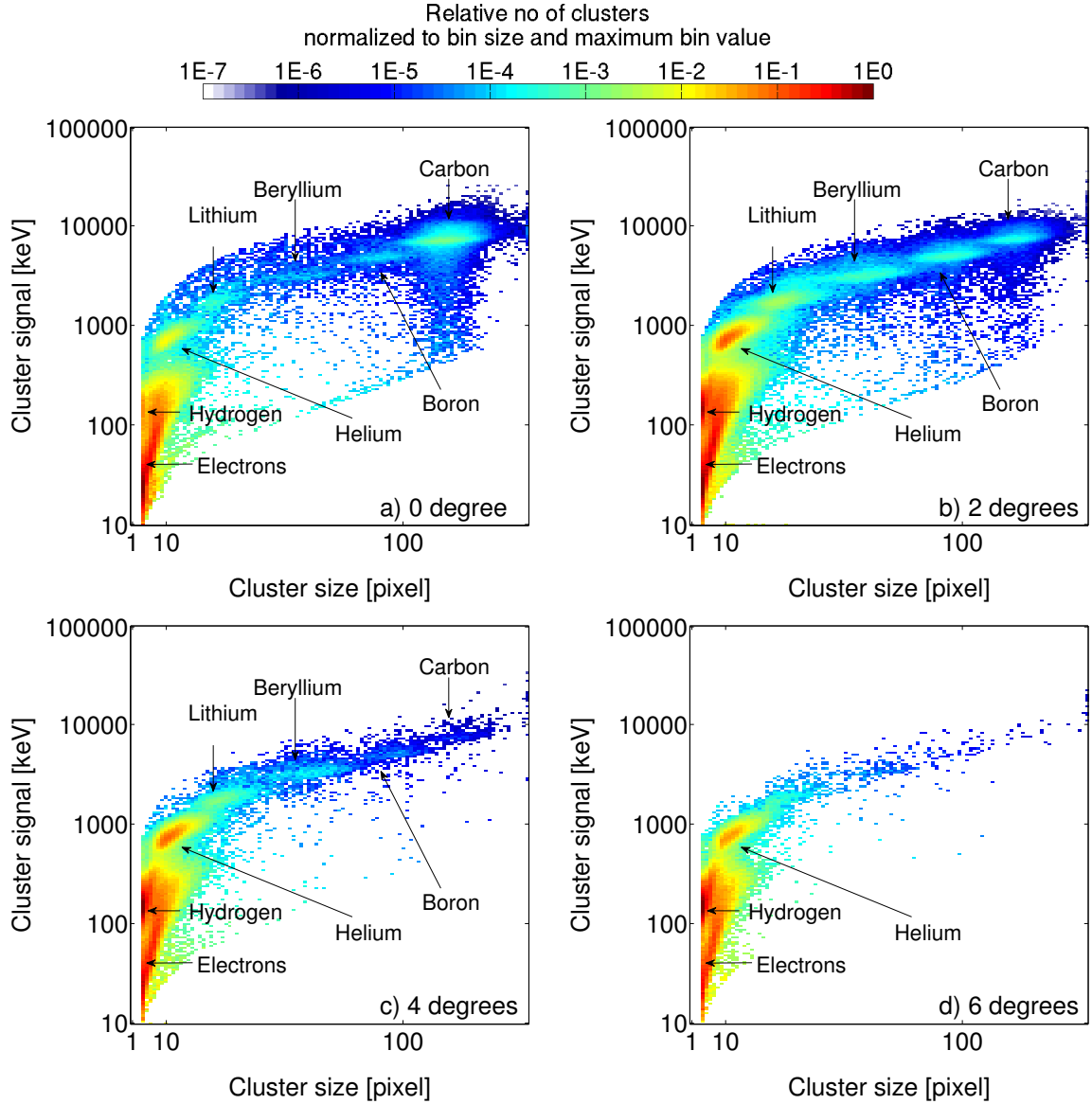


Figure 7.63: 2-dimensional distributions of cluster signal and cluster size obtained in carbon ion beams of $E_{\text{initial}}=400$ MeV/u in measurements behind a 158 mm thick water phantom at different angles from the beam axis. Each distribution is normalized to the maximum bin value. Settings: $t_{\text{acq}}=1$ ms, $V_{\text{bias}}=10$ V, $A_{\text{cluster}} \geq 4$ pixel, $\text{roundness}_{\text{cluster}}^{\text{min}}$ as depicted in Figure 6.8. To exclude detector artefacts from the analysis, a constraint on the maximum average cluster signal of 200 keV was used.

of 2° (deviation: 8.5%, agreement within $1.1 \Delta_{\text{ref}}$). For lithium the relative deviations to the reference are larger (2° : -18.3%, 4° : -28.9%, agreement within $2.3 \Delta_{\text{ref}}$).

Overall a good agreement was obtained. Based on this result, the identification of the different ion species can be considered as correct. Moreover, the hand-drawn regions of interest in the 2-dimensional distributions of cluster size and cluster signal offers an in first approximation good separation between the different fragment species. Further considerations on the evaluation of the measurements and related uncertainties are presented in Section 8.3.

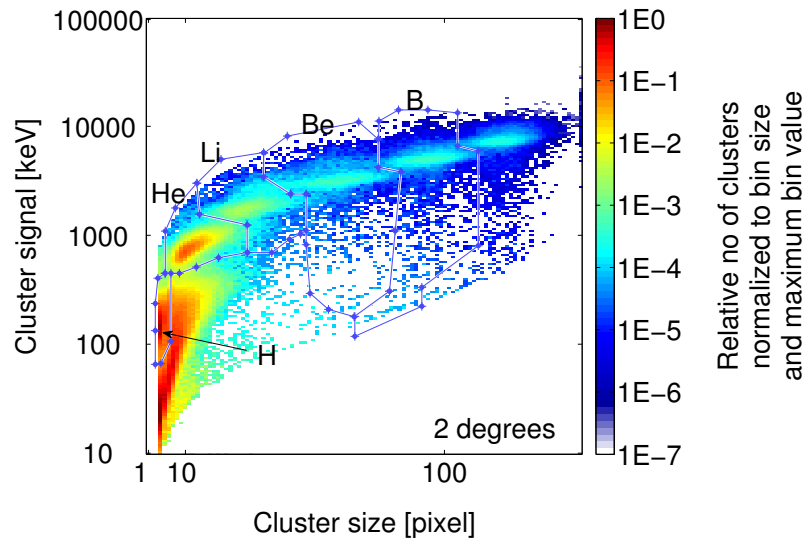


Figure 7.64: Investigation of the fragmentation of a carbon ion beam ($E_{\text{initial}}=400$ MeV/u) in a 158 mm thick water phantom. The 2-dimensional histogram showing the distribution of cluster signal and cluster size for the measurement at 2° from the beam axis (equivalent to Figure 7.63 b) is shown. The regions of interest used for the quantitative evaluation of the relative amounts of different fragment species are marked.

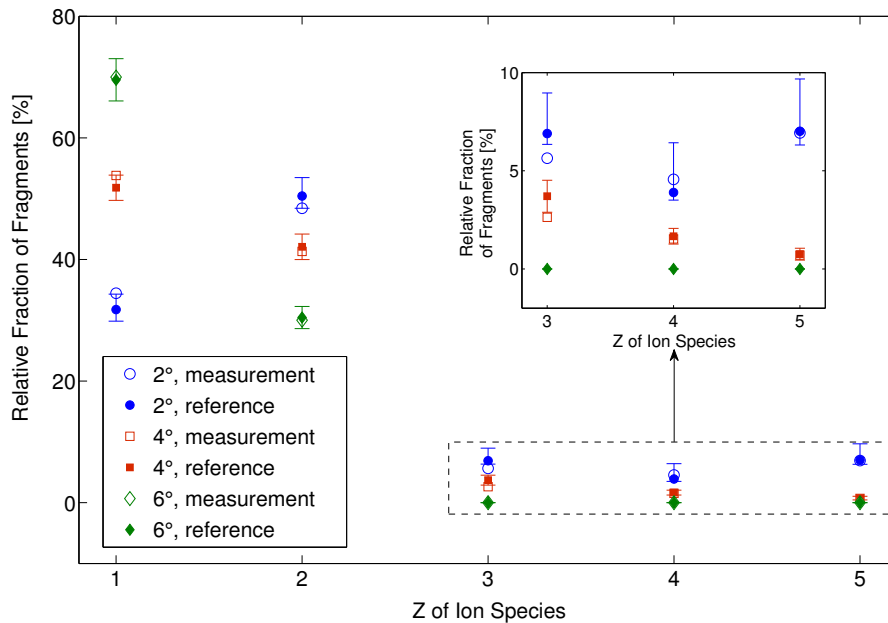


Figure 7.65: Comparison of ion spectroscopy measurements using the method presented in this thesis (open symbols) to the data presented by Haettner (2006) (filled symbols). The relative fractions of the different fragment species detected at angles of 2° , 4° , and 6° from the beam axis are shown. The subplot displays the data in the dashed box with enhanced ordinate scale. Preliminary results. Further considerations on the evaluation of the measurements and related uncertainties are presented in Section 8.3.

Table 7.4: Comparison of ion spectroscopy measurements using the method presented in this thesis (measurement) to the data presented by Haettner (2006) (reference). For angles of 2°, 4°, and 6° from the beam axis, the relative fractions of the different fragment species, as well as the deviations of the measurements from the reference are listed. Preliminary results.

Ion Species	Relative Fraction [%]		
	Reference ^a	Measurement	Relative Deviation [%]
2°			
H	31.76 ^{+2.54} _{-1.91}	34.45	+ 8.47
He	50.43 ^{+3.03} _{-2.02}	48.42	- 3.99
Li	6.90 ^{+2.07} _{-0.55}	5.64	- 18.26
Be	3.89 ^{+2.53} _{-0.39}	4.56	+ 17.22
B	7.01 ^{+2.67} _{-0.70}	6.93	- 1.14
4°			
H	51.80±2.07	53.82	+ 3.90
He	42.08±2.10	41.33	- 1.78
Li	3.70±0.81	2.63	- 28.92
Be	1.66±0.40	1.53	- 7.83
B	0.75±0.30	0.70	- 6.67
6°			
H	69.55±3.48	69.99	+ 0.63
He	30.45±1.83	30.01	- 1.44

7.3.3 Application I: Lateral Fragment Distributions

As described in Section 6.3.3, the analysis of lateral fragment distributions in or close behind phantoms is among the most important applications of the ion spectroscopy approach investigated in this work.

Employing the experimental set-up described in Section 6.3.3, the lateral distribution of fragments evolving from irradiation of a PMMA phantom with a carbon ion beam of $E_{\text{initial}}=271$ MeV/u was studied. Four different detector positions were used, resulting in an overall area covered by the detector of 1.4×5 cm². This area was divided into 16 circular bins centered around the beam axis, which are labeled with increasing numbers for increasing distances from the beam axis. Figure 7.66 shows examples of

^aHaettner (2006)

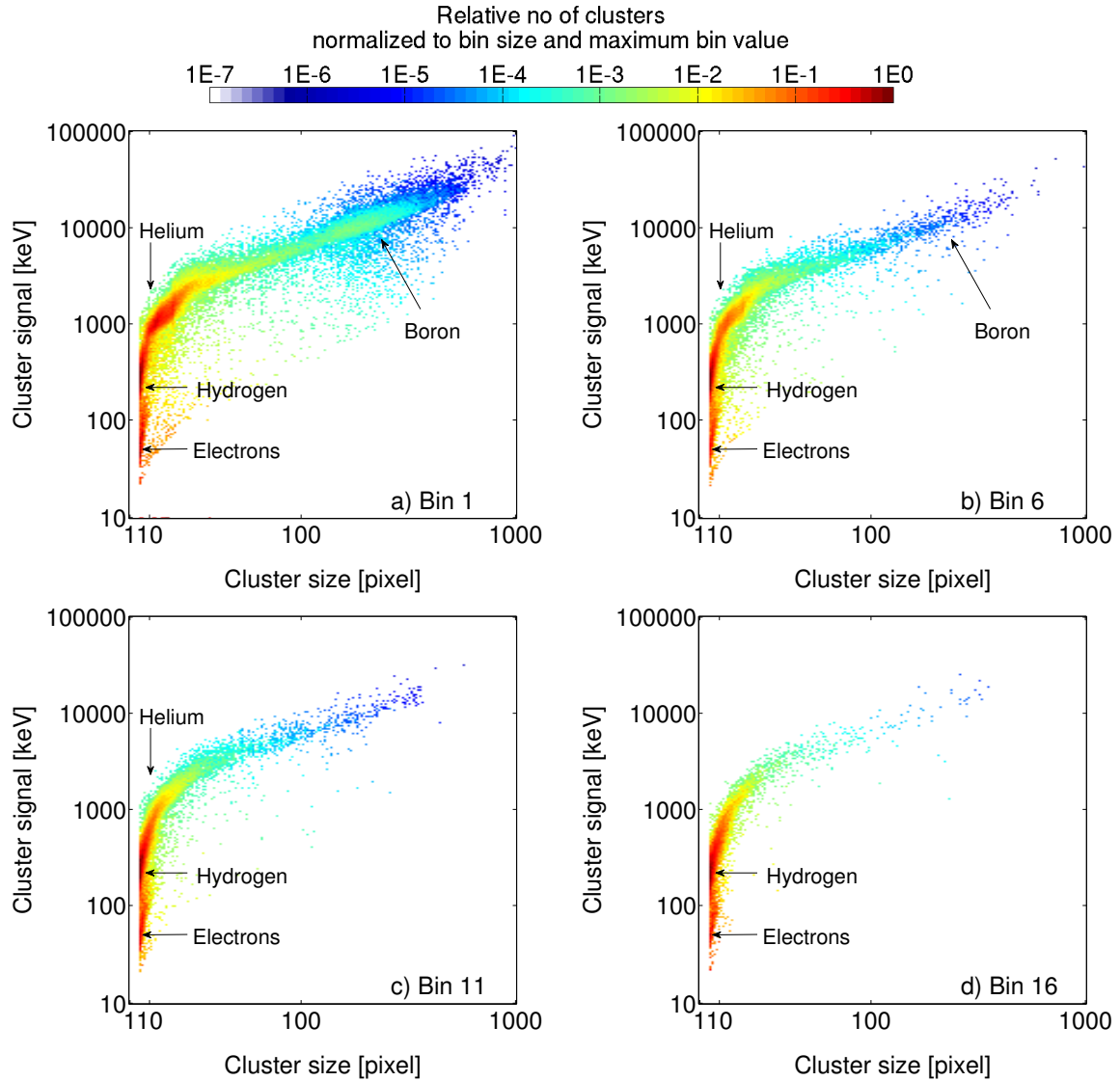


Figure 7.66: 2-dimensional histograms showing the distributions of cluster signal and cluster size for carbon ion beams of $E_{\text{initial}}=271$ MeV/u in measurements behind 127 mm PMMA in different distances from the beam axis. The width of each bin is 2.915 mm. Settings: $t_{\text{acq}}=1$ ms, $V_{\text{bias}}=10$ V, $A_{\text{cluster}} \geq 4$ pixel, $\text{roundness}_{\text{cluster}}^{\text{min}}$ as depicted in Figure 6.8. To exclude detector artefacts from the analysis, a constraint on the maximum average cluster signal of 200 keV was used.

the cluster signal and cluster size distributions for bins located on the central beam axis (Plot a: Bin 1) and in a distance of 14.6 mm (Plot b: Bin 6), 29.2 mm (Plot c: Bin 11) and 43.5 mm from the beam axis (Plot d: Bin 16). Distinct differences between the distributions can be seen. While on the central beam axis, regions containing the signal of boron, helium and hydrogen ions can be identified, at a larger distance to the beam axis the relative number of boron clusters decreases drastically (Bins 6 and 11). Far from the beam axis (Bin 16) also the number of helium ions is reduced, while the signal due to hydrogen ions is remaining. In all bins, a distinct area assigned to secondary electrons can be seen.

7 Results

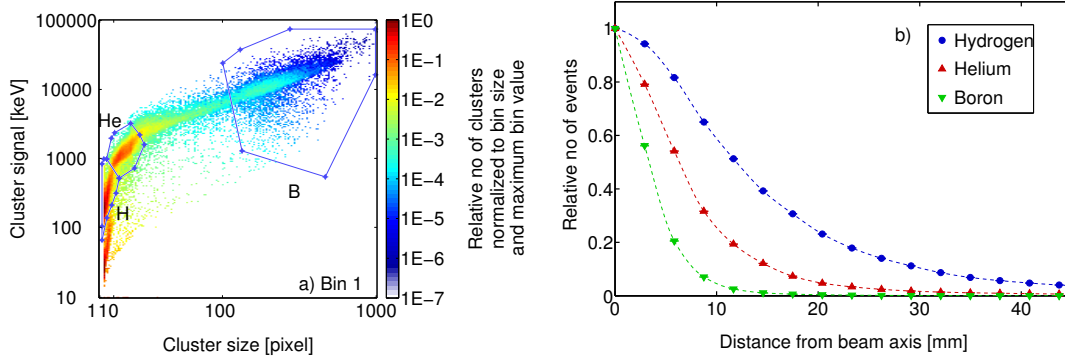


Figure 7.67: Quantitative evaluation of the measurements shown in Figure 7.66. a) 2-dimensional histogram showing the distribution of cluster signal and cluster size for the central bin. The regions of interest used for the evaluation of lateral distributions of hydrogen, helium and boron ions are marked. b) Distributions of hydrogen, helium and boron ions in dependence of the distance from the beam axis. The distributions are normalized to the respective number of ions detected in the central bin. The statistical uncertainties are smaller than the marker size.

To perform a quantitative evaluation of the measurements, regions of interest for hydrogen, helium and boron induced clusters were defined, as depicted in Figure 7.67 a). For the definition, the distribution measured in Bin 1, which is centered on the beam axis was used. The regions were selected according to visual judgment. Based on this selection, for each bin the number of clusters registered in the different regions was counted and normalized to the number of clusters detected in the respective region in the central bin. The relative numbers obtained are shown in Figure 7.67 b) in dependence of the distance of the respective bin from the beam axis. The widest distribution is found for hydrogen ions, while helium and boron ions show narrower distributions. These findings follow the expected trend. Due to effects in the nuclear interactions and increased influences of scattering for the lightest ions the widest distributions are expected.

7.3.4 Application II: Fragmentation in Different Materials

Another interesting application of the ion spectroscopy approach presented in this work, is the study of fragmentation in different materials, as described in Section 6.3.4. Exemplary, the fragmentation of carbon ions of $E_{\text{initial}}=430 \text{ MeV/u}$ in PMMA and steel phantoms of the same water-equivalent thickness was studied. For comparison, a measurement without phantom but with reduced initial ion energy was included in the study. The experimental set-up used is described in Section 6.3.4.

Figure 7.68 shows the 2-dimensional distributions of cluster signal and cluster size for the three measurements. To be able to better recognize differences between the measurements and to quantitatively compare them, the cluster size and cluster signal distributions (equivalent to projections of the 2-dimensional histograms on the respec-

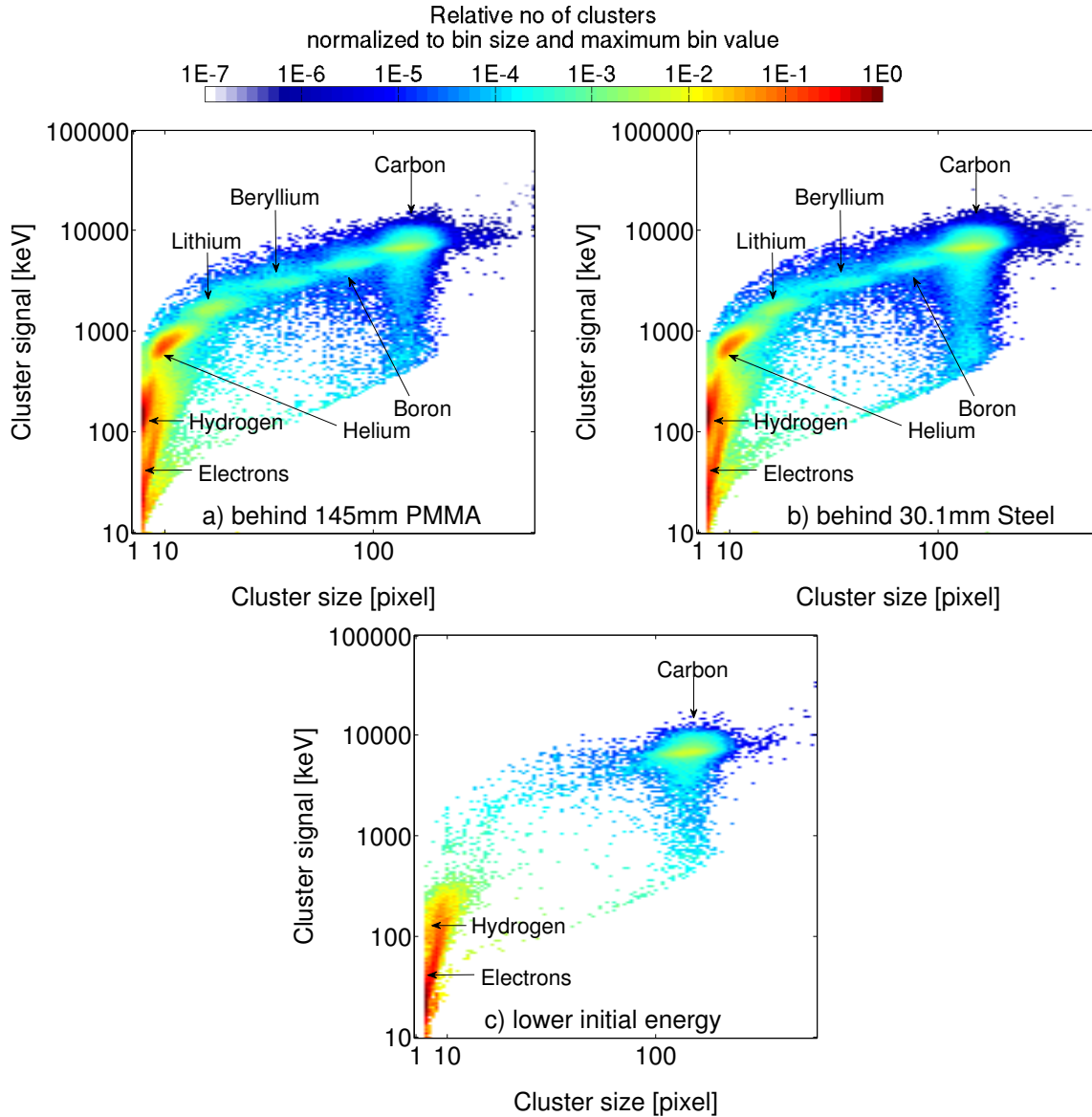


Figure 7.68: 2-dimensional histograms showing the distributions of cluster signal and cluster size for measurements in carbon ion beams of $E_{\text{initial}}=430$ MeV/u a) behind 145 mm PMMA and b) behind 30.1 mm of steel. c) Additional measurement with reduced ion energy of $E_{\text{initial}}=265$ MeV/u and no material in front of the detector. Settings: $t_{\text{acq}}=1$ ms, $V_{\text{bias}}=10$ V, $A_{\text{cluster}} \geq 4$ pixel, $\text{roundness}_{\text{cluster}}^{\text{min}}$ as depicted in Figure 6.8. To exclude detector artefacts from the analysis, a constraint on the maximum average cluster signal of 200 keV was used.

tive axes) are shown in Figure 7.69. Each distribution is normalized to the number of clusters with a signal between 5700 and 9000 keV, assumed to be induced by primary carbon ions. In comparison to the 2-dimensional histograms, in the distributions shown in Figure 7.69 clusters due to secondary electrons and hydrogen fragments are difficult to separate, due to their similar size and signal. For fragments heavier than hydrogen, distinct peaks can be seen in the cluster size and the cluster signal distribution for the measurements behind the PMMA and the steel phantom. Their relative number

7 Results

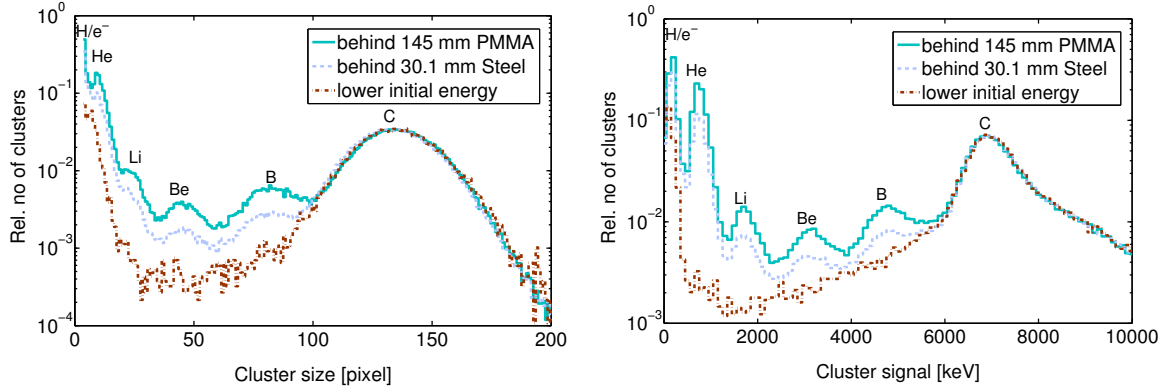


Figure 7.69: Projections of the measurements shown in Figure 7.68 on the cluster size- and cluster signal-axes. The distributions are normalized to the number of clusters with a signal between 5700 and 9000 keV detected, which are assumed to be induced by primary carbon ions.

is smaller for the measurement behind steel, compared to the measurement behind PMMA.

To evaluate the measurements behind PMMA and steel quantitatively, the ion species were discriminated using hand-drawn regions-of-interest in the 2-dimensional histograms displayed in Figure 7.68. The relative fractions of the ion species for the measurements are compared in Table 7.5. A lower number of secondary fragments relative to the number of primary carbon ions is detected in the measurement behind the steel phantom compared to the measurement behind PMMA, as was already expected based on the findings in Figure 7.69. The difference is 28.8% for hydrogen, 49.4% for helium, 49.2% for lithium, 48.3% for beryllium and 43.4% for boron ions.

Further considerations on the quantitative evaluation of the measurements and the related uncertainties are presented in Section 8.3.

Table 7.5: Relative fractions of the different ion species measured behind the PMMA phantom and the steel phantom. The values are normalized to the number of carbon ions detected. For discrimination between the ion species hand-drawn regions-of-interest in the 2-dimensional histograms of cluster signal and cluster size were used.

Ion Species	behind PMMA	behind Steel
H	62.1 %	44.2 %
He	63.8 %	31.5 %
Li	6.5 %	3.3 %
Be	5.8 %	2.8 %
B	12.9 %	5.6 %
C	100 %	100 %

For the free-in-air measurements of carbon ions with lower initial energy a distinct change of the distribution displayed in Figure 7.68 c) can be seen. While carbon ions are displayed in the same region as for the measurements behind phantoms, in regions where secondary fragments would be expected only very few clusters can be seen. The relative number of secondary electrons, in contrast, is very high. The clusters due to primary carbon ions show a similar size and signal as in the measurements behind the phantoms (see also Figure 7.69). Moreover, a good agreement of the width of the carbon ion peak in all cluster signal distributions can be seen. These results prove that both phantoms have the same water-equivalent thickness, leading to a reduction of the energy of initial carbon ions which is equivalent to the difference between the initial ion energies used for the measurements with and without phantom ($\Delta E_{\text{initial}}=165 \text{ MeV/u}$). In addition, the study confirms that energy straggling in the beam path is of minor relevance on the energy-loss straggling in the detector (see Section 7.2.2 for detailed studies on energy-loss straggling with the Timepix detector).

8 Discussion and Outlook

The experience of measurements with the Timepix detector in ion beams is very limited. In most publications available, ions with low energies (e.g. α -particles of 5.5 MeV) stopping in the detector sensor were studied (e.g. Jakubek et al. (2008); Pugatch et al. (2011); Granja et al. (2011)). Exposures with ion beams of high energies (e.g. 800 MeV/u Si or 500 MeV/u Fe) have been presented in Pinsky et al. (2010, 2011), while first studies in therapeutic ion beams have recently been shown in Hoang et al. (2012) and Opalka et al. (2013). However, no detailed study on the detector response to therapeutically used ion species and initial ion energies are available. Therefore, in this thesis the detector response in therapeutic ion beams was characterized in detail, before studying the detector's capability for energy-loss measurements and ion spectroscopy. In this chapter, the results of these studies are discussed and considerations on possibilities to enhance the presented methods and prospects on their future use are presented.

8.1 Characterization of Detector Response in Therapeutic Ion Beams

Since many of the findings for the detector response in therapeutic ion beams have been of direct relevance for the further work in this thesis, they are discussed in the respective paragraphs in Section 7.1. In the following only the most important results are discussed comprehensively.

Overshoots in the Preamplifier Output The results presented in Section 7.1.1 show that overshoots in the preamplifier output can lead to significantly increased cluster signals (see Figure 7.6 for an illustration) for ions depositing high energies in the silicon detector sensor (above approximately 1 MeV/pixel). For the Timepix detector, which has originally been designed for photon beam applications, this effect has not been described before. There are several impacts of the described overshoots on energy-loss and on ion spectroscopy measurements with the Timepix detector: On the one hand, for energy-loss measurements in ion beams depositing a large amount of energy in the sensor, the cluster signal distributions are artificially extended towards higher values.

For $t_{\text{acq}}=1$ ms (standard in this work), extensions were observed in the cluster signal distributions measured in low energy lithium ions, high energy carbon ions and high energy oxygen ions. For all of them, the expected mean energy-loss in the detector was above 5 MeV. The overshoots artificially broaden the measured cluster signal distributions and therefore distort studies of the mean energy-loss and energy-loss straggling. On the other hand, the overshoots are also of direct relevance to the presented ion spectroscopy approach, which exploits the cluster signal. An artificial broadening of the cluster signal distribution can result in a decreased separation capability between ion species.

For ions depositing a low amount of energy in the detector, like e.g. protons of therapeutically used energies, no effect of the overshoots on the cluster signal was observed (see Section 7.1.1). Nonetheless, overshoots can possibly exist but stay below the threshold. A precise value of the energy per pixel above which the overshoot effect starts to influence the measurement needs still to be determined. However, already this work shows that for standard pixel threshold values the overshoot effects start to influence the measurements at cluster heights, i.e. the signal in a single pixel, between 500 and 1700 keV. In the same energy range (at a signal in a pixel of approximately 900-1000 keV), the response of the pixels was found to start to grow unexpectedly steep in a previous study (Jakubek (2010)). While in the respective publication this non-linear behavior was assigned to problems with the constant current source I_{krum} , the findings in this work suggest that these earlier observations might also be related to the described overshoot effects.

A reduction of the influence of this effect on the measurements can presumably be achieved by employing new generation Timepix detectors (Timepix3), which enable simultaneous measurements of the particle arrival time and the energy information in each pixel (Poikela et al. (2012)). Having both information available, clusters influenced by overshoot effects, if these are still existing in the new detector type, could be excluded from further analysis based on their arrival time. Moreover, clusters containing left-over signals from particles arriving during the detector dead-time or clusters due to particles arriving at the very end of the acquisition time could be selected. Their signal was found to be reduced due to the remaining frame time being not sufficient to digitize the full signal (see Section 7.1.1 for details).

Saturation Effects In this thesis, the term saturation effect is used to describe incidences in which an increasing energy deposition in the sensor leads to a constant or decreased signal in the pixels. Possible reasons for saturation are increased recombination of the charge carriers released in the sensor and irregularity in the electronic response. In the investigations of bias voltage-dependent effects in carbon ion measurements presented in Section 7.1.2, interrelations between the applied bias voltage

and a saturation effect of the signal could be observed. The bias voltage is known to influence the charge diffusion and therefore the signal concentration to the central cluster pixels, in turn affecting the extent of saturation.

In Granja et al. (2011), the electronic response of the Timepix pixels was found to be distorted when the charge collected by a single pixel is above approximately 1 MeV/pixel. At higher amounts of charge collected, the pixel response gradually saturates, leading to a decrease in the recorded pixel value. To explain this effect, the course of the calibration curve above 1 MeV was recently tested qualitatively^a, as illustrated in Figure 7.16. While trends of dependencies of the mean cluster signal and the cluster profile on the bias voltage (Section 7.1.2) are in agreement with the qualitative course of the calibration curve (Figure 7.16), inconsistencies were observed in the cluster height distributions. The cluster height distributions show distinct falling edges (see Figures 7.15), which can be correlated to the signal, at which the calibration curve starts to drop due to saturation effects. However, the position of the falling edge was found to be dependent on the applied bias voltage. This indicates a bias voltage dependent course of the calibration curve for high pixel signals (above approximately 1.5 MeV), while up to now the detector calibration curve was considered to be bias voltage independent.

Moreover, also clusters with height values above the value corresponding to the falling edge position were observed, what is not explainable when the falling edge corresponds to the cusp of the calibration curve. These clusters were found to arrive early in the acquisition time, thus they are likely to be influenced by overshoot effects. A possible explanation for the observation is a recovery of the electronic pixel response from saturation effects in between the time the preamplifier output is above threshold due to the initial, real signal of the particle and the rerise above threshold due to the overshoot. This hypothesis has to be tested in future work.

Uniformity of the Detector Response over the Sensitive Area and Radiation Damage In addition to the variations of the detector response over the sensitive area (see Section 7.1.5), significant changes of the detector response were observed over the time of the studies presented in this thesis (see Section 7.1.6). Radiation damage of the sensor is known to result in a shorter life time of charge carriers and in a decrease of the material resistivity in the damaged zone (Jakubek et al. (2012)). The changes in the response could only be partially corrected for upon recalibrating the detector. On the other hand, healing of radiation damage with time could be observed in different regions.

Identifying the sources of the changes in the detector response turned out to be difficult, since in between the measurement campaigns at HIT the detector was used for

^aPersonal communication with J. Jakubek, IEAP, CTU in Prague.

other measurements, e.g. a long term study in a nuclear reactor, where the detector was exposed to intense neutron radiation^a. Details of these measurements or information on the dose the detector experienced are not available to the author. Therefore, a dedicated study is needed to quantify the radiation damage the detector suffers from ion beams.

The results presented in Section 7.1.6 show the importance of a frequent monitoring of the detector response. In addition, establishing a monitoring and correction procedure should be considered. Such approach however requires further studies. In particular, the relation between changes in the detector response and different ion species and energy spectra need to be understood.

8.2 Energy-Loss Measurements

The energy response of the Timepix detector is calibrated using photon beams (see Section 5.2.4 for details). No detailed analysis of the response in ion beams in the therapeutically used energy range, exhibiting much higher energy depositions in the detector, has been published before. Therefore, the potential of the Timepix detector for direct particle energy-loss measurements on a single ion basis was analyzed in Section 7.2. Different ion species and energy ranges were included in the study. Both, ions of low energies stopping in the sensor and ions of therapeutically used energies crossing the sensor, are present in mixed radiation fields resulting from fragmentation of carbon ions in a target or the patient and are therefore of clinical relevance. In the following, the findings of these studies are discussed.

Lithium (3.3- 4.7 MeV/u) Clusters due to lithium ions stopping in the detector show an up to -17.7% lower signal than predicted by theory. This was expected, since the high energy deposition in a small volume leads to saturation effects. Moreover, at the used bias voltage of 10 V, the sensor is known to have a non-depleted zone of approximately 100 μm thickness^b. The range of the lithium ions in the sensor is of the same order (approximately 120 μm for the lower lithium energy investigated). Due to the slower charge collection from this zone, the influence of recombination effects increases, resulting in a possible further decrease of the detected cluster signal. This hypothesis should be verified in measurements with a fully depleted sensor.

Due to the low range of the lithium ions, possible uncertainties in the measurement set-up assumed in the calculation, e.g. small changes in the water-equivalent-thickness of the air layer between vacuum exit window and detector from the actual experimental set-up, can result in large errors. A reduction of the set-up uncertainty can be achieved

^aPersonal communication with C. Granja, IEAP, CTU in Prague.

^bPersonal communication with P. Soukup, IEAP, CTU in Prague.

by performing measurements in vacuum, like it was done in the case of the low energy proton and deuterium ions studied, for which an agreement with the reference within $\pm 5.7\%$ was obtained. For high energy ion beams these uncertainties are less significant since in the corresponding region the depth dose distribution describing the ionization is flat, according to the Bethe-Bloch-equation.

Protons (0.55 - 221 MeV) For protons of therapeutically used initial energies, an agreement of the measured mean cluster signal and calculated mean energy-loss within $\pm 9\%$ was found. To determine the mean cluster signal, clusters due to particles arriving at the end of the acquisition time and clusters due to secondary radiation were excluded from the analysis using a constraint on the corresponding cluster signals (see Section 7.2.1 for details). However, the procedure applied in Section 7.2 also implies excluding clusters due to primary ions, e.g. for protons of high initial energies which show energy-loss distributions with extensions towards high values (Landau-tail). Cutting this extension leads to an underestimation of the mean cluster signal value, as was observed in the measurements. An improvement could be achieved by defining a different constraint to exclude clusters due to ions arriving at the end of the acquisition time. One possibility would be exploiting the information of the acquisition time itself, as will be available in the next detector generation (Poikela et al. (2012)).

Also for protons of very low initial energies (0.55 and 1 MeV) an agreement of the measured mean cluster signal to the expected energy-loss within $\pm 5.7\%$ was found. These findings indicate, that the Timepix detector is highly promising for measurements of 2-dimensional LET-distributions for proton beam therapy, from the entrance to the Bragg peak area.

Carbon and Oxygen (89 - 430 MeV/u) In carbon and oxygen ion beams of the highest initial energies available at HIT ($E_{\text{initial}}=430$ MeV/u) deviations of the mean cluster signal from the expected energy-loss values in the same range as for protons were observed. In the case of lower initial ion energies, i.e. an increasing energy deposition in the sensitive detector layer, the deviations increase up to -17.6% for carbon ions and up to -31.2% for oxygen ions. It was shown that the increasing deviations can be assigned to saturation effects in pixels located in the cluster center (see discussion on saturation effects in the previous section). Possible improvements could be achieved by spreading the deposited signal over more pixels and therefore reducing the influence of the saturation effect. While a reduction of the bias voltage to the lowest possible value of 5 V was found to be of limited effectiveness, tilting the detector as investigated in Opalka et al. (2013) involves other challenges, like for example an increased demand on precisely knowing the incident angle of the ion to correctly estimate the path length in the sensor.

A further idea to improve energy-loss measurements in carbon and oxygen ion beams is to exploit the information comprised in the signal of the low energy rim observed around high signal clusters^a. According to the most recent investigations, this rim is due to induced charge (see explanations in Section 5.2.2). The charge distribution induced in the electrodes is correlated to the charge released in the sensor by the ion. Therefore, the signal in the rim might provide enhanced information on the overall charge released, even if the overall signal itself is influenced by saturation effects. Before such a method can be applied for energy-loss measurements, further studies on the correlation of the signal in the rim to the deposited charge and the related uncertainties are required.

To understand the obtained deviations of the mean cluster signals from the expected energy-loss, in addition, influences of the bias voltage and changes of the detector response over time (see discussion in Section 7.2.4) need to be considered.

Reference Data In this work, the libamtrack software (see Section 5.4.3) was used to determine the expected energy-loss for high energy ions crossing the sensor. The calculation of the energy-loss in libamtrack is based on the Bethe-equation to calculate the stopping power and a continuous-slowing-down-approach. Therefore, the ions are assumed to traverse the stopping material on straight lines, neglecting an increase in the path length due to scattering.

Another possibility to determine the expected energy-loss is the use of stopping power tables, like the tables provided in ICRU49 (1999) and ICRU73 (2005). The deviations between the energy-loss in 300 μm silicon calculated with libamtrack as described in Section 6.2.1 and corresponding calculation based on the ICRU tables and linear interpolations between the tabulated data are -0.59% for protons of $E_{\text{initial}}=220$ MeV, i.e. the highest initial proton energy investigated, and -3.03% for carbon ions of $E_{\text{initial}}=89$ MeV/u, i.e. the lowest carbon ion energy studied.

A further possibility to derive energy-loss data are Monte Carlo simulations, using e.g. FLUKA (Ferrari et al. (2005); Battistoni et al. (2007)) or Geant4 code (Agostinelli et al. (2003); Allison et al. (2006)).

Energy-Loss Straggling For protons, the shapes of the measured cluster signal distributions follow the expected trends of the Vavilov theory for energy-loss distributions (see Section 7.2.2), being Gaussian-like for low initial proton energies and resembling a Landau-distribution for the higher initial proton energies studied. In general, the measured distributions are wider than the calculated distributions (5.8 - 16.7% in FWHM). This indicates that the energy-loss straggling in the material in the beam path cannot

^aPersonal communication with J. Jakubek, IEAP, CTU in Prague.

be neglected for protons. Scattering of protons in the tungsten wires of the multi-wire proportional chambers is expected to have a significant influence on the distributions. For two chambers the wires have a radius of 25 μm at a lattice constant of 1 mm, while for the other two the distance is 10 μm at a lattice constant of 2 mm (Parodi et al. (2012)). A possibility to account for the tungsten material in the chambers in a simple manner is to include a thin tungsten layer in Monte Carlo calculations, as proposed in Parodi et al. (2012).

In measurements in carbon ion beams of initial energies between 175 and 271 MeV/u, the distributions of the most probable cluster signal was found to agree well with the calculated energy-loss distributions, while for the highest carbon ion energy studied, the width of the measured distribution was found to be by -36% narrower than the calculated distribution, what is still to be understood. For carbon ions of 130 MeV/u and below, the cluster signal distributions were found to be significantly wider than the calculated energy-loss distributions. The deviations increase with decreasing ion energy. At the same time, effects of saturation on the cluster signal were found to increasingly influence the energy-loss measurements. It needs to be verified, whether the increasing widths of the distributions are also connected to the saturation effect. Further effects widening the distributions are overshoot effects and effects of particles arriving towards the end of the acquisition time. Also these effects get more significant with decreasing carbon ion energy, and the related increasing energy deposition in the sensor. As discussed above, both effects can likely be eliminated using detectors of the new Timepix3 generation. The results indicate that for carbon ions energy-loss straggling in the beam beam line constitutes does not influence the energy-loss straggling in the detector. For oxygen ions similar results as in carbon ion beams were obtained.

8.3 Ion Spectroscopy

The third part of the experiments and results presented in this thesis (Section 7.3) focuses on the possibility to perform ion spectroscopy measurements with the Timepix detector.

Identification of Ion Species and Verification The approach to ion spectroscopy presented in this work is based on the evaluation of 2-dimensional histograms showing the distributions of the cluster size and the cluster signal. To identify the ion species, measurements in different PMMA depths were used (see Section 7.3.1).

The assignment of the ion species to the various areas in the histograms, as well as the performance of the completely new concept, was verified by comparing the fragmentation of carbon ions in water to experimental data presented in Haettner (2006)

(see Section 7.3.2). To quantitatively evaluate the measurements, hand-drawn regions of interest were defined in the 2-dimensional cluster signal and cluster size distributions. Despite minor deviations in the experimental set-ups (see Table 6.2), the relative fractions of hydrogen, helium, beryllium, and boron fragments measured at angles of 2° , 4° , and 6° from the beam axis agree within the limits of uncertainties (Δ_{ref}) with the numbers presented in Haettner (2006), except for the relative fraction of hydrogen at an angle of 2° (deviation: 8.5%, within $1.1\Delta_{\text{ref}}$). For lithium ion species the relative deviations to the reference are larger (2° : -18.3%, 4° : -28.9%, within $2.3\Delta_{\text{ref}}$). Based on these results, the attained identification of ion species was considered as correct. Possibilities for further improvements and alternatives for the separation between ion species, currently performed according to visual judgment, will be discussed below.

Impact of the Energy-Loss Measurements on Ion Spectroscopy with the Timepix Detector

The quality of energy-loss measurements with the Timepix detector discussed in the previous section directly influences the quality of the input data for ion spectroscopy. The most significant influence observed is due to saturation effects, reducing the cluster signal in the case of ions depositing a high amount of energy in the sensor. Since the saturation effect increases with increasing energy deposition, above a certain energy-loss value a compression of the energy-loss distribution obtained in mixed particle fields is expected. Consequently, the potential of distinguishing between ion species according to the cluster signal is decreased. On the other hand, also the cluster size is dependent on the energy deposition of an ion in the sensor. It was observed to partially complement the cluster signal as a separation parameter. However, attention is needed when exploiting this parameter since the cluster size itself is more liable to influences by radiation damage in the detector than the cluster signal (see Section 7.1.5).

A comparison of the 2-dimensional distributions obtained in different PMMA depths visualizes differences in the separability between ion species. While in the entrance channel (e.g. for ^{12}C of $E_{\text{initial}}=271$ MeV/u behind 50 mm PMMA, Figure 7.62 b) all ion species between proton and carbon are clearly distinguishable, with increasing material depths the signals smear out and regions due to different ion species merge. A possible explanation for these findings is increasing energy-loss straggling of the secondary particles. The effect is of particular significance when the signal of a frequent ion species overlaps the signal of a rare ion species, as it was observed in the case of helium and lithium ions.

Investigations of Lateral Fragment Distributions In the investigations of lateral fragment distributions (see Section 7.3.3), the possibility to perform ion spectroscopy studies directly behind a phantom could be demonstrated. In this way, uncertainties

due to scattering behind the phantom can be reduced and the set-up can be used at irradiation sites with limited space.

To study the impact of scattering behind the phantom experimentally, the following approach could be used: For a given ion energy and angle from the beam axis, the fragment spectra is investigated at different distances behind a phantom, ranging between distances used in previous studies (e.g. 305 cm in Gunzert-Marx et al. (2008)) and the smallest distance possible with the Timepix detector (few mm). A comparison of the spectra could reveal influences of the interaction kinematics in the fragmentation processes in comparison to influences of scattering in the material (air) between phantom and detector and reduce possible related uncertainties in Monte Carlo simulations.

Fragmentation in Different Materials Using the advantage of the new flexible method, a study comparing fragment-distributions behind different materials was performed on the beam axis (see Section 7.3.4). An up to 48.5% lower number of fragments per primary carbon ion detected was observed behind steel than behind PMMA, while both phantoms have the same water-equivalent thickness.

Before drawing conclusions on the fragmentation processes itself, the intrinsic geometrical differences in the two measurement set-ups have to be eliminated. At the same water-equivalent thickness, the steel phantom is in beam direction approximately 4.8 times thinner than the PMMA phantom. Therefore, the angular distributions of the fragments behind the phantoms are expected to be different, even for the same reactions kinematics in single collisions. Further studies are needed to understand these aspects of the results quantitatively. Nonetheless, the measurements could be used straightforward, e.g. to benchmark Monte Carlo calculations, considering the given geometry also in the simulations.

Considerations on Detector Settings and Evaluation Parameters While dedicated parameters for the detector settings and the evaluation procedure were found in studies in pure ion beams for protons and carbon ions, measurements in mixed ion fields require settings applicable simultaneously for all ion species comprised in the mixed field. For further measurements, in particular a detailed study on dependencies of the separability between ion species on the bias voltage is needed. Also the employed modification of the roundness constraint and height of the roundness determination depending on the cluster size, as presented in Section 6.3, is to be considered as a first approximation and can certainly be optimized. Moreover, a detailed analysis on the nature of clusters excluded from the analysis due to either the size or the roundness constraint should be performed. For example, in the study of fragmentation in different materials, for the measurement behind PMMA almost 10% of the clusters were excluded from the analysis due to an insufficient roundness. The relative number

of suspended clusters can vary for different ion species, due to their different sizes. Further improvements could be achieved by separating clusters containing the signal of two or more ions, e.g. using information on the number of local maxima in each cluster, as proposed in Schellhammer (2013). In the future, a technique to include clusters due to particles traversing the detector not perpendicularly in the analysis by correcting for the increased cluster size and cluster signal should be considered. Conclusions on the azimuthal direction of the particles can be drawn from the shape and pixel values of the cluster, as shown in Hoang et al. (2012). In this case, variations of saturation effects due to the spread of the signal over a larger number of pixels and increased influences of energy-loss straggling have to be considered.

Possible Improvements in the Discrimination Between Ion Species a) To improve the accuracy of the separation between different ion species in the 2-dimensional histograms and to automate the procedure, a more sophisticated approach than the hand-drawn regions of interest applied in this work (see for example Figure 7.64) is required. One possibility is the implementation of an algorithm to find bottom reversal points in the distributions and separating the high intensity areas along the corresponding trajectories. Another possibility is the employment of clustering algorithms to assign the clusters according to their size and signal to groups representing the ion species. Besides an improvement in separation between different areas, also the overlap of areas containing the signal of different ion species should be accounted for, using e.g. fits of Vavilov distributions along the cluster signal axis.

b) The cluster size is largely influenced by the detector area in which the respective ion was registered (see Section 7.1.5). Therefore, an improvement of the resolution in terms of cluster size could be achieved by selecting only clusters detected in homogeneous detector areas. However, in the case of the detector used for this work areas which are homogeneous for all ion species and energies investigated are very small (see Appendix B). Therefore, employing a new, undamaged detector would presumably enhance the separability.

c) Further improvements could be achieved by complementing the cluster size and cluster signal currently used for discrimination by other parameters, for example exploiting the low signal rim, caused by induced currents, information on the dip in the center of high signal clusters, or the cluster height. For illustration, in Figure 8.1 a 2-dimensional histogram showing the cluster signal and the cluster height for the measurement behind steel (see Section 7.3) is shown. Different areas with intense cluster population can be seen. Detailed studies are needed to correctly assign these areas to the different ion species and to analyze the improvement which can be achieved when using the cluster height as a further separation parameter.

d) Further information could presumably be retrieved by determining the energy-loss

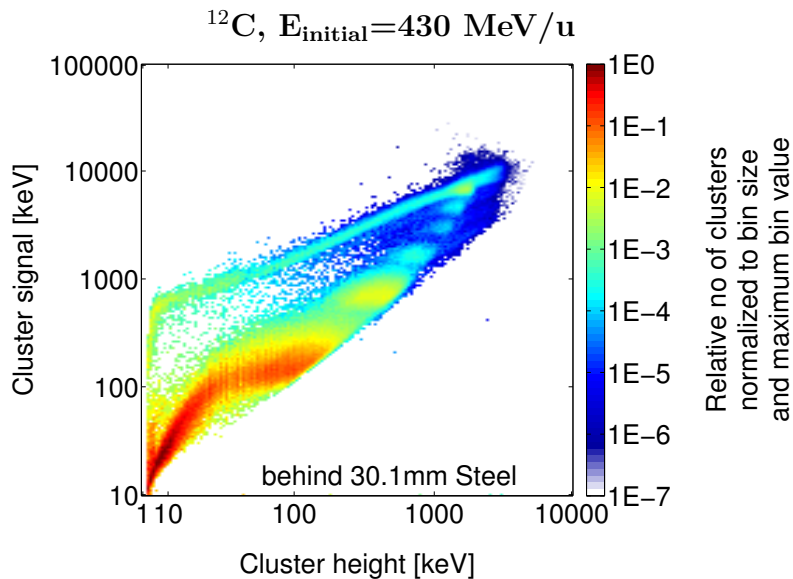


Figure 8.1: 2-dimensional histogram showing the distributions of cluster signal and cluster height for measurements behind 30.1 mm of steel. Settings: $t_{\text{acq}}=1$ ms, $V_{\text{bias}}=10$ V, $A_{\text{cluster}} \geq 4$ pixel, $\text{roundness}_{\text{cluster}}^{\text{min}}$ as depicted in Figure 6.8. To exclude detector artefacts from the analysis, a constraint on the maximum average cluster signal of 200 keV was used.

of a particle not in only one, but in two parallel detector layers, using the voxel geometry of Timepix (Soukup et al. (2011)). Since ions exhibit distinct energy-loss curves (Leo (1994)), especially for low energy ions the additional energy-loss measurement could improve the separation. To improve the resolution, deceleration of the particles between the detector layers should be tested. The additional material might however cause other problems, like scattering of the particles and resulting inaccuracies in the matching of the related clusters in both detector layers.

e) The information of two detectors operated in time coincidence is also exploited in an approach currently studied in the research group. A detector layer in front of the phantom registering the primary carbon ions is used for absolute normalization of the fragmentation data acquired behind the phantom.

f) Further information on the energy-loss characteristics of an ion using only one detector layer can be achieved by rotating the detector against the ion direction. This approach is currently under investigation at the Institute of Experimental and Applied Physics of the Czech Technical University in Prague (Opalka et al. (2012, 2013)).

8.4 Future Impact of the Results

With the novel approach to ion spectroscopy presented in this work, fragmentation studies which are in agreement with data acquired with standard methods can be carried out. The presented method was found to be in particular advantageous to study

distributions of ion species in the range of energy and target thickness combinations for which the influences of energy-loss straggling are low, but for which current methods based on time-of-flight measurements are afflicted with larger uncertainties.

After further developments, as discussed in the previous sections, the presented method is promising to enable different, clinically interesting investigations. In comparison to existing methods for ion spectroscopy, the new approach employs a much smaller and easier to handle set-up. Therefore, fast and straightforward sampling of data over a wide phase-space is possible. This includes also fragmentation studies in primary oxygen- and helium-ion beams, being the future candidates for heavy ion beam therapy, for which the amount of data currently available is even less than for carbon ions. Among the possible applications are studies of the fragmentation in different materials (e.g. water, PMMA, bone), experimental set-ups (e.g. very small targets) or in inhomogeneous phantoms. Due to the advantage that the detector can be placed close to the target, the resulting spectra are less influenced by scattering processes in the air behind the target than data available from current ion spectroscopy methods. Therefore, a prospective use of the presented method is to benchmark the fragmentation models used in current treatment planning systems.

While separation between different isotopes of an ion species, as for example presented in Gunzert-Marx et al. (2008) for protons, deuterium and tritium ions, is not yet possible, the new method might have advantages for heavier fragments, which show narrower angular distributions and have not been studied by Gunzert-Marx et al. (2008). In general, the presented new approach complements existing and future set-ups, like e.g. the FIRST experiment (Golosio et al. (2011); Pleskac et al. (2012); Agodi et al. (2012)) aiming for the measurement of double differential cross sections of nuclear fragmentation processes relevant to hadron therapy and space radiation protection applications (see Section 4 for details).

Moreover, the achieved differentiation between ion species can be used in further applications of the Timepix detector for ion beam therapy. One example is monitoring of carbon ion-beam therapy by tracking of secondary particles leaving the patient (Amaldi et al. (2010); Gwosch et al. (2013)). Including information on the detected ion species could possibly enhance the knowledge on the dose distribution in the patient.

A further advantage of the new system compared to existing methods, is the transportability of the set-up, enabling comparative investigations at different facilities. A possible application could be the investigation of fragments produced in the degrader material used in passive beam lines to govern the ion energy. A comparison of the spectra with measurements in a beam with active energy selection, e.g. at HIT, could verify the complete removal of these fragments at a glance.

9 Summary and Conclusions

In carbon ion radiotherapy, nuclear fragmentation processes in tissue lead to an attenuation of the primary particle flux and the build-up of lighter projectile fragments. The radio-biological effectiveness of these secondary particles differs from the primary ions and must be considered in the physical beam models used for treatment planning. To experimentally determine the ion spectra, up to now, mainly large apparatus based on scintillators and time-of-flight-measurements have been utilized (e.g. Matsufuji et al. (2003); Gunzert-Marx et al. (2008)). This limits the flexibility and the available data.

In this work, a novel experimental technique for ion spectroscopy of therapeutic ion beams based on a pixelated semiconductor detector is presented. The small and highly flexible Timepix detector has originally been designed for imaging applications in photon beams. It exhibits a high spatial resolution enabling the detection of single particles. It offers a straightforward operation, allowing its application in versatile experimental set-ups. Charge released in the sensor by an ion spreads out during charge collection and is collected by several adjacent pixels, forming so called signal clusters. The number of pixels in a cluster and the sum of the signal in these pixels is related to the energy-loss of the respective particle in the sensor.

Experiences on the detector response in therapeutic ion beams are limited. Against this background, the detector response in therapeutic ion beams was characterized in detail, before investigating its capability for energy-loss measurements on a single ion basis, and studying the possibility to perform ion spectroscopy measurements with the detector.

Characterization of the Detector Response in Therapeutic Ion Beams To characterize the detector response, influences on the signal of the acquisition time (i.e. the duration of one measurement frame), the applied bias voltage and the incident angle of a particle on the sensor were studied. Moreover, the uniformity of the detector response over the sensitive area and changes of the response with time were investigated. In addition, the sources of unexpected signal were identified.

The detector response to therapeutic proton beams was found to be as expected. In carbon ion beams of therapeutically used energies, the response was found to be largely different from the behavior in low energy ion (e.g. α -particles) or photon irradiation (see results presented in Section 7.1). The signal clusters created by the carbon ions

9 Summary and Conclusions

were found to depend on the ion energy, the applied bias voltage, and interplay effects between them.

Among the most significant findings are overshoots of the signal in single pixels due to oscillations in the pixel electronics, observed for high energy depositions in the sensor. This effect was found to influence the measured cluster signal distribution and is therefore of direct relevance for energy-loss and ion spectroscopy measurements with the detector. Moreover, complex dependencies of the detector response on the applied bias voltage were observed.

Concerning the uniformity of the detector response over the sensitive area, influences of the impact location of an ion on the sensor on the size of the evolving cluster were observed. The variations of the cluster sizes in different regions can be up to 60%. Differences in the overall cluster signal in different sensor regions were found to be up to 40%. Moreover, changes of the detector response with time, monitored in a dedicated study over a time interval of 16 months, were noticed, which could only be partially corrected for by recalibrating the energy response of the detector. Therefore, for a quantitative analysis of the cluster signal the detector should be regularly tested for possible changes in its response and if possible these changes should be corrected for. Since each sensor may exhibit specific characteristics, based e.g. on its radiation history, analogous studies of the detector response need to be repeated for new sensors.

Energy-Loss Measurements To study the feasibility of energy-loss measurements on a single ion basis with the Timepix detector, the measured mean cluster signals were compared to the expected mean energy loss (see Section 7.2).

For proton beams of therapeutically used initial energies (48 - 221 MeV) an agreement within $\pm 8.8\%$ was observed. For the investigated proton energies, the mean cluster signal of up to approximately 800 keV is below the signal range at which overshoot effects and saturation start to affect the calibration curve (900 - 1000 keV/pixel). It can be concluded that the Timepix detector, with the current assumption of the calibration curve being linear above approximately 20 keV, is well suited for energy-loss measurements of protons with therapeutically used initial energies. Also in low energy proton and deuterium beams (down to 0.5 MeV/u) a good agreement of the mean cluster signal with the theoretical value was obtained for a fully-depleted sensor (within $\pm 5.7\%$ for $V_{\text{bias}}=22\text{ V}$).

In contrast, for low energy lithium ions (3.3 - 4.7 MeV/u), as well as for carbon ions (89 - 430 MeV/u) and oxygen ions (127 - 421 MeV/u), mean cluster signals lower than expected were observed. The deviations are up to -31.2% (^{16}O , $E_{\text{initial}}=430\text{ MeV/u}$, $V_{\text{bias}}=10\text{ V}$). Possible reasons for this saturation effect are recombination of charge carriers in the sensor and a different behavior of the pixel electronics for such a high signal. The findings of the studies indicate that the currently used linear extrapolation

tion of the calibration curve towards high energy levels is not suitable for energy-loss measurements of ions depositing high energies in the sensor.

Besides the mean energy loss, the energy loss straggling in the silicon sensor was investigated and compared to calculated energy loss distributions (Vavilov theory). Evolutions in the cluster signal distributions from Gaussian- to Landau-shape with increasing ion energy follow the expected trends. For protons, a systematic broadening (5.8-16.7% increase in FWHM) of the measured compared to the calculated distributions was observed. The reason is presumably insufficient modeling of the beam line components in the reference calculations and incomplete signal digitization for some of the clusters. The capabilities of new generation detectors (Timepix3) can most likely eliminate this effect.

For carbon and oxygen ions of medium energies available at HIT (130-271 MeV/u) an agreement of the FWHM with calculated energy loss distributions within $\pm 25\%$ was found, while for the highest energy studied even narrower distributions than expected from calculations were observed in the measurements (deviations of up to -36%). For lower initial ion energies, the measured distributions were found to be significantly broader (up to 120% increase in FWHM compared to calculations). Saturation effects, overshoot effects and insufficient time for digitization of the signal for particles arriving at the end of the acquisition time supposedly contribute to the broadening.

Ion Spectroscopy The presented approach to ion spectroscopy measurements using pattern recognition analysis in a single pixelated silicon detector fundamentally differs from time-of-flight measurements and energy measurements in scintillators used up to now for this purpose. The discrimination between ion species is based on the parameters cluster size and cluster signal (see Section 7.3). To identify the ion species in the obtained spectra, measurements in different material depths were performed using the knowledge that lighter fragments have larger ranges in tissue and that for heavier ions larger energy depositions in the sensor and therefore higher cluster signals are expected.

To verify the method, a comparison of the fragmentation of carbon ions (400MeV/u) in 15.8 cm water to experimental data obtained with an established method (Haettner (2006)) was performed. In the spectra measured at angles of 2, 4, and 6° from the beam axis, the relative fractions of hydrogen, helium, beryllium and boron ions agree within the limits of uncertainty (Δ_{ref}) with the reference, except for the relative fraction of hydrogen at an angle of 2° (agreement within 1.1 Δ_{ref}). For lithium the agreement is within 2.3 Δ_{ref} .

Possible applications of the new ion spectroscopy method were also presented. It was shown that direct comparisons of fragment spectra measured behind different phantom materials are possible in a fast and straightforward manner. Moreover, measurements

9 Summary and Conclusions

directly behind targets can reduce uncertainties due to scattering of the fragments in the air between phantom and detector on the measured spectra. As an example, for ^{12}C -ions of $E_{\text{initial}}=430\text{ MeV/u}$, deviations in the fractions of the fragment species measured behind a PMMA and a steel phantom (both of 169 mm water-equivalent-thickness) normalized to the number of carbon ions detected of up to 49.4% were observed. The results of such studies are of interest for benchmarking physical models used for Monte Carlo simulations and treatment planning.

Concluding Remarks The presented results demonstrate, that with the presented approach, based on the evaluation of two cluster parameters and hand-drawn regions-of-interest in the spectra to discriminate between ion species, ion spectroscopy with a pixelated silicon detector is feasible for the investigated cases. The main advantages of the method are the flexibility of the small set-up and fast data acquisition. To extend the applicability of the method, in particular towards lower primary ion energies resulting in mixed ion spectra with increased influences of energy-loss straggling in the sensor, further investigations are needed. Employing a new generation of Timepix detectors (Timepix3) can presumably resolve a part of the existing problems. Combined with the suggested improvements, the presented method is promising to enable studies for a wide range of target materials and beam parameters in the future and to complement large experimental set-ups, like the FIRST experiment (Golosio et al. (2011); Pleskac et al. (2012); Agodi et al. (2012)).

Appendices

Appendix A: Determination of Cluster Signal in Mixed Operation Mode

In the following, the approximations needed in order to evaluate the results obtained in mixed operation mode presented in Section 7.1.1 are examined. For the determination of the cluster signal in mixed detector operation mode, pseudo energy values were calculated for all pixels operated in Timepix mode by averaging the signal of the adjacent pixels operated in energy mode. Furthermore, as described in Section 6.1.1, in the mixed operation mode a five times lower detector clock frequency was employed relative to the frequency used in the calibration measurement. This was corrected for by multiplying the pixel values by a factor of five before calibrating the data. To test the applicability of both approximations, in Figure A1 the resulting cluster signal distribution is compared to the cluster signal distribution obtained for the same ion species and energy with all detector pixels operated in energy mode. For both detector operation modes two peaks in the cluster signal distributions can be seen. There is however a shift in their positions towards lower cluster signals for measurements in mixed detector operation mode. Furthermore, the distribution obtained in mixed mode shows a larger spread of the cluster signal values, i.e. wider peaks. If the pixels operated in Timepix mode contain a large part of the cluster signal, creating a pseudo pixel value by calculating the mean value of the adjacent pixels can lead to a significant underestimation of the pixel value. Therefore, the mixed operation mode cannot be used to determine the exact cluster signal distributions. Its use to study acquisition time dependent effects of the cluster signal is however appropriate.

For small clusters like those induced by protons, the determination of the pseudo energy values for pixels operated in Timepix mode is less reliable than for larger clusters (e.g. induced by carbon ions). Due to the small size of the clusters, the main signal is

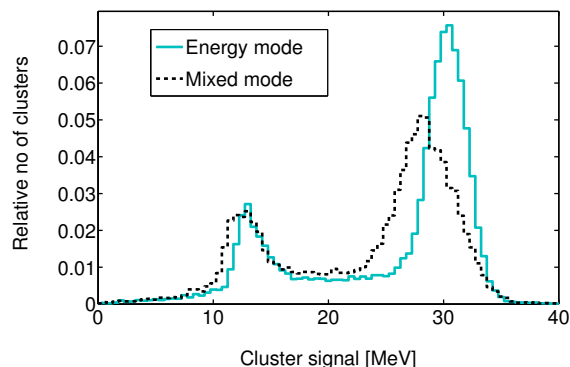


Figure A1: Cluster signal distribution obtained in a ^{12}C -beam of $E_{\text{initial}}=89\text{ MeV/u}$ for different detector operation modes. The distribution for the energy mode is the same as shown in Figure 7.3. In the mixed mode one out of four pixel was operated in Timepix mode. Settings: $V_{\text{bias}}=10\text{ V}$, $t_{\text{acq}}=5\text{ ms}$, $A_{\text{cluster}} \geq 30\text{ pixel}$, $\text{roundness}_{\text{cluster}} > 0.7375$ at 10% of cluster height.

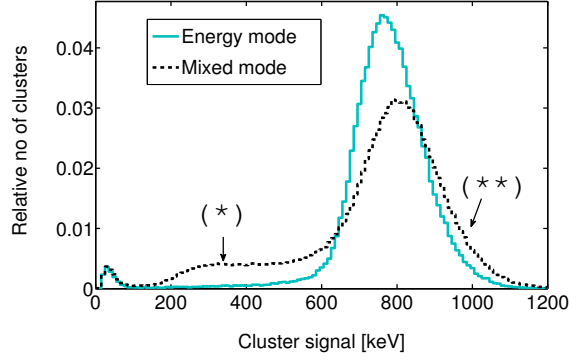


Figure A2: Cluster signal distribution obtained in a ^1H -beam of $E_{\text{initial}}=48$ MeV for different detector operation modes. The distribution for the energy mode is the same as shown in Figure 7.1. In the mixed mode one out of nine pixel was operated in Timepix mode. Explanations for differences in regions (*) and (**) are given in the text. Settings: $V_{\text{bias}}=10$ V, $t_{\text{acq}}=5$ ms, $A_{\text{cluster}} \geq 4$ pixel, $\text{roundness}_{\text{cluster}} > 0.6625$ at 5% of cluster height.

often concentrated in only one pixel. If this pixel is operated in Timepix-mode, the pixel value derived with the pseudo energy method is usually much lower than the initial signal in the pixel, leading to a lower overall cluster signal compared to measurements in pure energy mode (see Figure A2, (*)). On the other hand, if a pixel placed next to the pixel with a very high signal is operated in Timepix mode, the pixel value derived in the pseudo energy mode is higher than the initial signal in the pixel (**). This effect is however less significant, as high pixel values are statistically less probable. Influences of the described effects can be seen in the comparison of cluster signal distributions obtained for protons of $E_{\text{initial}}=48$ MeV in energy mode and in mixed mode shown in Figure A2.

Appendix B: Uniformity of the Detector Response over the Sensitive Area

The uniformity of the detector response over the sensitive area was studied as described in Section 6.1.5. For the evaluation, maps showing the distributions of the average cluster size, cluster signal and cluster height over the sensor were established. While in Section 7.1.5 only selected results of the study are presented, in this appendix an overview of all results obtained in the study can be found.

Figure A3 shows the results obtained in carbon ion beams of $E_{\text{initial}}=89, 271,$ and 430 MeV/u at a bias voltage of 10 V , while in Figures A4 and A5 the results for bias voltages of $5, 10,$ and 15 V for $E_{\text{initial}}=271$ and 430 MeV/u , respectively, are compared.

Similarly, in Figure A6 the results obtained in proton beams of $E_{\text{initial}}=48, 143,$ and 221 MeV at a bias voltage of 10 V are shown, while in Figures A7 to A9 for each respective energy the results for bias voltages of $5, 10,$ and 15 V are compared.

Explanations for the effects observed in different sensor areas can be found in Section 7.1.5.

^{12}C , $V_{\text{bias}}=10\text{ V}$

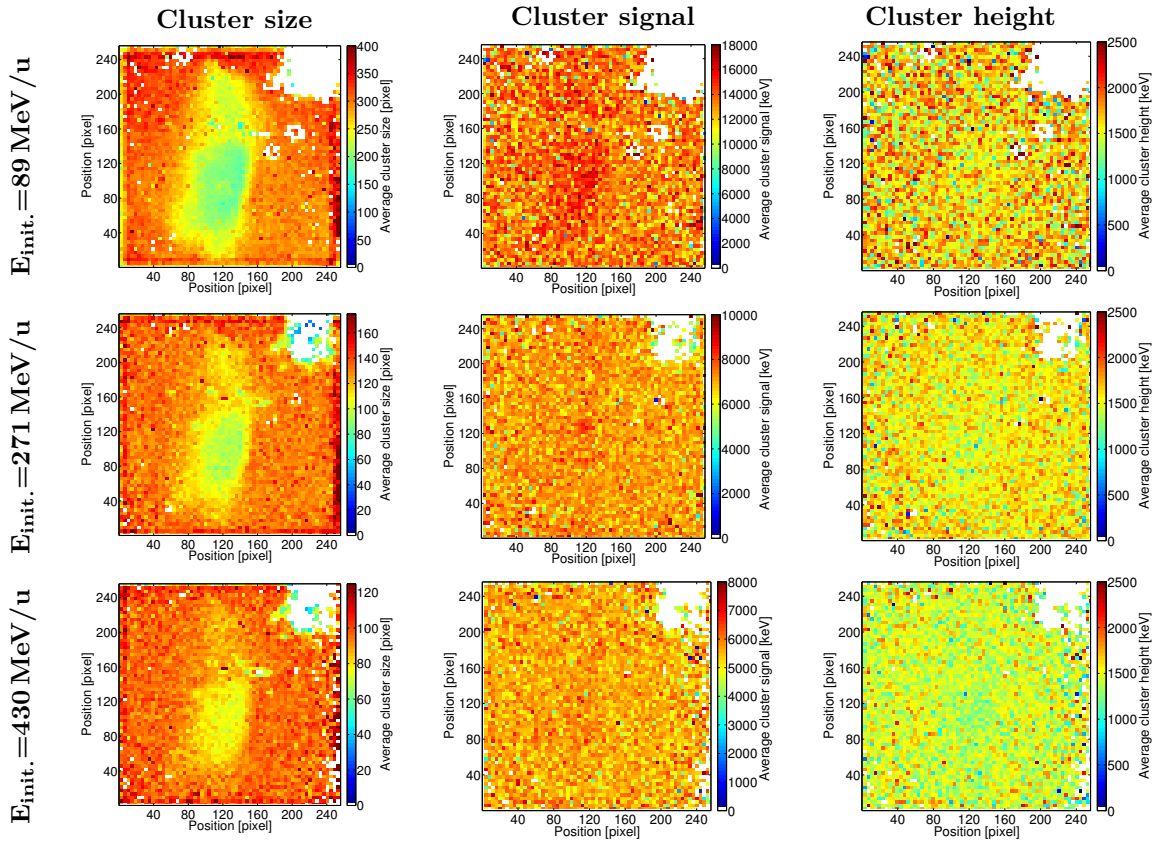


Figure A3: Distributions of average cluster size, cluster signal and cluster height over the sensitive detector area for carbon ions of different energies. Settings: $V_{\text{bias}}=10\text{ V}$, $t_{\text{acq}}=1\text{ ms}$, $A_{\text{cluster}} \geq 30\text{ pixel}$, $\text{roundness}_{\text{cluster}} > 0.7375$ at 10% of cluster height.

^{12}C , $E_{\text{initial}}=271\text{ MeV/u}$

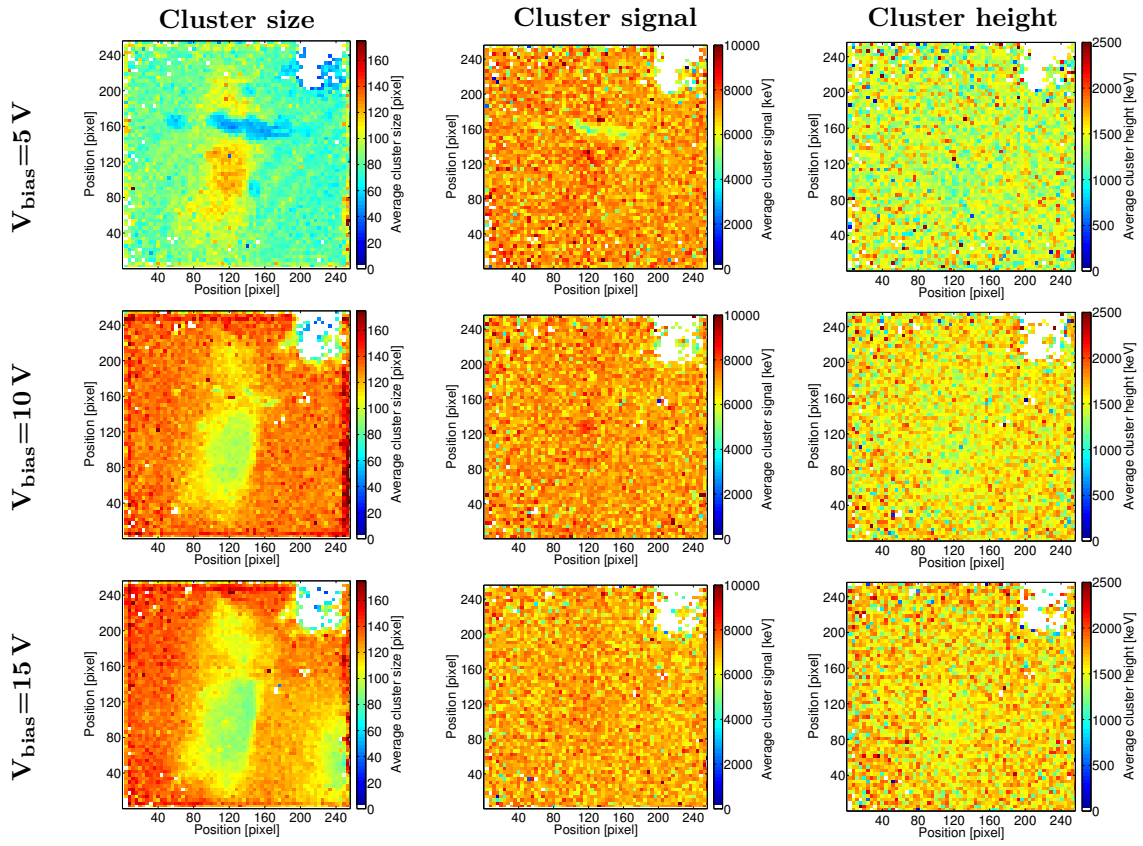


Figure A4: Distributions of average cluster size, cluster signal and cluster height over the sensitive detector area for different detector bias voltages. Settings: $V_{\text{bias}}=10\text{ V}$, $t_{\text{acq}}=1\text{ ms}$, $A_{\text{cluster}} \geq 30\text{ pixel}$, $\text{roundness}_{\text{cluster}} > 0.7375$ at 10% of cluster height.

^{12}C , $E_{\text{initial}}=430 \text{ MeV/u}$

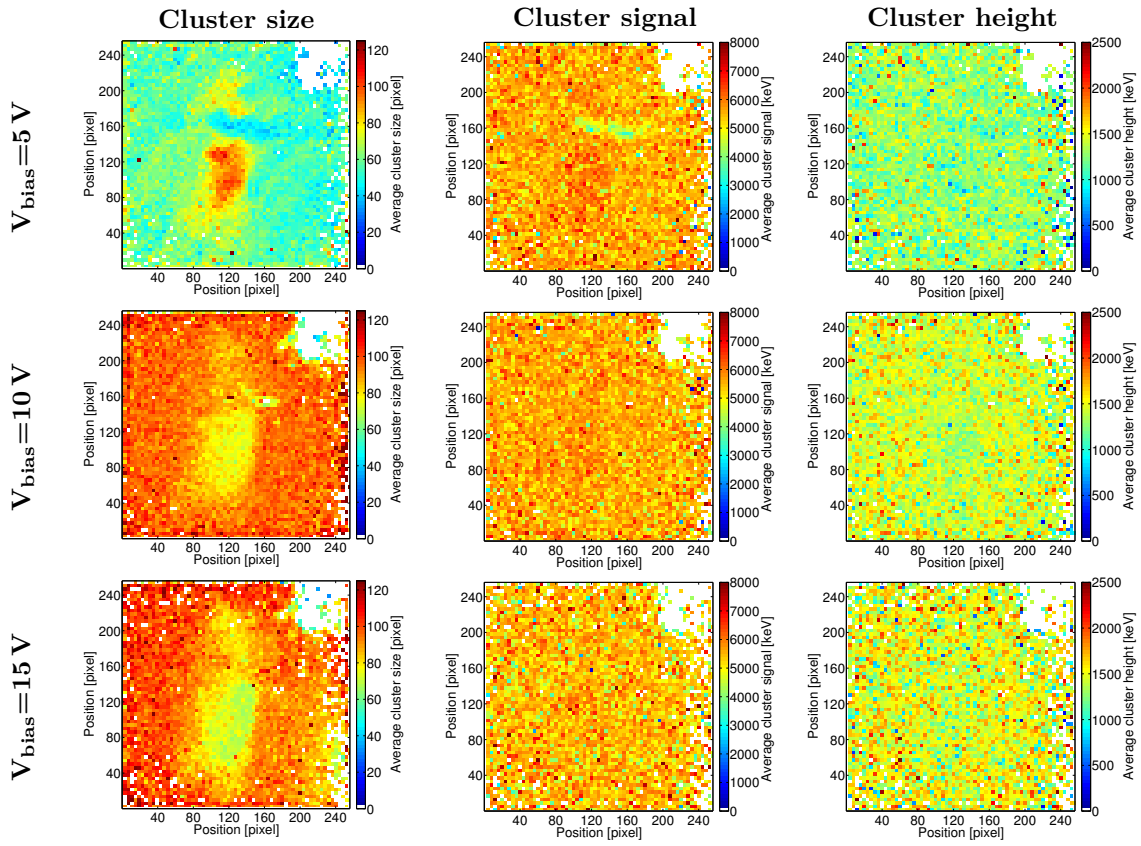


Figure A5: Distributions of average cluster size, cluster signal and cluster height over the sensitive detector area for different detector bias voltages. Settings: $V_{\text{bias}}=10 \text{ V}$, $t_{\text{acq}}=1 \text{ ms}$, $A_{\text{cluster}} \geq 30 \text{ pixel}$, $\text{roundness}_{\text{cluster}} > 0.7375$ at 10% of cluster height.

^1H , $V_{\text{bias}}=10\text{ V}$

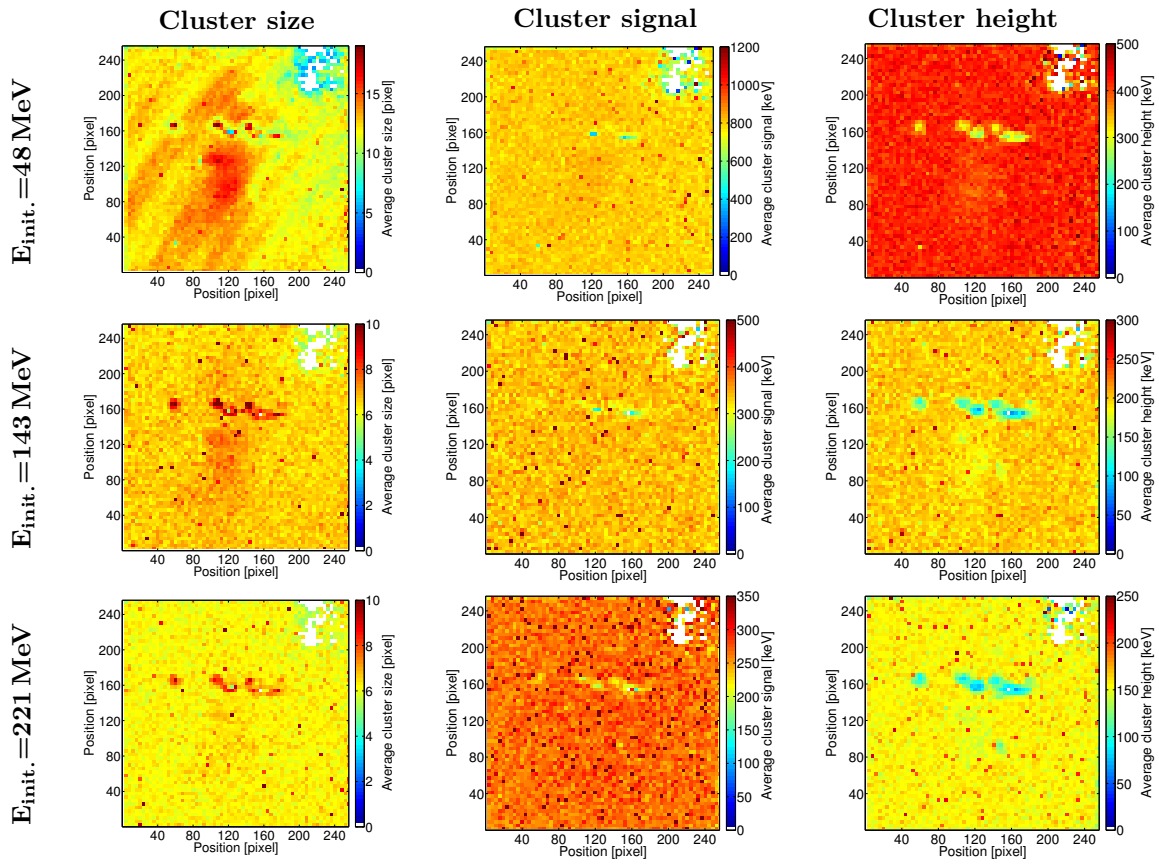


Figure A6: Distributions of average cluster size, cluster signal and cluster height over the sensitive detector area for protons of different energies. Settings: $V_{\text{bias}}=10\text{ V}$, $t_{\text{acq}}=1\text{ ms}$, $A_{\text{cluster}} \geq 4\text{ pixel}$, $\text{roundness}_{\text{cluster}} > 0.6625$ at 5% of cluster height.

${}^1\text{H}$, $E_{\text{initial}}=48\text{ MeV}$

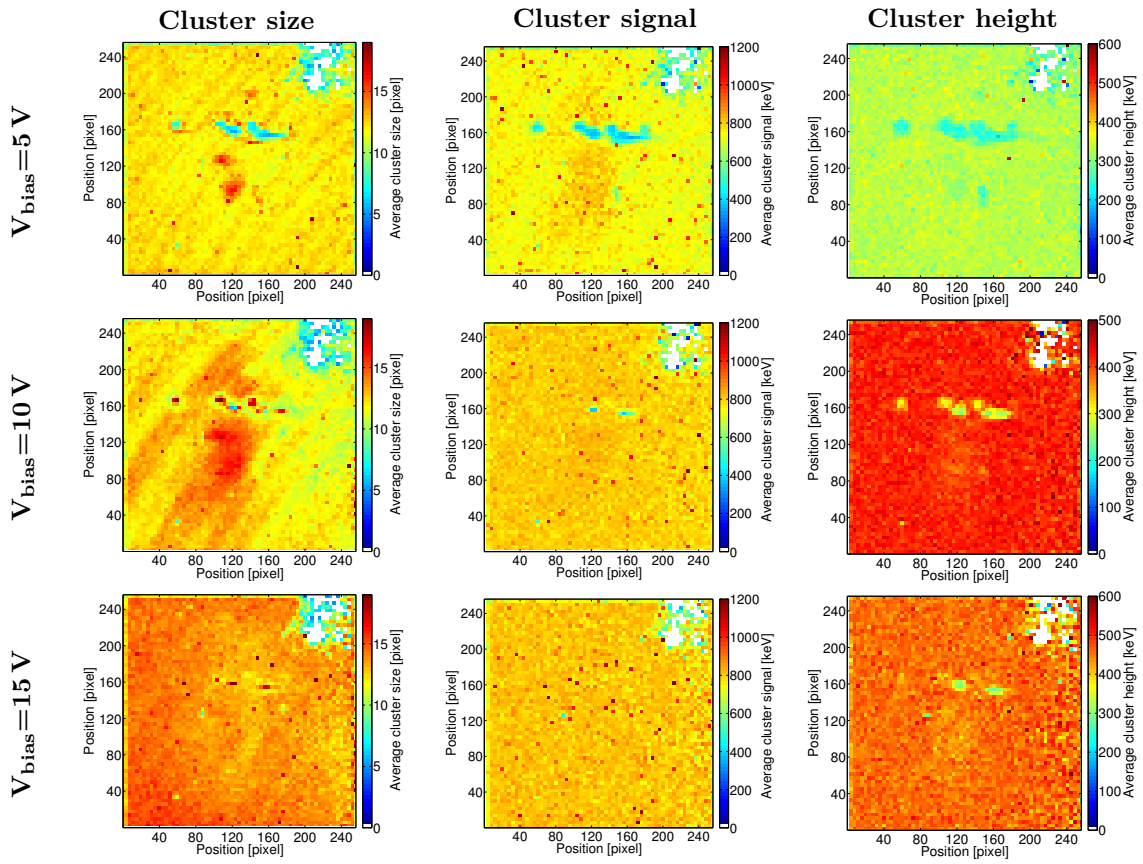


Figure A7: Distributions of average cluster size, cluster signal and cluster height over the sensitive detector area for different detector bias voltages. Settings: $V_{\text{bias}}=10\text{ V}$, $t_{\text{acq}}=1\text{ ms}$, $A_{\text{cluster}} \geq 4\text{ pixel}$, $\text{roundness}_{\text{cluster}} > 0.6625$ at 5% of cluster height.

^1H , $E_{\text{initial}}=143\text{ MeV}$

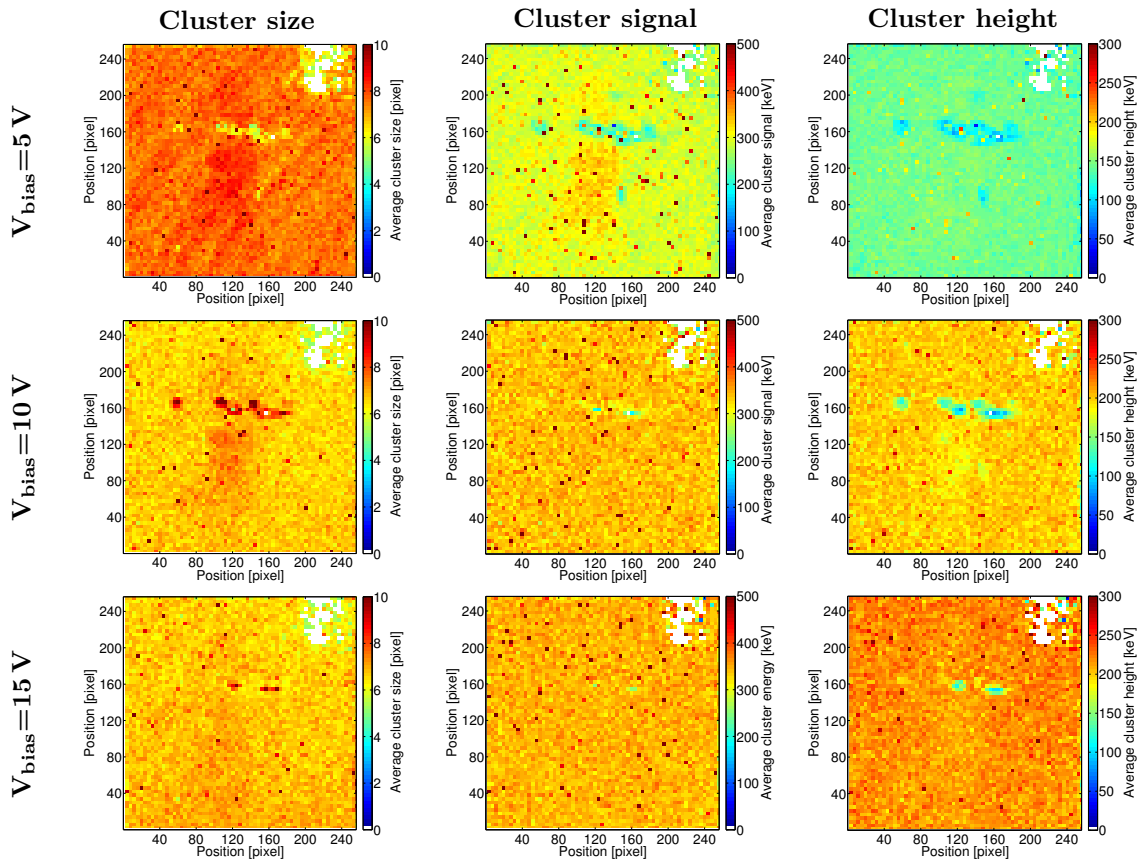


Figure A8: Distributions of average cluster size, cluster signal and cluster height over the sensitive detector area for different detector bias voltages. Settings: $V_{\text{bias}}=10\text{ V}$, $t_{\text{acq}}=1\text{ ms}$, $A_{\text{cluster}} \geq 4\text{ pixel}$, $\text{roundness}_{\text{cluster}} > 0.6625$ at 5% of cluster height.

^1H , $E_{\text{initial}}=221\text{ MeV}$

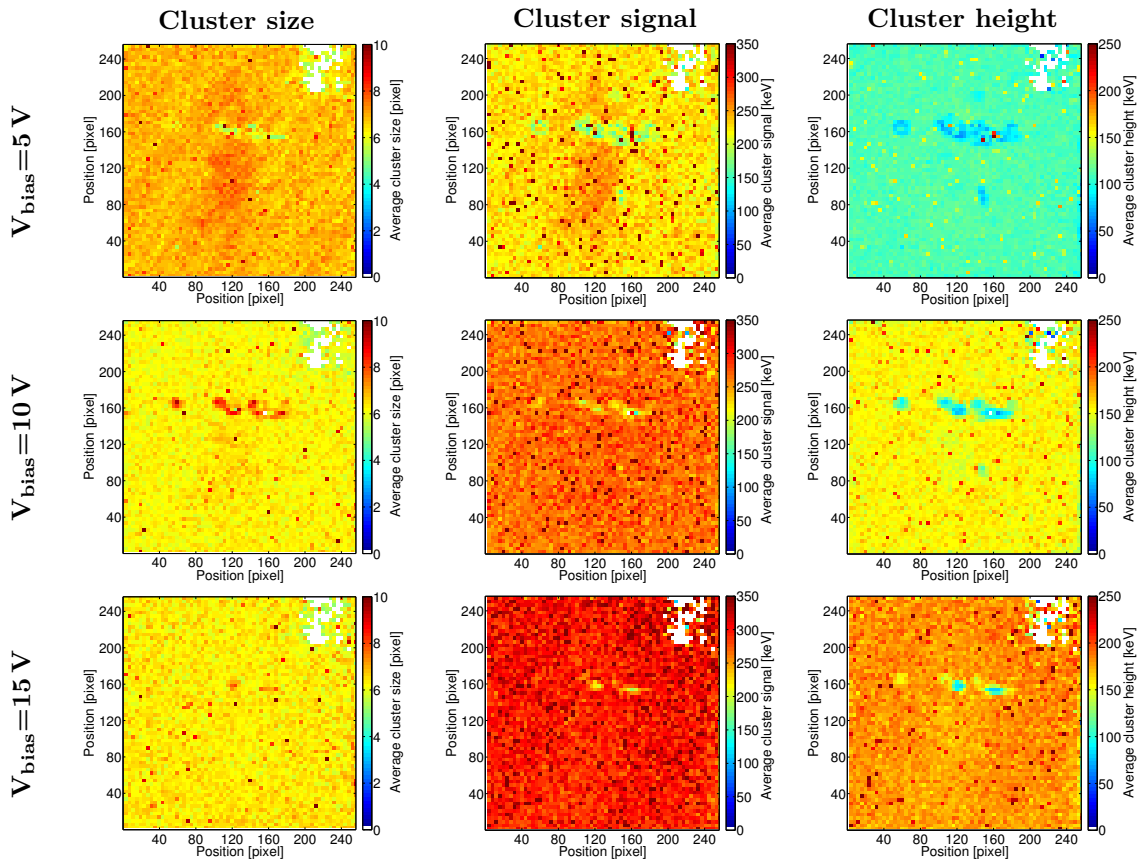


Figure A9: Distributions of average cluster size, cluster signal and cluster height over the sensitive detector area for different detector bias voltages. Settings: $V_{\text{bias}}=10\text{ V}$, $t_{\text{acq}}=1\text{ ms}$, $A_{\text{cluster}} \geq 4\text{ pixel}$, $\text{roundness}_{\text{cluster}} > 0.6625$ at 5% of cluster height.

Appendix C: Changes of the Uniformity of the Detector Response over the Sensitive Area with Time

The changes of the detector response with time were studied with the methodology described in Section 6.1.6. Besides investigating changes in the cluster size and cluster signal, maps of the cluster parameter distributions over the sensitive area were studied. While in Section 7.1.6 only selected results are presented, in the following an overview of all maps derived from the studies can be found. Information on which ion species and energies were studied in the four campaigns between October 2011 and January 2013 can be found in Table 7.1.

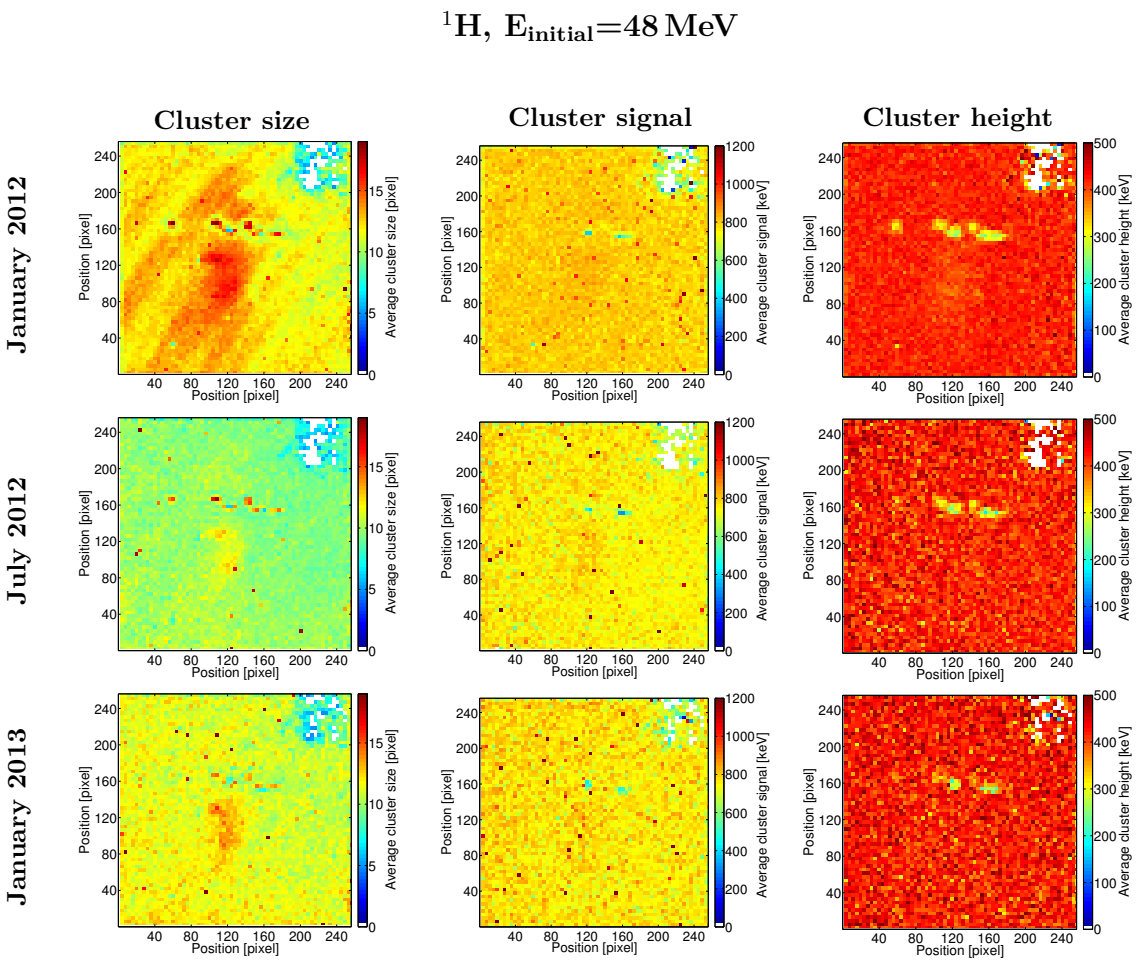


Figure A10: Maps showing the distributions of average cluster size, cluster signal and cluster height over the sensitive detector area for different measurement dates. Settings: $V_{\text{bias}}=10\text{ V}$, $t_{\text{acq}}=1\text{ ms}$, $A_{\text{cluster}} \geq 4\text{ pixel}$, $\text{roundness}_{\text{cluster}} > 0.6625$ at 5% of cluster height.

^1H , $E_{\text{initial}}=143\text{ MeV}$

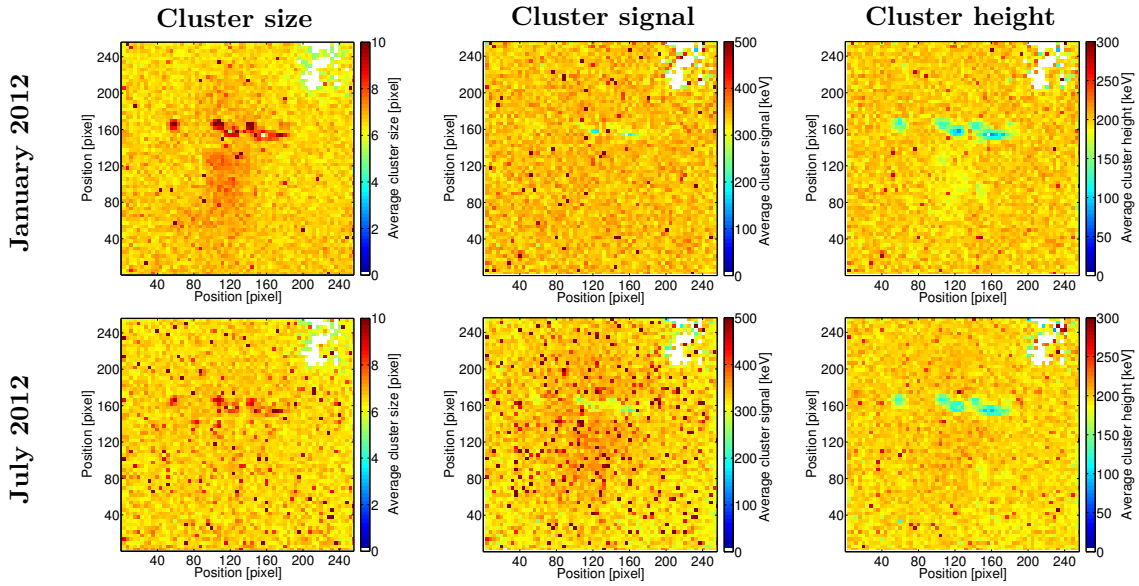


Figure A11: Maps showing the distributions of average cluster size, cluster signal and cluster height over the sensitive detector area for different measurement dates. Settings: $V_{\text{bias}}=10\text{ V}$, $t_{\text{acq}}=1\text{ ms}$, $A_{\text{cluster}} \geq 4\text{ pixel}$, $\text{roundness}_{\text{cluster}} > 0.6625$ at 5% of cluster height.

^1H , $E_{\text{initial}}=221\text{ MeV}$

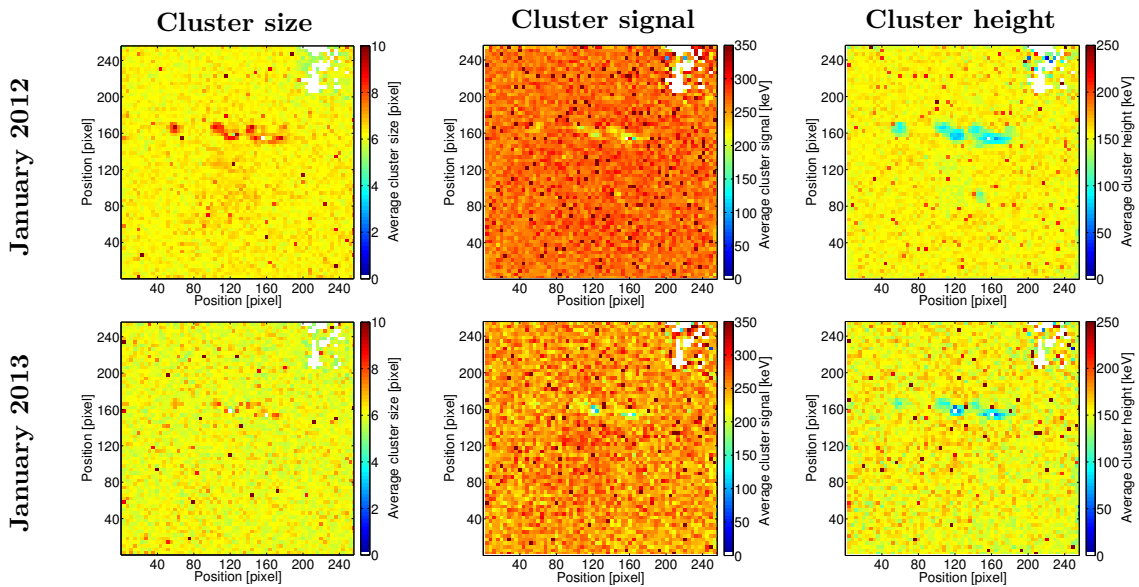


Figure A12: Maps showing the distributions of average cluster size, cluster signal and cluster height over the sensitive detector area for different measurement dates. Settings: $V_{\text{bias}}=10\text{ V}$, $t_{\text{acq}}=1\text{ ms}$, $A_{\text{cluster}} \geq 4\text{ pixel}$, $\text{roundness}_{\text{cluster}} > 0.6625$ at 5% of cluster height.

^{12}C , $E_{\text{initial}}=89\text{ MeV/u}$

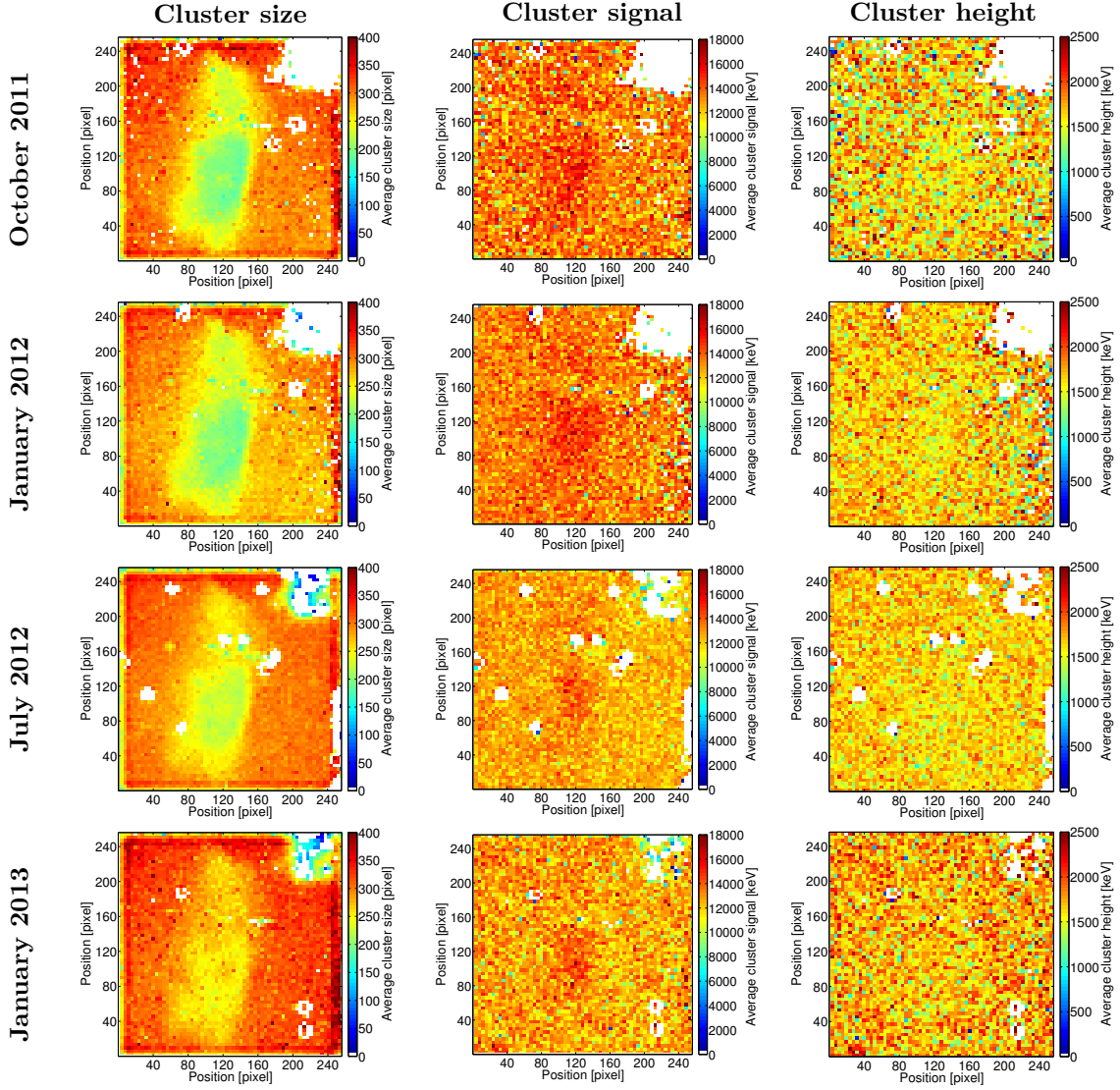


Figure A13: Maps showing the distributions of average cluster size, cluster signal and cluster height over the sensitive detector area for different measurement dates. Settings: $V_{\text{bias}}=10\text{ V}$, $t_{\text{acq}}=1\text{ ms}$, $A_{\text{cluster}} \geq 30\text{ pixel}$, $\text{roundness}_{\text{cluster}} > 0.7375$ at 10% of cluster height.

^{12}C , $E_{\text{initial}}=271 \text{ MeV/u}$

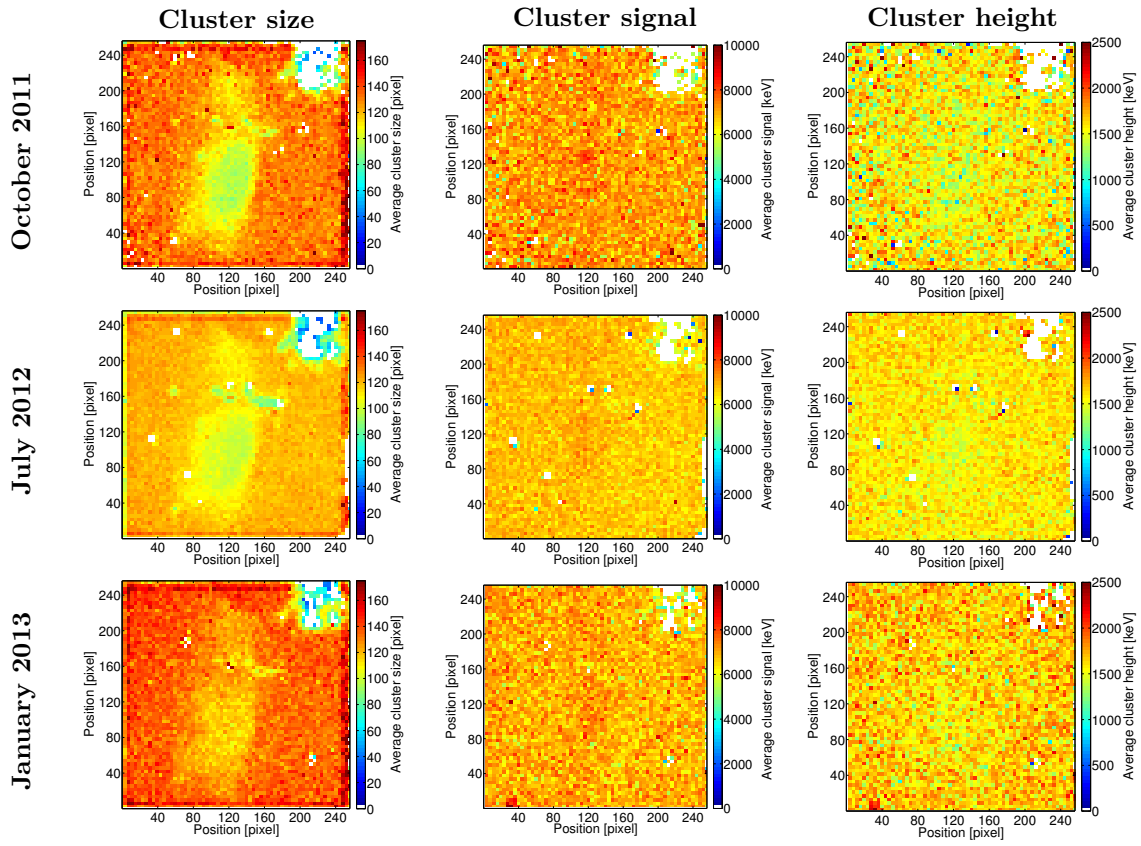


Figure A14: Maps showing the distributions of average cluster size, cluster signal and cluster height over the sensitive detector area for different measurement dates. Settings: $V_{\text{bias}}=10 \text{ V}$, $t_{\text{acq}}=1 \text{ ms}$, $A_{\text{cluster}} \geq 30 \text{ pixel}$, $\text{roundness}_{\text{cluster}} > 0.7375$ at 10% of cluster height.

^{12}C , $E_{\text{initial}}=430\text{ MeV/u}$

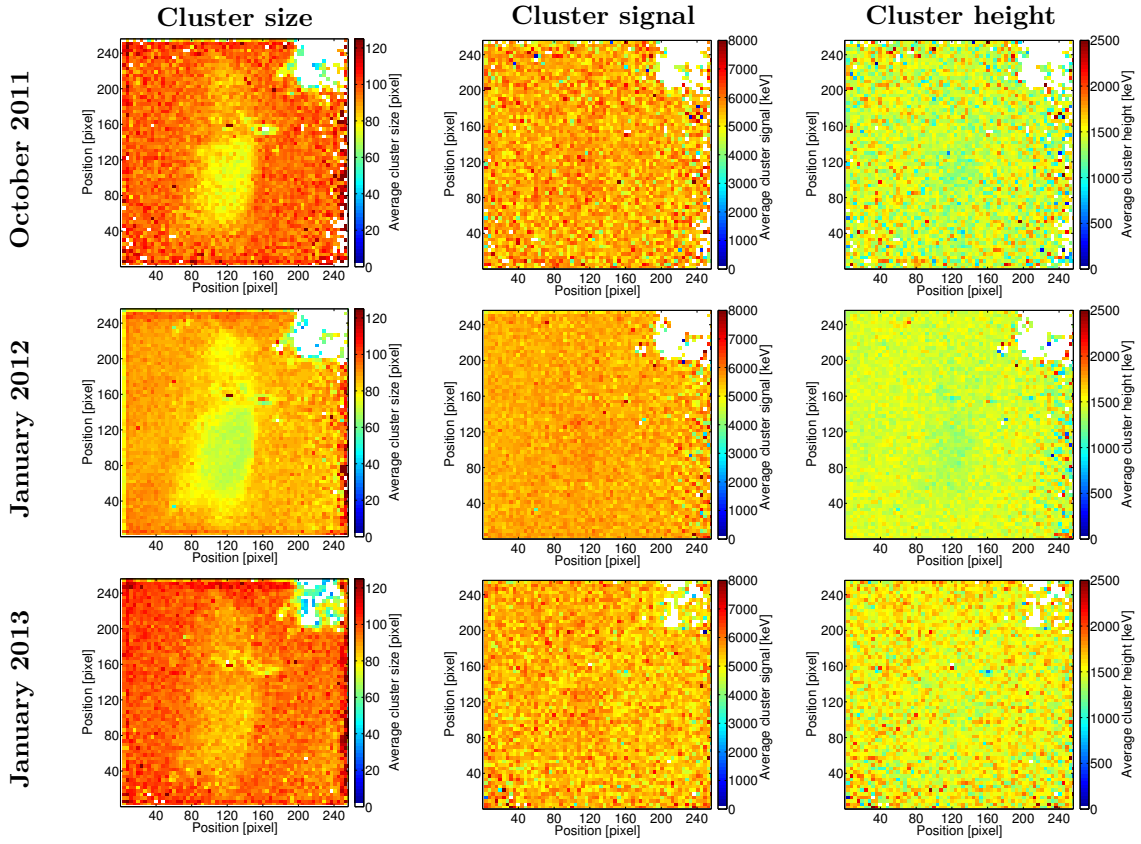


Figure A15: Maps showing the distributions of average cluster size, cluster signal and cluster height over the sensitive detector area for different measurement dates. Settings: $V_{\text{bias}}=10\text{ V}$, $t_{\text{acq}}=1\text{ ms}$, $A_{\text{cluster}} \geq 30\text{ pixel}$, $\text{roundness}_{\text{cluster}} > 0.7375$ at 10% of cluster height.

Appendix D: Energy-Loss Straggling - Results for All Investigated Energies

Cluster signal distributions measured in proton and carbon ion beams free-in-air were compared to calculated energy-loss distributions with the methodology described in Section 6.2.2. While in Section 7.2.2 only the results for selected energies are shown, in the following the results for all investigated ion energies are presented. For further analysis and discussion, see Section 7.2.2.

High Energy Protons

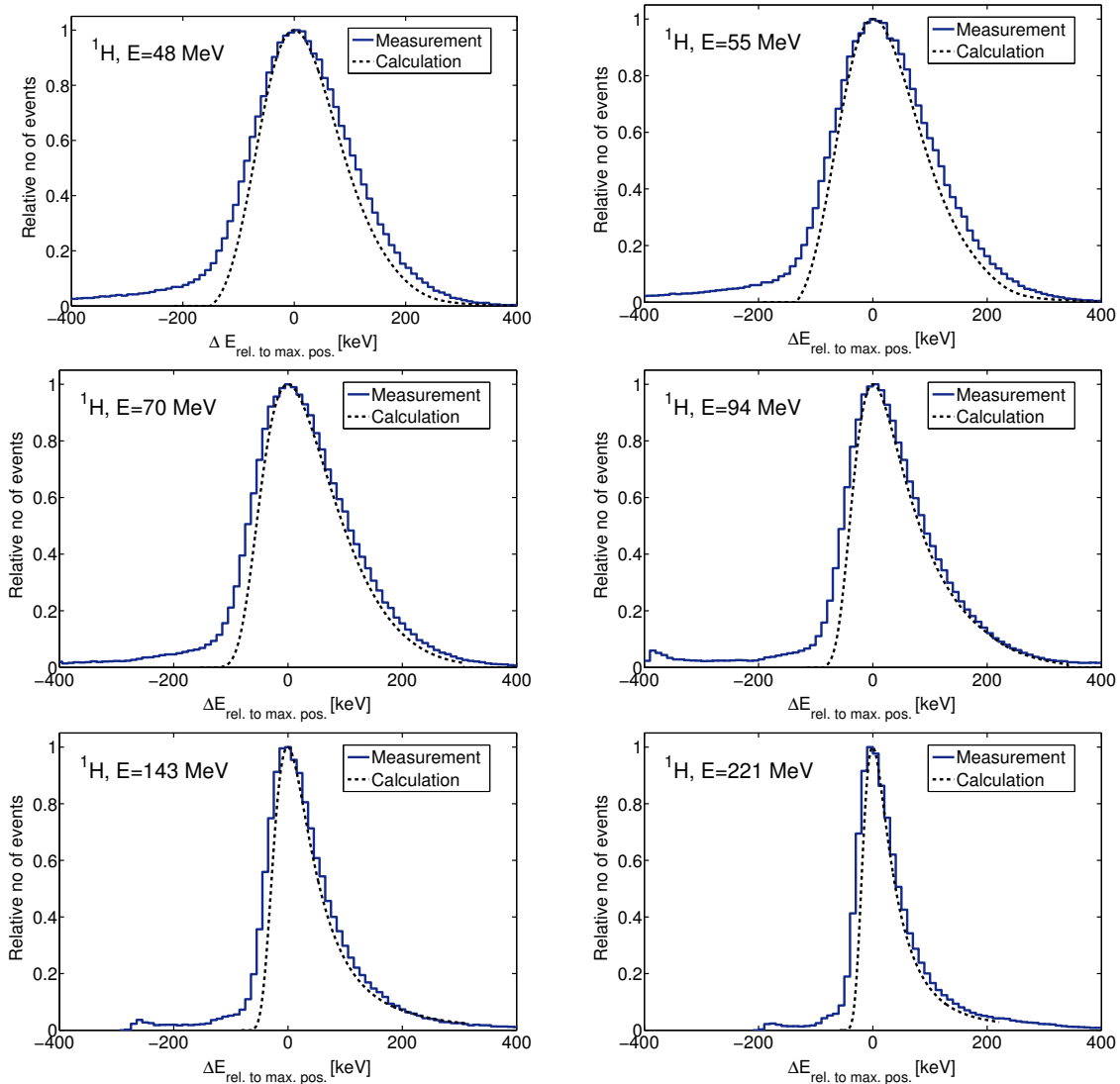


Figure A16: Comparison of measured cluster signal distributions and calculated energy-loss distributions (Vavilov theory) for proton beams covering the initial energy range available at HIT. The distributions are normalized to their maximum values and the positions of the maxima are shifted to zero. Settings: $t_{\text{acq}}=1$ ms, $V_{\text{bias}}=10$ V, $A_{\text{cluster}} \geq 4$ pixel, $\text{roundness}_{\text{cluster}} > 0.6625$ at 5% of cluster height.

High Energy Carbon Ions

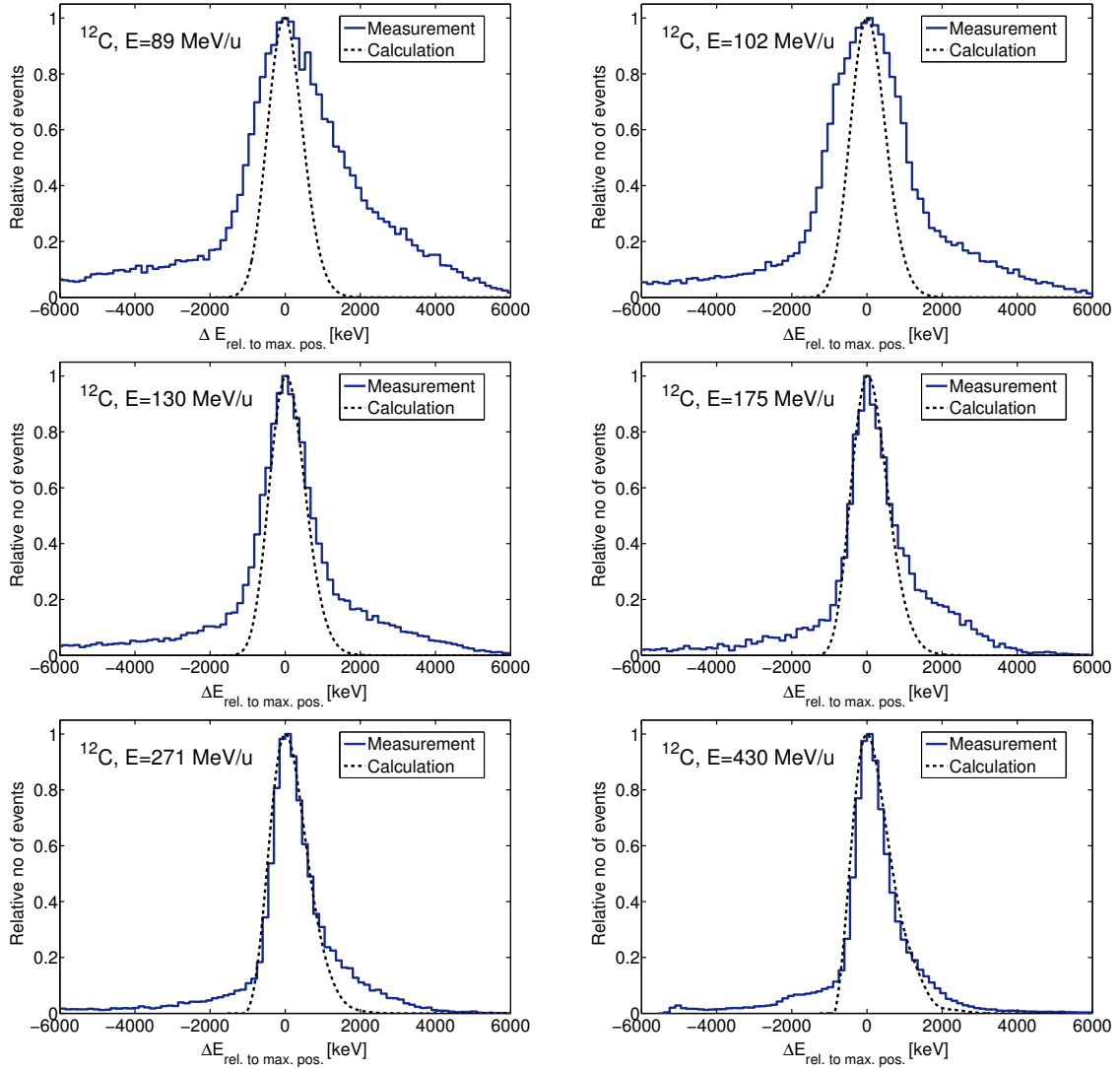


Figure A17: Comparison of measured cluster signal distributions and calculated energy-loss distributions (Vavilov theory) for carbon ion beams covering the initial energy range available at HIT. The distributions are normalized to their maximum values and the positions of the maxima are shifted to zero. Settings: $t_{\text{acq}}=1$ ms, $V_{\text{bias}}=10$ V, $A_{\text{cluster}} \geq 30$ pixel, $\text{roundness}_{\text{cluster}} > 0.7375$ at 10% of cluster height.

Appendix E: Comparison of $V_{\text{bias}}=10$ and 22 V for ion spectroscopy measurements

Depending on the ion species, different bias voltage values were found to result in better agreement with expected values for energy-loss measurements (see Section 7.2). For measurements in proton beams and in low energy (0.5 MeV/u) deuterium irradiation a bias voltage of 22 V showed smaller deviations from calculated or theoretically expected energy-loss compared to a bias voltage of 10 V, while for measurements in carbon ion beams of therapeutically used energies the trend is vice versa.

While in energy-loss measurements a bias voltage resulting in accurate energy-loss values is required, for ion spectroscopy measurements the bias voltage resulting in the best separation between the various ion species is preferable. Therefore, a separate study is needed to determine the bias voltage beneficial for measurements in mixed radiation fields containing different ion species. In this work, the study was concentrated to bias voltages of 10 and 22 V, which were found to offer advantages in either proton or carbon ion measurements (see Section 7.1.2 for details).

Experimental Set-Up The detector was placed in the isocenter, with its surface aligned perpendicular to the beam axis. A steel phantom was placed in front of the detector, with the distance between steel and the detector being 5.5 cm. The thickness of the steel in beam direction was 30.1 mm, corresponding to a water-equivalent thickness of 169.4 mm. A carbon ion beam of $E_{\text{initial}}=430$ MeV/u (range in water: approx. 30 cm) was directed on the phantom. The primary carbon ions and secondary particles leaving the steel phantom were detected.

The capability for separation of clusters originating from different particle species using the cluster parameters size and signal was evaluated and compared for both investigated bias voltages.

Results For the evaluation, histograms showing the 2-dimensional distributions of the measured cluster signal and cluster size were established for both investigated bias voltages (10 and 22 V). They are presented in Figure A18. Several areas showing concentrations of clusters are visible. These areas are due to different particle species. For ion spectroscopy, a good separability of the areas is needed. The comparison of the distributions in Figure A18 shows advantages in the separation of particular regions, e.g. the two areas at low cluster size and cluster signal, for $V_{\text{bias}}=10$ V. Therefore, for the further ion spectroscopy studies, this detector bias voltage was used.

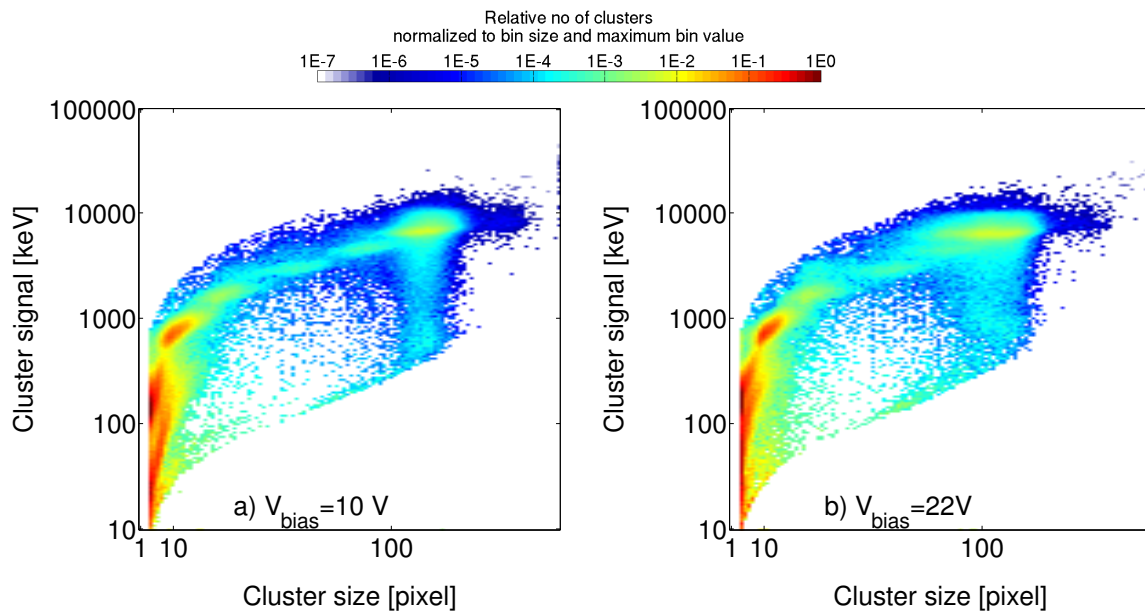


Figure A18: 2-dimensional histograms showing the distributions of cluster signal and cluster size for detector bias voltages of 10 V (a) and 22 V (b). The measurements were performed in carbon ion beams of $E_{\text{initial}}=430 \text{ MeV/u}$ behind 30.1 mm of steel. The distributions are normalized to the maximum bin. Further settings: $t_{\text{acq}}=1 \text{ ms}$, $A_{\text{cluster}} \geq 4 \text{ pixel}$, $\text{roundness}_{\text{cluster}}$ as depicted in Figure 6.8.

Bibliography

- Agodi, C., Battistoni, G., Bellini, F., et al. (2012). Charged particle's flux measurement from PMMA irradiated by 80 MeV/u carbon ion beam. *Physics in Medicine and Biology*, 57:5667–5678. (Cited on pages 18, 22, 154, and 158).
- Agostinelli, S., Allison, J., Amako, K., et al. (2003). Geant4 – a simulation toolkit. *Nuclear Instruments and Methods in Physics Research Section A*, 506:250–303. (Cited on page 148).
- Allison, J., Amako, K., Apostolakis, J., et al. (2006). Geant4 developments and applications. *IEEE Transactions on Nuclear Science*, 53:270–278. (Cited on page 148).
- Amaldi, U., Hajdas, W., Iliescu, S., et al. (2010). Advanced Quality Assurance for CNAO. *Nuclear Instruments and Methods in Physics Research Section A*, 617:248–249. (Cited on pages 22 and 154).
- Amaldi, U. & Kraft, G. (2005). Radiotherapy with beams of carbon ions. *Reports on Progress in Physics*, 68:1861–1882. (Cited on pages 1, 20, and 24).
- Anton, G., Gebert, U., Michel, T., et al. (2009). A hybrid photodetector using the Timepix semiconductor assembly for photoelectron detection. *Nuclear Instruments and Methods in Physics Research Section A*, 602:205–208. (Cited on pages 31 and 32).
- Battistoni, G., Muraro, S., Sala, P. R., et al. (2007). The FLUKA code: description and benchmarking. In: *Proceedings of the Hadronic Shower Simulation Workshop 2006, Fermilab 6–8 September 2006*, pages 31–49. (Cited on page 148).
- Bethe, H. (1930). Zur Theorie des Durchgangs schneller Korpuskularstrahlen durch Materie. *Annalen der Physik*, 397:325–400. (Cited on page 6).
- Bethe, H. (1953). Molière's Theory of Multiple Scattering. *Physical Review*, 89:1256–1266. (Cited on page 12).
- Bloch, F. (1933). Zur Bremsung rasch bewegter Teilchen beim Durchgang durch Materie. *Annalen der Physik*, 408:285–320. (Cited on page 6).

BIBLIOGRAPHY

- Blunck, O. & Leisegang, S. (1950). Zum Energieverlust schneller Elektronen in dünnen Schichten. *Zeitschrift für Physik*, 128:500–505. (Cited on page 10).
- Bom, V., Joulaeizadeh, L., & Beekman, F. (2012). Real-time prompt gamma monitoring in spot-scanning proton therapy using imaging through a knife-edge-shaped slit. *Physics in Medicine and Biology*, 57:297–308. (Cited on page 21).
- Bouchami, J., Gutiérrez, A., Holy, T., et al. (2011a). Measurement of pattern recognition efficiency of tracks generated by ionizing radiation in a Medipix2 device. *Nuclear Instruments and Methods in Physics Research Section A*, 633:S187–S189. (Cited on page 40).
- Bouchami, J., Gutiérrez, A., Houdayer, A., et al. (2011b). Study of the charge sharing in silicon pixel detector by means of heavy ionizing particles interacting with a Medipix2 device. *Nuclear Instruments and Methods in Physics Research Section A*, 633:S117–S120. (Cited on page 40).
- Bragg, W. & Kleeman, R. (1904). LXXIV. On the ionization curves of radium. *Philosophical Magazine Series 6*, 8:726–738. (Cited on page 1).
- Braunn, B., Labalme, M., Ban, G., et al. (2011). Nuclear reaction measurements of 95MeV/u ^{12}C interactions on PMMA for hadrontherapy. *Nuclear Instruments and Methods in Physics Research Section B*, 269:2676–2684. (Cited on page 17).
- Campbell, M., Heijne, E., Holý, T., et al. (2008). Study of the charge sharing in a silicon pixel detector by means of α -particles interacting with a Medipix2 device. *Nuclear Instruments and Methods in Physics Research Section A*, 591:38–41. (Cited on pages 35 and 36).
- Choi, J. & Kang, J. O. (2012). Basics of particle therapy II: relative biological effectiveness. *Radiation Oncology Journal*, 30:1–13. (Cited on page 24).
- Chu, W. (2006). Overview of Light-Ion Beam Therapy. In: *Columbus-Ohio, ICRU-IAEA meeting, 18-20 March 2006*. (Cited on page 2).
- Chu, W. T., Ludewigt, B. A., & Renner, T. R. (1993). Instrumentation for treatment of cancer using proton and light-ion beams. *Review of Scientific Instruments*, 64:2055–2122. (Cited on pages 20 and 22).
- Combs, S. E., Jäkel, O., Haberer, T., et al. (2010). Particle therapy at the Heidelberg Ion Therapy Center (HIT) – Integrated research-driven university-hospital-based radiation oncology service in Heidelberg, Germany. *Radiotherapy and Oncology: Journal of the European Society for Therapeutic Radiology and Oncology*, 95:41–44. (Cited on page 27).

- De Lellis, G., Buontempo, S., Di Capua, F., et al. (2011). Measurement of the fragmentation of Carbon nuclei used in hadron-therapy. *Nuclear Physics A*, 853:124–134. (Cited on page 18).
- De Napoli, M., Agodi, C., Battistoni, G., et al. (2012). Carbon fragmentation measurements and validation of the Geant4 nuclear reaction models for hadrontherapy. *Physics in Medicine and Biology*, 57:7651–7671. (Cited on page 18).
- Dudouet, J., Juliani, D., Labalme, M., et al. (2013). Double-differential fragmentation cross-section measurements of 95 MeV/nucleon C beams on thin targets for hadron therapy. *Physical Review C*, 88:024606. (Cited on page 17).
- Elsässer, T., Gemmel, A., Scholz, M., et al. (2009). The relevance of very low energy ions for heavy-ion therapy. *Physics in Medicine and Biology*, 54:N101–N106. (Cited on page 6).
- Enghardt, W., Crespo, P., Fiedler, F., et al. (2004). Charged hadron tumour therapy monitoring by means of PET. *Nuclear Instruments and Methods in Physics Research Section A*, 525:284–288. (Cited on page 21).
- Fano, U. (1963). Penetration of Protons, Alpha Particles, and Mesons. *Annual Review of Nuclear Science*, 13:1–66. (Cited on page 6).
- Ferrari, A., Sala, P., Fassö, A., et al. (2005). FLUKA: a multi-particle transport code. Technical report, CERN Yellow Report No. CERN 2005–10, INFN/TC 05/11, SLAC–R–77. (Cited on page 148).
- Freier, P., Lofgren, E., Ney, E., et al. (1948). The Heavy Component of Primary Cosmic Rays. *Physical Review*, 74:1818–1827. (Cited on page 15).
- Friedrich, T., Weyrather, W., Elsässer, T., et al. (2010). Accuracy of RBE: experimental and theoretical considerations. *Radiation and Environmental Biophysics*, 49:345–349. (Cited on page 22).
- Goitein, M. & Chen, G. T. (1983). Beam scanning for heavy charged particle radiotherapy. *Medical Physics*, 10:831–840. (Cited on page 1).
- Goldhaber, A. S. & Heckman, H. H. (1978). High Energy Interactions of Nuclei. *Annual Review of Nuclear and Particle Science*, 28:161–205. (Cited on page 15).
- Golosio, B., Abou-Haidar, Z., Agodi, C., et al. (2011). The FIRST experiment for nuclear fragmentation measurements at GSI. In: *2011 IEEE Nuclear Science Symposium Conference Record*, pages 2277–2280. (Cited on pages 18, 154, and 158).

BIBLIOGRAPHY

- Golovchenko, A. N., Skvarc, J., Ilic, R., et al. (1999). Fragmentation of 200 and 244 MeV/u carbon beams in thick tissue-like absorbers. *Nuclear Instruments and Methods in Physics Research Section B*, 159:233–240. (Cited on page 18).
- Golovkov, M., Aleksandrow, D., Chulkov, L., et al. (1997). Fragmentation of 270 A MeV carbon ions in water. In: *Contribution to Second Int. Symposium on Hadrontherapy, Switzerland, 9-13 Sept. 1996*. (Cited on pages 2 and 16).
- Gottschalk, B., Koehler, A. M., Schneider, R. J., et al. (1993). Multiple Coulomb scattering of 160 MeV protons. *Nuclear Instruments and Methods in Physics Research Section B*, 74:467–490. (Cited on page 12).
- Granja, C., Jakubek, J., Köster, U., et al. (2011). Response of the pixel detector Timepix to heavy ions. *Nuclear Instruments and Methods in Physics Research Section A*, 633:S198–S202. (Cited on pages 3, 40, 143, and 145).
- Greulich, S., Grzanka, L., Bassler, N., et al. (2010). Amorphous track models: A numerical comparison study. *Radiation Measurements*, 45:1406–1409. (Cited on page 46).
- Gunzert-Marx, K. (2004). *Nachweis leichter Fragmente aus Schwerionenreaktionen mit einem BaF₂-Teleskop-Detektor*. PhD thesis, Technische Universität Darmstadt. (Cited on pages 13, 17, and 20).
- Gunzert-Marx, K., Iwase, H., Schardt, D., et al. (2008). Secondary beam fragments produced by 200 MeV u⁻¹ ¹²C ions in water and their dose contributions in carbon ion radiotherapy. *New Journal of Physics*, 10:075003. (Cited on pages 2, 3, 13, 17, 151, 154, and 155).
- Gwosch, K., Hartmann, B., Jakubek, J., et al. (2013). Non-invasive monitoring of therapeutic carbon ion beams in a homogeneous phantom by tracking of secondary ions. *Physics in Medicine and Biology*, 58:3755–3773. (Cited on pages 22 and 154).
- Gwosch, K. C. (2012). *Non-Invasive Monitoring of Carbon Ion Beam Therapy by Tracking of Secondary Ions – An Initial Study*. Diploma thesis, University of Heidelberg. (Cited on pages 2, 13, 33, and 35).
- Haberer, T., Becher, W., Schardt, D., et al. (1993). Magnetic scanning system for heavy ion therapy. *Nuclear Instruments and Methods in Physics Research Section A*, 330:296–305. (Cited on pages 1 and 28).
- Haberer, T., Debus, J., Eickhoff, H., et al. (2004). The Heidelberg Ion Therapy Center. *Radiotherapy and Oncology : Journal of the European Society for Therapeutic Radiology and Oncology*, 73 Suppl 2:S186–S190. (Cited on page 28).

- Haettner, E. (2006). *Experimental study on carbon ion fragmentation in water using GSI therapy beams*. Master of science thesis, Kungliga tekniska högskolan Stockholm, Data available online in the XFOR database <http://www-nds.iaea.org/exfor/exfor.htm>. (Cited on pages 17, 20, 65, 66, 133, 135, 136, 149, 150, and 157).
- Haettner, E., Iwase, H., & Schardt, D. (2006). Experimental fragmentation studies with ^{12}C therapy beams. *Radiation Protection Dosimetry*, 122:485–487. (Cited on page 17).
- Henriquet, P., Testa, E., Chevallier, M., et al. (2012). Interaction vertex imaging (IVI) for carbon ion therapy monitoring: a feasibility study. *Physics in Medicine and Biology*, 57:4655–4669. (Cited on page 22).
- Highland, V. L. (1975). Some practical remarks on multiple scattering. *Nuclear Instruments and Methods*, 129:497–499. (Cited on page 12).
- Hoang, S., Pinsky, L., Vilalta, R., et al. (2012). LET Estimation of Heavy Ion Particles based on a Timepix-Based Si Detector. *Journal of Physics: Conference Series*, 396:022023. (Cited on pages 143 and 152).
- Holy, T., Heijne, E., Jakubek, J., et al. (2008). Pattern recognition of tracks induced by individual quanta of ionizing radiation in Medipix2 silicon detector. *Nuclear Instruments and Methods in Physics Research Section A*, 591:287–290. (Cited on page 40).
- Huber, L. (2011). *Patient Position Verification in Ion Beam Therapy Using Silicon Detectors And Ion Beams*. Diploma thesis, University of Heidelberg. (Cited on page 29).
- ICRU30 (1979). Quantitative Concepts and Dosimetry in Radiobiology (ICRU Report 30). *Journal of the ICRU*. (Cited on page 22).
- ICRU49 (1999). Stopping Powers and Ranges for Protons and Alpha Particles (ICRU Report 49). *Journal of the ICRU*. (Cited on pages 11 and 148).
- ICRU73 (2005). Stopping Of Ions Heavier Than Helium (ICRU Report 73). *Journal of the ICRU*. (Cited on pages 10, 11, 58, and 148).
- Jäkel, O. (2006). Ranges of ions in metals for use in particle treatment planning. *Physics in Medicine and Biology*, 51:N173–N177. (Cited on page 43).
- Jäkel, O. (2007). State of the Art in Hadron Therapy. In: *AIP Conference Proceedings*, C. Granja, C. Leroy, & L. Stekl, ed., pages 70–77. (Cited on page 24).

BIBLIOGRAPHY

- Jäkel, O., Jacob, C., Schardt, D., et al. (2001). Relation between carbon ion ranges and x-ray CT numbers. *Medical Physics*, 28:701–703. (Cited on pages 43 and 44).
- Jakubek, J. (2009a). Energy-sensitive X-ray radiography and charge sharing effect in pixelated detector. *Nuclear Instruments and Methods in Physics Research Section A*, 607:192–195. (Cited on pages 36 and 38).
- Jakubek, J. (2009b). Semiconductor Pixel detectors and their applications in life sciences. *Journal of Instrumentation*, 4:P03013. (Cited on pages 31, 34, 35, and 39).
- Jakubek, J. (2010). Precise energy calibration of pixel detector working in time-over-threshold mode. *Nuclear Instruments and Methods in Physics Research Section A*, 633:S262–S266. (Cited on pages 40 and 144).
- Jakubek, J., Cejnarova, A., Holy, T., et al. (2008). Pixel detectors for imaging with heavy charged particles. *Nuclear Instruments and Methods in Physics Research Section A*, 591:155–158. (Cited on pages 3, 38, 39, and 143).
- Jakubek, J., Granja, C., Hartmann, B., et al. (2011). Selective detection of secondary particles and neutrons produced in ion beam therapy with 3D sensitive voxel detector. *Journal of Instrumentation*, 6:C12010. (Cited on page 38).
- Jakubek, M., Jakubek, J., Zemlicka, J., et al. (2012). Probe and scanning system for 3D response mapping of pixelated semiconductor detector with X-rays and the timepix device. In: *IX Latin American Symposium on Nuclear Physics and Applications, AIP Conference Proceedings 1423*, pages 461–466. (Cited on pages 99, 103, and 145).
- Jakubek, M., Jakubek, J., Zemlicka, J., et al. (2013). 3D imaging of radiation damage in silicon sensor and spatial mapping of charge collection efficiency. *Journal of Instrumentation*, 8:C03023. (Cited on pages 37 and 38).
- Kraft, G. (1999). RBE and its interpretation. *Strahlentherapie und Onkologie: Organ der Deutschen Röntgengesellschaft*, 175 Suppl 2:44–47. (Cited on pages 22 and 23).
- Kraft, G. (2000). Tumor therapy with heavy charged particles. *Progress in Particle and Nuclear Physics*, 45:S473–S544. (Cited on page 13).
- Krämer, M., Jäkel, O., Haberer, T., et al. (2000). Treatment planning for heavy-ion radiotherapy: physical beam model and dose optimization. *Physics in Medicine and Biology*, 45:3299–3317. (Cited on page 28).
- Kraus, V., Holik, M., Jakubek, J., et al. (2011). FITPix – fast interface for Timepix pixel detectors. *Journal of Instrumentation*, 6:C01079. (Cited on page 33).

- Kuchling, H. (2004). *Taschenbuch der Physik*, volume 18. Fachbuchverlag Leipzig im Carl Hanser Verlag. (Cited on page 8).
- Kurosawa, T., Nakamura, T., Nakao, N., et al. (1999). Spectral measurements of neutrons, protons, deuterons and tritons produced by 100 MeV/nucleon He bombardment. *Nuclear Instruments and Methods in Physics Research Section A*, 430:400–422. (Cited on page 16).
- Landau, L. (1944). On the energy loss of fast particles by ionization. *Journal of Physics (USSR)*, 8:201–205. (Cited on pages 8 and 9).
- Leo, W. R. (1994). *Techniques for Nuclear and Particle Physics Experiments: A How-To Approach*. Springer-Verlag. (Cited on pages 7, 8, 9, 10, 12, 60, and 153).
- Leroy, C. & Rancoita, P.-G. (2011). *Principles of Radiation Interaction In Matter And Detection (3rd Edition)*. World Scientific Publishing Co. Pte. Ltd. (Cited on pages 11, 30, 31, 34, 35, 36, 38, and 59).
- Llacer, J. (1984). On-line characterization of heavy-ion beams with semiconductor detectors. *Medical Physics*, 11:266–278. (Cited on page 16).
- Llacer, J. (1990a). Characterization of fragmented heavy-ion beams using a three-stage telescope detector: Detector configuration and instrumentation. *Medical Physics*, 17:158–162. (Cited on page 16).
- Llacer, J. (1990b). Characterization of fragmented heavy-ion beams using a three-stage telescope detector: Measurements of 670-MeV/amu ^{20}Ne beams. *Medical Physics*, 17:151–157. (Cited on page 16).
- Llopart, X., Ballabriga, R., Campbell, M., et al. (2007). Timepix, a 65k programmable pixel readout chip for arrival time, energy and/or photon counting measurements. *Nuclear Instruments and Methods in Physics Research A*, 581:485–494. (Cited on pages 3, 30, 31, and 32).
- Llopart, X., Campbell, M., Dinapoli, R., et al. (2002). Medipix2: A 64-k pixel readout chip with 55- μm square elements working in single photon counting mode. In: *IEEE Transactions on Nuclear Science*, volume 49, pages 2279–2283. (Cited on page 30).
- Ma, C.-M. C. & Lomax, T. (2012). *Proton and Carbon Ion Therapy (Imaging in Medical Diagnosis and Therapy)*. CRC Press. (Cited on page 15).
- Maccabee, H. D. & Ritter, M. A. (1974). Fragmentation of High-Energy Oxygen-Ion Beams in Water. *Radiation Research*, 60:409–421. (Cited on page 15).

BIBLIOGRAPHY

- Mairani, A. (2007). *Nucleus-Nucleus Interaction Modelling and Applications in Ion Therapy Treatment Planning*. PhD thesis, Universita degli studi di Pavia. (Cited on page 17).
- Matsufuji, N., Fukumura, A., Komori, M., et al. (2003). Influence of fragment reaction of relativistic heavy charged particles on heavy-ion radiotherapy. *Physics in Medicine and Biology*, 48:1605–1623. (Cited on pages 2, 3, 16, 17, 130, and 155).
- Matsufuji, N., Komori, M., Sasaki, H., et al. (2005). Spatial fragment distribution from a therapeutic pencil-like carbon beam in water. *Physics in Medicine and Biology*, 50:3393–3403. (Cited on page 17).
- Meroli, S., Passeri, D., & Servoli, L. (2011). Energy loss measurement for charged particles in very thin silicon layers. *Journal of Instrumentation*, 6:P06013. (Cited on page 9).
- Min, C.-H., Kim, C. H., Youn, M.-Y., et al. (2006). Prompt gamma measurements for locating the dose falloff region in the proton therapy. *Applied Physics Letters*, 89:183517. (Cited on page 21).
- Molière, G. (1948). Theorie der Streuung schneller geladener Teilchen II. Mehrfach- und Vielfachstreuung. *Zeitschrift Naturforschung Teil A*, 3:78–97. (Cited on page 12).
- Mrázová, Z., Jadrníčková, I., Brabcová, K., et al. (2010). Fragmentation of Ne ions with energy 400 MeV/u behind targets from different materials measured with PNTD. *Radiation Measurements*, 45:1438–1440. (Cited on page 18).
- Opalka, L., Granja, C., Hartmann, B., et al. (2012). 3D measurement of the radiation distribution in a water phantom in a hadron therapy beam. *Journal of Instrumentation*, 7:C01085. (Cited on pages 42 and 153).
- Opalka, L., Granja, C., Hartmann, B., et al. (2013). Linear energy transfer and track pattern recognition of secondary radiation generated in hadron therapy beam in a PMMA target. *Journal of Instrumentation*, 8:C02047. (Cited on pages 143, 147, and 153).
- Oura, K., Lifshits, V., Saranin, A., et al. (2003). *Surface Science: An Introduction (Advanced Texts in Physics)*. Springer-Verlag. (Cited on page 57).
- Paganetti, H. (2002). Nuclear interactions in proton therapy: dose and relative biological effect distributions originating from primary and secondary particles. *Physics in Medicine and Biology*, 47:747–764. (Cited on pages 23 and 24).

- Parodi, K., Bortfeld, T., Enghardt, W., et al. (2008). PET imaging for treatment verification of ion therapy: Implementation and experience at GSI Darmstadt and MGH Boston. *Nuclear Instruments and Methods in Physics Research Section A*, 591:282–286. (Cited on page 21).
- Parodi, K., Mairani, A., Brons, S., et al. (2012). Monte Carlo simulations to support start-up and treatment planning of scanned proton and carbon ion therapy at a synchrotron-based facility. *Physics in Medicine and Biology*, 57:3759–3784. (Cited on pages 29 and 149).
- Pedroni, E., Scheib, S., Böhringer, T., et al. (2005). Experimental characterization and physical modelling of the dose distribution of scanned proton pencil beams. *Physics in Medicine and Biology*, 50:541–561. (Cited on pages 14 and 22).
- Pinsky, L., Stoffle, N., Jakubek, J., et al. (2011). Application of the Medipix2 technology to space radiation dosimetry and hadron therapy beam monitoring. *Nuclear Instruments and Methods in Physics Research Section A*, 628:226–229. (Cited on pages 3 and 143).
- Pinsky, L. S., Empl, A., Gutierrez, A., et al. (2010). Penetrating heavy ion charge and velocity discrimination with a TimePix-based Si detector (for space radiation applications). *Nuclear Instruments and Methods in Physics Research A*, 633:S190–S193. (Cited on page 143).
- Plackett, R., Akiba, K., Artuso, M., et al. (2009). Preliminary Results using Timepix as a Particle Tracking Detector. In: *Proceedings of the 18th International Workshop on Vertex detectors. September 13 -18 2009. Veluwe, the Netherlands*, page 24. (Cited on pages 32 and 33).
- Platkevic, M., Jakubek, J., Havranek, V., et al. (2013). Evaluation of local radiation damage in silicon sensor via charge collection mapping with the Timepix read-out chip. *Journal of Instrumentation*, 8:C04001. (Cited on pages 37 and 38).
- Pleskac, R., Abou-Haidar, Z., Agodi, C., et al. (2012). The FIRST experiment at GSI. *Nuclear Instruments and Methods in Physics Research Section A*, 678:130–138. (Cited on pages 18, 154, and 158).
- Poikela, T., Plosila, J., Westerlund, T., et al. (2012). Architectural modeling of pixel readout chips Velopix and Timepix3. *Journal of Instrumentation*, 7:C01093. (Cited on pages 144 and 147).
- PTW Freiburg. Acrylic and RW3 Slab Phantoms, available at http://www.ptw.de/acrylic_and_rw3_slab_phantoms0.html, accessed September 2013. (Cited on page 43).

BIBLIOGRAPHY

- Pugatch, V., Tlustos, L., Chaus, A., et al. (2011). Metal and hybrid TimePix detectors imaging beams of particles. *Nuclear Instruments and Methods in Physics Research Section A*, 650:194–197. (Cited on page 143).
- Reinhardt, S., Draxinger, W., Schreiber, J., et al. (2013). A pixel detector system for laser-accelerated ion detection. *Journal of Instrumentation*, 8:P03008. (Cited on page 30).
- Reinhardt, S., Granja, C., Krejci, F., et al. (2011). Test of pixel detectors for laser-driven accelerated particle beams. *Journal of Instrumentation*, 6:C12030. (Cited on page 30).
- Rotondi, A. & Montagna, P. (1990). Fast calculation of Vavilov distribution. *Nuclear Instruments and Methods in Physics Research Section B*, 47:215–223. (Cited on page 59).
- Sánchez-Parcerisa, D., Gemmel, A., Jäkel, O., et al. (2012). Experimental study of the water-to-air stopping power ratio of monoenergetic carbon ion beams for particle therapy. *Physics in Medicine and Biology*, 57:3629–3641. (Cited on page 43).
- Schall, I., Schardt, D., Geissel, H., et al. (1996). Charge-changing nuclear reactions of relativistic light-ion beams ($5 \leq Z \leq 10$) passing through thick absorbers. *Nuclear Instruments and Methods in Physics Research Section B*, 117:221–234. (Cited on pages 16 and 21).
- Schardt, D. (2007). Tumor therapy with high-energy carbon ion beams. *Nuclear Physics A*, 787:633–641. (Cited on pages 20 and 21).
- Schardt, D., Elsässer, T., & Schulz-Ertner, D. (2010). Heavy-ion tumor therapy: Physical and radiobiological benefits. *Reviews of Modern Physics*, 82:383–425. (Cited on pages 6, 12, 13, 16, 19, 21, 23, and 25).
- Schellhammer, S. (2013). *Single Particle Detection in a Therapeutic Proton Beam*. Bachelor's thesis, University of Heidelberg. (Cited on pages 124, 125, and 152).
- Schimmerling, W., Miller, J., Wong, M., et al. (1989). The Fragmentation of 670 A MeV Neon-20 as a Function of Depth in Water. I. Experiment. *Radiation Research*, 120:36–71. (Cited on page 16).
- Schimmerling, W., Subramanian, T., McDonald, W., et al. (1983). Beam analysis spectrometer for relativistic heavy ions. *Nuclear Instruments and Methods in Physics Research*, 205:531–543. (Cited on page 15).
- Schimmerling, W., Vosburgh, K. G., & Todd, P. W. (1971). Interaction of 3.9-Gev Nitrogen Ions with Matter. *Science*, 174:1123–1125. (Cited on page 15).

- Scholz, M. (2006). Dose Response of Biological Systems to Low- and High- LET Radiation. In: *Microdosimetric Response of Physical and Biological Systems to Low- and High- LET Radiations. Theory and Applications to Dosimetry*, Y. Horowitz, ed., chapter 1, pages 1–73. (Cited on page 23).
- Scholz, M. & Kraft, G. (1994). Calculation of Heavy Ion Inactivation Probabilities Based on Track Structure, X Ray Sensitivity and Target Size. *Radiation Protection Dosimetry*, 52:29–33. (Cited on page 25).
- Serber, R. (1947). Nuclear Reactions at High Energies. *Physical Review*, 72:1114–1115. (Cited on page 13).
- Shulek, P., Golovin, B., Kulyukina, L., et al. (1966). Fluctuations of Ionization Losses. *Yadernaya Fizika*, 4:564–566. (Cited on page 10).
- Sigmund, P. (2004). *Stopping of Heavy Ions: A Theoretical Approach (Springer Tracts in Modern Physics) (v. 204)*. Springer-Verlag. (Cited on page 6).
- Sihver, L., Tsao, C. H., Silberberg, R., et al. (1993). Total reaction and partial cross section calculations in proton-nucleus ($Z_t \leq 26$) and nucleus-nucleus reactions (Z_p and $Z_t \leq 26$). *Physical Review C: Nuclear Physics*, 47:1225–1236. (Cited on page 21).
- Smeets, J., Roellinghoff, F., Priels, D., et al. (2012). Prompt gamma imaging with a slit camera for real-time range control in proton therapy. *Physics in Medicine and Biology*, 57:3371–3405. (Cited on page 21).
- Soukup, P., Jakubek, J., & Vykydal, Z. (2011). 3D sensitive voxel detector of ionizing radiation based on Timepix device. *Journal of Instrumentation*, 6:C01060. (Cited on page 153).
- Telsemeyer, J. (2012). *Investigation of an Amorphous Silicon Flat-Panel Detector for Ion Radiography*. PhD thesis, University of Heidelberg. (Cited on page 28).
- Testa, E., Bajard, M., Chevallier, M., et al. (2008). Monitoring the Bragg peak location of 73 MeV u^{-1} carbon ions by means of prompt γ -ray measurements. *Applied Physics Letters*, 93:093506. (Cited on page 21).
- Tsai, Y.-S. (1974). Pair production and bremsstrahlung of charged leptons. *Reviews of Modern Physics*, 46:815–851. (Cited on page 12).
- Turecek, D., Holy, T., Jakubek, J., et al. (2011). Pixelman: a multi-platform data acquisition and processing software package for Medipix2, Timepix and Medipix3 detectors. In: *12th International Workshop on Radiation Imaging Detectors, July*

BIBLIOGRAPHY

- 11th – 15th 2010, Robinson College, Cambridge, U.K.*, page C01046. (Cited on pages 33 and 45).
- Weber, M. & Herlitzius, C. (2010). Heavy Ion Scattering at the Tandem Accelerator. Technical report, Technische Universität München. (Cited on page 30).
- Weber, U. & Kraft, G. (1999). Design and construction of a ripple filter for a smoothed depth dose distribution in conformal particle therapy. *Physics in Medicine and Biology*, 44:2765–2775. (Cited on page 29).
- Zeitlin, C., Guetersloh, S., Heilbronn, L., et al. (2007). Fragmentation cross sections of 290 and 400 MeV/nucleon C12 beams on elemental targets. *Physical Review C*, 76:014911. (Cited on page 16).
- Ziegler, J. F. (1999). Stopping of energetic light ions in elemental matter. *Journal of Applied Physics*, 85:1249. (Cited on pages 6 and 7).

Acknowledgements

The time of my PhD work has been filled with invaluable experiences. My gratitude is addressed to all who contributed.

I would like to thank Prof. Dr. Dr. Jürgen Debus, Medical Director of the Department of Radiation Oncology and Radiation Therapy at the Heidelberg University Medical Center, for employing me in his division. My gratitude is addressed to Prof. Dr. Wolfgang Schlegel, head of the department of Medical Physics in Radiation Oncology at DKFZ, for accepting me as a PhD student in his research division and for being the first referee of this thesis. I wish to thank Prof. Dr. Oliver Jäkel, leader of the research group Heavy Ion Therapy at DKFZ, for the opportunity to write this thesis in his group, for the funding within the HGF Virtual Institute under contract no. VH-VI-303 and for serving as the second referee. His support and advice throughout the last years were highly encouraging. Furthermore, I would like to thank Prof. Dr. Christian Karger and Prof. Dr. Katia Parodi for serving as members of my thesis advisory committee and Prof. Dr. Schultz-Coulon and Prof. Dr. Joerg Jaeckel for being members of my examination committee.

Above all, I want to thank Dr. Mária Martišíková, for entrusting me with the idea for this project and for being the best supervisor I could have imagined. Her advice and constructive critic, her confidence in me and the project and her unlimited support have been of inestimable value to me.

I am indebted to the Institute of Experimental and Applied Physics at the Czech Technical University in Prague, who enabled to perform this work within the Medipix Collaboration. Without their support, both in providing the detector and their knowledge, this thesis would have not been possible. My sincere thanks go to Prof. Stanislav Pospíšil, Jan Jakůbek, Ph.D., Carlos Granja, Ph.D., Pavel Soukup, Ph.D., and Lukáš Opalka, as well as all other colleagues, who helped in manifold ways. Srdečné díky!

I would like to express my gratitude towards the Heidelberg Ion Beam Therapy Center for providing me with the beam time and the assistance by many colleagues. In particular, my thanks are addressed to Dr. Stephan Brons, for arranging the measurements, and for his support at any day and night time, during weekends and on public holidays. Moreover, I want to thank the accelerator team at HIT, who readily spent many night shifts down-regulating the beam intensity for me.

BIBLIOGRAPHY

Many thanks also to Dr. Sabine Reinhardt who organized the beam time at MLL in Garching.

All current and former group members of E0409 I would like to thank for their support during beam times, the inspiring conversations, the pleasant atmosphere, enjoyable lunch breaks and the 'group activities'. My special thanks go to our former Diploma student Klaus Gwosch. Our discussions largely contributed to my understanding of 'cryptic' measurement results. Many thanks to Merle for carefully proofreading parts of this thesis. And I would like to thank Julia-Maria for willingly listen to my sorrows and for our little coffee breaks. Thanks also to Julia Telsemeyer, Nora, Stefan and Martin for sharing the PhD experiences with me.

Last, but by no means least, I would like to thank my family from the bottom of my heart. This thesis is dedicated to them. To my parents Rita and Georg, my sister Judith and my brother Patrick, thank you for your unconditional love and support. Moreover, I owe particular thanks to my brother-in-law Florian for proofreading this thesis and his valuable suggestions. Finally, and most importantly, I thank Mathies, for his patience, trust and love! Dankeschön!